3D RADIATIVE TRANSFER – CONTINUUM AND LINE FORMATION IN HOT STAR WINDS

Levin Georg Hennicker

3D RADIATIVE TRANSFER – CONTINUUM AND LINE FORMATION IN HOT STAR WINDS

Dissertation

an der
Ludwig–Maximilians–Universität (LMU) München

Ph.D. Thesis

at the
Ludwig–Maximilians–University (LMU) Munich

submitted by

Levin Georg Hennicker

born on 2nd December 1988 in Munich, Germany

Munich, December 16th 2019

1st Evaluator: Priv. Doz. Dr. Joachim Puls
2nd Evaluator: Prof. Dr. Barbara Ercolano

Date of the oral exam: 30th January 2020

Contents

List of Figures

List of Tables

Zusammenfassung

Von der Entstehung bis zu ihrem Ende als Supernovae bilden heiße, massereiche Sterne einen Grundpfeiler unseres Verständnisses über das Universum als Ganzes. Aufgrund der hohen Leuchtkräfte spielen dabei verschiedene 'feedback'-Mechanismen (z. B. in Form von kinetischer Energie und ionisierender Strahlung) eine zentrale Rolle, welche die Entwicklung ganzer Galaxien sowohl im heutigen als auch im frühen Universum beeinflussen.

Zur Quantifizierung dieser 'feedback'-Mechanismen müssen heiße, massereiche Sterne während all ihrer Entwicklungsstufen möglichst genau beschrieben werden, wobei unser heutiges Verständnis auf detaillierten Analysen von beobachteten und numerisch modellierten Sternspektren basiert. Unter der Annahme von sphärischer Symmetrie berücksichtigen moderne Spektralanalyse-Codes Abweichungen vom lokalen thermischen Gleichgewicht (NLTE), um die Interaktion des Strahlungsfelds mit den Besetzungszahlen einer Vielzahl von Elementen zu bestimmen. Allerdings gibt es viele Effekte, die zu räumlichen Asymmetrien führen, und dementsprechend mit mehrdimensionalen Analysewerkzeugen behandelt werden sollten.

In vorliegender Arbeit werden zu diesem Zweck numerische Methoden entwickelt, die einen ersten Schritt in Richtung selbst-konsistenter 3D NLTE Modelle darstellen. Wir stellen einen neu entwickelten 3D Strahlungstransport-Code vor, welcher in den Winden heißer, massereicher Sterne sowohl Resonanzlinien-Übergänge als auch ein vereinfachtes Kontinuum behandelt. Um das Strahlungsfeld zu berechnen, implementieren wir mit der Finite-Volumen-Methode (FVM) und der 'Short-Characteristics (SC) Methode' einen differentiellen und einen integralen Ansatz, wobei wir für beide Lösungsschemata ein unregelmäßiges kartesisches Gitter verwenden. Streuprozesse werden vermittels der 'beschleunigten Λ-Iteration' eingebunden. Um ein stabiles Konvergenzverhalten zu gewährleisten, entwickeln wir entsprechende nicht-lokale Operatoren.

Ein zweites zentrales Ziel dieser Dissertation ist die Untersuchung beider Methoden hinsichtlich ihrer Genauigkeit. Bezüglich sphärisch symmetrischer Test-Atmosphären erhielten wir zumeist sehr überzeugende Ergebnisse. Im Gegensatz zur SC-Methode scheitert die FVM allerdings an der Berechnung von Kontinua hoher optischer Tiefe. Bei der Berechnung von Resonanzlinien liefern dagegen beide Lösungsmethoden eine hohe Genauigkeit für alle betrachteten Test-Modelle, wobei die SC Methode in der Regel zu etwas besseren Ergebnissen führt.

Im dritten Teil dieser Arbeit wenden wir die 3D Strahlungstransport-Methoden auf verschiedene Problemstellungen in nicht-sphärischen Windschichtungen an, um einerseits das Leistungsvermögen unseres Codes unter realistischen Bedingungen zu überprüfen, und andererseits aktuellen Fragestellungen nachzugehen. Als erste Anwendung des 3D Kontinuum-Strahlungstransports betrachteten wir

das sogenannte 'Wind-Ablations-Modell', welches nach heutigem Stand der Forschung die Interaktion einer Akkretionsscheibe mit einem strahlungsdruck-getriebenen Sternwind beschreibt. Unter Verwendung unseres 3D Codes konnten wir zeigen, dass die Linienstärkenverteilung (welche zur Berechnung der Linien-Strahlungsbeschleunigung benötigt wird und selbst vom Strahlungsfeld abhängt) zumindest in den oberen Scheibenschichten, also dort wo Wind-Ablation eine zentrale Rolle spielt, von 1D Modellen adaptiert werden kann. Dies war eine bis dato unbestätigte Grundannahme innerhalb gegenwärtiger hydrodynamischer Simulationen.

Desweiteren analysierten wir die Auswirkungen von schneller Rotation und von dynamischen Magnetosphären auf die Spektraldiagnostik von UV Resonanzlinien. So zeigten wir, dass die Linienprofile von schnell rotierenden Sternwinden aufgrund der spezifischen Windstruktur und der Gravitationsverdunkelung stark von der Rotationsrate und der Inklination abhängen. Zur Untersuchung von dynamischen Magnetosphären beschrieben wir die Windschichtung einerseits durch magneto-hydrodynamische Simulationen und andererseits durch eine oftmals verwendete, vereinfachte Beschreibung von magnetischen Winden, dem sogenannten 'analytic dynamical magnetosphere'-Modell. Durch den Vergleich der daraus resultierenden Linienprofile zeigten wir, dass manche Annahmen innerhalb der vereinfachten Beschreibung überarbeitet werden müssen.

Zusammenfassend schließen wir, dass unsere 3D Strahlungstransport-Methoden für eine Vielzahl von asymmetrischen (nicht-relativistischen) Sternwinden verwendet werden kann. Während die FVM qualitative Untersuchungen von UV Resonanzlinien zulässt, sollte die SC-Methode angewendet werden, um quantitative Analysen durchzuführen. Desweiteren ist die FVM lediglich zur Berechnung von optisch dünnen oder geringfügig optisch dichten Kontinua geeignet, wohingegen die SC-Methode auch bei hohen optischen Tiefen realistische Ergebnisse liefert.

Abstract

Hot, massive stars form a keystone for understanding our Universe as a whole. During their lifetime, and also when they finally explode as a supernova, such objects shape their surroundings by feedback of kinetic energy, ionizing radiation, and nuclear processed material. Thus, hot, massive stars are frequently considered as 'cosmic engines' (see Bresolin et al. 2008), influencing the evolution of galaxies within the present and the early Universe.

To quantify such feedback effects, hot, massive stars need to be correctly described during all their evolutionary phases. Current knowledge is usually inferred by modelling their atmospheres (photosphere + wind), and by comparing the resulting synthetic spectra with observations. State-of-the-art spectrum-synthesis codes typically determine the radiation field and level populations in parallel, by assuming 1D spherical symmetry, and accounting for non-equilibrium (NLTE) conditions. Specific effects such as magnetic fields, however, can lead to deviations from spherical symmetry, rendering the results from 1D codes questionable.

The major objective of this thesis work is therefore defined by the development of 3D radiative transfer tools, which shall serve as a first step towards a full 3D NLTE modelling. We present a newly developed 3D code, considering the UV resonance-line formation and a simplified description of the continuum in the winds of hot, massive stars. To calculate the radiation field, we implement two independent methods, a finite-volume method (FVM) and a short-characteristics (SC) method, and discretize the equation of radiative transfer on a non-uniform Cartesian grid. For scattering-dominated problems, both solution schemes are augmented by an 'accelerated Λ-iteration' scheme, using newly developed non-local operators to ensure convergence.

Besides the development of the code, particular emphasis has been put on extensive tests of our radiative transfer modules, focussing on certain advantages and disadvantages of the developed tools. For spherically symmetric test models, we mostly found reasonable results. When calculating optically thick continua, however, the FVM breaks down, contrasted to the more elaborate SC method. The UV resonance-line formation, on the other hand, performs excellently for all applied methods and models, with slight advantages for the SC method when compared with the FVM.

Convinced about the performance of our 3D solution schemes, we applied the code to non-spherical wind models, in order to test the capabilities of the developed tools under realistic conditions, and to tackle specific questions related to current research. As a first application of our continuum solver, we considered the 'wind-ablation' model (describing the interaction of an accretion disc with a radiation-driven stellar wind). For such models, we validated an important assumption of current radiation-hydrodynamic simulations, namely that the so-called line-strength distribution function

(which is required for calculating the radiative line acceleration, and which depends on the radiation field) can indeed be adapted from 1D calculations, at least in the outer disc layers where wind ablation plays a primary role.

Further, we analysed the UV resonance-line formation both in fast rotating winds and in dynamical magnetospheres of hot, massive stars. For rapidly rotating wind models, the predicted line-profile shapes depend on the considered rotation rate, and on inclination. Their distinct behaviour is related to the description of gravity darkening, and the specific wind structure. When investigating the line formation in dynamical magnetospheres, we considered the wind structure as determined from magneto-hydrodynamic simulations, or calculated from a simplified – though frequently applied – description via the so-called 'analytic dynamical magnetosphere' (ADM) framework. By comparing the resulting line profiles obtained from our 3D code, we showed that the ADM needs to be partly revised, to enable a proper description of all relevant processes.

In summary, our 3D radiative transfer methods can be readily applied to (arbitrary, non-relativistic) winds of hot, massive stars that deviate from spherical symmetry. While the FVM allows us to qualitatively investigate the UV resonance-line formation, the SC method should be used for quantitative studies. Moreover, the FVM should be only applied to optically thin or marginally optically thick continua, whereas the SC method gives reliable results also for large optical depths.

Preamble

This thesis is about the numerical solution of 3D radiative-transfer problems in the winds of hot, massive stars, with particular emphasis on the development and extensive testing of a code using two independent solution schemes, the finite-volume method and the short-characteristics method. The discussion and first applications of each method have already been published in peer-reviewed journals:

- Hennicker L., Puls J., Kee N. D., Sundqvist J. O., 2018: *"3D radiative transfer: Continuum and line scattering in non-spherical winds from OB stars"* (A&A, 616, A140);

- Hennicker L., Puls J., Kee N. D., Sundqvist J. O., 2019: *"A 3D short-characteristics method for continuum and line scattering problems in the winds of hot stars"* (accepted for publication in A&A);

Since a re-formulation of the (already published) text would – in most cases – blur the major argumentation, parts of this thesis have been adopted from these two papers. Sections and subsections have been rearranged in order to enable a clear structure within this thesis, and to avoid overlaps. Further, we have re-formulated some paragraphs to enable a correct referencing, and to provide additional explanations.

To ensure an appropriate citation convention, we apply the following rules:

(i) If a complete chapter within this thesis is based, to a major part, on Hennicker et al. (2018) and/or Hennicker et al. (2019), we explicitly point this out at the beginning of the chapter.

(ii) If a section or subsection within this thesis is based, to a major part, on Hennicker et al. (2018) and/or Hennicker et al. (2019), we explicitly cite the corresponding publication with a footnote attached to the section title.

(iii) If only individual sentences have been copied from Hennicker et al. (2018) or Hennicker et al. (2019), we mark these sentences by $^\dagger\ldots^\dagger$ or $^\ddagger\ldots^\ddagger$, respectively.

Chapter 1

Introduction

1.1 Hot, massive stars in the context of modern astrophysics

The understanding of hot, massive stars is a basic prerequisite for interpreting fundamental properties of our Universe throughout its history. Already the first generation of hot, massive stars (Pop III stars) is thought to have contributed significantly to the reionization[1] of the Universe due to their strong, ionizing radiation field. The details, however, strongly depend on the initial mass function (IMF, i.e., the initial mass distribution for a stellar population), and are only poorly understood due to the lack of observations. Particularly the upper-mass limit and the slope of the IMF play a key role for constraining the reionization from stellar feedback quantitatively, since the luminosity typically depends over-proportionally on the stellar mass ($L_* \propto M_*^\alpha$, $\alpha \in [1,3]$, e.g., Owocki 2010, with L_* and M_* the stellar luminosity and mass, respectively). Additionally, Pop III stars are thought to be responsible for the first metal[2] enrichment of the early Universe, thus affecting the star formation rates of later stellar populations by shaping the cooling properties of star-forming regions. For a detailed understanding of the reionization and the first metal enrichment, a sound theoretical description of Pop III stars is required, together with observations.

But also in later epochs, hot, massive stars are of central importance, particularly regarding star-formation rates (again), and the chemical evolution of galaxies. On the one hand side, the strong radiation field of hot, massive stars can heat nearby star-forming regions, possibly preventing the collapse of molecular clouds from which stars are typically formed. On the other hand, the ionizing radiation and the resulting dynamical effects can also amplify over-densities within the interstellar medium (ISM), thus inducing star formation (Gritschneder et al. 2009). In this respect, both the deaths of hot, massive stars and their (supersonic) stellar winds are even more important. Since such objects typically end their lives as core-collapse supernovae (CC-SN), the associated shock fronts

---

[1] White et al. (2003) detected a complete Gunn-Peterson trough (i.e., a vanishing flux at wavelengths below the red-shifted Lyman-α line) for a quasar at redshift $z = 6.28$, whereas no such trough could be observed for quasars at $z \lesssim 6$. These findings suggest that the Universe entered the reionization epoch at red-shifts $z \approx 6$. We note, that (at least) the reionization of hydrogen cannot be explained by the number of ionizing photons emitted from quasars alone (Willott et al. 2005). A quantitative assessment in the early Universe, however, is difficult since the radiative feedback of both (massive) stars and quasars can only be estimated to date.

[2] The term 'metals' refers to all elements heavier than Helium, as commonly defined in astronomy.

possibly trigger star formation, resulting in a new generation of (massive) stars. Since the competition between heating and triggering is not completely clarified to date, particularly this topic is subject of current research. Additionally, the ISM becomes enriched with metals by supernovae explosions, thus affecting the chemical evolution of the host galaxy. Consequently, the cooling rates within following star-formation epochs become modified, again impacting the IMF of following stellar generations.

To enable quantitative predictions about the effects described above, a detailed understanding of hot, massive stars is required. In this respect, particularly the theory of star formation (determining the IMF) and stellar evolution (affecting the end products) are of key importance in both the early and the present Universe.

Star formation

In general, stars are formed by the collapse of molecular clouds, when gravitational forces overwhelm all counteracting forces (e.g., centrifugal forces, pressure gradients from thermal and turbulent motions, and, in later phases, possibly from radiation pressure). Since gravitational energy is transformed to heat during collapse, efficient cooling channels are required to keep the gas pressure on a reasonable scale. In the present Universe, cooling is typically realized by collisional excitation and radiative de-excitation of metals and molecules, as well as by dust radiation (e.g., Bodenheimer 2011). In the early Universe, however, neither metals nor dust were abundant. From a theoretical point of view, cooling in the early epochs has possibly been realized via the dissociation of molecular hydrogen and by atomic/molecular line cooling of hydrogen (see again Bodenheimer 2011). Since the ability of forming a star crucially depends on the cooling rate, the existence of massive stars in the early Universe is still under debate. Besides efficient cooling mechanisms, also external heating of molecular clouds, for instance by nearby hot stars, cosmic rays, or, in the early Universe, by the cosmic microwave background, plays a key role as well, and possibly halts or even prevents the collapse of a molecular cloud. The star-formation rate is thus constrained by the delicate interplay of various heating and cooling processes, and obviously depends on the occurrence and mass distribution of massive stars in the vicinity of star-forming regions.

When both heating and cooling allow for a collapse, a protostar develops which typically accretes mass further through a disc, and eventually starts nuclear fusion of hydrogen to helium within the core. An important difference between the formation of hot, massive stars, and cooler, less massive ones, is the timescale for accretion. While cool stars typically accrete the complete gas/dust reservoir before the collapse of the protostar onto the main sequence (MS)[3] has finished, massive stars typically still accrete mass during their early MS evolution (e.g., Bodenheimer 2011). Thus, massive stars are born within a cocoon of dust, and are therefore difficult to be observed directly during such evolutionary phases. A sound theoretical description is required, which – at least in the late formation phases – needs to account for the coupling of the hydrodynamic equations with radiation pressure terms, and the resulting competition between outflow and accretion rate (e.g., Kuiper et al. 2015, Kuiper & Hosokawa 2018). Since numerical modelling the complete problem is computationally challenging, these studies rely on certain simplifications, which need to be checked, and possibly relaxed in future

---

[3] The main sequence describes stars during core hydrogen burning. The begin and end of hydrogen burning in the core is entitled with zero-age main sequence (ZAMS) and terminal-age main sequence (TAMS), respectively.

studies.

The complete picture becomes complicated further, when additionally accounting for fragmentation. While the IMF needs to be constrained from the fragmentation on large scales (i.e., from the collapse of giant molecular clouds), the formation of multi-star systems and the occurrence of planetary systems needs to be explained on small scales. Thus, fragmentation is also an urgent topic of current research.

Finally, the question for the upper-mass limit of massive stars has not been answered to date. While in the present Universe, an upper-mass limit can be qualitatively defined by the strong radiation pressure originating from scattering and absorption at metal-lines, the maximum possible stellar mass in the early Universe (and in low-metallicity environments) is probably much larger, if there existed a strict upper limit at all (e.g., Crowther et al. 2012)[4].

Stellar evolution

Besides a detailed understanding of star-formation processes, also the evolution and late phases of hot, massive stars are of key interest in current research. Particularly the chemical and dynamical evolution of galaxies can be severely affected by stellar evolution, and even more by the deaths of hot, massive stars. Unlike cold stars, such stars develop a strong stellar wind (see below) with mass-loss rates up to $\dot{M} \approx 10^{-6} \cdots 10^{-4} M_\odot \mathrm{yr}^{-1}$, and terminal velocities of $v_\infty \approx 200 \cdots 3000\,\mathrm{km\,s}^{-1}$. Thus, already during their lifetime ($\approx 10^7\,\mathrm{yr}$), hot, massive stars can loose the major part of their initial mass, enriching the ISM with metals that have been produced in their cores by nuclear fusion processes. Additionally, the mass-loss significantly reduces the rotational rates due to the transport of angular momentum, thus affecting internal mixing processes, and possibly the wind-outflow due to decreased centrifugal forces. Although the MS evolution is relatively well understood (at least for spherically symmetric objects), there are still a lot of problems that need to be solved. Particularly, effects resulting from rotation, convection, mixing, core-overshoots, and magnetic fields can significantly impact current stellar evolution models, and need to be investigated.

Evenly (or even more) important is a sound quantitative description of the mass loss, which defines the mass of a star during its MS and post-MS evolution, and consequently the final fate of a considered star (see below), thus affecting the metal enrichment of the ISM. From a theoretical point of view, there exist various difficulties of mass-loss prescriptions already during the MS evolution, which are mainly related to clumping, (fast) rotation, magnetic fields, and pulsations. After core-hydrogen burning, eruptive explosions (with mass-loss rates of several solar masses per decade, as observed for the luminous blue variable η Car, e.g., Smith & Owocki 2006) complicate the complete picture even further. In these late evolutionary stages, large parts of the stellar envelope can be expelled into the ISM. To date, the nature of such violent eruptions is still under debate. One possibility is, that those are triggered by continuum driven outbursts (Smith & Owocki 2006) when a star approaches the Eddington limit[5].

---

[4] From an observational perspective, the largest stellar mass measured to date has been found in the star-forming region R136 of the Tarantula Nebula in the Large Magellanic Cloud, with $M_* \lesssim 170\,M_\odot$ corresponding to an initial mass $M_* \lesssim 195\,M_\odot$ (Rubio-Díez et al. 2017).

[5] At the Eddington limit, gravity is exactly balanced by radiation pressure from Thomson scattering (i.e., coherent electron

After core-hydrogen burning, heavier elements are successively produced, until the core consists only of iron[6], while nuclear fusion of Si, O, Ne, C, He, and H is still maintained in onion-like shell structures. Mixing processes, however, might play a significant role. For instance, rotationally induced mixing in (fast) rotating stars could prevent the formation of shell-structures, motivating a (chemically) homogeneous evolution. Within standard-evolutionary models, hot, massive stars evolve on the post-MS to red supergiants (RSG), blue supergiants (BSG), luminous blue variables (LBV), Wolf-Rayet (WR) stars, or to a sequence of some of these types.

In the early Universe, the evolution of massive stars is thought to be somewhat different due to the lack of metals and an inefficient radiative driving of a (steady) stellar wind (see below). Consequently, such stars presumably are fast rotators, since no angular momentum is lost with the stellar wind. We note, however, that when the star expands to the supergiant phase, conservation of angular momentum certainly forces the star to spin down. Additionally, the ZAMS and TAMS masses presumably coincide, such that those stars are thought to be more massive than their counterparts in the local Universe. The above mentioned continuum driven outbursts, however, might play a significant role also for Pop III stars. Due to the lack of observations, one can only theoretically speculate about such objects. With future observations by the James Webb Space Telescope (JWST), direct observations of Pop III stars might become possible.

The fate of hot, massive stars

When the nuclear fuel in the stellar core is exhausted, the star collapses due to gravity, and with the only (significantly) counteracting force originating from electron degeneracy pressure. At sufficiently high temperatures and densities, as found in the cores of collapsing massive stars, electrons are captured by protons (within the heavy nuclei), forming neutrons and neutrinos. Thus, while neutrons are accumulated, the electron degeneracy pressure becomes diminished, enabling a further collapse of the stellar core, until the pressure exerted by the neutrons (primarily originating from the repulsive component of the short-range nuclear force, see, e.g., Woosley & Janka 2005) potentially stops further collapse. At high stellar masses, the neutron pressure cannot overcome gravity, and the star collapses directly into a black hole.

During electron capture, a large amount of energy is released by the emission of neutrinos, which can interact with the (dense) infalling stellar envelope (although the cross section and thus the interaction probability is small). Due to the transfer of momentum, and due to reverse shocks originating from the infalling material crashing onto the neutron core, the outer layers can be expelled in a supernova explosion leaving behind a neutron star. If the (kinetic and potential) energy of the infalling layers overwhelms the transferred energy from the neutrinos, a black hole is produced by fallback. The transition between neutron star and black-hole formation depends sensitively on the mass of the star during collapse, and thus on the initial mass and on the various mass-loss mechanisms (see Heger et al. 2003).

We emphasize that, at least in theory, very massive stars could end their lives also as so-called

---

scattering).

[6] Since the binding energy per nucleon is largest for iron group elements, energy can only be produced by nuclear fusion of lighter elements, or by nuclear fission of heavier ones.

'pair-instability supernovae' (e.g., Kozyreva 2014). In such objects, electron-positron pairs are created after core-carbon burning by pair production and the destruction of high-energy photons. The radiation pressure becomes diminished and the stellar core is heated by contraction. With the sudden begin of nuclear fusion, the star can be completely disrupted. When assuming negligible mass loss of Pop III stars, pair-instability SN could have played a key role in the early Universe. To date, however, only few observed SN have been proposed to originate from the pair-instability scenario (e.g., Gal-Yam et al. 2009), indicating that Pop III stars possibly suffer from severe mass-loss mechanisms, which still need to be investigated in detail.

Therefore, the chemical enrichment of the ISM crucially depends on the end product of massive stars, with pair-instability SN ejecting the complete initial mass, whereas BH progenitors barely contribute at all. Additionally, one could aim at measuring the primordial IMF by counting different SN types and black holes in the early Universe (the latter possibly enabled by lensing techniques). To infer the IMF from such observables, a detailed understanding of the evolution of the progenitor objects is required.

Further complications

Thus far, we essentially neglected additional effects such as magnetic fields or (fast) rotation. Due to the transport of angular momentum with the stellar wind, the latter assumption seems to be reasonable for the later evolutionary phases of hot, massive stars in the present Universe. In the early Universe, however, rotation probably played a key role. For instance, the most energetic flashes in the Universe, the so-called 'long-duration Gamma-ray bursts' are thought to form by the collapse of rapidly rotating WR stars, and an associated accretion disc around a black hole (e.g., Woosley 1993, Woosley & Heger 2006). To date, the theoretical description is still far from being complete.

[‡]With the advent of gravitational wave (GW) observations (e.g., the black hole merger GW150914 with masses $M_1 \approx 36\,M_\odot$, $M_2 \approx 29\,M_\odot$, and redshift $z \approx 0.1$, observed at the advanced Laser Interferometric Gravitational-Wave Observatory (aLIGO), Abbott et al. 2016), the formation of heavy stellar-mass black holes became of key interest also in the (quasi) local Universe. Since massive stars are frequently found to be members of multiple star systems (see, e.g., Mason et al. 2009, Sana et al. 2013), they might explain the occurrence of GW events in the correct mass range. At least the formation of heavy black holes from single-star evolution, however, requires comparatively moderate mass loss rates (e.g., in low metalicity environments, or mass-loss quenching by magnetic fields, Petit et al. 2017, Keszthelyi et al. 2017).[‡]

Another issue of stellar evolution is the occurrence of (close) binaries, suffering from Roche-lobe overflow, common-envelope phases, and possibly even merging (e.g., de Mink et al. 2013). Particularly internal mixing and the rotation rates of the individual stars in a multi-star system can be severely affected.

To push the understanding of the present and early Universe further, a detailed understanding of hot, massive stars is required, particularly regarding the interplay of star formation, stellar evolution and feedback effects after stellar death. To date, there are still many open questions (as described above), that need to be answered. The general strategy to understand the complete picture consists of:

(i) Developing a sound theoretical description of stellar populations, with particular emphasis on

star formation, stellar evolution, and on the effects of mass-loss and the final fate of hot, massive stars. Due to the complexity of all these problems, a numerical approach needs to be applied, in order to evaluate the coupling of hydrodynamics with the radiation field, and possibly with small- and large-scale magnetic fields.

(ii) Developing numerical tools to translate the theoretical description into observable quantities (e.g., the spectra of single stars and multiple stellar systems, or composite spectra of whole galaxies). ‡For hot, massive stars, current knowledge is thus inferred from quantitative spectroscopy, i.e., by comparing observed spectra with synthetic ones, the latter obtained from numerically modelling their stellar atmospheres (photosphere + wind). State of the art atmospheric modelling is still performed by assuming spherical symmetry (e.g., CMFGEN: Hillier & Miller 1998; PHOENIX: Hauschildt 1992; PoWR: Gräfener et al. 2002; WM-BASIC: Pauldrach et al. 2001; FASTWIND: Puls et al. 2005 and Rivero González et al. 2012).‡

(iii) Observing hot, massive stars at each evolutionary stage in the present and early Universe, to rate the theoretical predictions.

For both points (i) and (ii), an adequate description of the radiative transfer is required. Since many problems deviate from spherical or other symmetries, results from 1D codes are questionable for such objects. In this thesis, we therefore aim at developing radiative transfer tools in 3D, which can be used for both consistent hydrodynamical modelling (in the distant future), and for spectral synthesis models (with certain simplifications, see Sect. 1.3, already now). Additionally, we consider only a small piece of the complete picture, by focussing on stellar winds during the MS evolution of hot, massive stars. Since a major uncertainty in the determination of the final mass of a star is mass-loss, we provide a brief introduction about typical mass-loss mechanisms in the following, focussing on the standard theory of line-driven stellar winds and various deviations from this description.

1.2   Stellar winds

In cool stars (e.g., the Sun, and similar stellar types), a thermally-driven wind can be generated by gas-pressure gradients within and from the hot corona ($\gtrsim 10^6$ K) to the interstellar medium (e.g., Hubeny & Mihalas 2014). With typical mass-loss rates of few $10^{-14} M_\odot \mathrm{yr}^{-1}$, such winds are too weak to effectively influence the evolution of their host stars.

Dust-driven stellar winds typically arise in asymptotic giant branch (AGB) stars, and possibly also in cool supergiants (e.g., in RSGs). Such winds are primarily accelerated by the absorption of photons at dust grains, which can be formed in the outer atmospheric layers in shock waves generated by pulsations. The quantitative description of dust-driven winds strongly depends on the condensation of the dust particles, and on their absorption properties. For RSGs, the mass-loss rate is typically on the same order as the mass-loss rate for line-driven stellar winds (e.g., van Loon 2010). Therefore, such stellar winds can have a severe impact during the late evolutionary stages of hot, massive stars.

As described above, the most violent ejecta during massive star evolution are found in LBVs, and presumably result from stars that approach or even exceed the Eddington limit. Since homogeneous,

super-Eddington stars are – independent of their radius[7] – unstable, such objects should not exist, at least theoretically. In clumped, porous media, however, some regions of the atmosphere might exceed the Eddington-limit, whereas others stay below, eventually resulting in massive continuum-driven outbursts (Shaviv 1998, see also Owocki et al. 2004).

In this thesis, we are primarily concerned with another type of mass-loss, namely with winds driven by the transfer of momentum due to scattering, absorption and emission of photons in atomic line transitions. Due to symmetry, the net momentum transferred by emission processes can be neglected. In the following, we briefly discuss the standard (spherically symmetric) line-driven wind theory to explain the basic physics, and describe various deviations from spherical symmetry that are to be discussed in this thesis.

1.2.1 Spherically symmetric line-driven stellar winds

Generally, an (arbitrary, multi-D) wind structure can be calculated by simultaneously solving the equation of continuity, momentum equation, energy equation, and the equation of state, accounting for all involved forces and energy reservoirs (originating from, e.g., gravity, rotation, magnetic fields[8], shear stresses, and radiation). Typically, these equations can only be solved numerically, which becomes computationally challenging particularly when considering expanding atmospheres. The major problem is introduced when radiation and flow quantities are coupled non-locally by, e.g., scattering of photons at free electrons or non-locally coupled line transitions (as occurring for non-monotonic velocity fields). Indeed, a fully consistent, multi-dimensional treatment of the radiation field together with the (time-dependent) hydrodynamic equations governing mass, momentum, and energy conservation, is computationally prohibitive to date.

To understand the underlying physics in the winds of hot stars, however, several simplifying assumptions can be applied. To this end, we follow Castor et al. (1975, hereafter CAK), and consider a stationary, spherically symmetric, line-driven stellar wind, with an optically thin background continuum such that the radiation emitted from the wind becomes negligible compared to the radiation emitted from the stellar core. For simplicity, we further neglect the finite-cone angle effect resulting from the different directions of incoming photons emitted from an extended stellar disc, only noting that an extension accounting for this effect has meanwhile been included within present day wind theory by Pauldrach et al. (1986) and Friend & Abbott (1986). Using the Sobolev method[9] to calculate radiation variables, and applying a prescribed distribution of available line transitions in frequency as well as line-strength range, the total acceleration exerted by all line transitions reads (see also Puls et al. 2000):

$$g_{\text{rad}} \propto \frac{N_0 \int L_\nu f_\nu(\nu)\nu \mathrm{d}\nu}{r^2} \left[\frac{1}{\rho} \frac{\mathrm{d}v}{\mathrm{d}r} \right]^\alpha, \tag{1.1}$$

---

[7] Similar to the inwards directed gravitational force, the outwards directed radiative force from Thomson scattering scales with $1/r^2$ due to the dilution of the radiation field. Thus, the ratio of radiative to gravitational acceleration remains spatially constant.

[8] To include magnetic fields, the Maxwell equations need to be accounted for as well.

[9] In Sobolev theory, the radiation field can be expressed by purely local quantities, assuming that the interaction region of the radiation field with the atmosphere is limited to a narrow spatial range. For more details, we refer to Sect. 2.2.6.

with r the radial coordinate, ρ, v the density and (radial) velocity of the wind, ν the frequency, L_ν the luminosity in the frequency interval $[\nu, \nu + d\nu]$, $f_\nu(v)$ the spectral distribution of available line transitions, $\alpha \in [0, 1]$ the power-law index (related to the distribution of the line-strength), and N_0 the normalization constant for the complete distribution function (related to the total number of lines). Eq. (1.1) has the following implications for a stellar wind:

(i) Due to the Sobolev approximation, the line force can be described by purely local quantities, simplifying the solution of the radiation hydrodynamic equations significantly. However, multi-resonances and line-overlaps have been intrinsically neglected, introducing severe uncertainties of the solution, when compared with models accounting for this effect, or when calculating time-dependent or magnetic winds, for instance.

(ii) The radiative force depends on the luminosity and the spectral distribution of available line transitions. In contrast to cool stars, a line-driven wind can be launched in the atmospheres of hot, massive stars due to the high luminosity and the occurrence of (strong) line transitions in the appropriate frequency range.

(iii) The line-strength becomes diminished with decreasing metallicity, resulting in a reduction of the line acceleration and mass loss. This effect can be deduced when considering the normalization constant, N_0. The number of lines within the contributing line-strength intervals scales as $N_0(z) \propto z^{1-\alpha}$ (see Puls et al. 2000, their Eq. 79), with z the metallicity. Thus, in low-metallicity environments (e.g., in the early Universe), the mass-loss rate becomes significantly reduced.

(iv) The line force depends on the gradient of the velocity field. This (in the entire Universe presumably) unique dependence is introduced by the Doppler effect, since the interaction of a photon with a given line transition is limited to the width of the profile function. For expanding atmospheres, the profile width is related to a length scale (the so-called Sobolev length) defined by the velocity gradient.

With the line acceleration given by Eq. (1.1), CAK were able to solve the radiation hydrodynamic equations for stationary problems. Based on their solution, present wind modelling is performed by applying a generalized form for the velocity field, the so-called β-velocity law:

$$v(r) = v_\infty \Big(1 - b\frac{R_*}{r}\Big)^\beta, \qquad b = 1 - \Big(\frac{v_{\min}}{v_\infty}\Big)^{1/\beta}, \qquad \rho(r) = \frac{\dot{M}}{4\pi r^2 v(r)}, \qquad (1.2)$$

with R_* the stellar radius, $v_{\min}$ and v_∞ the terminal and (photospheric) minimum velocity, respectively, and with the density derived from the continuity equation for a given mass-loss rate, $\dot{M}$.

While the analytic description of the winds in hot, massive stars by means of Eq. (1.2) avoids elaborate numerical simulations for determining the wind structure, the resulting solution certainly oversimplifies the problem. For instance, it became evident from both a theoretical and observational point of view that the winds of hot stars often deviate from spherical symmetry, show time-dependent variations of observed UV line profiles induced by, e.g., magnetic fields (Marcolino et al. 2013) or co-rotating interaction regions (Lobel & Blomme 2008), and typically are clumped. In the following, we summarize some of such problems, focussing on those topics that are to be examined within this thesis (i.e., fast rotation, magnetic winds, and wind ablation).

1.2.2 Time-dependent winds: Wind clumping

Already decades ago, Lamers & Morton (1976) noted that certain observations in the winds of hot, massive stars (e.g., the occurrence of highly ionized elements such as O VI) cannot be explained by a stationary wind, since the radiation energy is not sufficient to heat the wind to the necessary temperatures of $T \gtrsim 10^5$ K. Furthermore, hot, massive stars are typically soft X-ray emitters (see, e.g., the review by Kudritzki & Puls 2000 and references therein), which again cannot be explained by a smooth wind structure. These findings are meanwhile assumed to originate from a clumpy wind by clump-clump collisions, and from wind-embedded shocks induced by the line-driven instability (LDI, e.g., Lucy & Solomon 1970, Owocki & Rybicki 1984, Feldmeier et al. 1995).

From a theoretical point of view, the LDI is an intrinsic instability that is generally caused by the line-driving in expanding atmospheres. Formally, the LDI arises from Eq. (1.1)[10] and a small perturbation of the velocity field, which becomes amplified by the resulting perturbation of the radiative acceleration. Physically, the local comoving-frame transition frequencies at a given point in the wind are shifted out of the shadow of neighbouring material by a small perturbation of the velocity field. The number of line-driving photons, and consequently also the radiative acceleration, thus becomes significantly enhanced, until a shock is formed, with high temperatures ($\gtrsim 10^6$ K) and high densities in the post-shock regime. A clumpy wind structure develops, consisting of dense clumps within a fast and rarefied medium. Due to the shift of line-transition frequencies, the LDI is also named 'line de-shadowing instability'.

Since a time- and space-averaged clumped wind is quite similar to the smooth description of the wind (e.g., Feldmeier et al. 1995), the mass-loss is (if at all) only mildly affected, and evolutionary models should be independent of wind clumping. On the other hand, the line diagnostics for both recombination and UV resonance lines are severely influenced, and strongly depend on the assumed distribution of clumps (e.g., Sundqvist et al. 2010). Thus, current 1D spectral synthesis codes typically use a statistical approach to account for the clumped nature of the line-driven stellar wind by incorporating the so-called clumping factor, $\langle \rho^2 \rangle / \langle \rho \rangle^2$ (e.g., Owocki et al. 1988), while the velocity field is assumed to still follow a smooth description, particularly because non-monotonic velocity fields are very difficult to implement in current (typically comoving-frame) spectral synthesis codes (see Sect 2.2.2). While recombination lines (such as H_α), which quadratically depend on density, give very accurate estimates for the mass-loss rates in a smooth wind, the derived mass-loss rates from this diagnostic react sensitively on the distribution of clumps.

Besides the assumed smooth velocity field, a major drawback of the above described statistical approach is the definition of clumps as spherical shells within current 1D models. As shown by Sundqvist et al. (2018) using 2D radiation hydrodynamic simulations, however, the LDI in multi dimensions rather leads to complex 2D structures of the velocity and density. The impact of such structures on line synthesis models still needs to be investigated, which requires a consistent modelling of multi-D radiative transfer.

---

[10] Strictly speaking, Eq. (1.1) only holds for perturbations on scales larger than the Sobolev-length. For a qualitative explanation of the LDI, however, we can still use the radiative acceleration as given by Eq. (1.1).

1.2.3 Fast rotation

As outlined in Sect. 1.1, stars are formed from the collapse of a molecular cloud. During collapse, an initially slowly rotating cloud spins up due to conservation of angular momentum. The distribution of rotational velocities at the ZAMS depends on the details of the collapse, particularly on the initial angular momentum of the cloud, shear stresses, magnetic torques, and fragmentation processes. Due to the complexity of the problem, and because direct observations of hot, massive stars just entering the ZAMS are difficult (see above), the actual distribution of rotational velocities on the ZAMS is still not known.

At later evolutionary stages, hot, massive stars are expected to spin down due to the transport of angular momentum in the stellar interior (by, e.g., differential rotation) and with the stellar wind, by magnetic braking (if magnetic fields play a significant role), and/or by the expansion of the envelope when evolving to the blue or red supergiant phases. Thus, a wide variety of observed rotational velocities is to be expected.

Indeed, observations of O stars in the Large Magellanic Cloud (LMC) within the VLT-FLAMES Tarantula survey (VFTS) show a distribution of projected rotational velocities peaking at relatively low values ($v \sin i \approx 50 - 100 \, \text{km s}^{-1}$), and an extended tail towards higher ones (Ramírez-Agudelo et al. 2013). Within this sample one also finds those (hot, massive) stars hosting the highest rotation rates known to date, VFTS102 (O9 Vnnne, Dufton et al. 2011) and VFTS285 (O7.5 Vnnn, Walborn et al. 2012), rotating with a projected velocity $v \sin i \lesssim 600 \, \text{km s}^{-1}$. In both, the Small Magellanic Cloud (SMC) and in the Milky Way, a similar picture shows up, with maximum rotational speeds at somewhat lower values ($v \sin i \approx 400 \, \text{km s}^{-1}$, e.g., Penny & Gies 2009). When considering the B-star population within the VFTS, Dufton et al. (2013) showed that the projected velocities follow a bi-modal distribution with peaks at $v \sin i \approx 40 \, \text{km s}^{-1}$ and $v \sin i \approx 175 \, \text{km s}^{-1}$, and an extended high-velocity tail. In this study, the generally rapidly rotating Be stars have been excluded. From such and similar observations of hot, massive stars with different mass, metallicity, and multiplicity properties at different evolutionary stages, the distribution of rotational velocities at the ZAMS might be inferred, if all mass-loss and angular-momentum transport mechanisms were understood (e.g., Simón-Díaz & Herrero 2014), which might allow us to conclude about different angular-momentum transport mechanisms during star formation.

Although the rotational velocities on the ZAMS are not known, one might argue that newly born, hot, massive stars rotate at nearly their breakup velocity, due to the typically high initial angular momentum of the parental molecular clouds (Ramírez-Agudelo et al. 2013). If hot, massive stars were born with such high rotation rates, however, the stellar wind of (at least) B and late O type stars is neither efficient enough to reduce the stellar rotation rate to the observed low velocity peak, nor is it that inefficient to explain the observed maximum rotational velocities. While the low velocity peak may be explained by magnetic breaking (e.g., Dufton et al. 2013), the high rotation tail could originate from binary interactions by Roche-lobe overflow and the resulting spin-up of the companion (mass receiver) star. Both of these statements are speculative, and topic of current research. In any case, (fast) rotating stars show highly interesting phenomena, that affect the stellar interior via mixing processes, the stellar surface due to centrifugal forces, the stellar wind, and thus also the evolution and end products.
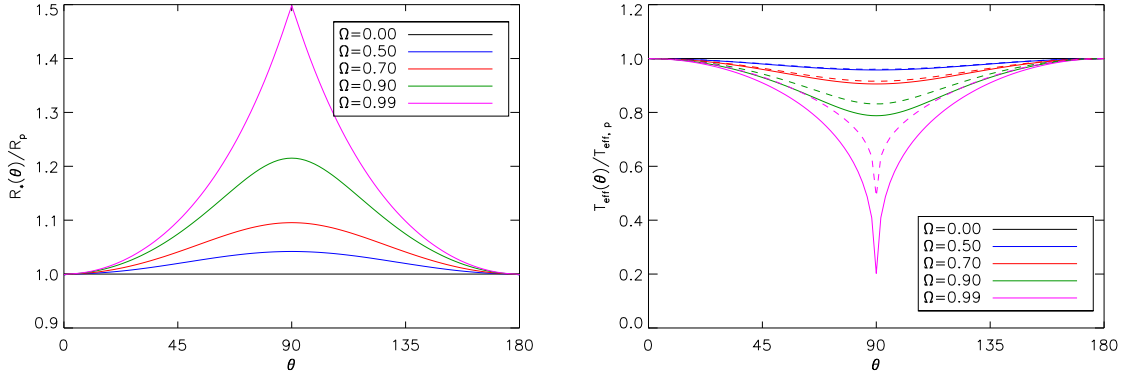
Figure 1.1: Left panel: Stellar surface distortion for different rotational parameters Ω, in units of the polar radius R_p. Right panel: Effective temperature variation (scaled by the polar effective temperature) for models with different rotational parameters Ω. The solid and dashed lines correspond to the von-Zeipel and ω-model, respectively (see text).

Surface distortion

Due to centrifugal forces, the surface of any rotating star becomes distorted. Assuming that the centrifugal force can be derived from a potential (e.g., for uniform or cylindrical rotation), and that the mass within the stellar surface can be approximated as a point mass located at the origin, the effective gravitational potential can be described by a Roche model (e.g., Collins 1963):

$$\Phi(r,\Theta) = -\frac{GM_*}{r} - \frac{\omega^2 r^2 \sin^2(\Theta)}{2}, \tag{1.3}$$

with angular velocity ω, and co-latitude Θ. The stellar radius as a function of co-latitude can then be found on equipotential lines, $\Phi(R_*(\Theta),\Theta) = \text{const}$. We emphasize that the stellar mass in Eq. (1.3) should be corrected for the Eddington parameter to account (at least) for the radiation pressure from Thomson scattering. Since, however, the radiative flux – and thus also the radiative acceleration – depends on the local gravity due to gravity darkening (see below), the Eddington parameter becomes a function of the potential. For simplicity, a correction due to electron scattering has therefore been discarded, rendering Eq. (1.3) only valid for low Eddington parameters. For supergiants, Eq. (1.3) needs certainly to be revised, although such objects should be only slow rotators. Under the above assumptions, the left panel of Fig. 1.1 shows the distorted stellar surface for different rotational parameters $\Omega = v_{\text{rot}}/v_{\text{crit}}$, where v_{rot} is the rotational speed of a considered star, and $v_{\text{crit}} = \sqrt{GM_*/R_{\text{eq}}}$ is its critical velocity with equatorial radius R_{eq}. We have defined the critical velocity as the rotational velocity for which the centrifugal acceleration at the equator exactly balances gravity, again neglecting additional outward radiative accelerations, e.g., from Thomson scattering, however for a different reason: Since at near breakup rotation rates, the equatorial flux at the equator becomes diminished in any case (see below), radiation pressure can indeed be neglected in equatorial regions. For $\Omega \to 1$ the surface becomes highly distorted, with the ratio $R_{\text{eq}}/R_{\text{pole}} \to 3/2$.

Gravity darkening and von Zeipel's theorem

von Zeipel (1924) showed that the radiative flux of rotating stars depends on the effective gravity (corrected for centrifugal accelerations). When the centrifugal force can be derived from a potential (e.g., within the Roche model, Eq. 1.3), the equation governing hydrostatic equilibrium reads:

$$\boldsymbol{\nabla} p_{\mathrm{g}} = -\rho \boldsymbol{\nabla} \Phi, \tag{1.4}$$

where ρ is the density, p_{g} describes the gas pressure, and Φ is the effective potential. The hydrostatic equilibrium condition requires that $\boldsymbol{\nabla} p_{\mathrm{g}}$ is anti-parallel to $\boldsymbol{\nabla} \Phi$. Thus, equipotential lines and isobars coincide, and the gas pressure can be described as a function of the potential alone, $p_{\mathrm{g}} = p_{\mathrm{g}}(\Phi)$. Additionally, noting that $\boldsymbol{\nabla} \times (\boldsymbol{\nabla} \phi) = \boldsymbol{0}$ for an arbitrary scalar field ϕ, one can easily show that also $\boldsymbol{\nabla} \rho$ is parallel (or anti-parallel) to the gradient of the potential, and therefore can be described as a function of the potential as well:

$$\boldsymbol{\nabla} \times \left(\boldsymbol{\nabla} p_{\mathrm{g}} \right) = \boldsymbol{0} = -(\boldsymbol{\nabla} \rho) \times (\boldsymbol{\nabla} \Phi) - \rho \underbrace{\boldsymbol{\nabla} \times (\boldsymbol{\nabla} \Phi)}_{\boldsymbol{0}} \qquad \Longleftrightarrow \qquad \boldsymbol{\nabla} \rho \parallel \boldsymbol{\nabla} \Phi. \tag{1.5}$$

Finally, the temperature can be calculated from the equation of state. Since $p_{\mathrm{g}} = p_{\mathrm{g}}(\Phi)$ and $\rho = \rho(\Phi)$, also the temperature can be written as a function of the potential, $T = T(\Phi)$, for an ideal, chemically homogeneous gas (with mean molecular weight $\mu = \mathrm{const.}$). Thus, from the hydrostatic equilibrium assumption, we find that equipotential lines, isobars, isodensities and isotherms all coincide, resulting in a 'barotropic' stellar structure. To deduce von Zeipel's theorem, we assume that energy is completely transported by radiation (radiative equilibrium), and that no energy is produced by, e.g., nuclear fusion processes. Assuming further that the energy transport can be described by a diffusive process (e.g., at large optical depths in 1D, $F \propto \dfrac{T^3}{\bar{\chi}_{\mathrm{R}}} \dfrac{\mathrm{d}T}{\mathrm{d}r}$, with $\bar{\chi}_{\mathrm{R}}$ the Rosseland opacity), one obtains:

$$\boldsymbol{\nabla} F = \boldsymbol{\nabla}(D \boldsymbol{\nabla} T) = 0, \tag{1.6}$$

where T is the temperature, $\boldsymbol{F}$ is the total radiative flux, and $D = D(\rho, T) = D(\Phi)$ is the diffusion coefficient that again can be described as a function of the potential. The radiative flux is then easily calculated as

$$\boldsymbol{F} = D \boldsymbol{\nabla} T = D \frac{\mathrm{d}T}{\mathrm{d}\Phi} \boldsymbol{\nabla} \Phi = -D \frac{\mathrm{d}T}{\mathrm{d}\Phi} \boldsymbol{g}_{\mathrm{eff}} = C \boldsymbol{g}_{\mathrm{eff}} \qquad \Longrightarrow \qquad T_{\mathrm{eff}} \propto |\boldsymbol{g}_{\mathrm{eff}}|^{1/4}, \tag{1.7}$$

with T_{eff} the effective temperature, and $C = \mathrm{const.}$ on equipotential lines. Since the effective gravity becomes reduced towards the equator due to increasing centrifugal forces, the radiative flux, and thus also the surface temperature, becomes reduced. The right panel of Fig. 1.1 shows the surface temperature (scaled by the polar value) for different rotational speeds.

Eddington (1925) suggested that the latitude-dependent temperature stratification could give rise to global, meridional circulating flows by generating a latitudinal pressure gradient (see also Sweet 1950). This effect would then affect the mixing in the stellar interior, and therefore possibly has a severe impact on stellar evolution. We emphasize, however, that both the original von-Zeipel-theory and the 'Eddington-Sweet' circulation are purely theoretical predictions, and still need to be confirmed by

observations. Particularly the underlying assumptions might need to be revised. For instance, Zahn (1992) generalized von-Zeipel's theorem for the case of a shellular rotation law (with ω = const. on horizontal surfaces, and including shear viscosity from the differential rotation). The qualitative picture, however, remains the same. Espinosa Lara & Rieutord (2011) presented an independent description of the gravity darkening by introducing the so-called ω-model, using an Ansatz $\boldsymbol{F} = -f(r, \Theta)\boldsymbol{g}_{\text{eff}}$, and solving for the unknown function $f(r, \Theta)$. The resulting gravity darkening law compares very well with solutions obtained from numerical modelling using the ESTER (EVOLUTION STELLAIRE EN ROTATION, see Rieutord et al. 2016 and references therein for a description of the numerical implementation) code, at least for a $3\,M_\odot$ star with a convective core and a radiative envelope, and assuming solid-body rotation at the stellar surface. The latitudinal variation of the surface temperature when calculated from the ω-model is weaker than in the 'standard' von Zeipel model (see Fig. 1.1).

From an observational point of view, the gravity darkening law is often approximated by $T_{\text{eff}}(\Theta) \propto |\boldsymbol{g}_{\text{eff}}(\Theta)|^{\beta_Z}$, where β_Z is used as a fit parameter. Indeed, β_Z is generally found to be smaller than the expected von-Zeipel value, $\beta_Z = 1/4$ (e.g., Domiciano de Souza et al. 2014), more consistent with the ω-model. For stars with a convective envelope, gravity darkening is thought to be suppressed with $\beta_Z \lesssim 0.08$ (Lucy 1967).

For a further understanding, observations of rapidly rotating stars are required. Since a latitude-dependent radiative surface flux should also affect the stellar wind in hot, massive stars, observations of wind lines might possibly serve as an indirect probe of the gravity darkening law.

Effects on the stellar wind[11]

The first attempt to model the winds of fast rotating OB stars was made by Bjorkman & Cassinelli (1993). These authors considered a purely radial line force, and neglected gravity darkening and the surface distortion. Within these approximations, a 'wind compressed disc' is formed in the equatorial plane. Cranmer & Owocki (1995) and Owocki et al. (1996) included the effects of non-radial line-forces into their 2D radiation-hydrodynamic simulations, and showed that the formation of the disc becomes suppressed due to a small, but significant polewards acceleration, giving rise to an associated polar velocity component that prevents the formation of a disc. When also accounting for gravity darkening (i.e., a decreased radial acceleration in equatorial regions), Owocki et al. (1996) further showed that a prolate wind structure develops, with decreased equatorial mass loss and velocity (see also the review by Owocki et al. 1998). Maeder (1999) proposed that an oblate wind structure might still be possible, when accounting for a polar variation of the ionization equilibrium induced by gravity darkening. This effect becomes particularly important when the local effective temperature drops below the bi-stability jump temperature[12]. Petrenz & Puls (2000) extended the hydrodynamic calculations from above by allowing for spatially varying line force multipliers, and showed that no major differences from the prolate wind structure arise, at least for OB stars above $T_{\text{eff}} \gtrsim 20\,\text{kK}$ with an optically thin Lyman continuum. Recently, Gagnier et al. (2019) reinvestigated the effects of rota-

---

[11] This Section has been copied – to a major part – from Hennicker et al. (2019, Sect. 5).

[12] The jump temperature is theoretically motivated by a stronger radiative line-driving due to lower ionization stages of iron for $T_{\text{eff}} \lesssim T_{\text{jump}} \approx 25\,\text{kK}$ (Vink et al. 1999). More recently, Petrov et al. (2016) predicted a somewhat lower jump temperature, $T_{\text{jump}} \approx 20\,\text{kK}$.

tion using 2D ESTER models, and predict either a 'single-wind regime' (with enhanced polar mass loss) or a 'two-wind regime' (with enhanced mass loss at latitudes where the effective temperature drops below the bi-stability jump temperature). However, the bi-stability jump is a purely theoretical prediction, that – at least quantitatively – has not been directly confirmed by observations to date. Furthermore, not even the actual shape of line-driven winds of (fast) rotating stars is completely clarified yet. While the Be phenomenon can clearly be associated with a disc, theory would (at least if the bi-stability plays only a minor role) predict a prolate wind structure. Since particularly the angular momentum loss depends strongly on the different descriptions of the stellar wind, the evolution of rotational velocities and thus the stellar evolution as a whole and the resulting end products of (fast) rotating, hot, massive stars are severely affected (e.g., by rotational mixing). Thus, rotating massive stars need to be further investigated. To understand which of the different models represents reality best (in different temperature regimes), one needs to compare synthetic profiles with observations. In this respect, investigating the effects of prolate and oblate wind structures is particularly important to distinguish between different theories.

1.2.4   Binary interaction

During star formation, fragmentation of a collapsing molecular cloud often leads to multi-star systems that can be found in a wide range of separations and mass ratios. Indeed, more than 50 % of the observed O-star population in the Tarantula nebula (Sana et al. 2013) are members of binary (or multiple) star systems. A similar picture arises for Galactic O stars (e.g., Mason et al. 2009), which additionally show a clear trend to smaller binary fractions for field stars when compared with stars located in clusters and associations.

Depending on separation and mass ratio, the individual stars in a multi-star system can interact already during the MS via tidal forces, Roche-lobe overflow or even merging (see, e.g., Vanbeveren 1991, de Mink et al. 2013). Considering the Roche-lobe overflow, the transport of angular momentum is particularly interesting: While the donor star spins down, the companion spins up, possibly yielding rotational velocities near the critical one. Thus, binary interactions could be responsible for the high-velocity tail of v_{rot} described in Sect. 1.2.3, and all its (theoretical predicted) implications. Furthermore, the evolution of both the primary and the secondary star is affected by the evolution of rotational velocities and related mixing processes.

Additionally, binary star systems are X-ray sources. One typically distinguishes between low-mass X-ray binaries (where the source of X-ray emission originates from the gravitational energy of a typically low-mass star filling its Roche lobe while orbiting a neutron star or a black hole) and high-mass X-ray binaries (where the X-rays are thought to be produced by wind-accretion from a massive star).

Further, X-ray emission can also be generated from the shock-heated gas when the stellar wind of a hot, massive star either collides with the surface of the companion, or within a wind-wind collision zone (if the companion has a significant stellar wind by itself, see Prilutskii & Usov 1976, Cherepashchuk 1976). Due to the dilution of the wind material, the X-ray flux depends on the separation of the binary system. Stevens et al. (1992) and Pittard (2009) investigated the dynamical effects of such wind-wind collisions using 2D and 3D hydrodynamical models, respectively. Again, depend-

ing on the separation and mass ratio, these authors predict a distinct density and velocity structure, that deviates from spherical symmetry. Thus, one can expect a variation of wind lines with orbital phase, and a dependence on inclination angle with respect to (w.r.t.) the observer. Future observations of such wind lines could provide an independent measurement of orbital parameters, if correctly modelled and interpreted.

1.2.5 Magnetic winds

Within the Magnetism in Massive Stars (MiMeS) survey, Wade et al. (2012) showed that $\lesssim 10\,\%$ of OB stars in the Milky Way have detectable magnetic fields ranging from $\approx 100\,\mathrm{G}$ to several kG (see also Grunhut et al. 2017 for Galactic O stars). The origin of such large-scale magnetic fields, which mainly show an ordered dipole configuration, is still under debate (see, e.g., the review by Walder et al. 2012).

While the magnetic fields of cool stars typically originate from subsurface convection layers and a resulting dynamo mechanism, such a scenario is not efficient in the radiative envelope of hot, massive stars. Although magnetic fields of OB stars could be generated within the convective core (see Charbonneau & MacGregor 2001), the major challenge from a theoretical point of view is the transport of the magnetic field from the interior to the stellar surface. Thus, also this type of dynamo is typically ruled out for explaining the surface magnetic fields (e.g., Neiner et al. 2015). Another scenario is provided by the generation of a magnetic field in the radiative envelope by differential rotation and the so-called Tayler-Spruit dynamo (see Spruit 1999, Spruit 2002, Maeder & Meynet 2004). A correlation of rotational properties with the magnetic field would then be expected, which has not been observed to date. Furthermore, independent numerical simulations by Braithwaite (2006) and Zahn et al. (2007) give contradictory conclusions about the existence of a self-stabilising dynamo effect. Thus, the Tayler-Spruit dynamo appears to be 'unlikely' for generating the large-scale magnetic fields in hot, massive stars, which are therefore commonly thought to be of fossil origin (e.g., Alecian et al. 2013), where the fossil field is possibly imparted from the molecular cloud during the formation phase, and is amplified/preserved during the (fully convective) pre main-sequence evolution by a dynamo mechanism. This scenario, however, needs to explain why only a subset of hot, massive stars is hosting detectable surface magnetic fields, although the involved physical processes should be the same for all stars during star formation. Alternatively, the magnetic fields of OB stars could also originate from binary interactions (merging or mass-transfer) during the pre-MS and MS evolution, resulting in a period of strong differential rotation that possibly gives rise to large-scale magnetic fields (e.g., Ferrario et al. 2009, see also Schneider et al. 2016). The above described problem of the fossil-field scenario would then automatically be avoided. Particularly for the most plausible scenarios (fossil-field and binaries), however, the details are still not clarified and need further investigations.

Due to the interaction of the (highly ionized) wind with the magnetic field, one expects deviations from the standard line-driven wind theory in any case, thus altering mass-loss rates, and the evolution and final fate of magnetic OB stars. [†]Indeed, magneto-hydrodynamic (MHD) calculations from ud-Doula & Owocki (2002) and ud-Doula et al. (2008) revealed that large-scale magnetic fields have a direct impact on the stellar wind, by channeling the wind outflow along magnetic-field lines, often producing disc-like structures around the magnetic equator.[†] These authors describe the competition

between the magnetic field energy and the kinetic wind energy by

$$\eta(r, \Theta) = \frac{\boldsymbol{B} \cdot \boldsymbol{B}}{4\pi\rho v^2} = \frac{v_A^2}{v^2} = \frac{1}{M_A^2} \, , \tag{1.8}$$

where Θ is the co-latitude measured from the magnetic pole, $\boldsymbol{B}(r, \Theta)$ is the magnetic flux density, and $v_A(r, \Theta)$, $M_A(r, \Theta)$ is the Alfvén speed (describing the propagation velocity of a magnetohydrodynamic wave, the so-called Alfvén wave) and the Alfvénic Mach number, respectively. In regions where $\eta \gg 1$ (i.e., $M_A \ll 1$), the magnetic field will channel the wind outflow, while for $\eta \ll 1$ (i.e., $M_A \gg 1$), the magnetic field lines are guided by the wind. In the winds of hot stars, $\eta(r, \Theta)$ can be estimated by considering a dipole magnetic field in competition with a spherically symmetric wind described by a β-velocity law (Eq. 1.2). At the magnetic equator, we easily obtain (see also ud-Doula & Owocki 2002):

$$\eta_{\mathrm{eq}}(r) = \frac{B_{\mathrm{p}}^2 R_*^2}{4\dot{M}_{\mathrm{B}=0}v_\infty} \frac{1}{\left(\dfrac{r}{R_*}\right)^4 \left(1 - b\dfrac{R_*}{r}\right)^\beta} =: \eta_* \frac{1}{\left(\dfrac{r}{R_*}\right)^4 \left(1 - b\dfrac{R_*}{r}\right)^\beta} \, , \tag{1.9}$$

with wind-confinement parameter η_*, polar magnetic field B_{p}, and $\dot{M}_{\mathrm{B}=0}$, v_∞ the mass-loss rate and terminal velocity of the star if no B-field was present. With Eq. (1.9), the transition point where the magnetic field lines are guided by the wind is then found where the Alfvénic Mach number at the equator becomes unity, $M_A(\Theta = 90°) = 1$. For the associated, so-called Alfvén-radius, R_A, we find:

$$\frac{R_A}{R_*} := \frac{r\big(\eta_{\mathrm{eq}} = 1\big)}{R_*} \approx 0.3 + \left(\eta_* + \frac{1}{4}\right)^{1/4} \, , \tag{1.10}$$

where the second equality is obtained from numerical fitting, assuming $\beta = 1$ and $b = 1$ (see ud-Doula et al. 2008). Thus, magnetic field lines with apex-radius[13] $r_{\mathrm{m}} \lesssim R_A$ are dominated by the (dipole) magnetic field, and the wind becomes essentially trapped. Furthermore, material originating from opposite footpoints eventually shocks in the equatorial plane, resulting in enhanced X-ray emission. The radiative force ($\propto \rho^{-\alpha}$, see Eq. 1.1 for the qualitative scaling) exerted on the dense post-shock material becomes diminished. If stellar rotation is negligible, the trapped material therefore falls back onto the stellar surface in a 'snake-like' pattern, and a 'dynamical magnetosphere' is formed. For high rotation rates, on the other hand, the trapped material is supported by centrifugal forces, forming a quite stable and strongly confined disc structure, a so-called 'centrifugal magnetosphere'. Since the magnetic field (at least within closed magnetic field lines) holds the material in rigid body rotation, we can define a limiting radius, R_K, where centrifugal and gravitational forces exactly balance (see ud-Doula et al. 2008):

$$\frac{GM_*}{R_K^2} = \frac{v_\Phi^2(R_K)}{R_K} \quad \underset{v_\Phi = v_{\mathrm{rot}}r/R_*}{\Longleftrightarrow} \quad \frac{R_K}{R_*} = \left(\frac{GM_*}{R_*} \frac{1}{v_{\mathrm{rot}}^2}\right)^{1/3} \, , \tag{1.11}$$

---

[13] The apex radius is here defined as the distance between the intersection point of a closed magnetic-field line with the equatorial plane, to the origin.
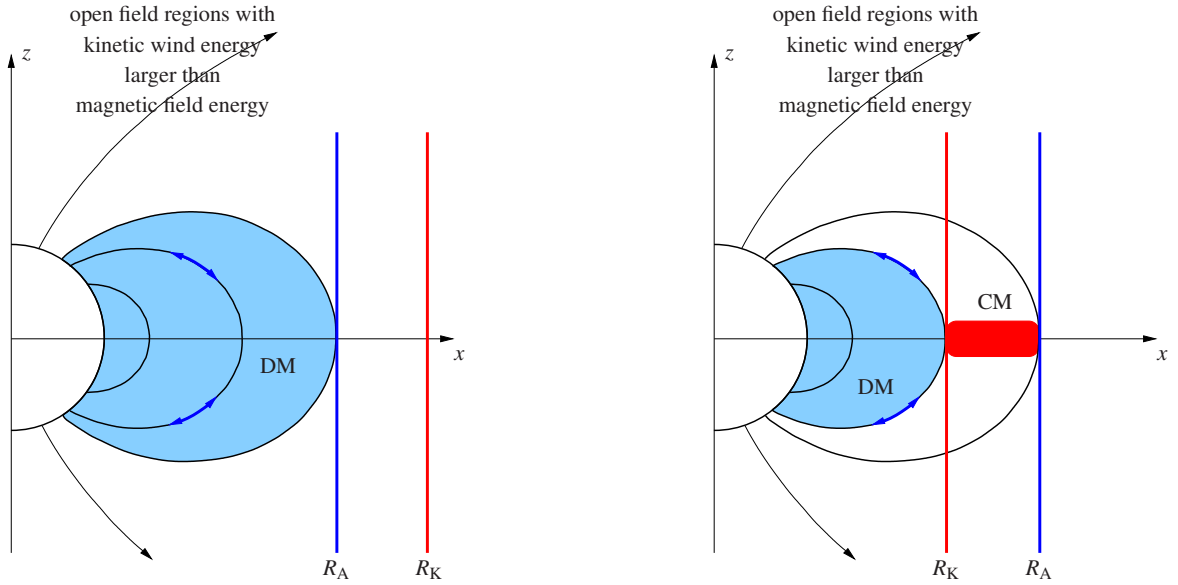
Figure 1.2: Illustration for the dynamical (left panel, DM) and centrifugal (right panel, CM) magnetosphere. For $R_A < R_K$, one obtains a dynamical magnetosphere where wind material becomes trapped in closed magnetic field regions, and falls back onto the stellar surface in a snake-like pattern. If $R_A > R_K$, material becomes centrifugally supported for $r > R_K$, and a strongly confined and stable centrifugal magnetosphere exhibits. For apex radii $r_m > R_A$, the magnetic field lines follow the (nearly) spherical stellar wind. Only this region contributes to the mass-loss. Adapted from Petit et al. (2013).

with v_{rot} the rotational velocity at the stellar surface. Thus, material is typically not supported by centrifugal accelerations for $r < R_K$, whereas material at $r > R_K$ is pulled outwards. Fig. 1.2 illustrates the formation of both the dynamical and centrifugal magnetosphere, with a dynamical magnetosphere obtained for $r < R_A < R_K$, and a centrifugal one in regions $R_K < r < R_A$ (see also Petit et al. 2013).

Since outflowing material is trapped within closed magnetic field lines, the mass-loss becomes significantly reduced (see, e.g., Babel & Montmerle 1997, Owocki & ud-Doula 2004, ud-Doula et al. 2008, Petit et al. 2017 for this and related effects). Thus, the final fate of magnetic OB stars is expected to be altered when compared with 'standard' evolutionary models. For quantitative predictions, however, the theoretical model needs to be rated against observations.

[†]Townsend & Owocki (2005) were able to explain the observed Balmer-line variability in σ Ori E, a magnetic Bp star, by applying the oblique-rotator model (with a tilt between the rotation and magnetic axes). Recently, Owocki et al. (2016) developed a simplified model, the 'analytic dynamical magnetosphere' (ADM), in order to provide a framework for the analysis of magnetic winds, and were able to reproduce the observed H_α-line variations of the magnetic Of?p star HD191612 (see Sect. 5.2).[†] Independent investigations using, e.g., UV resonance lines, however, have only been performed (if at all) in an approximate way (e.g., Marcolino et al. 2013).

1.2.6   Wind ablation

During the collapse of a molecular cloud, mass is typically accreted onto the protostellar core through a disc (e.g., Yorke & Sonnhalter 2002, Bodenheimer 2011). For hot, massive stars that have already ignited hydrogen, the nuclear energy can then be released by bipolar outflows and non-isotropic radiation, in contrast to a purely spherical accretion scenario where radiation pressure would halt accretion. Such objects, that are formally on the main sequence while still accreting through a disc will be named 'accreting high-mass stars' within this thesis. Depending on the luminosity of a considered star, the disc will be dissipated shortly after hydrogen ignition by radiative feedback (dominated by photoevaporation and radiative forces). The details, however, are still under investigation (see also Kuiper & Hosokawa 2018). In this respect, the implementation of radiation forces within their multi-D hydrodynamic numerical solution schemes is particularly challenging.

Furthermore, since accreting high-mass stars are both relatively scarce in number and difficult to be observed directly, current knowledge is typically based on purely theoretical investigations. The theoretical predictions for the interaction of a strong radiation field with a circumstellar disc, however, could be tested by comparing with observations of classical Be stars. Such stars constitute a significant fraction of main-sequence B stars, that harbour discs from which material is decreted by various (still unknown) processes (see, e.g., the review by Rivinius et al. 2013). Both the generation and the destruction of such decretion discs is still not completely clarified. While the occurrence of decretion discs is probably related to the (typically) high rotation rates of Be stars (at nearly critical rotational velocities, see Townsend et al. 2004) together with non-radial pulsations, the destruction of the circumstellar disc is thought to result from wind-ablation, i.e., from radiative forces along the disc surface (Kee et al. 2016). The latter process presumably plays also a significant role for accreting high-mass stars. Kee et al. (2016) applied certain assumptions (further discussed in Sect. 5.1, see also Kee 2015) to efficiently calculate the line force at the disc's surface layers. For instance, these authors applied a line-strength distribution function based on 1D spherically symmetric models even within the disc layers, although particularly the (local) ionization stages possibly strongly differ in such regions due to the shadow of the disc (that essentially blocks the irradiation from the star's backward hemisphere). Since, however, the line-strength distribution function – and thus also the line force – crucially depends on the ionizations stages, a consistent treatment of the continuum radiative transfer is required, at least to check the validity of the above mentioned assumptions.

1.3   Outline of the thesis

As described in the previous sections, extending our knowledge about hot, massive stars is required to understand our Universe as a whole. In this respect, mass loss plays a key role by affecting stellar evolution, stellar death, and stellar birth of new generations. To push our understanding about hot, massive stars further, such objects need to be modelled numerically, and the resulting synthetic spectra are to be compared with observations. An accurate treatment of radiative transfer becomes particularly important for both the numerical model (by affecting radiative forces and the energy budget within radiation hydrodynamic simulations) and for the calculation of synthetic spectra. Since many objects differ from the typically applied spherical symmetry, the radiative transfer needs to be calculated in

multi-D.

This thesis is a first step towards a 3D treatment of fully-consistent radiative transfer problems in the winds of hot, massive stars, where we focus on the development, implementation and extensive tests of various numerical tools. We aim at developing a 3D code to solve the time-independent equation of radiative transfer on a non-uniform Cartesian grid, applying the observer's frame formulation. To minimize turn-around times for determining the formal solution (i.e., the calculation of the radiation field for given sources and sink terms), we implement a finite-volume method (FVM, e.g., Patankar 1980 in the context of heat transfer), and a short-characteristics method (SC, Kunasz & Auer 1988) using different kinds of interpolations[14]. While the 3D FVM has already been applied in the context of 3D expanding wind structures (e.g., Adam 1990, Stenholm et al. 1991, Lobel & Blomme 2008), the 3D SC method has only been implemented for test cases (Ibgui et al. 2013a). These studies, however, are lacking a suitable accelerated Λ-iteration scheme (ALI). Thus, in this thesis, we implement an ALI scheme using newly-developed non-local operators, in order to calculate scattering dominated problems in optically thick environments.

Due to the computational complexity of 3D radiative transfer in expanding atmospheres with non-monotonic velocity fields, we follow the philosophy of simplifying the problem as much as possible, while still allowing us to analyse numerical inaccuracies inherent to each solution scheme, and to answer particular questions related to current research. To this end, we consider the line formation with an optically thin background continuum, and the continuum transfer in the absence of a line. While line-transitions are treated within the two-level-atom approach, the continuum will be calculated by accounting for electron scattering and thermal processes (described by the thermalization parameter, ϵ_C). The developed methods, however, will be extended for future applications.

This thesis is structured as follows:

(i) In Chapter 2, we introduce the basic theory of radiative transfer, discuss advantages and disadvantages of various numerical solution methods, and motivate several applied techniques (such as the observer's frame formulation, or the usage of Cartesian coordinates).

(ii) In Chapter 3, the actually applied numerical tools for obtaining the formal solution (including frequency and angular integrals) are discussed in more detail, together with the implementation of the ALI scheme, the spatial grid-construction procedure, and a long-characteristics post-processing routine for calculating synthetic line profiles. Additionally, we briefly present the applied parallelization strategy, and comment on the required computation time of each method.

(iii) In Chapter 4, we answer questions related to the reliability of the applied methods. To this end, we perform extensive tests, beginning with the searchlight-beam test and the calculation of zero-opacity models. For scattering dominated problems, we test our code by considering 1D spherically symmetric atmospheres. We discuss the convergence behaviour for different approximate Λ-operators, applied to different regimes, and rate the solutions obtained from the 3D FVM and SC method against solutions calculated with an accurate 1D code.

---

[14] As described in Sect. 2.2.4, the computation time of the so-called long-characteristics method can be significantly reduced when massively parallelized. We believe, however, that the (finally published) code shall also be used by those parts of the community that have no access to massively parallelizable architectures.

(iv) In Chapter 5, we apply our 3D solver to non-spherical stellar winds, in order to show the capability of our code, and to tackle some open questions of current research. As a first application to continuum transfer problems, we study specific aspects related to wind ablation in circumstellar discs of accreting high-mass stars. Further, we calculate the UV resonance-line formation in magnetically confined winds, and discuss the implications on magnetic-wind theory. Additionally, we predict UV resonance-line profiles for rapidly rotating stars, with the wind described by a prolate structure.

(v) In Chapter 6, we finish this thesis, by giving an outlook to future investigations, and point towards future extensions of the code developed during this thesis project.

Chapter 2

Theory of radiative transfer in expanding atmospheres

Since the primary objective of this thesis is the development of numerical methods for the solution of multi-D radiative transfer problems in the winds of hot stars, we discuss the basic theory of radiative transfer in the first part of this Chapter. Most derivations can also be found in textbooks, e.g., Mihalas (1978), Hubeny & Mihalas (2014). In the second part of this Chapter, we comment on various peculiarities of the radiative transfer in expanding atmospheres, and briefly review different numerical approaches for solving radiative transfer problems in multi-D.

2.1 Basic theory

2.1.1 The equation of radiative transfer

To derive a meaningful description of the radiation field within a stellar atmosphere, we start with the Boltzmann equation (e.g., Mihalas 1978, p. 33):

$$\frac{\partial f}{\partial t} + \boldsymbol{v} \cdot \boldsymbol{\nabla} f + \boldsymbol{F} \cdot \boldsymbol{\nabla}_p f = \left[\frac{\delta f}{\delta t}\right]_{\text{coll}}, \tag{2.1}$$

which describes the temporal evolution of the particle distribution $f(\boldsymbol{r}, \boldsymbol{p}, t)$ in phase-space, with spatial- and momentum-coordinates $\boldsymbol{r}$ and $\boldsymbol{p}$. $\boldsymbol{v}$ describes the corresponding velocity coordinates, $\boldsymbol{F}$ is an external force acting on the particles, $\boldsymbol{\nabla}_p$ is the gradient with respect to the momentum coordinates, and $[\delta f / \delta t]_{\text{coll}}$ is the change of the particle distribution function due to (generalized) collisions. Identifying now $f(\boldsymbol{r}, \boldsymbol{p}, t)$ with the distribution of photons, we find for the total number of photons within a phase-space volume element $[\boldsymbol{r} + \mathbf{d}\boldsymbol{r}, \boldsymbol{p} + \mathbf{d}\boldsymbol{p}]$:

$$\delta N = f(\boldsymbol{r}, \boldsymbol{p}, t) \, \mathrm{d}^3 r \, \mathrm{d}^3 p. \tag{2.2}$$

When considering a particular direction of propagation $\boldsymbol{n}$ (with $\boldsymbol{v} = c\boldsymbol{n}$, and the speed of light, c), the phase-space volume element can be transformed as

$$\mathrm{d}^3 r \, \mathrm{d}^3 p = \boldsymbol{n} \cdot \mathbf{d}\boldsymbol{S} \, c \, \mathrm{d}t \, p^2 \, \mathrm{d}p \, \mathrm{d}\Omega = \frac{h^3 \nu^2}{c^2} \boldsymbol{n} \cdot \mathbf{d}\boldsymbol{S} \, \mathrm{d}t \, \mathrm{d}\nu \, \mathrm{d}\Omega, \tag{2.3}$$

where $\mathbf{d}S$ is a (spatial) surface element through which the photons are propagating, $d\Omega$ is the solid angle into which the photons are propagating, and $d\nu$ is the frequency interval of the photons with momentum $p = h\nu/c$. For the transported energy, we obtain with Eq. (2.2) and Eq. (2.3):

$$\delta E = h\nu \delta N = \frac{h^4 \nu^3}{c^2} f(\mathbf{r}, \mathbf{p}, t) \mathbf{n} \cdot \mathbf{d}S \, dt \, d\nu \, d\Omega =: I_\nu \mathbf{n} \cdot \mathbf{d}S \, dt \, d\nu \, d\Omega. \tag{2.4}$$

The specific intensity, I_ν, is thus a distribution function, and defines the radiation energy in the frequency interval $[\nu, \nu + d\nu]$, that is transported per time dt and solid angle $d\Omega$ into a direction $\mathbf{n}$ through a surface $\mathbf{d}S$, and has units $[I_\nu] = \mathrm{erg\,cm^{-2}Hz^{-1}s^{-1}sr^{-1}}$. With this definition, and neglecting effects from general relativity such that external forces vanish, we can rewrite the Boltzmann equation in terms of the specific intensity:

$$\frac{\partial I_\nu}{\partial t} + c\mathbf{n} \cdot \boldsymbol{\nabla} I_\nu = c\frac{\delta I_\nu^+ - \delta I_\nu^-}{ds}, \tag{2.5}$$

again using $\mathbf{v} = c\mathbf{n}$. The collisional term describes the interaction of photons with matter along a path length $ds = cdt$, and is composed of emission and absorption terms. Defining macroscopic emission and absorption coefficients as

$$\delta E^+ =: \eta_\nu \mathbf{n} \cdot \mathbf{d}S \, dt \, d\nu \, d\Omega \, ds \qquad \Longleftrightarrow \qquad \delta I^+ = \eta_\nu ds \tag{2.6}$$

$$\delta E^- =: \chi_\nu I_\nu \mathbf{n} \cdot \mathbf{d}S \, dt \, d\nu \, d\Omega \, ds \qquad \Longleftrightarrow \qquad \delta I^- = \chi_\nu I_\nu ds \tag{2.7}$$

the equation of radiative transfer finally reads:

$$\begin{aligned}
\frac{1}{c}\frac{\partial I_\nu(\mathbf{n},\mathbf{r},t)}{\partial t} + \mathbf{n} \cdot \boldsymbol{\nabla} I_\nu(\mathbf{n},\mathbf{r},t) &= \eta_\nu(\mathbf{n},\mathbf{r},t) - \chi_\nu(\mathbf{n},\mathbf{r},t) I_\nu(\mathbf{n},\mathbf{r},t) \\
&= \chi_\nu(\mathbf{n},\mathbf{r},t)(S_\nu(\mathbf{n},\mathbf{r},t) - I_\nu(\mathbf{n},\mathbf{r},t)),
\end{aligned} \tag{2.8}$$

where we have introduced the source function $S_\nu = \eta_\nu/\chi_\nu$, which generally depends on frequency, direction vector, spatial coordinate, and time. For a particular direction $\mathbf{n}$, the equation of radiative transfer can also be formulated along a path s, yielding:

$$\frac{1}{c}\frac{\partial I_\nu(s,t)}{\partial t} + \frac{\partial I_\nu(s,t)}{\partial s} = \eta_\nu(s,t) - \chi_\nu(s,t) I_\nu(s,t). \tag{2.9}$$

2.1.2   Moments of the specific intensity

With the definition of the specific intensity, Eq. (2.4), we define the zeroth and first angular moment as:

$$J_\nu := \frac{1}{4\pi} \int I_\nu d\Omega \tag{2.10}$$

$$\boldsymbol{H}_\nu := \frac{1}{4\pi} \int I_\nu \mathbf{n} d\Omega, \tag{2.11}$$

called the 'mean intensity' and the 'Eddington flux', respectively. The mean intensity is related to the spectral energy density (per volume and frequency) of the radiation field via

$$u_\nu = \int_\Omega \frac{\delta E}{d^3 r \, d\nu} = \int_\Omega \frac{h^4 \nu^3}{c^3} f d\Omega = \frac{1}{c}\int_\Omega I_\nu d\Omega = \frac{4\pi}{c} J_\nu, \tag{2.12}$$

and the radiative flux through a surface (and per frequency) is related to the Eddington flux[1]:

$$\boldsymbol{F}_\nu = \int_\Omega \frac{\delta E}{\mathrm{d}\nu \mathrm{d}t \mathbf{d}\boldsymbol{S}} = \int_\Omega I_\nu \boldsymbol{n} \mathrm{d}\Omega = 4\pi \boldsymbol{H}_\nu. \tag{2.13}$$

A discussion of the second angular moment, K_ν, is skipped here for simplicity. We note, however, that K_ν is related to the radiation pressure, and thus is required when calculating the radiative force within (fully consistent) radiation-hydrodynamic simulations.

2.1.3 Rate equations

To describe the state of the gas, we apply the Boltzmann equation, Eq. (2.1), to material of a species i with corresponding particle distribution function f_i, where the subscript i corresponds to a particular element in a particular ionization stage and excitation state. When integrating over momentum space, we obtain:

$$\underbrace{\frac{\partial}{\partial t} \int f_i \mathrm{d}^3 p}_{\text{(I)}} + \underbrace{\int \boldsymbol{v} \cdot \boldsymbol{\nabla} f_i \mathrm{d}^3 p}_{\text{(II)}} + \underbrace{\int \boldsymbol{F} \cdot \boldsymbol{\nabla}_p f_i \mathrm{d}^3 p}_{\text{(III)}} = \underbrace{\int \left[\frac{\delta f_i}{\delta t} \right]_{\text{coll}} \mathrm{d}^3 p}_{\text{(IV)}}. \tag{2.14}$$

With the particle density as a function of $\boldsymbol{r}, t$

$$n_i(\boldsymbol{r},t) = \int f_i \mathrm{d}^3 p, \tag{2.15}$$

the average value of any quantity q is given by

$$\langle q \rangle(\boldsymbol{r},t) = \int \tilde{f}_i q \mathrm{d}^3 p = \int \frac{f_i}{\int f_i \mathrm{d}^3 p} q \mathrm{d}^3 p = \frac{\int f_i q \mathrm{d}^3 p}{\int f_i \mathrm{d}^3 p} = \frac{\int f_i q \mathrm{d}^3 p}{n_i}, \tag{2.16}$$

where $\tilde{f}_i$ is the distribution function normalized with respect to momentum. Since in phase space, the momentum coordinates (with corresponding velocity coordinates $\boldsymbol{v}$) and spatial coordinates are independent, such that $\boldsymbol{\nabla}\boldsymbol{v} = 0$, the individual terms in Eq. (2.14) are easily calculated as:

$$\text{(I)} = \frac{\partial n_i}{\partial t} \tag{2.17}$$

$$\text{(II)} = \int \boldsymbol{\nabla}(\boldsymbol{v} f_i) \mathrm{d}^3 p - \int f_i \underbrace{\boldsymbol{\nabla}\boldsymbol{v}}_{=0} \mathrm{d}^3 p = \boldsymbol{\nabla} \cdot \int \boldsymbol{v} f_i \mathrm{d}^3 p = \boldsymbol{\nabla} \cdot (n_i \langle \boldsymbol{v} \rangle) \tag{2.18}$$

$$\text{(III)} = \sum_j \int F_j \frac{\partial}{\partial p_j} f_i \mathrm{d}^3 p = \int \underbrace{[F_1 f_i]_{-\infty}^\infty}_{=0} \mathrm{d}p_2 \mathrm{d}p_3 + \cdots - \sum_j \int f_i \underbrace{\frac{\partial F_j}{\partial p_j}}_{=0} \mathrm{d}^3 p = 0, \tag{2.19}$$

where we have used that the phase-space density, f_i, approaches zero at infinite momentum since no particles with infinite momentum are allowed to exist, and that external forces should be independent

---

[1] Although $\boldsymbol{F}_\nu$ is actually a flux density, i.e., the radiation energy per time, per frequency, and *per* surface element, in astrophysics, $\boldsymbol{F}_\nu$ is commonly labelled simply as 'flux'.

of the particle's momentum-coordinates, such that $\nabla_p F = 0$. Finally, the collisional term can be written as:

$$(\text{IV}) = \left[\frac{\delta n_i}{\delta t} \right]_{\text{coll}} = -n_i \sum_{j \neq i} P_{ij} + \sum_{j \neq i} n_j P_{ji}, \tag{2.20}$$

with the so-called rate coefficients, $P_{ij} = R_{ij} + C_{ij}$ and $P_{ji} = R_{ji} + C_{ji}$, describing the rates per particle for depopulating and populating a given species i by radiative and collisional transitions. The NLTE[2] rate equations are then given by:

$$\frac{\partial n_i}{\partial t} + \nabla(n_i \langle v \rangle) = \sum_{j \neq i} n_j (R_{ji} + C_{ji}) - n_i \sum_{j \neq i} (R_{ij} + C_{ij}). \tag{2.21}$$

Throughout this thesis, we assume that (i) the level population are time-independent (stationary case), and (ii) that the kinematic timescale is much larger than the transition timescale. Then, the left-hand side of Eq. (2.21) becomes zero. Particularly when calculating level-populations including very high velocity fields (e.g., for supernovae), the latter assumption may have to be revised. We have sketched the most prominent radiative and collisional transitions occurring in hot stars and their winds in Fig. 2.1. Among those, one can distinguish between:

- Bound-bound transitions: An atom in an electron configuration i can be excited to an electron configuration j by absorbing a photon with corresponding transition frequency, or by a collision with a free electron. In the former case, the absorbed energy may be either re-emitted into a different direction (and possibly frequency through down-cascading), or be transferred to the thermal energy of the gas by collisional de-excitation. After collisional excitation, thermal energy from the gas can either be transformed to radiation energy by spontaneous emission, or, again, be re-transferred to the thermal pool by collisional de-excitation.

- Bound-free transitions: Energy can either be removed from the radiation field by photo-ionization, or added to the radiation field through recombination processes followed by radiative de-excitations of high electron configuration states. Similarly, collisional recombination processes can add energy from the thermal pool of the gas to the radiation field.

- Electron scattering: Photons are scattered, and become redistributed over angle (and frequency).

In the winds of hot stars, the transitions are dominated by radiative bound-bound and bound-free processes, since collisional processes are rare in such low-density environments, as well as by 'Thomson scattering' (i.e., coherent electron scattering, see Sect. 2.1.5).

2.1.4   Bound-bound transitions

To calculate the radiative rates for bound-bound transitions with levels $i < j$, one can use the Einstein coefficients for emission and absorption. The Einstein coefficient for absorption, B_{ij}, is defined such

---

[2] NLTE=non-LTE=non local-thermal-equilibrium, i.e., a deviation of occupation numbers from the equilibrium values defined by the local temperature.
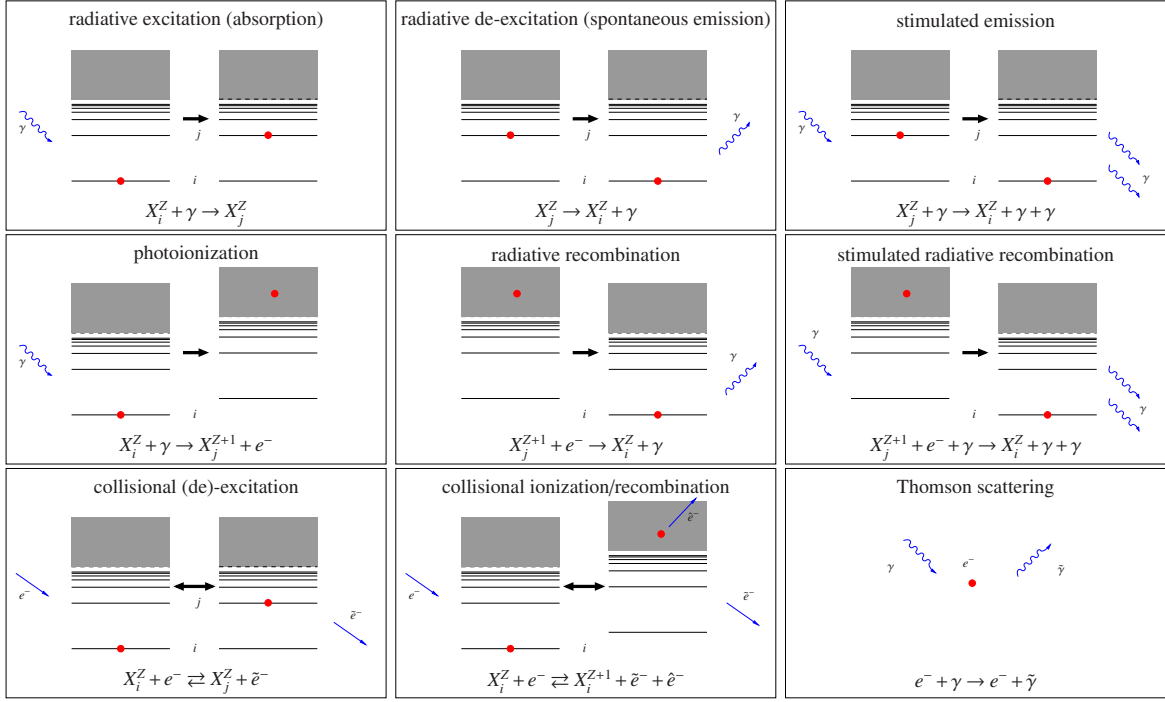
Figure 2.1: Most prominent (radiative and collisional) transitions occurring in the winds of hot stars. The reaction equations describe an element X with charge Z and at level i or level j, with γ, $\tilde{\gamma}$, e^-, $\tilde{e}^-$ and $\hat{e}^-$ describing photons and electrons of (potentially) different energy and direction. The red dots represent the electron either in a bound state or within the continuum (indicated by the grey shaded area). Collisions with other atoms can been neglected, since the collisions with free electrons dominate in the (highly) ionized plasma. Auto-ionizations and dielectronic recombination are not shown here.

that

$$\frac{\delta N_{\text{abs}}}{\mathrm{d}^3 r \, \mathrm{d}t} = n_i B_{ij} I_\nu \Phi_{ij}(\nu) \mathrm{d}\nu \frac{\mathrm{d}\Omega}{4\pi} \tag{2.22}$$

gives the transition rate from level i to level j produced by absorption of radiative energy with specific intensity I_ν in a frequency interval $[\nu, \nu + \mathrm{d}\nu]$ and solid angle $[\Omega, \Omega + \mathrm{d}\Omega]$. n_i is the particle density in level i, and $\Phi_{ij}(\nu)$ is the profile function for absorption in the comoving frame. $\Phi_{ij}(\nu)$ describes the conditional probability for absorbing a photon in the frequency range $[\nu, \nu + \mathrm{d}\nu]$, if an absorption event has happened. Since the corresponding radiative rate coefficient is given by the total number of absorptions divided by the total number of absorbers, we obtain, by integrating Eq. (2.22) over solid angle and frequency:

$$R_{ij} = B_{ij} \frac{1}{4\pi} \int \Phi_\nu I_\nu \mathrm{d}\nu \mathrm{d}\Omega =: B_{ij} \bar{J}, \tag{2.23}$$

with $\bar{J}$ the 'scattering integral'. Analogously, one may define the Einstein coefficient for stimulated emission, B_{ji}, by

$$\frac{\delta N_{\text{stim. em}}}{\mathrm{d}^3 r \mathrm{d}t} = n_j B_{ji} I_\nu \Psi_{ij}(\nu) \mathrm{d}\nu \frac{\mathrm{d}\Omega}{4\pi}, \tag{2.24}$$

where $\Psi_{ij}(\nu)$ is the emission profile describing the conditional probability that a photon is emitted in a frequency range $[\nu, \nu + \mathrm{d}\nu]$. For simplicity, we assume complete redistribution throughout this thesis, i.e., the frequency and angular distribution of an emitted photon shall be independent of the process that excited the atom to a state j in the first place. Then, $\Psi_{ij} = \Phi_{ij}$. To calculate the total rate, we additionally need to account for spontaneous emission events. For those, the corresponding Einstein coefficient, A_{ji}, is defined as

$$\frac{\delta N_{\text{spont. em}}}{\mathrm{d}^3 r \mathrm{d}t} = n_j A_{ji} \Psi_{ij}(\nu) \mathrm{d}\nu \frac{\mathrm{d}\Omega}{4\pi} \rightarrow n_j A_{ji} \Phi_{ij}(\nu) \mathrm{d}\nu \frac{\mathrm{d}\Omega}{4\pi}, \tag{2.25}$$

where again we have assumed complete redistribution. Noting that the profile function is normalized, we find for the downward transition rate coefficient after some algebra:

$$R_{ji} = A_{ji} + B_{ji} \frac{1}{4\pi} \int \Phi_\nu I_\nu \mathrm{d}\nu \mathrm{d}\Omega = A_{ji} + B_{ji} \bar{J}. \tag{2.26}$$

When identifying induced emission processes as 'negative' absorption, the net absorbed energy for a bound-bound transition can be calculated using Eqs. (2.22) and (2.24):

$$\frac{\delta E^-}{\mathrm{d}^3 r \mathrm{d}t} = h\nu_{ij} \left[\frac{\delta N_{\text{abs}}}{\mathrm{d}^3 r \mathrm{d}t} - \frac{\delta N_{\text{stim. em}}}{\mathrm{d}^3 r \mathrm{d}t} \right] = \frac{h\nu_{ij}}{4\pi} \Phi_{ij}(\nu)(n_i B_{ij} - n_j B_{ji}) I_\nu \mathrm{d}\nu \mathrm{d}\Omega, \tag{2.27}$$

with ν_{ij} the rest-frame frequency of the considered line transition. Thus, the corresponding opacity can be found by comparing the absorbed energy with the definition of the absorption coefficient (Eq. 2.7):

$$\chi_{ij} = \frac{h\nu_{ij}}{4\pi} \Phi_{ij}(\nu)(n_i B_{ij} - n_j B_{ji}) = \frac{\pi e^2}{m_e c}(gf)\left[\frac{n_i}{g_i} - \frac{n_j}{g_j} \right] \Phi_{ij}(\nu), \tag{2.28}$$

where the Einstein coefficients (that can be calculated from quantum mechanics and are therefore determined solely from atomic properties[3]) have been expressed by means of the oscillator strength f, (gf) is the gf-value of the considered transition, g_i, g_j are the statistical weights of the lower and upper level, respectively, and m_e, e are the electron's rest mass and the elementary charge. The opacity for a single line transition is given by the profile function and a frequency-independent part (the so-called 'frequency integrated opacity', due to the normalization of the line profile). In analogy, the emission coefficient is simply given by:

$$\eta_{ij} = \frac{h\nu_{ij}}{4\pi} \Phi_{ij}(\nu) n_j A_{ji}. \tag{2.29}$$

---

[3] Following, e.g., Hubeny & Mihalas (2014, p. 136), $\frac{h\nu_{ij}}{4\pi} B_{ij} = \frac{\pi e^2}{m_e c} \frac{\sum_{i' j'} g_{i'} f_{i' j'}}{g_i} = \frac{\pi e^2}{m_e c} \frac{(gf)}{g_i}$, with the summation performed over all substates of the transition $i \rightarrow j$. Further, the Einstein coefficients are related by $g_i B_{ij} = g_j B_{ji}$ and $A_{ji} = \frac{2h\nu_{ij}^3}{c^2} B_{ji}$ (e.g., Hubeny & Mihalas 2014, p. 120).

The above equations already show the basic problem of radiative transfer: On the one hand side, the intensity depends on the occupation numbers via the opacity and emissivity occurring in the equation of radiative transfer (Eq. 2.8). On the other hand, the occupation numbers depend on the specific intensity (integrated over frequency and solid angle) through the rate equations and corresponding radiative rates (Eqs. 2.21, 2.23, 2.26). If collisional transitions are dominating, LTE is obtained, and this problem can be avoided. In the winds of hot stars, however, the radiative rates typically dominate over the collisional ones, giving rise to profound non-LTE effects. Furthermore, one needs to account for a large number of elements and lines, in order to correctly describe the full problem. For current computer power, a full treatment in three (spatial) dimensions is still prohibitive. Thus, in this thesis, we focus on the so-called two-level-atom (TLA) approach (see Sect. 2.2.1 and Sect. 2.3), that considerably simplifies the problem while still allowing us to analyse resonance-line transitions, which can be described by the transition rates between the ground and a (strongly dominating) excited state. At least for testing different numerical tools, the TLA approach already provides a reasonable framework. For simplicity, we additionally neglect photo-ionization and recombination rates, and (sensibly) assume almost constant ionization stages within the line-driven stellar wind.

2.1.5 Continuum scattering

From a classical point of view, charged particles oscillate in the presence of a radiation field, which consequently becomes redistributed in angle (and frequency). Due to the powerful radiation field of hot stars, most elements occurring in the wind are either completely ionized (e.g., H, He), or in high ionization stages. Thus, the major contribution to the continuum comes from the interaction of light with free electrons. From simple kinematics, it can be shown that the re-distribution in frequency follows from (e.g., Rybicki & Lightman 1986, p. 196):

$$\nu = \frac{\tilde{\nu}}{1 + \frac{h\tilde{\nu}}{m_e c^2}(1 - \cos(\theta))}, \tag{2.30}$$

where ν and $\tilde{\nu}$ are the frequency of the scattered and incoming photon, respectively, and θ is the scattering angle. For the frequency range considered within this thesis (corresponding to wavelengths $\lambda > 100\,\text{Å}$), the scattering at free electrons is nearly coherent, $\nu \approx \tilde{\nu}$. The corresponding cross section is given by the Klein-Nishina formula, which then reduces to:

$$\sigma_{\text{Th}} = \frac{8\pi e^4}{3m_e^2 c^4} \approx 6.65 \cdot 10^{-25}\, cm^2. \tag{2.31}$$

We note that the cross section for protons or other ions in a completely ionized stage can be calculated by simply replacing the elementary charge and the electron's mass with the ion's charge and mass, respectively. The resulting cross-sections, however, are very low (at least for moderate charges), and corresponding scattering events can be neglected. Since highly ionized elements typically have low abundances, such ions do not contribute to the continuum scattering either. Also, Raman/Rayleigh scattering (i.e., line scattering far away from the line centre, where virtual states of bound electrons can be excited) is negligible in the winds of hot stars, since most abundant elements (H, He) are

completely ionized. In summary, continuum scattering in the winds of hot stars is therefore mainly controlled by Thomson scattering.

Because the cross section for Thomson scattering is, to a good approximation, isotropic and coherent, the energy absorbed (i.e., scattered out) from a beam with direction $\boldsymbol{n}$ is given by

$$\frac{\delta E^-}{\mathrm{d}^3 r\,\mathrm{d}t} = n_\mathrm{e}\sigma_\mathrm{Th}I_\nu(\boldsymbol{n})\mathrm{d}\nu\mathrm{d}\Omega \quad \Longleftrightarrow \quad \chi_\mathrm{Th} = n_\mathrm{e}\sigma_\mathrm{Th}, \tag{2.32}$$

with n_e the electron density (corresponding to the number of available scattering centres). Accounting for all incoming beams with directions $\tilde{\boldsymbol{n}}$, the energy emitted (i.e., added) to a beam with direction $\boldsymbol{n}$ is accordingly:

$$\frac{\delta E^+}{\mathrm{d}^3 r\,\mathrm{d}t} = \left[\int n_\mathrm{e}\sigma_\mathrm{Th}g(\tilde{\boldsymbol{n}},\boldsymbol{n})I_\nu(\tilde{\boldsymbol{n}})\frac{\mathrm{d}\tilde{\Omega}}{4\pi}\right]\mathrm{d}\nu\mathrm{d}\Omega, \tag{2.33}$$

where $g(\tilde{\boldsymbol{n}},\boldsymbol{n})$ is the angular phase function describing the angular redistribution of a scattering event. Throughout this thesis, we assume isotropic scattering with $g(\tilde{\boldsymbol{n}},\boldsymbol{n}) = 1$. The associated error introduced by this approximation should be very small (Mihalas 1978, p. 30). Then, the emissivity for Thomson-scattering is simply given by:

$$\eta_\mathrm{Th} = n_\mathrm{e}\sigma_\mathrm{Th}J_\nu. \tag{2.34}$$

As was the case for the bound-bound transitions, continuum scattering complicates the solution of the equation of radiative transfer significantly, since the emissivity depends again on the radiation field, and vice versa. This dependency corresponds to a non-local coupling of the radiation field.

2.2 Numerical treatment of 3D radiative transfer problems

To solve the coupled problem of unknown occupation numbers and the unknown radiation field, an iteration scheme is required (the so-called Λ-iteration scheme and associated acceleration techniques). Particularly for 3D problems, a direct inversion is prohibitive due to memory limitations. Generally, one starts with an initial guess for the opacity and emissivity, and numerically solves the equation of radiative transfer for many angles and frequencies (the so-called formal solution). The scattering integrals, $\bar{J}$, and mean intensities, J_ν, are then obtained by integrating the specific intensity over frequency and/or solid angle, and the rate equations can be solved. With the new occupation numbers, the emissivities and opacities are updated, and the iteration cycle starts from the beginning. Thus, $N_\Omega \times N_\nu$ formal solutions are required on a 3D grid with N^3 grid points, where N_Ω and N_ν describe the number of angular and frequency points, respectively. To solve this computationally challenging problem, efficient solution methods are required. In the following, we briefly discuss some simplifying assumptions used within this thesis, and give an overview of available techniques for the solution of the equation of radiative transfer. We note already here, that we will use 3D Cartesian coordinates within this thesis, and refer to Sect. 2.2.7 for a discussion about alternative coordinate systems.

2.2.1 Simplifying assumptions

As one aim of this thesis is to test different numerical methods, we use certain simplifying assumptions that allow us to consider test problems under realistic conditions, while avoiding the solution of the complete rate equations. Generally, we consider the continuum formation in the absence of a line, and approximate the line formation by a two-level atom assuming an optically thin continuum.

Continuum

To calculate the continuum, we account for Thomson scattering, and consider all other processes as interacting with the thermal pool ('true processes'). For the opacity and emissivity, we then find:

$$\chi_\nu = \chi_{\text{true}} + \chi_{\text{Th}} \tag{2.35}$$

$$\eta_\nu = \eta_{\text{true}} + \eta_{\text{Th}} = \chi_{\text{true}} B_\nu + \chi_{\text{Th}} J_\nu, \tag{2.36}$$

where the Kirchhoff-Plank law ($\eta_{\text{true}} = \chi_{\text{true}} B_\nu$) states that in thermal equilibrium (and often also in LTE), the true emissivity is related to the Planck function B_ν. The continuum source function can then be calculated as:

$$S_C = \frac{\eta_\nu}{\chi_\nu} = (1 - \epsilon_C) J_\nu + \epsilon_C B_\nu, \tag{2.37}$$

with thermalization parameter $\epsilon_C = \chi_{\text{true}}/(\chi_{\text{true}} + \chi_{\text{Th}})$ describing the photon-destruction probability. In the absence of a line, and considering only a narrow frequency band, we only need to consider one frequency point, and the amount of required calculations becomes considerably reduced.

Line

The line source function for a two-level atom can be calculated from Eqs. (2.28) and (2.29), and is given as (see also, e.g., Mihalas (1978)):

$$S_L = (1 - \epsilon_L)\bar{J} + \epsilon_L B_{\nu_{ij}} \tag{2.38}$$

$$\epsilon_L = \frac{\epsilon'}{1 + \epsilon'}, \quad \epsilon' = \frac{C_{ji}}{A_{ji}}\left[1 - \exp\left(-\frac{h\nu_{ij}}{k_B T}\right)\right],$$

†with C_{ji} and A_{ji} being the collisional rate coefficient (from the upper to the lower level) and the Einstein-coefficient for spontaneous emission, respectively.† We note that the line source function is independent of the (observer's frame) frequency. As in the continuum case, ϵ_L can be interpreted as a photon-destruction probability (per scattering event).

2.2.2 Comoving and observer's frame

Within the two-level approach, the number of required frequency points is limited to a reasonable resolution of the profile function in the comoving frame. Since photons appear red/blue shifted for atoms moving with a velocity relative to the emitting source due to the Doppler effect, the number of (observer's frame) frequency points can be relatively large, in order to cover the complete profile
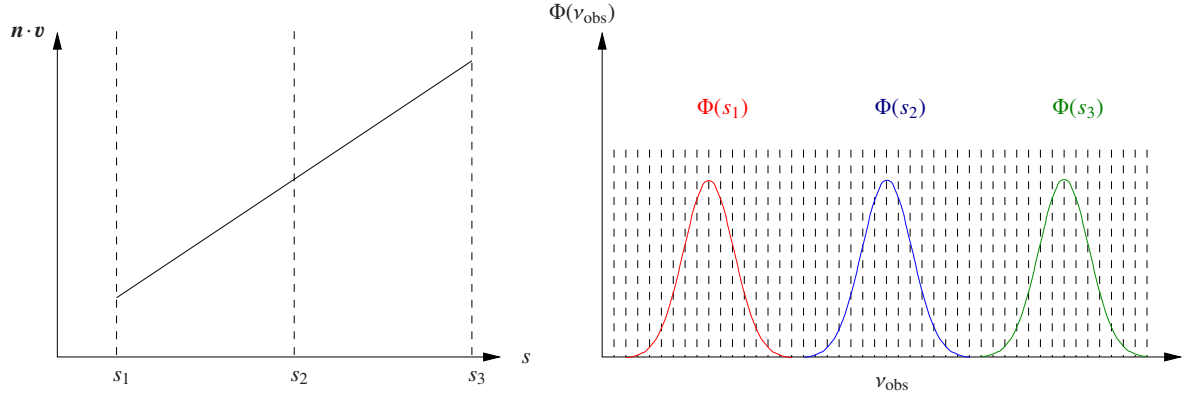
Figure 2.2: Resonance regions in the observer's frame along a given ray. The left panel shows an artificial velocity law along the ray, here assumed to be linear. The right panel shows the profile function as a function of the observer's frame frequency at three distinct positions s_1, s_2, s_3. In the observer's frame, the frequency grid (indicated by the vertical dashed lines) needs to cover a large region.

function (including all Doppler shifts). Thus, a first possibility to minimize the computation time is to solve the equation of radiative transfer in the comoving frame. Then, the number of required frequency grid points becomes significantly reduced. If we consider a single line transition that can be described by a Doppler profile[4],

$$\Phi_{ij} = \frac{1}{\sqrt{\pi}\Delta\nu_D} \exp\left[-\left(\frac{\nu_{cmf} - \nu_{ij}}{\Delta\nu_D}\right)^2\right], \tag{2.39}$$

where ν_{cmf} is the comoving-frame frequency w.r.t. the global velocity field, ν_{ij} is the transition frequency in the atom's rest frame, and $\Delta\nu_D = \nu_{ij}v_{th}/c$ is the Doppler-width with thermal velocity v_{th}, a frequency range $\nu_{cmf} \in [\nu_{ij} - 3\Delta\nu_D, \nu_{ij} + 3\Delta\nu_D]$ is usually sufficient to capture the complete profile. Using a reasonable resolution of $\Delta\nu_{cmf} = \Delta\nu_D/3$ in the following work, the number of frequency points in the comoving frame is then fixed at $N_\nu = 19$.

On the other hand, when using the observer's frame with the (non-relativistic) transformation

$$\nu_{cmf} = \nu_{obs} - \nu_{ij}\frac{\boldsymbol{n}\cdot\boldsymbol{v}}{c}, \tag{2.40}$$

where $\boldsymbol{v}$ is the velocity vector, one would have to cover the complete range $\nu_{obs} \in [\nu_{ij} - 3\Delta\nu_D - \Delta\nu_D \max(\boldsymbol{n}\cdot\boldsymbol{v}/v_{th}), \nu_{ij} + 3\Delta\nu_D + \Delta\nu_D \max(\boldsymbol{n}\cdot\boldsymbol{v}/v_{th})]$, yielding a number of $N_\nu \approx 18 + 6\max(\boldsymbol{n}\cdot\boldsymbol{v}/v_{th}) + 1$ required frequency grid points (see also Fig. 2.2). Thus, the number of frequency points in the observer's frame depends on the maximum (projected) velocity within the wind, and on the thermal speed. For carbon, e.g., this would require $N_\nu \approx 1600$ grid points for maximum projected velocities $\max(\boldsymbol{n}\cdot\boldsymbol{v}) = 2000\,\mathrm{km\,s^{-1}}$, and a thermal velocity (neglecting micro-turbulent velocities), $v_{th} \approx 8\,\mathrm{km\,s^{-1}}$.

---

[4] For a Doppler profile, the (microscopic) random motion of the gas has to follow a Maxwellian distribution, and the (shallow) profile wings introduced by pressure broadening are neglected.

On the other hand, a comoving-frame formulation becomes complicated since the equation of radiative transfer together with all quantities η_ν, χ_ν, I_ν, $\boldsymbol{n}$, and the $\boldsymbol{\nabla}$-operator need to be transformed by applying Lorentz transformations (e.g., Castor 1972 for spherically symmetric flows). In the following, we skip a detailed derivation, and only explain (in a somewhat heuristic way) the major problem of comoving-frame radiative transfer when applied to non-monotonic velocity fields as aimed at in this thesis. The spatial derivative at constant observer's frame frequency (as required to solve the equation of radiative transfer) can be transformed via:

$$\left(\frac{\partial}{\partial s}\right)_{\nu_{\mathrm{obs}}=\mathrm{const.}} \rightarrow \left(\frac{\partial}{\partial s}\right)_{\nu_{\mathrm{cmf}}=\mathrm{const.}} + \left(\frac{\partial \nu_{\mathrm{cmf}}}{\partial s}\right)_{\nu_{\mathrm{obs}}=\mathrm{const.}} \left(\frac{\partial}{\partial \nu_{\mathrm{cmf}}}\right)_{s=\mathrm{const.}}. \tag{2.41}$$

The second term arises since the comoving-frame frequency varies as a function of s, when a ray passes through an expanding atmosphere at constant observer's frame frequency. Using Eq. (2.40) to calculate the variation of the comoving-frame frequency along the ray, the time-independent radiative transfer equation in the comoving frame becomes to first order in $(\boldsymbol{nv}/c)$ (e.g., Lucy 1971):

$$\frac{\partial I_{\nu_{\mathrm{cmf}}}}{\partial s} - \frac{\nu_{ij}}{c}\frac{\partial(\boldsymbol{nv})}{\partial s}\frac{\partial I_{\nu_{\mathrm{cmf}}}}{\partial \nu_{\mathrm{cmf}}} = \eta_{\nu_{\mathrm{cmf}}} - \chi_{\nu_{\mathrm{cmf}}}I_{\nu_{\mathrm{cmf}}}. \tag{2.42}$$

Eq. (2.42) is an initial boundary problem, for which a spatial boundary condition is required, together with a spectral initial condition at all grid points. The condition that photons can interact with the atmosphere at a given position, s, is:

$$\nu_{\mathrm{cmf}}(s) \in \left[\nu_{ij} - 3\Delta\nu_{\mathrm{D}}, \nu_{ij} + 3\Delta\nu_{\mathrm{D}}\right] \iff \nu_{\mathrm{obs}}(s) \in \left[\nu_{ij}\left(1 + \frac{v_n(s)}{c}\right) - 3\Delta\nu_{\mathrm{D}}, \nu_{ij}\left(1 + \frac{v_n(s)}{c}\right) + 3\Delta\nu_{\mathrm{D}}\right], \tag{2.43}$$

with v_n the projected velocity along a considered ray. Thus, two different positions, s and s', can only interact with each other if

$$\exists \nu_{\mathrm{obs}}(s') \quad \text{such that} \quad \nu_{\mathrm{obs}}(s') \in \left[\nu_{ij}\left(1 + \frac{v_n(s)}{c}\right) - 3\Delta\nu_{\mathrm{D}}, \nu_{ij}\left(1 + \frac{v_n(s)}{c}\right) + 3\Delta\nu_{\mathrm{D}}\right]. \tag{2.44}$$

In the following, we consider two examples considering a monotonic increasing and a non-monotonic velocity field specified at three given points s_1, s_2, s_3 (see Fig. 2.3).

(i) For *monotonic* increasing velocity fields, photons emitted from the inner parts of an atmosphere always appear red-shifted for a (comoving) observer located in the outer parts. Since $v_n(s_1) < v_n(s_2) < v_n(s_3)$, one can easily show that the blue-wing frequency defined as $\nu_{\mathrm{cmf}}^{\mathrm{(blue)}} = \nu_{ij} + 3\Delta\nu_{\mathrm{D}}$ gives $\nu_{\mathrm{obs}}^{\mathrm{(blue)}}(s_1) < \nu_{\mathrm{obs}}^{\mathrm{(blue)}}(s_2) < \nu_{\mathrm{obs}}^{\mathrm{(blue)}}(s_3)$ in the observer's frame. Thus, there is no interaction of the blue-wing photons with the inner layers, and the initial condition is simply given by specifying the intensity $I(s, \nu_{ij} + 3\Delta\nu_{\mathrm{D}})$ either from a precalculated continuum, or from the irradiation by the central star. We note that for monotonic decreasing velocity fields (e.g., when considering the opposite direction), one can accordingly define the initial condition at the red wing.

(ii) For *non-monotonic* velocity fields, the situation becomes much more complicated, because, in terms of the example from Fig. 2.3, one obtains for the blue and red wings:

$$\nu_{\mathrm{obs}}^{\mathrm{(blue,red)}}(s_1) < \nu_{\mathrm{obs}}^{\mathrm{(blue,red)}}(s_2) \quad \text{and} \quad \nu_{\mathrm{obs}}^{\mathrm{(blue,red)}}(s_2) > \nu_{\mathrm{obs}}^{\mathrm{(blue,red)}}(s_3),$$

given that $v_n(s_1) < v_n(s_2)$ and $v_n(s_2) > v_n(s_3)$. Since, for a given direction, blue-wing photons at point s_3 now can interact with the previous grid point s_2, and because the red-wing photons at point s_2 can interact with the previous point s_1, the initial condition becomes very cumbersome to formulate (if it is possible at all). The only simple possibility to solve this issue would be to extend the comoving-frame frequency range to essentially the same frequency range as used within the observer's frame, and nothing would have been won. Furthermore, the switch of the sign, as introduced in front of the frequency derivative term in Eq. (2.42) by the non-monotonic velocity field, complicates the complete situation even further, since the different regions (with positive or negative projected velocities) would need to be treated separately.

Finally, a third problem, although not as severe as the previously mentioned ones, arises when considering a multitude of lines, which potentially can overlap due to the involved velocity fields and the Doppler effect. Already for monotonic velocity fields, different wind regions can then be coupled via different line transitions. We therefore will apply an observer's frame formulation within this thesis, since both non-monotonic velocity fields and wind-induced line overlaps are 'automatically' accounted for.

2.2.3   Differential methods

The most easy approach to solve the equation of radiative transfer numerically is to replace the ∇-operator in Eq. (2.8) by finite differences:

$$\nabla I_\nu \rightarrow \frac{I_{ijk} - I_{i-1,j,k}}{x_i - x_{i-1}} \boldsymbol{e}_x + \frac{I_{ijk} - I_{i,j-1,k}}{y_j - y_{j-1}} \boldsymbol{e}_y + \frac{I_{ijk} - I_{i,j,k-1}}{z_k - z_{k-1}} \boldsymbol{e}_z. \tag{2.45}$$

where the indices i, j, k describe the position on a 3D Cartesian grid with unit vectors $\boldsymbol{e}_x, \boldsymbol{e}_y, \boldsymbol{e}_z$. Mathematically, this method corresponds to the group of finite-volume methods. Basically, the radiative transfer equation is integrated over a finite control volume surrounding a given grid point (vertex-centred), or spanned by the grid points (cell-centred, see Fig. 2.4). The resulting integrals can be solved by applying certain assumptions regarding the behaviour of the intensity, opacity and source function within the control volume. We note that the cell-centred method can yield negative – thus prohibited – intensities in special situations (see Appendix B). Therefore, the vertex-centred approach is typically applied, and one assumes that all quantities are constant within the control volume, yielding a very simple and stable discretization of the equation of radiative transfer (see Sect. 3.1 for the detailed implementation of this method within our code). The intensity for a given frequency and direction at any point in the atmosphere then depends solely on the local opacity and source function, as well as on the illuminating intensities at the neighbouring grid points on the upstream side of a given direction. Thus, one can simply sweep through the Cartesian grid along the specified direction (Fig. 2.4). Since the FVM has already been applied to 3D astrophysical radiative transfer problems by Adam (1990), and Lobel & Blomme (2008), we implement a similar technique as a first step (Sect. 3.1). In Chapter 4, we focus on the accuracy of this simple discretization technique, and show that the method suffers from various numerical inaccuracies, mainly related to numerical diffusion introduced by assuming constant intensities within each control volume. Applying high-order interpolation schemes (e.g., a trilinear interpolation), however, can, similarly to the cell-centred FVM, yield negative intensities (see Appendix B), and are therefore prohibitive as well.
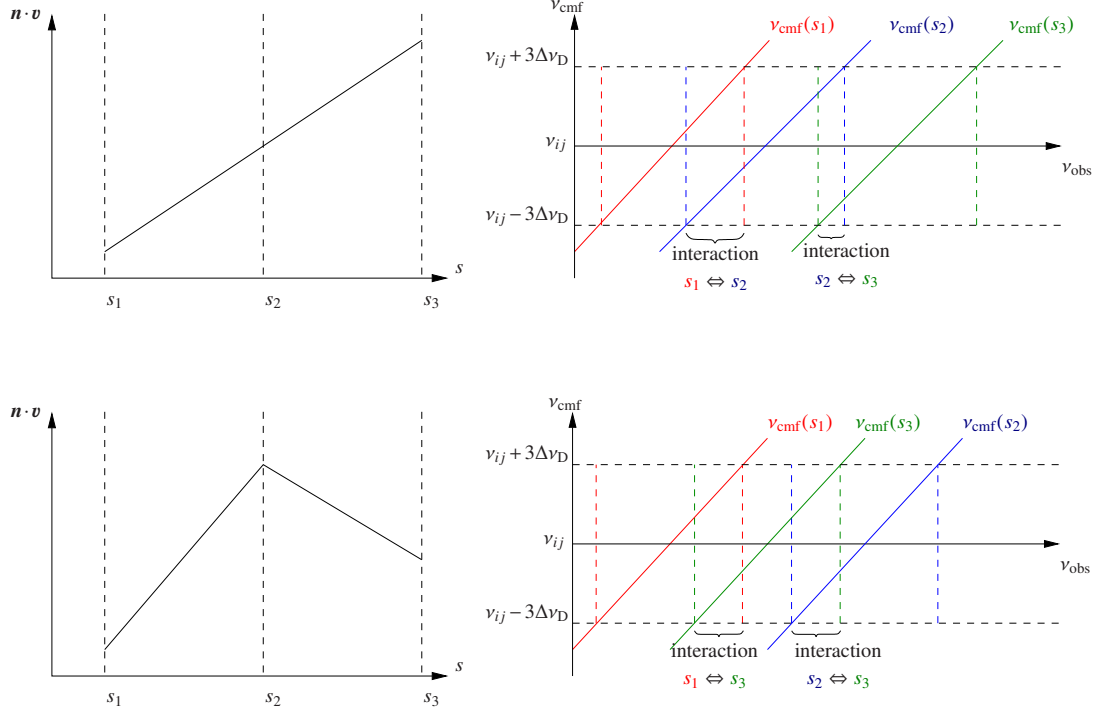
Figure 2.3: Initial conditions for the comoving-frame radiative transport with a monotonic increasing velocity field (upper panel) and a non-monotonic velocity field (lower panel). The comoving-frame frequency for three distinct positions s_1, s_2, s_3 is shown as a function of the observer's frame frequency in the right panels, together with the observer's frame frequency range where the spatial grid points can interact with each other. While photons on the blue wing at $\nu_{\mathrm{cmf}} = \nu_{ij} + 3\Delta\nu_{\mathrm{D}}$ never interact with previous layers for monotonic velocity fields, the formulation of the initial condition becomes problematic for non-monotonic velocity fields.

2.2.4   Integral methods

Within the integral methods, the radiative transfer equation for a given frequency is solved along a particular ray (the so-called 'characteristic') until a grid point is hit. Defining the optical depth along the ray as

$$\mathrm{d}\tau_\nu = \chi_\nu \mathrm{d}s \quad \Longleftrightarrow \quad \Delta\tau_\nu = \int_0^{\Delta s} \chi_\nu \mathrm{d}s, \tag{2.46}$$

where Δs is the path-length, and $\Delta\tau_\nu$ is measured along the path, the time-independent equation of radiative transfer, Eq. (2.9), can be solved analytically by using integrating factors. Along a ray, we obtain:

$$I_\nu(\Delta\tau_\nu) = I_{\mathrm{inc}}\mathrm{e}^{-\Delta\tau_\nu} + \int_0^{\Delta\tau_\nu} \mathrm{e}^{-(\Delta\tau_\nu - t_\nu)} S_\nu(t_\nu) \mathrm{d}t_\nu, \tag{2.47}$$
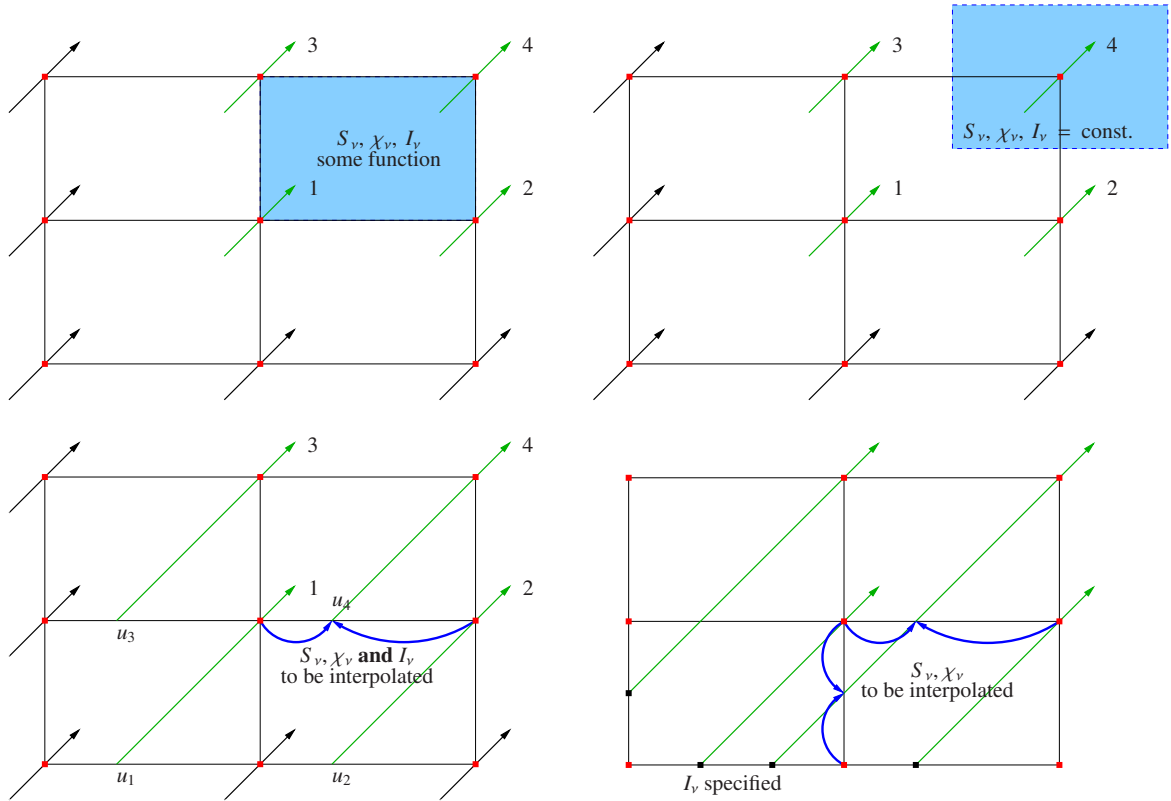
Figure 2.4: Different solution methods for multi-D radiative transfer problems. The upper left and upper right panels show the cell-centred and vertex-centred finite-volume method, respectively, with the control-volume indicated by the blue-shaded area. The equation of radiative transfer can be solved for a given direction and frequency by sweeping through the grid from points $1 \rightarrow 2 \rightarrow 3 \rightarrow 4$ or $1 \rightarrow 3 \rightarrow 2 \rightarrow 4$. Lower left panel: short-characteristics method with upwind points u_1, u_2, u_3, u_4. For point u_4, the interpolation of the source function, opacity **and** intensity is indicated. In order that the intensity at all upwind points can be interpolated, the sweeping through the grid needs to be be performed again from $1 \rightarrow 2 \rightarrow 3 \rightarrow 4$ or from $1 \rightarrow 3 \rightarrow 2 \rightarrow 4$. Lower right panel: long-characteristics method following a particular ray from the boundary to a given grid point. Depending on the required accuracy, the source functions and opacities need to be interpolated onto each ray. Since the incident intensity is specified only at the grid boundary, the order of the sweep can be chosen arbitrarily.

with I_{inc} the incident intensity at the starting point of the ray. Eq. (2.47) needs then to be solved for characteristics intersecting all grid points, and for many frequencies and directions.

Long characteristics

One possibility to obtain the formal solution is by applying the long-characteristics method (LC, see Jones & Skumanich 1973, Jones 1973, and Fig. 2.4). Within the LC method, the characteristic is defined from the boundary of the spatial domain to a considered grid point. To calculate the intensity, both the stratification of the source function and of the opacity (to calculate the optical

depth) is required along a considered ray. Typically, one discretizes the characteristic such that the (still unknown) $\Delta\tau_\nu$ and ΔS_ν steps ideally become equidistant. If the 3D spatial grid represents the 3D stratification of opacities and source functions, one could, for instance, define a mesh along the ray by the intersections of the ray with the 3D spatial grid, with corresponding opacities and source-functions obtained from interpolation. Along the characteristic, all quantities are then approximated by piecewise linear functions in τ_ν, or with polynomials of higher order, and Eq. (2.47) can be solved analytically. For a 3D grid with N^3 grid points, the number of points along the ray is, on average, $N/2$. Thus, roughly $N^4/2$ operations are required to solve the equation of radiative transfer along a ray together with another $N^4/2$ operations for interpolating all quantities onto the ray. The N^4 scaling of the computational effort can be circumvented by applying an effective parallelization strategy. In this respect, we emphasize that the intensities at all 3D grid points are independent of the formal solution at neighbouring grid points, and the LC solution scheme can be easily parallelized for each ray. In principle, if enough CPU's are available, all N^3 rays (per frequency and solid angle) can be calculated in parallel. The overhead, however, might be significant since grid points located far from the boundary require much more operations than grid points located near to the boundary.

Short characteristics

Alternatively, one may apply the short-characteristics method (SC, Kunasz & Auer 1988) to reduce the N^4 scaling of required operations. Within this method, the radiative transfer equation is solved only for each grid cell (Fig. 2.4, lower left panel). The starting point of each characteristic ('upwind point') is then defined at the intersection of a considered ray with the neighbouring grid layers. In addition to the opacities and source functions at the upwind point, also the intensity needs to be determined by interpolation from neighbouring grid points. The interpolation of intensities, however, may be problematic (e.g., when the intensity has sharp edges), possibly giving rise to numerical diffusion errors. On the other hand, only N^3 evaluations of the radiative transfer equation are required together with N^3 interpolations (including upwind intensities) to obtain the formal solution at all 3D grid points. Thus, when comparing SC and LC method, the computational complexity of the problem is reduced by a factor of $N/2$. We note, however, that the parallelization strategy needs to be changed since the intensity at each grid point explicitly depends on the intensities at the neighbouring grid points. The most reasonable approach is to parallelize the problem in the spectral or directional domain, where a *private copy* of the 3D intensity is required for each (parallel) frequency or solid-angle node. When using super-computers, such private copies are typically not allowed due to memory limitations. Since our code shall be executed on personal computers anyway, and because we are convinced by the reduction of computational cost by the factor of $N/2$, we develop and implement the SC method with corresponding tools in Sect 3.2, and apply the LC method only to calculate synthetic line profiles (Sect. 3.7).
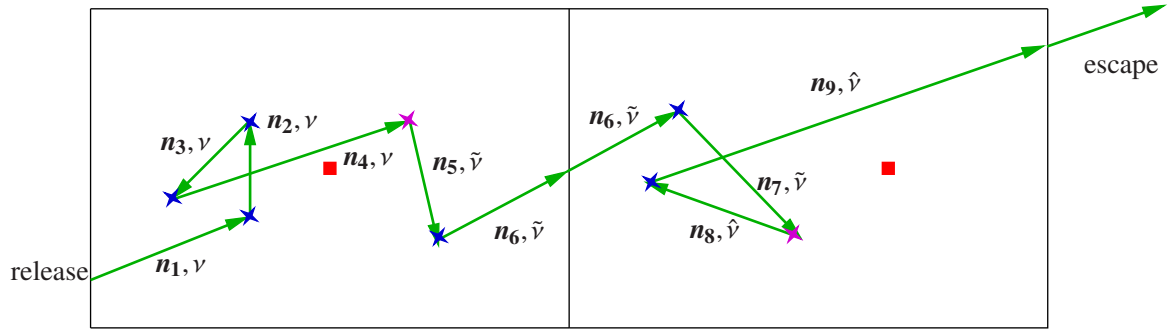
Figure 2.5: Random walk of a photon packet within the Monte-Carlo radiative transfer method. Grid points are indicated as red dots with the corresponding grid cells represented by the black solid lines. The photon packet undergoes numerous coherent scattering (blue stars) or absorption/re-emission (magenta stars) events. In the former case, only the direction becomes redistributed, while in the latter case, also the frequency changes. The complete trajectory is indicated by the green arrows.

2.2.5 Stochastic methods

To solve the coupled problem of the microscopic interaction of matter with the radiation field, also a statistical approach can be applied by using Monte-Carlo simulations[5]. Particularly for 2D and 3D problems, this approach may be advantageous since the overall $N_\nu N_\Omega N^3$ scaling of the computational effort could be further reduced. Within the Monte-Carlo method for radiative transfer (MC-RT, e.g., Lucy 1999a, Ercolano et al. 2003, Ercolano et al. 2005), photon packets of random frequency are released from the inner boundary into random direction, and their trajectories are calculated accounting for (in principle) all microphysical processes (scattering, absorption and re-emission), until each photon packet escapes from the computational domain, or is back-scattered onto the inner boundary. The numerical accuracy then depends solely on the number of released photon packets, N_{MC}. Since the computational effort is proportional to $N_{MC}N_{event}$, where N_{event} is the number of events (including the crossing of a grid cell) until the photon packet escapes, the MC-RT method can (but not necessarily has to!) be more efficient in terms of computational cost than the (above described) classical methods.

To set up the MC-RT method, the spatial domain is initially discretized similarly to the vertex-centred finite-volume method. All quantities describing the state of the gas are given at each grid point, and are assumed to be constant within the surrounding cell. To calculate the trajectory of a released photon packet, we consider the probability that a packet is absorbed (or scattered) within an interval $[0, \tau_\nu]$ along the packet's path. Using only the absorption part of Eq. (2.47), we obtain:

$$P(\tau_\nu) = 1 - \frac{\text{\# photons survived along } \tau_\nu}{\text{\# incident photons}} = 1 - \frac{I_\nu(\tau_\nu)}{I_u} = 1 - e^{-\tau_\nu}. \tag{2.48}$$

By drawing a random number r from a uniform distribution, we obtain the optical depth that is realized

---

[5] The name indeed refers to the Monte Carlo Casino in Monaco.

when an absorption or scattering event has happened:

$$\tau_\nu = -\ln(1 - r) = \chi_\nu \Delta s, \tag{2.49}$$

with corresponding length-scale Δs. For large Δs, the photon packet potentially crosses the grid-cell boundary. Then, a new random number is picked, and a new path length is calculated within the next grid cell starting at the cell boundary[6]. On the other hand, if Δs is smaller than the distance to the grid-cell boundary, the photon-packet undergoes an event either by coherent scattering or by absorption (and immediate re-emission). In the former case, only the direction becomes redistributed (again by drawing random numbers), while in the latter case, also the frequency of the photon-packet becomes redistributed by considering the (thermal) emissivity in the considered grid cell. An exemplary trajectory for a photon packet suffering from different events is shown in Fig. 2.5. Defining the energy of absorbed and re-emitted radiation as $\epsilon(\nu_a) = \epsilon(\nu_e) = \epsilon_0 = $ const., i.e., only the photon number of the packet in each frequency interval changes, the total radiation energy is automatically conserved globally (over the complete frequency range). The mean intensity in each cell could then be calculated by considering the relation between mean intensity and energy density, Eq. (2.10). Since each photon packet on a trajectory within a given volume carries an energy $\epsilon_0 \delta t / \Delta t$, where $\delta t = \Delta s / c$ is the time the photon package spends on the trajectory, and Δt is the duration of the MC experiment, we obtain (see, e.g., Lucy 1999a):

$$J_\nu = \frac{c}{4\pi} \sum \frac{\epsilon_0 \delta t / \Delta t}{V} = \frac{1}{4\pi} \frac{\epsilon_0}{\Delta t} \frac{1}{V} \sum \Delta s. \tag{2.50}$$

V is the volume of the grid cell, and the sum is performed over all trajectories within the volume with photon packets of frequency ν. For the problem of continuum photons as described here, no iteration procedure is required (if the temperature stratification was known), and the (diffuse) radiation field can directly be found from the MC simulation. We note, however, that for optically thick problems, photon packets can be scattered (or absorbed/re-emitted) very often, increasing N_{event} significantly. Thus, for such problems, the MC-RT method might become inefficient.

Another problem arises when the emissivity is not known. While the continuum is mainly composed of electron scattering and true processes, the thermal emissivity in that case is simply given by $\eta_{\text{true}} = \chi_{\text{true}} B_\nu$. When considering a line transition, however, the situation becomes much more complicated due to spontaneous emission events. In that case, one might use the MC-RT approach as defined above with an initial guess for the emissivity, and using single photons instead of (constant) energy packets. Since the emissivity depends on the radiation field and vice versa, an iterative procedure is needed, which might require a large number of iteration steps until convergence. Another problem in this respect is the calculation of the scattering integral. At least in principle, we can obtain the scattering integral by counting the number of photons in a given frequency range through a surface within a given grid-cell, multiplied with the profile function (in the comoving frame). The definition of the surface, however, is not trivial. Furthermore, we would require a large number of photons with different frequencies and directions within each volume element in order to obtain an accurate solution. Finally, the problem of essentially trapped photons with a very large number of scattering

---

[6] Lucy (1999a) noted that no bias is created by picking a new random number, because the probability for an event to happen is independent of the previous travelling history of a photon packet.
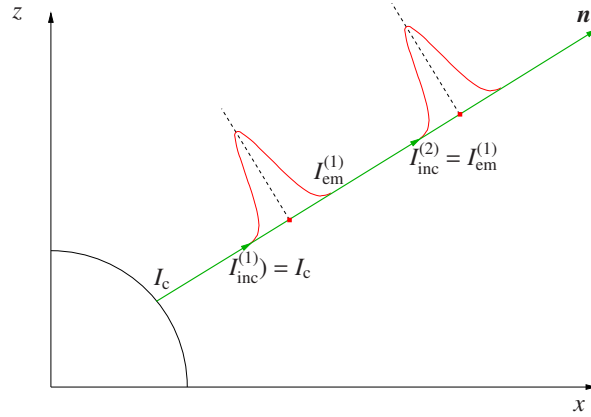
Figure 2.6: Multiple resonance zones along a ray with a given observer's frame frequency and with direction n (green arrow). At the first resonance region, the incident intensity is given by the intensity emerging from the stellar core, I_c. At the second resonance region, the incident intensity is given by the emergent intensity from the first resonance region. The profile functions indicate the interaction regions, and are displayed with red solid lines.

events becomes particularly pronounced for strong resonance lines, since the optical depth can become extremely large in the line core. In this respect, also the accurate description of thermalized (i.e., thermally destroyed) photons becomes problematic, since already few thermal processes might be sufficient to thermalize a considered photon during millions of scattering events. We emphasize that the problem of thermalized photons plays a significant role within optically thick continua as well.

In summary, the MC-RT can presumably be applied *efficiently* 'only' to pure scattering lines, or to radiative transfer problems that remain mostly optically thin (but see also Lucy 1999b and Lucy 2002). Since the coupling of the radiation field with the NLTE rate equations becomes complex as well, and due to the computational effort of essentially trapped photons, we thus preferred to focus on the deterministic methods within this thesis.

2.2.6 Semi-analytic methods: Sobolev approximation

The Sobolev method (Sobolev 1960) is a very elegant, semi-analytical solution scheme for calculating line transitions in rapidly expanding atmospheres. In the following, we assume an optically thin background continuum (though extensions to include continuum processes have been developed by, e.g., Hummer & Rybicki 1985). Within the Sobolev method (see Appendix A for a detailed derivation), we consider a position on a ray with direction n satisfying the resonance condition $v_{cmf}(r) = v_{ij}$. To calculate the specific intensity at that position analytically, Eq. (2.47) is applied assuming that

(i) all quantities describing the local state of the gas (source function and frequency-independent part of the opacity) are constant over the width of the profile function (i.e., within the interaction region of the radiation with the gas). This assumption requires a rather steep gradient of the projected velocity along the ray, and implies that the Sobolev approximation is valid only where

$v_n > v_{th}$, with v_n the projected velocity along the ray. Thus, the Sobolev method mostly fails to represent the radiation field in photospheric layers.

(ii) the projected velocity along the considered ray can be approximated by a linear function, at least over the width of the interaction region. Thus, when curvature terms become important (e.g., in the transonic region of the atmosphere), the Sobolev method again provides only a crude approximation of the radiation field.

Under these assumptions, the specific intensity at a given point can be expressed by the incident intensity at the begin of the resonance region (which for non-monotonic velocity fields depends on previous resonance regions), and purely local quantities (Eqs. A.12-A.13). For monotonic velocity fields and an optically thin continuum, the incident intensity is simply given by the intensity emerging from the stellar core if the considered ray intersects the stellar surface (Fig. 2.6), and zero else. For such problems, the scattering integral can be calculated by local quantities alone, and the solution for the source function of the line-scattering problem is readily obtained from Eq. (A.17).

For non-monotonic velocity fields, the incident intensity at the begin of the resonance region is not known a priori, due to the interaction of the radiation along a given ray in several resonance regions, and the formulation of the Sobolev method becomes complex (though possible, see Rybicki & Hummer 1978). Two major problems arise, that destroy many benefits of the method. On the one hand, an efficient algorithm is required to locate all resonance regions along a ray, which may become quite time-consuming. On the other hand, analogously to the differential and integral methods, a Λ-iteration scheme is required to account for the non-local coupling of the radiation field between multi-resonances (e.g., Puls et al. 1993). Furthermore, the implementation of wind-induced overlaps from different line transitions can become quite complex (already for monotonic velocity fields). Thus, and to avoid potentially severe approximations (particularly for shallow velocity gradients, or in the transonic region where the velocity field shows a strong curvature), we decided to implement the 3D Sobolev approximation (neglecting multi-resonances for simplicity) only to calculate starting values for the more elaborate methods discussed above (and in the following).

2.2.7 Coordinate systems

Thus far, we have used a 3D Cartesian grid to describe the global coordinate system. Since the intensity is a function of spatial coordinate *and* of direction, the formulation of the FVM and SC method in other coordinate systems becomes problematic, as shown below.

The FVM in arbitrary orthogonal curvilinear coordinates

Since in curvilinear orthogonal coordinates, the basis vectors are a function of position, the spatial derivative within the equation of radiative transfer needs to account for the change of the representation of the direction vector in such a coordinate system. For an arbitrary orthogonal curvilinear system
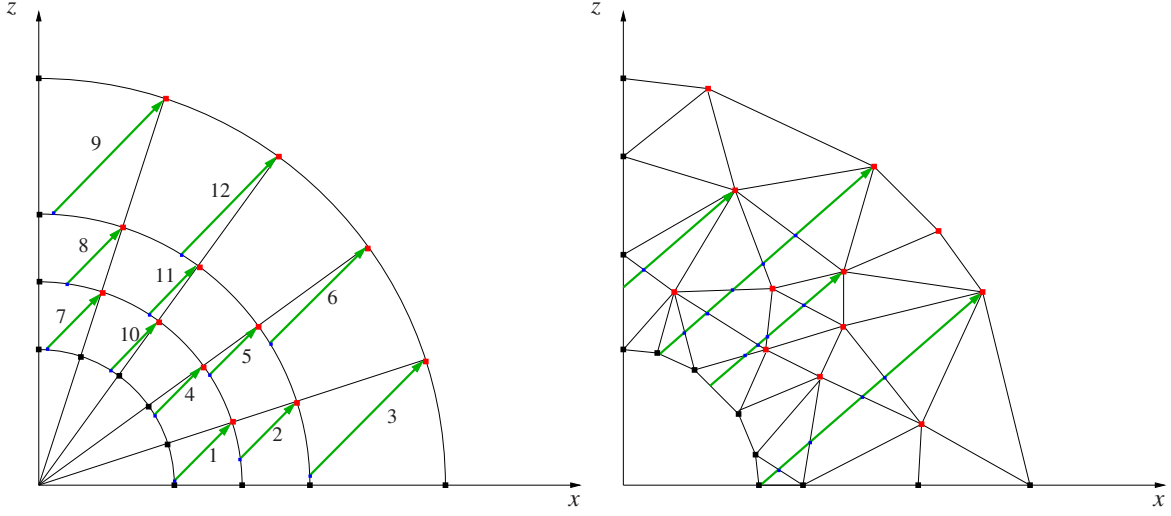
Figure 2.7: Spatial gridding for 3D radiative transfer methods in the *xz*-plane. Red dots represent grid points within the computational domain, while black dots correspond to grid points on the boundary. The left panel shows a spherical grid with short characteristics indicated by green arrows. In order to interpolate intensities onto the upwind points (blue dots), the sweep through the grid needs to be performed from grid points $1 \rightarrow \cdots \rightarrow 12$. The right panel shows an arbitrary distribution of grid points with corresponding triangulation. Long-characteristics are displayed with green arrows, where source functions and opacities need to interpolated onto the intersection points of each ray with the triangular grid (blue dots).

(q_1, q_2, q_3), the equation of radiative transfer becomes (see also Rozanov 2001, p. 30):

$$
\begin{aligned}
\boldsymbol{n} \cdot \boldsymbol{\nabla} I_\nu &= \boldsymbol{n} \cdot \sum_{i=1}^{3} \frac{1}{|\mathrm{d}\boldsymbol{r}/\mathrm{d}q_i|} \boldsymbol{e}_i \frac{\mathrm{d}I_\nu}{\mathrm{d}q_i} \\
&= \boldsymbol{n} \cdot \sum_{i=1}^{3} \frac{1}{|\mathrm{d}\boldsymbol{r}/\mathrm{d}q_i|} \boldsymbol{e}_i \left[\left(\frac{\partial I_\nu}{\partial q_i} \right)_{\boldsymbol{n}=\text{const.}} + \left(\frac{\partial \theta}{\partial q_i} \frac{\partial I_\nu}{\partial \theta} + \frac{\partial \phi}{\partial q_i} \frac{\partial I_\nu}{\partial \phi} \right)_{q_i=\text{const.}} \right] = \chi_\nu \left(S_\nu - I_\nu \right), \quad (2.51)
\end{aligned}
$$

with $\boldsymbol{e}_i$ the unit-vectors of the curvilinear coordinate system, and θ, ϕ the angles describing the direction vector. Within the finite-volume method, the angular derivatives in Eq. (2.51) lead to a severe complication for the discretization of the radiative transfer equation. On the other hand, when using Cartesian coordinates, all terms $\partial\theta/\partial q_i$ and $\partial\phi/\partial q_i$ vanish, and the required volume integrals can be easily performed. We note that only for 1D spherically symmetric problems, the differential approach can be re-formulated by applying the *pz*-geometry (e.g., Mihalas 1978), and solving the radiative transfer along rays with a one-to-one correspondence between impact parameter p and the angular variation of the radiation field.

The characteristics methods in arbitrary orthogonal curvilinear coordinates

The characteristics methods solve the radiative transfer equation along a given ray with prespecified direction, independent of the representation of the considered direction vector in an orthogonal curvi-

linear coordinate system. For a single ray, one can thus always define a local coordinate system with constant radiation coordinates.

For the SC method, however, the interpolation of upwind intensities becomes problematic (see, e.g., Busche & Hillier 2000). For instance, if the upwind point is located on a given Θ-level of a 2D spherical grid, where Θ is the co-latitude, the upwind intensity needs to be interpolated along the radial grid via

$$
\begin{aligned}
I_\nu(r_\mathrm{u}, \theta(r_\mathrm{u})) &= I_\nu(r_0, \theta(r_0)) + \frac{\mathrm{d}I_\nu(r, \theta(r))}{\mathrm{d}r}(r - r_0) \\
&= I_\nu(r_0, \theta(r_0)) \left[\left(\frac{\partial I_\nu}{\partial r} \right)_{\theta = \mathrm{const.}} + \left(\frac{\partial \theta}{\partial r} \frac{\partial I_\nu}{\partial \theta} \right)_{r = \mathrm{const.}} \right] (r - r_0),
\end{aligned}
\tag{2.52}
$$

where we have used a linear interpolation law to describe the variation between the r_0 and r_u radius-levels for illustrative reasons. Since a lot of such interpolations need to be performed, the computation time of the SC method formulated in a curvilinear coordinate system might become significantly enhanced when compared to a formulation in Cartesian coordinates (for which no such angular interpolations need to be performed). Additionally, when using curvilinear coordinates, the sweeping through the grid needs to be adapted for each considered direction, in order that neighbouring grid-points have previously been calculated (see Fig. 2.7, left panel). Thus, a formulation of the SC method in Cartesian coordinates is clearly advantageous in terms of computation time.

For the LC and Monte-Carlo methods, no interpolations of intensities are required, and the above described problems are avoided. The calculation of the intersection of a given ray/trajectory with a grid-cell boundary (required – at least – within the SC and MC method, and potentially also within the LC method), however, can become computationally challenging (e.g., Hubber et al. 2016, and Fig. 2.7, right panel).

2.2.8 Available codes[7]

Meanwhile, various 2D and 3D codes exist, with widely differing assumptions on the underlying geometry and designated applications. In this respect, one important point is the assumption of LTE, which cannot be applied in expanding atmospheres, when the radiation field dominates the level populations. For the latter problem, the coupling between the NLTE rate equations and radiation field is mostly performed using the aforementioned acceleration techniques (e.g., the accelerated Λ-iteration, ALI). We briefly mention specific codes designed for a multi-D radiative transfer in stellar atmospheres (for other applications, there are many more such codes; e.g., for multi-D codes related to the ionization balance in the interstellar medium, see Weber et al. 2013 and references therein):

WIND3D (Lobel & Blomme 2008) is a 3D FVM code, which has been developed to calculate the line transport in scattering dominated environments using Cartesian coordinates, and with level populations approximated by a two-level-atom. It adopts the classical Λ-iteration scheme, which has poor convergence properties for optically thick, scattering-dominated lines. WIND3D is thus restricted to the treatment of weak lines. For those, however, Lobel & Blomme (2008) were able to model the time variations of discrete absorption components (DACs), as observed for the Si IV 1400 Å doublet of

---

[7] This Section has been copied – to a major part – from Hennicker et al. (2018, Sect. 1).

the B0.5Ib supergiant HD 64760. Together with the hydrodynamic code ZEUS3D, these authors have reproduced the DACs, supporting the suggestion of Mullan (1984), that they arise from co-rotating interaction regions (see also Cranmer & Owocki 1996).

ASTAROTH (Georgiev et al. 2006 and Zsargó et al. 2006) is a 2D SC code, which is capable of solving the radiative transfer in parallel with the NLTE rate equations for axisymmetric problems with non-monotonic velocity fields. It uses spherical coordinates and includes a (local) ALI scheme. Many tests have been performed by a comparison to 1D spherically symmetric models from CMFGEN, giving errors of a few percent only. Zsargó et al. (2008) applied the code to investigate the H and He ionization stages in the envelopes of B[e] supergiants, and modelled, among others, the H_α line.

IRIS (Ibgui et al. 2013a) is a 3D SC code, which, to our knowledge, has been only applied for studying laboratory-generated radiative shocks (Ibgui et al. 2013b) thus far. Ibgui et al. (2013a) investigated test problems (searchlight beam test, and 1D plane-parallel models), which show an astonishing accuracy for the solution of intensity, mean intensity, radiative flux, and radiation pressure tensor, on non-uniform Cartesian coordinates and including velocity field gradients. By now, the code assumes LTE. However, the inclusion of scattering terms is planned for the future. For the plane layers as considered in IRIS, only few direction vectors ($N_\Omega \approx 100$) are required to accurately calculate the moments of the specific intensity. Since the number of required directions becomes significantly enhanced ($N_\Omega \gtrsim 2000$) for the problems considered within this thesis (where photons can propagate over large distances), the high-order interpolation schemes as applied in IRIS might become prohibitive in terms of computation time.

MULTI3D (Leenaarts & Carlsson 2009) is a 3D SC code developed to accurately solve the NLTE rate equations in cool FGK-type stars. Amarsi et al. (2016) used this code to predict, among other lines, the O I 777nm line for a grid of 3D hydrodynamical models, by setting up a 23-level model atom. This code, however, has been developed (and optimized) for the application to cool stars (with subsonic velocity fields, at most), and cannot be used in our context. Furthermore, only the plane layers of the atmosphere are treated, with the angular quadrature performed over solely $N_\Omega = 24$ directions.

PHOENIX/3D (Hauschildt & Baron 2006 and other papers in this series) is a 3D LC solver, which is capable of solving the radiative transfer together with the multi-level NLTE rate equations. They use spherical, cylindrical or Cartesian coordinates, and implemented a non-local ALI scheme. With the extension from Seelmann et al. (2010), arbitrary velocity fields can be included as well. To our knowledge, PHOENIX/3D has not been applied, thus far, to real, multi-dimensional, problems.

MOCASSIN (Ercolano et al. 2003, Ercolano et al. 2005) is a 3D Monte-Carlo code for calculating photo-ionization rates and dust radiative transfer within arbitrary density distributions. The original formulation in Cartesian coordinates has meanwhile been extended to an arbitrary distribution of grid points using Voronoi cells (Hubber et al. 2016). To date, MOCASSIN is widely applied to, e.g., photoevaporation in protoplanetary discs (Ercolano et al. 2008) or to the ionization feedback in star forming regions (Ercolano & Gritschneder 2011). For the problems considered in this thesis (e.g., strong scattering lines with a weak thermal component), however, MC-RT methods probably become inefficient in terms of computation time (see Sect. 2.2.5).

2.3 Summary of basic assumptions[8]

The problems considered within this thesis assume an (almost) stationary atmospheric structure, meaning that the densities, velocities and boundary conditions are assumed to be constant in time, or are at least changing much slower than the radiation field. Thus, we use the time-independent equation of radiative transfer:

$$\boldsymbol{n} \cdot \boldsymbol{\nabla} I_\nu(\boldsymbol{r}, \boldsymbol{n}) = \chi_\nu(\boldsymbol{r}, \boldsymbol{n})(S_\nu(\boldsymbol{r}, \boldsymbol{n}) - I_\nu(\boldsymbol{r}, \boldsymbol{n})). \tag{2.53}$$

In the following Chapters, we skip the explicit notation for the spatial ($\boldsymbol{r}$) and directional ($\boldsymbol{n}$) dependencies, and keep the notation of the frequency dependence only when appropriate. The source function, S_ν, and the opacity, χ_ν, consist of the sum of continuum and line processes. By splitting the continuum emissivity and opacity into true and scattering processes, the corresponding source function can be parameterized by the thermalization parameter, ϵ_C (Eq. 2.37). As a first approach, we treat the line transfer similarly by considering a TLA (within an optically thin continuum), with the corresponding source function given by Eq. (2.38). The TLA is well suited to describe resonance lines, but for future applications the complete rate equations need to be taken into account, of course.

The profile function, Φ_x, will be approximated by a Doppler profile. Further, we do not calculate the profile in frequency space, but rather in the variable x_{cmf}, describing the comoving-frame frequency shift from line centre, in units of a fiducial Doppler width, $\Delta\nu_D^*$:

$$x_{cmf} = \frac{\nu_{cmf} - \nu_{ij}}{\Delta\nu_D^*}; \quad \Delta\nu_D^* = \frac{\nu_{ij}\upsilon_{th}^*}{c}, \tag{2.54}$$

where ν_{ij} and υ_{th}^* are the line-centre transition frequency, and the fiducial thermal velocity, respectively. The fiducial width is required to enable a depth-independent frequency grid[9]. x_{cmf} is related to the corresponding observer's frame quantity via $x_{cmf} = x_{obs} - \boldsymbol{n} \cdot \boldsymbol{V}$, with $\boldsymbol{V} = \boldsymbol{v}/\upsilon_{th}^*$ the local velocity vector in units of υ_{th}^*. In most cases, we do not label x explicitly to distinguish between comoving and observer's frame (nor from the spatial x-coordinate), since the meaning should be clear wherever it occurs.

The profile function (in frequency space), Eq. (2.39), then becomes:

$$\Phi_\nu = \frac{1}{\sqrt{\pi}\Delta\nu_D} \exp\left[-\left(\frac{\nu_{cmf} - \nu_{ij}}{\Delta\nu_D}\right)^2\right] = \frac{1}{\sqrt{\pi}\Delta\nu_D} \exp\left[-\left(\frac{x_{cmf}}{\delta}\right)^2\right], \tag{2.55}$$

where

$$\delta = \frac{1}{\upsilon_{th}^*} \sqrt{\frac{2k_B T}{m_A} + \upsilon_{turb}^2} \tag{2.56}$$

is the ratio between the local thermal velocity (including microturbulence, see Sect. 3.4.2) and the fiducial velocity, T is the local temperature, and m_A is the mass of the considered ion. With the profile

---

[8] This Section has been copied – to a major part – from (Hennicker et al. 2018, Sect. 2).

[9] The actual profile width depends on the local gas temperature and on micro-turbulent velocities, that can both vary as a function of position in the atmosphere. Thus, a frequency sampling with equidistant steps of the line-profile width would become depth-dependent.

function, normalized in x-space,

$$\Phi_x = \frac{1}{\sqrt{\pi}\delta} \exp\left[-\left(\frac{x_{\mathrm{cmf}}}{\delta}\right)^2\right] = \frac{1}{\sqrt{\pi}\delta} \exp\left[-\left(\frac{x_{\mathrm{obs}} - \boldsymbol{n} \cdot \boldsymbol{V}}{\delta}\right)^2\right], \tag{2.57}$$

the line opacity, which needs to be described in frequency-space (because the radiative transfer and Planck function are formulated w.r.t. frequency), is given from Eq. (2.28):

$$\chi_{\mathrm{L}}(\nu) = \bar{\chi}_0 \Phi_\nu = \bar{\chi}_{\mathrm{L}} \Phi_x \tag{2.58}$$

$$\bar{\chi}_0 = \frac{\pi e^2}{m_e c}(gf)\left[\frac{n_{\mathrm{l}}}{g_{\mathrm{l}}} - \frac{n_{\mathrm{u}}}{g_{\mathrm{u}}}\right] \approx \frac{\pi e^2}{m_e c} \cdot f \cdot n_{\mathrm{l}}, \tag{2.59}$$

with $n_{\mathrm{l}}, n_{\mathrm{u}}, g_{\mathrm{l}}, g_{\mathrm{u}}$ the occupation numbers and statistical weights of the lower and upper level, respectively. Since $n_{\mathrm{l}} \gg n_{\mathrm{u}}$ for resonance lines, we have neglected stimulated emission on the right-hand side. $\bar{\chi}_0$ is the frequency integrated opacity[10], and is related to $\bar{\chi}_{\mathrm{L}}$ by

$$\bar{\chi}_{\mathrm{L}} = \frac{\delta}{\Delta\nu_{\mathrm{D}}}\bar{\chi}_0 = \frac{\bar{\chi}_0}{\Delta\nu_{\mathrm{D}}^*}. \tag{2.60}$$

We finally parameterize the continuum and line opacities in terms of the Thomson-opacity, $\chi_{\mathrm{Th}} = n_e \sigma_e$,

$$\chi_{\mathrm{L}} = k_{\mathrm{L}} \cdot \chi_{\mathrm{Th}} \cdot \Phi_x \quad \Longleftrightarrow \quad k_{\mathrm{L}} := \frac{\bar{\chi}_{\mathrm{L}}}{\chi_{\mathrm{Th}}} = \frac{\bar{\chi}_0}{\Delta\nu_{\mathrm{D}}^* n_e \sigma_e} \tag{2.61}$$

$$\chi_{\mathrm{C}} = k_{\mathrm{C}} \cdot \chi_{\mathrm{Th}}, \tag{2.62}$$

where we use k_{L} as a depth-independent parameter, since the ratio n_{l}/n_e remains almost constant in the atmosphere for resonance lines (almost frozen-in ionization).

In the next Chapter, we present (efficient) numerical tools for solving the coupled equations (2.53) and (2.37)/(2.38). Although this coupled problem could be solved directly, at least in principle, we note already here that this would require the inversion of a very large matrix, which is computationally prohibitive in 3D calculations (see Sect. 3.5). Thus, we apply a Λ-iteration, for which a formal solution of the radiative transfer equation is obtained, given the continuum and line source functions. These are subsequently updated according to Eq. (2.37) and (2.38), given the formal solution of the previous iterate. For large optical depths and low ϵ_{C} (ϵ_{L}), however, the strong non-local coupling between the source functions and the radiation field results in the well known convergence-problem of the classical Λ-iteration. This problem is based on the fact that, due to scattering processes, photons can travel over many mean-free-paths before being destroyed or escaping from the atmosphere. On the other hand, information is propagated in each iteration step only over roughly one mean-free-path. Therefore, a large number of iteration steps would be required, until a consistent solution was obtained (if at all). Thus, acceleration techniques are urgently needed, and developed in this thesis in terms of an ALI scheme using operator-splitting techniques (Cannon 1973).

Since we aim at modelling non-monotonic velocity fields, for which a comoving-frame formulation, if at all, is very complicated to implement, we solve the equation of radiative transfer in the observer's frame. We also use a Cartesian coordinate system, which has the advantage of constant angular directions w.r.t. the spatial grid. Anyhow, a description of the atmospheric structure in spherical coordinates loses its advantages for the non-spherical problems considered in this (and future) work.

---

[10] We stress that the frequency integrated opacity is often written as $\bar{\chi}_{\mathrm{L}}$, and must not be confused with the quantity defined by the same symbol as defined here (different normalization!).

Chapter 3

Numerical methods

This chapter has been copied - in parts - from Hennicker et al. (2018) and Hennicker et al. (2019).

3.1 Finite-volume method[1]

3.1.1 The discretized equation of radiative transfer within the FVM

The main ideas of the FVM originate from heat transfer (Patankar 1980), and have been already applied to radiative transfer problems in accretion discs by Adam (1990), as well as to the formation of discrete absorption components in hot star winds (Lobel & Blomme 2008). We note that (at least in principle), a large number of different formulations can be derived, that vary in the definition of control volumes (cell-centred vs. vertex-centred, see Sect. 2.2.3), or differ in the applied interpolation technique to solve the volume-integrals. Since the cell-centred approach can result in negative (thus unphysical) intensities (see Appendix B for an example in 1D), we apply a vertex-centred FVM. Although the derivation of the discretized equation of radiative transfer can be found, for instance, in Adam (1990), we outline the basic ideas in more detail in the following. At each grid point, Eq. (2.53) is integrated over a finite control volume (see Fig. 3.1). Applying Gauss's theorem, we obtain:

$$\underbrace{\int_{\partial V} I \boldsymbol{n} \cdot \mathbf{d}\boldsymbol{S}}_{\text{(I)}} = \underbrace{\int_{V} \chi(S - I)\, \mathrm{d}V}_{\text{(II)}}. \qquad (3.1)$$

The left-hand side of Eq. (3.1) describes the intensity propagating into and out of the control-volume surfaces, and the right-hand side corresponds to the grid-cell contribution from sources and sinks. To solve the volume integral, we assume that all quantities given at the grid points are appropriate (constant) mean values within the corresponding control volume, since higher order schemes could lead, similarly to the cell-centred approach, to negative intensities (see Appendix B). Then, the right-hand side is easily integrated, yielding

$$\text{(II)} = \int_{V} \chi(S - I)\, \mathrm{d}V = \chi_{ijk}(S_{ijk} - I_{ijk})(x_{i+1/2} - x_{i-1/2})(y_{j+1/2} - y_{j-1/2})(z_{k+1/2} - z_{k-1/2}), \qquad (3.2)$$

---

[1] based on Hennicker et al. (2018, Sect. 3, Sect. 3.1, and Appendix A).
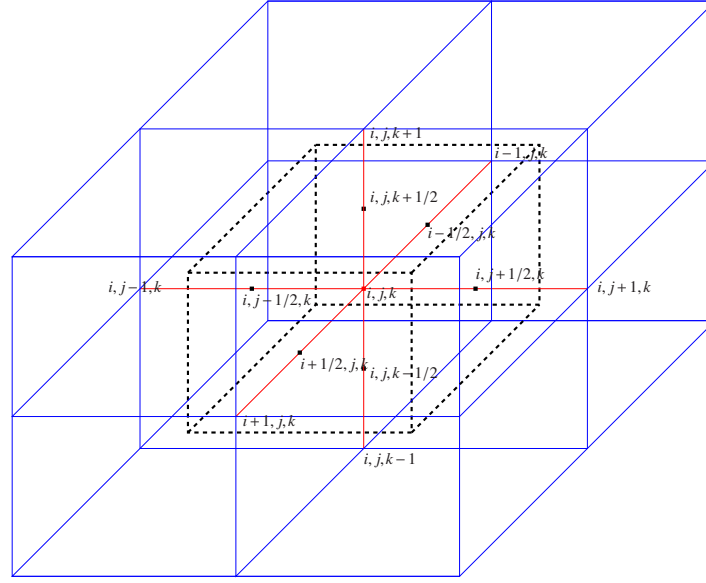
Figure 3.1: Geometry used within the vertex-centred control-volume approach: The discretized 3D spatial grid is shown in blue. The dashed lines indicate the control volume, corresponding to a grid-point (ijk). The control-volume surfaces are located at the centre between the grid-point coordinates. From Hennicker et al. (2018).

for a grid point (ijk). Since we are using Cartesian coordinates, the integral on the left-hand side can be readily calculated:

$$
\begin{aligned}
(\mathrm{I}) = \int_{\partial V} I\boldsymbol{n} \cdot \mathbf{dS} \;=\;\; & n_x \int_{y_{j-1/2}}^{y_{j+1/2}} \int_{z_{k-1/2}}^{z_{k+1/2}} I(x_{i+1/2},y,z) - I(x_{i-1/2},y,z) \,\mathrm{d}y\mathrm{d}z \\
+\;\; & n_y \int_{x_{i-1/2}}^{x_{i+1/2}} \int_{z_{k-1/2}}^{z_{k+1/2}} I(x,y_{j+1/2},z) - I(x,y_{j-1/2},z) \,\mathrm{d}x\mathrm{d}z \\
+\;\; & n_z \int_{x_{i-1/2}}^{x_{i+1/2}} \int_{y_{j-1/2}}^{y_{j+1/2}} I(x,y,z_{k+1/2}) - I(x,y,z_{k-1/2}) \,\mathrm{d}x\mathrm{d}y \,.
\end{aligned}
$$

Again, assuming that the intensities at the midpoints of the control-volume surfaces are representative averages of the corresponding surfaces, we obtain:

$$
\begin{aligned}
(\mathrm{I}) = \int_{\partial V} I\boldsymbol{n} \cdot \mathbf{dS} \;=\;\; & n_x(I_{i+1/2,j,k} - I_{i-1/2,j,k})(y_{j+1/2} - y_{j-1/2})(z_{k+1/2} - z_{k-1/2}) \\
+\;\; & n_y(I_{i,j+1/2,k} - I_{i,j-1/2,k})(x_{i+1/2} - x_{i-1/2})(z_{k+1/2} - z_{k-1/2}) \\
+\;\; & n_z(I_{i,j,k+1/2} - I_{i,j,k-1/2})(x_{i+1/2} - x_{i-1/2})(y_{j+1/2} - y_{j-1/2}) \,. \qquad (3.3)
\end{aligned}
$$

Since the control-volume coordinates are positioned at the midpoints of the grid coordinates, we substitute:

$$
x_{i+1/2} - x_{i-1/2} = \frac{x_{i+1} - x_{i-1}}{2}\,, \quad y_{j+1/2} - y_{j-1/2} = \frac{y_{j+1} - y_{j-1}}{2}\,, \quad z_{k+1/2} - z_{k-1/2} = \frac{z_{k+1} - z_{k-1}}{2}\,. \quad (3.4)
$$

Finally, we use the upwind approximation to replace the (unknown) intensities at the control-volume surfaces:

$$
\left.\begin{aligned}
I_{i+1/2,j,k} &\to I_{i,j,k} \\
I_{i-1/2,j,k} &\to I_{i-1,j,k} \\
\alpha &:= 1
\end{aligned}\right\} \text{for } n_x > 0, \quad
\left.\begin{aligned}
I_{i+1/2,j,k} &\to I_{i+1,j,k} \\
I_{i-1/2,j,k} &\to I_{i,j,k} \\
\alpha &:= -1
\end{aligned}\right\} \text{for } n_x < 0,
$$

$$
\left.\begin{aligned}
I_{i,j+1/2,k} &\to I_{i,j,k} \\
I_{i,j-1/2,k} &\to I_{i,j-1,k} \\
\beta &:= 1
\end{aligned}\right\} \text{for } n_y > 0, \quad
\left.\begin{aligned}
I_{i,j+1/2,k} &\to I_{i,j+1,k} \\
I_{i,j-1/2,k} &\to I_{i,j,k} \\
\beta &:= -1
\end{aligned}\right\} \text{for } n_y < 0,
$$

$$
\left.\begin{aligned}
I_{i,j,k+1/2} &\to I_{i,j,k} \\
I_{i,j,k-1/2} &\to I_{i,j,k-1} \\
\gamma &:= 1
\end{aligned}\right\} \text{for } n_z > 0, \quad
\left.\begin{aligned}
I_{i,j,k+1/2} &\to I_{i,j,k+1} \\
I_{i,j,k-1/2} &\to I_{i,j,k} \\
\gamma &:= -1
\end{aligned}\right\} \text{for } n_z < 0.
$$

Combining Eqs. (3.1), (3.2), (3.3), (3.4), and using the definitions of α,β,γ, the discretized equation of radiative transfer finally reads:

$$
n_x\left(I_{ijk} - I_{i-\alpha,j,k}\right)\Delta y_j \Delta z_k + n_y\left(I_{ijk} - I_{i,j-\beta,k}\right)\Delta x_i \Delta z_k + n_z\left(I_{ijk} - I_{i,j,k-\gamma}\right)\Delta x_i \Delta y_j =
$$
$$
= \left[\chi_{ijk}^{(C)}S_{ijk}^{(C)} + \bar{\chi}_{ijk}^{(L)}\Phi_x^{(ijk)}S_{ijk}^{(L)} - \left(\chi_{ijk}^{(C)} + \bar{\chi}_{ijk}^{(L)}\Phi_x^{(ijk)}\right)I_{ijk}\right]\Delta x_i \Delta y_j \Delta z_k, \quad (3.5)
$$

with $\Delta x_i := (x_{i+\alpha} - x_{i-\alpha})/2$, $\Delta y_j := (y_{j+\beta} - y_{j-\beta})/2$, $\Delta z_k := (z_{k+\gamma} - z_{k-\gamma})/2$, and where we already have separated the continuum and line contribution of the opacity and source function. Collecting terms, and solving for I_{ijk} leads to:

$$
I_{ijk} = a_{ijk}S_{ijk}^{(C)} + b_{ijk}S_{ijk}^{(L)} + c_{ijk}I_{i-\alpha,j,k} + d_{ijk}I_{i,j-\beta,k} + e_{ijk}I_{i,j,k-\gamma}, \tag{3.6}
$$

with

$$
f_{ijk} = \chi_{ijk}^{(C)} + \bar{\chi}_{ijk}^{(L)}\Phi_x^{(ijk)} + \frac{n_x}{\Delta x_i} + \frac{n_y}{\Delta y_j} + \frac{n_z}{\Delta z_k},
$$

$$
a_{ijk} = \frac{\chi_{ijk}^{(C)}}{f_{ijk}}, \qquad b_{ijk} = \frac{\bar{\chi}_{ijk}^{(L)}\Phi_x^{(ijk)}}{f_{ijk}},
$$

$$
c_{ijk} = \frac{n_x}{\Delta x_i f_{ijk}}, \qquad d_{ijk} = \frac{n_y}{\Delta y_j f_{ijk}}, \qquad e_{ijk} = \frac{n_z}{\Delta z_k f_{ijk}},
$$

and α,β,γ set to ± 1 for direction-vector components $n_x, n_y, n_z \gtrless 0$. All quantities except χ_C, $\bar{\chi}_L$, and the source terms, depend on the considered direction $\boldsymbol{n}$ as well as on frequency. Eq. (3.6) represents a pure upwind scheme, with projected $\Delta\tau$-steps[2] calculated from a central-differencing approach (following Patankar 1980). Due to the upwind scheme, and because the coefficients $a_{ijk} \ldots e_{ijk} \in [0,1]$, the solution method is unconditionally stable (Adam 1990). On the other hand, the accuracy of the FVM as formulated above is only of first-order[3] in $\Delta\tau$. Thus, we emphasize that a large number of grid

---

[2] The projected $\Delta\tau$-steps represent the optical depth of the cell for a given direction, and are easily obtained from Eq. (3.6) and the definition of the coefficients $c_{ijk} \ldots e_{ijk}$, e.g., $c_{ijk} =: 1/(1+\Delta\tau_x)$.

[3] Actually, our FVM is a first-order scheme only for large optical-depth steps. For small optical-depth steps, the method becomes second-order accurate.
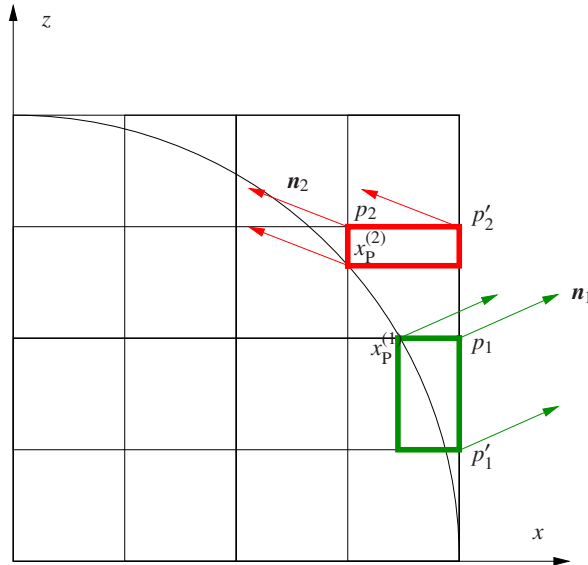
Figure 3.2: Boundary conditions for two different points, p_1, p_2, and different directions, $\boldsymbol{n}_1$, $\boldsymbol{n}_2$. *Green:* A ray originating from the stellar photosphere. To calculate the intensity at p_1 in direction $\boldsymbol{n}_1$, the intensities at the neighbouring grid points, $x_{\mathrm{P}}^{(1)}$ and p'_1, need to be known. A boundary condition is required for grid point $x_{\mathrm{P}}^{(1)}$, while the intensity at p'_1 results within the 'normal' RT-scheme. *Red:* A ray originating from outside the photosphere. For the grid point p_2, a boundary condition has to be specified at the corresponding phantom point, $x_{\mathrm{P}}^{(2)}$. From Hennicker et al. (2018).

points would be required to properly describe the radiation field in the optically thick limit, since a first-order scheme is generally unable to reproduce the (second-order) diffusion equation. Contrasted to our central-differencing approach, Adam (1990) and Lobel & Blomme (2008) used backward differences for the calculation of the $\Delta\tau$-steps. We have tested both methods, and found superior results when using central differences.

With Eq. (3.6), we are able to calculate the specific intensity for known source-functions and opacities by simply sweeping through the spatial domain grid point by grid point, when boundary conditions are specified.

3.1.2 Boundary conditions within the FVM

At the outer boundary, the intensities coming from outside are set to zero, whereas those coming from inside are calculated within the RT scheme, and need not to be specified. Close to the star, the situation is more complicated, [‡]since the inner boundary is usually not aligned with the 3D Cartesian grid (e.g., a spherical star at the origin)[‡]. The intensities at the inner grid points close to the boundary are calculated by the standard FVM-RT (Eq. 3.6), but using different grid cells, defined by the intersection(s) of the original grid cell with the (spherical) photosphere (see Fig. 3.2). The intensity for certain directions needs to be specified at those so-called phantom points. Figure 3.2 displays phantom points corresponding to two distinct grid points, p_1, p_2, and different ray directions, $\boldsymbol{n}_1$, $\boldsymbol{n}_2$. For radiation

originating from the stellar surface (direction $\boldsymbol{n}_1$ in Fig. 3.2), we use a core-halo approximation[4], [‡]and set $I_{\text{phantom}-\text{point}} = I_c^+ = B_\nu(T_{\text{rad}})$ at the corresponding phantom point $x_P^{(1)}$, with I_c^+ the emergent intensity from the core, and T_{rad} the radiation temperature. Unless explicitly noted, we assume $T_{\text{rad}} = T_{\text{eff}}$ throughout this work.[‡] For some grid points and ray directions, however (e.g., direction $\boldsymbol{n}_2$ in Fig. 3.2), even intensities incident onto the photosphere need to be specified at the corresponding phantom point.

Within the core-halo approximation used here, inwards directed intensities should, in principle, be set to zero at the lower boundary, that is $I_{\text{phantom}-\text{point}} = I_c^- = 0$. If, on the other hand, the lower boundary is located at significant optical depths (as for the majority of the cases considered in this thesis), a specification within a simplified diffusion approximation, $I_{\text{phantom}-\text{point}} = I_c^- \approx B_\nu(T_{\text{rad}})$, is more appropriate. Although the diffusion approximation is no longer justified when concentrating on purely scattering atmospheres, backscattering of photons in such environments mimics a similar effect, at least if the optical depths are not too low.

We have tested this issue by considering an optically thin model as the most extreme test-bed, using both alternative descriptions for those critical directions. The mean relative errors for both alternatives are of the same order, and do not significantly differ from those arising under more physical conditions discussed later (with larger optical depths at the lower boundary, see Chapter 4 and Table 4.3). Thus, we apply $I_c^- \approx B_\nu(T_{\text{rad}})$ as the inner boundary condition for those critical rays as well, also because this procedure is less time-consuming, since it avoids conditional clauses in the innermost loop of the code.

3.2 Short-characteristics method[5]

In Chapter 4, we will show that a formal solution obtained using the FVM suffers from various numerical inaccuracies related to numerical diffusion and to the order of accuracy, the latter influencing the solution particularly in the optically thick regime. To avoid these errors, we implement an integral method along short characteristics. When compared with a long-characteristics solution scheme, the computation time becomes reduced by roughly a factor of $N/2$, with N the number of spatial grid points per dimension (see Chapter 1).

SC methods have been successfully implemented already for 3D non-LTE (NLTE) radiative transfer problems in cool stars (e.g., Vath 1994, Leenaarts & Carlsson 2009, Hayek et al. 2010, Holzreuter & Solanki 2012). These codes, however, are mostly designed for planar geometries, and only account for subsonic and slightly supersonic velocity fields. For scattering problems including highly supersonic velocity fields, there exist, to our knowledge, only the 2D codes by Dullemond & Turolla (2000) (planar/spherical), van Noort et al. (2002) (planar/spherical/cylindrical), Georgiev et al. (2006) and Zsargó et al. (2006) (spherical). The only 3D SC code including arbitrary velocity fields, IRIS (Ibgui et al. 2013a), has also been formulated for planar geometries, and lacks the implementation of a Λ-iteration scheme thus far. As has been shown in all these studies, the final performance of the SC method crucially depends on the choice of the applied interpolation schemes.

---

[4] In future applications, we will include the diffusion limit at the lower boundary.
[5] based on Hennicker et al. (2019, Sect. 3).

3.2.1   The discretized equation of radiative transfer along a ray

The time-independent equation of radiative transfer along a given direction can be written as

$$\frac{dI}{d\tau} = S - I, \tag{3.7}$$

where $d\tau := \chi ds$ is the optical depth length along a ray segment ds. As before, the notation for the frequency dependence has been skipped. Further, we explicitly distinguish between continuum and line only when appropriate. Eq. (3.7) can be solved by using integrating factors:

$$\frac{d(Ie^{\tau})}{d\tau} = Ie^{\tau} + e^{\tau}\frac{dI}{d\tau} \underset{\text{Eq. (3.7)}}{=} Ie^{\tau} + (S - I)e^{\tau} = Se^{\tau}. \tag{3.8}$$

Eq. (3.8) is integrated along a ray propagating through a current grid point p with Cartesian grid indices (ijk) and corresponding upwind point $u^{(ijk)}$. The geometry for a 3D Cartesian grid is shown in the upper panel of Fig. 3.3. For such a ray segment, we obtain:

$$\int_{u}^{p} d(Ie^{\tau}) = I_{p}e^{\tau_{p}} - I_{u}e^{\tau_{u}} = \int_{\tau_{u}}^{\tau_{p}} S(\tau)e^{\tau}d\tau. \tag{3.9}$$

Solving for the (unknown) intensity at point p (with indices ijk), we find the formal solution for the ray segment. In the following, upwind and downwind quantities corresponding to a considered grid point (ijk) are indicated by $q_{u}^{(ijk)}$ and $q_{d}^{(ijk)}$, while local quantities are denoted either as $q_{p}^{(ijk)}$ or simply q_{ijk}. We then obtain:

$$I_{ijk} = I_{u}^{(ijk)}e^{-(\tau_{p}-\tau_{u})} + \int_{\tau_{u}}^{\tau_{p}} e^{-(\tau_{p}-\tau)}S(\tau)d\tau = I_{u}^{(ijk)}e^{-\Delta\tau_{u}} + e^{-\Delta\tau_{u}}\int_{0}^{\Delta\tau_{u}} e^{t}S(t+\tau_{u})dt, \tag{3.10}$$

with upwind optical-depth increment $\Delta\tau_{u} := \tau_{p} - \tau_{u} \geq 0$, and $t := \tau - \tau_{u}$. For the SC solution scheme, the location of the reference point, $\tau = 0$, plays no role, since only the optical-depth increments, $\Delta\tau_{u}$ and $\Delta\tau_{d}$ (see below), are required within our calculations. To calculate the source contribution, the source function is commonly approximated by first- or second-order polynomials (Kunasz & Auer 1988, van Noort et al. 2002), Bézier curves (Hayek et al. 2010, Holzreuter & Solanki 2012, Auer 2003) or cubic Hermite splines (Ibgui et al. 2013a). While the 2nd- (and higher) order methods reproduce the diffusion limit in optically thick media, they suffer from overshoots and need to be monotonized with some effort to ensure that any interpolated quantity remains positive between two given grid points. Monotonicity is usually obtained by manipulating the interpolation scheme whenever overshoots occur. Thus, the actual interpolation crucially depends on the specific stratification of the considered quantity (e.g., the source function). The Λ-operator then becomes non-linear, because its elements now explicitly depend on the stratification of source functions (via corresponding interpolation/integration coefficients). Within any Λ-iteration scheme, this non-linearity can lead to oscillations. In extreme cases, 'flip-flop situations' (Holzreuter & Solanki 2012, their Appendix A) may occur, which do not converge at all.

For the source contribution, we implement both a linear approximation as the fastest and most stable method (monotonicity is always provided), and a quadratic Bézier approximation (see Appendix

C.1) for higher accuracy[6], which allows us to preserve monotonicity in a rather simple way. The Bézier interpolation is constructed from two given data points and one control point, the latter setting the slope of the interpolating curve. The control point is located at the centre of the data-points abscissae, with the ordinate calculated by accounting for the information of a third data point to yield the parabola intersecting all three data points. Whenever overshoots occur, the value of the control point will be manipulated to ensure monotonicity (see Fig. C.1). The corresponding formulation is given in Appendix C.1, Eqs. (C.7)-(C.10). Applying these equations to describe the behaviour of the source function along the optical path, and identifying the indices $(i-1)$, (i), $(i+1)$ with the upwind, current and downwind points, we find, after reordering for the t^0, t^1, t^2 terms:

$$S(t + \tau_{\mathrm{u}}) = S_{\mathrm{u}}^{(ijk)} \quad + \quad \left[\frac{(\omega - 2)}{\Delta\tau_{\mathrm{u}}} S_{\mathrm{u}}^{(ijk)} + \frac{(1-\omega)\Delta\tau_{\mathrm{u}} + (2-\omega)\Delta\tau_{\mathrm{d}}}{\Delta\tau_{\mathrm{u}}\Delta\tau_{\mathrm{d}}} S_{\mathrm{p}}^{(ijk)} + \frac{(\omega - 1)}{\Delta\tau_{\mathrm{d}}} S_{\mathrm{d}}^{(ijk)} \right] \cdot t$$

$$+ \quad \left[\frac{(1-\omega)}{\Delta\tau_{\mathrm{u}}^2} S_{\mathrm{u}}^{(ijk)} + \frac{(\omega - 1)(\Delta\tau_{\mathrm{u}} + \Delta\tau_{\mathrm{d}})}{\Delta\tau_{\mathrm{u}}^2\Delta\tau_{\mathrm{d}}} S_{\mathrm{p}}^{(ijk)} + \frac{(1-\omega)}{\Delta\tau_{\mathrm{u}}\Delta\tau_{\mathrm{d}}} S_{\mathrm{d}}^{(ijk)} \right] \cdot t^2 , \qquad (3.11)$$

with downwind optical-depth increment, $\Delta\tau_{\mathrm{d}} = \tau_{\mathrm{d}} - \tau_{\mathrm{p}} \geq 0$. The parameter ω defines the ordinate of the control point (Eq. C.4). Within the Bézier interpolation, we emphasize that ω may explicitly depend on $S_{\mathrm{u}}^{(ijk)}$, $S_{\mathrm{p}}^{(ijk)}$, and $S_{\mathrm{d}}^{(ijk)}$ to ensure monotonicity, and not solely on the grid spacing. A major advantage of this parameterization is that we can globally define a minimum allowed ω that can be adapted during the iteration process. The flip-flop situations discussed above can then be avoided by gradually increasing $\omega_{\min}$ towards unity ($\omega \equiv 1$ corresponds to a linear interpolation), that is, by suppressing the curvature of the Bézier interpolation. This way, we can construct an always-convergent iteration scheme, though with the drawback of using less accurate interpolations.

Integrating Eq. (3.10) together with a source function described by Eq. (3.11), we obtain the discretized equation of radiative transfer:

$$I_{ijk} = a_{ijk} S_{\mathrm{u}}^{(ijk)} + b_{ijk} S_{\mathrm{p}}^{(ijk)} + c_{ijk} S_{\mathrm{d}}^{(ijk)} + d_{ijk} I_{\mathrm{u}}^{(ijk)} , \qquad (3.12)$$

with

$$a_{ijk} := e_0 + \frac{\omega - 2}{\Delta\tau_{\mathrm{u}}} e_1 + \frac{1-\omega}{\Delta\tau_{\mathrm{u}}^2} e_2 , \qquad b_{ijk} := \frac{(1-\omega)\Delta\tau_{\mathrm{u}} + (2-\omega)\Delta\tau_{\mathrm{d}}}{\Delta\tau_{\mathrm{u}}\Delta\tau_{\mathrm{d}}} e_1 + \frac{(\omega - 1)(\Delta\tau_{\mathrm{u}} + \Delta\tau_{\mathrm{d}})}{\Delta\tau_{\mathrm{u}}^2\Delta\tau_{\mathrm{d}}} e_2 ,$$

$$c_{ijk} := \frac{\omega - 1}{\Delta\tau_{\mathrm{d}}} e_1 + \frac{1-\omega}{\Delta\tau_{\mathrm{u}}\Delta\tau_{\mathrm{d}}} e_2 , \qquad d_{ijk} := \mathrm{e}^{-\Delta\tau_{\mathrm{u}}} ,$$

$$e_0 := \mathrm{e}^{-\Delta\tau_{\mathrm{u}}} \int_0^{\Delta\tau_u} \mathrm{e}^t \mathrm{d}t = 1 - \mathrm{e}^{-\Delta\tau_{\mathrm{u}}} ,$$

$$e_1 := \mathrm{e}^{-\Delta\tau_{\mathrm{u}}} \int_0^{\Delta\tau_u} t\mathrm{e}^t \mathrm{d}t = \Delta\tau_{\mathrm{u}} - e_0 ,$$

$$e_2 := \mathrm{e}^{-\Delta\tau_{\mathrm{u}}} \int_0^{\Delta\tau_u} t^2\mathrm{e}^t \mathrm{d}t = \Delta\tau_{\mathrm{u}}^2 - 2e_1 .$$

---

[6] In this thesis, different interpolation schemes are tested by considering simplified (though physically relevant) continuum and line scattering problems. We emphasize that our code will be further developed to enable the solution of more complex, multi-level problems in 3D. For such problems, highly accurate interpolation schemes are required to describe the variation of the mean intensities along a ray.

The calculation of the upwind and downwind $\Delta\tau$-steps proceeds similarly, where now the opacity is integrated using the Bézier interpolation. Using Eqs. (C.3), (C.4) for the upwind interval, and Eqs. (C.11), (C.12) for the downwind interval, one easily obtains:

$$\Delta\tau_{\mathrm{u}} \quad = \quad \int_{\mathrm{u}}^{\mathrm{p}} \chi(s)\mathrm{d}s = \frac{\Delta s_{\mathrm{u}}}{3}(\chi_{\mathrm{u}} + \chi_{\mathrm{c}}^{[\mathrm{u},\mathrm{p}]} + \chi_{\mathrm{p}}) \tag{3.13}$$

$$\Delta\tau_{\mathrm{d}} \quad = \quad \int_{\mathrm{p}}^{\mathrm{d}} \chi(s)\mathrm{d}s = \frac{\Delta s_{\mathrm{d}}}{3}(\chi_{\mathrm{p}} + \chi_{\mathrm{c}}^{[\mathrm{p},\mathrm{d}]} + \chi_{\mathrm{d}}), \tag{3.14}$$

where Δs_{u}, Δs_{d} describe the path lengths of the upwind and downwind intervals, respectively, and $\chi_{\mathrm{c}}^{[\mathrm{u},\mathrm{p}]}$, $\chi_{\mathrm{c}}^{[\mathrm{p},\mathrm{d}]}$ refer to the opacity at the control points in each interval.

3.2.2 Grid refinement

Since the opacity of a line transition depends on the velocity field through the Doppler effect, regions of significant opacity may become spatially confined in a highly supersonic wind with strong acceleration. Thus, a grid refinement along the short characteristic might be required to correctly account for all resonance zones. Because the profile function is approximated by a Doppler profile and rapidly vanishes for $|x_{\mathrm{cmf}}/\delta| \gtrsim 3$, e.g., $\Phi_x(|x_{\mathrm{cmf}}/\delta| = 3) \approx 10^{-4}\Phi_x(x_{\mathrm{cmf}}/\delta = 0)$, a resonance zone is here defined by a region where $x_{\mathrm{cmf}}/\delta \in [-3, 3]$.

A numerically sufficient condition to resolve all such resonance zones along a given ray is to demand that $|\Delta x_{\mathrm{cmf}}|/\delta = |\Delta V_n|/\delta \lesssim 1/3$ if a resonance zone lies in between the points $[\mathrm{u}^{(ijk)}, \mathrm{p}]$, where ΔV_n is the projected velocity step along the ray in units of v_{th}^*. Assuming a linear dependence of the projected velocities on the ray coordinate s, this condition directly translates to an equidistant refined spatial grid along the ray. For short ray segments (as is mostly the case within our calculations), neglecting the second-order (curvature) terms of the projected velocity influences the solution only weakly. In the deeper atmospheric layers, where the velocity field is transonic, curvature effects potentially play an important role, and our grid-refinement method needs to be revised[7]. The line source function on the refined grid is obtained by Bézier interpolation in s-space (Eqs. C.7-C.9):

$$S_{\mathrm{L}}(s_\ell) = S_\ell = \tilde{a}_\ell S_{\mathrm{u}}^{(ijk)} + \tilde{b}_\ell S_{\mathrm{p}}^{(ijk)} + \tilde{c}_\ell S_{\mathrm{d}}^{(ijk)}, \tag{3.15}$$

where the index ℓ refers to the points on the refined grid, and $\mathrm{u}^{(ijk)}, \mathrm{p}^{(ijk)}, \mathrm{d}^{(ijk)}$ describe the original geometry of the short characteristic. $\bar{\chi}_{\mathrm{L}}$ is obtained analogously, and the required $\Delta\tau_\ell$ steps are calculated with the trapezoidal rule, for simplicity. Contrasted to the Sobolev method (which also assumes a linear velocity law along the ray segment, e.g., Rybicki & Hummer 1978 and Appendix A), our grid refinement procedure explicitly accounts for variations of the opacity and the source function.

Using Eq. (3.12) for the inter-grid points, such that the (local) upwind, current, and downwind

---

[7] Ideally, such layers would already be highly resolved by the 3D spatial grid, such that a grid-refinement along the characteristic is not necessarily required.

quantities are now described by the indices $[\ell-1, \ell, \ell+1]$, we obtain:

$$
\begin{aligned}
I_\ell = I_{\ell-1}e^{-\Delta\tau_\ell} \quad &+ \quad \left(a_\ell\tilde{a}_{\ell-1} + b_\ell\tilde{a}_\ell + c_\ell\tilde{a}_{\ell+1}\right)S_{\mathrm{u}}^{(ijk)} \\
&+ \quad \left(a_\ell\tilde{b}_{\ell-1} + b_\ell\tilde{b}_\ell + c_\ell\tilde{b}_{\ell+1}\right)S_{\mathrm{p}}^{(ijk)} \\
&+ \quad \left(a_\ell\tilde{c}_{\ell-1} + b_\ell\tilde{c}_\ell + c_\ell\tilde{c}_{\ell+1}\right)S_{\mathrm{d}}^{(ijk)} \\
:= I_{\ell-1}e^{-\Delta\tau_\ell} \quad &+ \quad \tilde{\alpha}_\ell S_{\mathrm{u}}^{(ijk)} + \tilde{\beta}_\ell S_{\mathrm{p}}^{(ijk)} + \tilde{\gamma}_\ell S_{\mathrm{d}}^{(ijk)}.
\end{aligned} \tag{3.16}
$$

For a number of N_{ref} refinement points (including the upwind and current point) within the interval $[\mathrm{u}^{(ijk)}, \mathrm{p}^{(ijk)}]$, the intensity at point $\mathrm{p}^{(ijk)}$ is finally given by:

$$
I_{ijk} = I_{\mathrm{u}}^{(ijk)}e^{-\sum_{m=2}^{N_{\mathrm{ref}}}\Delta\tau_m} + S_{\mathrm{u}}^{(ijk)}\sum_{m=2}^{N_{\mathrm{ref}}}\tilde{\alpha}_m e^{-\sum_{n=m+1}^{N_{\mathrm{ref}}}\Delta\tau_n} + S_{\mathrm{p}}^{(ijk)}\sum_{m=2}^{N_{\mathrm{ref}}}\tilde{\beta}_m e^{-\sum_{n=m+1}^{N_{\mathrm{ref}}}\Delta\tau_n} + S_{\mathrm{d}}^{(ijk)}\sum_{m=2}^{N_{\mathrm{ref}}}\tilde{\gamma}_m e^{-\sum_{n=m+1}^{N_{\mathrm{ref}}}\Delta\tau_n},
$$
$$
\tag{3.17}
$$

where the upwind and current points always correspond to the indices $m = 1$ and $m = N_{\mathrm{ref}}$, respectively, and the sum over m is performed over $N_{\mathrm{ref}} - 1$ intervals. The discretized radiative transfer equation for the refined grid obviously has the same form as for the standard short characteristic (Eq. 3.12), with different coefficients though.

3.2.3 Upwind and downwind interpolations

To solve the discretized equation of radiative transfer, the opacities $\chi_{\mathrm{C(u,d)}}$, $\bar{\chi}_{\mathrm{L(u,d)}}$, source functions $S_{\mathrm{C(u,d)}}$, $S_{\mathrm{L(u,d)}}$, and velocity vectors, $V_{\mathrm{(u,d)}}$, are required at the upwind and downwind points, together with the incident intensity, I_{u}. We emphasize that the subscript C describes continuum quantities, and should not be confused with the subscript c denoting the control points of the interpolation scheme.

All required quantities are obtained from a 2D Bézier interpolation (see Appendix C.2) on the surfaces that intersect with a given ray. The intersection surfaces depend on the considered direction and the size of the upwind and downwind grid cells. For a given direction

$$
\boldsymbol{n} = \begin{pmatrix} n_x \\ n_y \\ n_z \end{pmatrix} = \begin{pmatrix} \sin(\theta)\cos(\phi) \\ \sin(\theta)\sin(\phi) \\ \cos(\theta) \end{pmatrix}, \tag{3.18}
$$

where θ is the co-latitude (measured from the z-axis), and ϕ is the azimuth (measured from the x-axis), the distances from a considered grid point to the neighbouring xy-, xz-, and yz-planes are calculated from trigonometry and yield:

$$
\Delta s_{xy}^{(\mathrm{u})} = \frac{z_k - z_{k-\gamma}}{n_z} \qquad \Delta s_{xz}^{(\mathrm{u})} = \frac{y_j - y_{j-\beta}}{n_y} \qquad \Delta s_{yz}^{(\mathrm{u})} = \frac{x_i - x_{i-\alpha}}{n_x}
$$

$$
\Delta s_{xy}^{(\mathrm{d})} = \frac{z_{k+\gamma} - z_k}{n_z} \qquad \Delta s_{xz}^{(\mathrm{d})} = \frac{y_{j+\beta} - y_j}{n_y} \qquad \Delta s_{yz}^{(\mathrm{d})} = \frac{x_{i+\alpha} - x_i}{n_x},
$$

with α, β, γ set to ± 1 for direction-vector components $n_x, n_y, n_z \gtrless 0$, as in Sect. 3.1.1. The intersection surface on the upwind and downwind side are then found at the minimum of $\Delta s_{xy}^{(\mathrm{u,d})}, \Delta s_{xz}^{(\mathrm{u,d})}, \Delta s_{yz}^{(\mathrm{u,d})}$, and the corresponding coordinates are easily calculated.
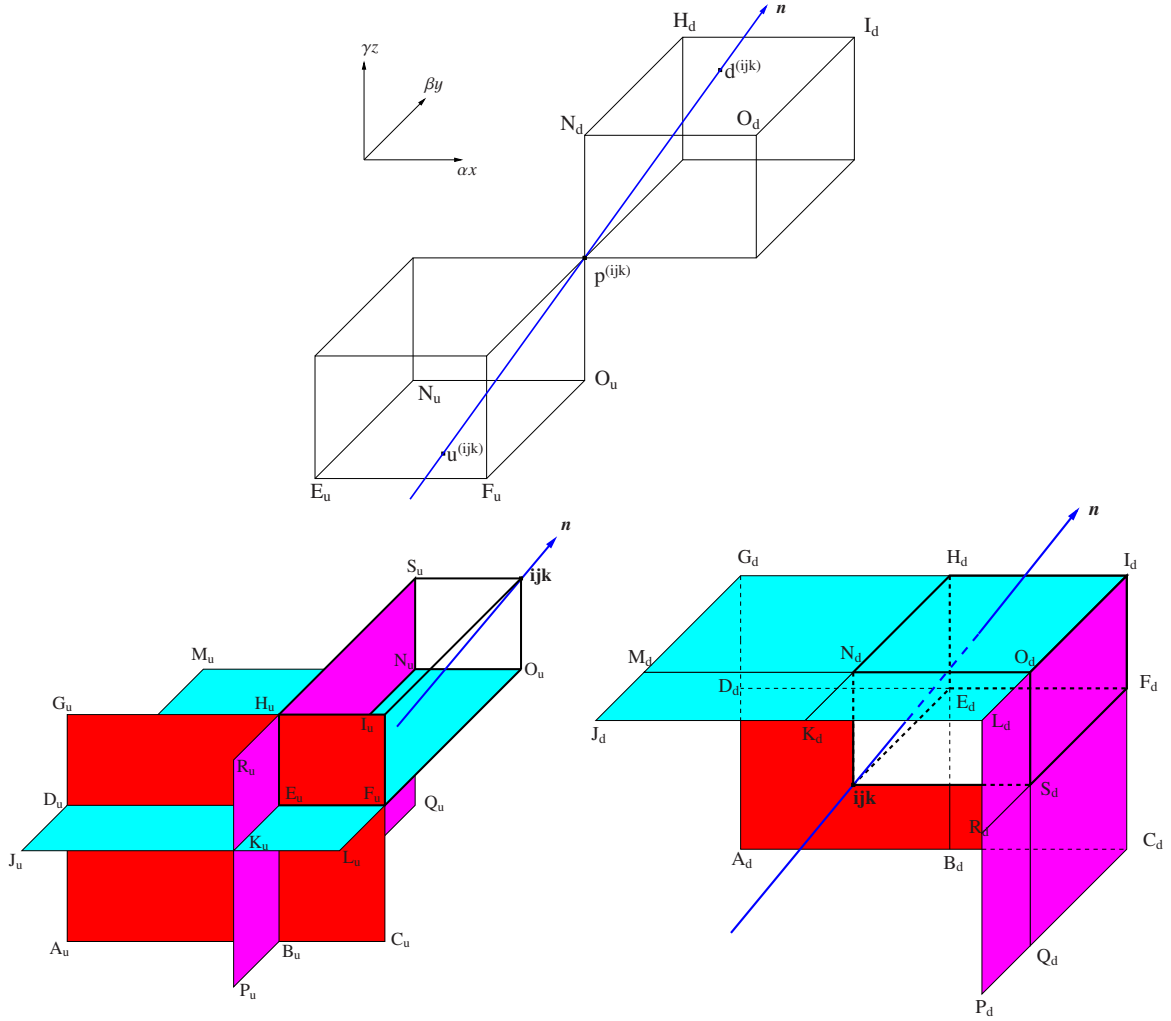
Figure 3.3: Upper panel: Geometry of the SC method for a particular ray with direction **n** propagating from the upwind point u$^{(ijk)}$ to a considered grid point p$^{(ijk)}$. The downwind point d$^{(ijk)}$ is required to set the slope of a Bézier curve representing the opacities and source functions along the ray. The lower left and lower right panels display all possible upwind and downwind intersection surfaces for a short characteristic at a grid point (ijk). For rays intersecting the xy-, xz-, and yz-planes, the 2D Bézier interpolation is obtained from given quantities at grid points located in the cyan, red, and magenta shaded surfaces, respectively. The coordinate system is indicated at the upper left, where α, β, γ determine the direction of the coordinate-axes and are defined in Sect. 3.2.3. From Hennicker et al. (2019).

For each surface, the interpolation requires nine points within the corresponding plane (see Fig. 3.3 and Eq. C.19). In each considered plane, we generally use grid points running from (index-2) to (index) to determine upwind quantities, while downwind quantities are calculated from (index-1) to (index+1). Such a formulation greatly simplifies the calculation of the Λ-matrix elements (see Appendix D). In Fig. 3.3, we show an example for a ray intersecting the xy-plane at the upwind

side. The 2D Bézier interpolation for the upwind point then consists of three 1D Bézier interpolations along the x-axis using the points (J_u, K_u, L_u), (D_u, E_u, F_u), (M_u, N_u, O_u), followed by another 1D Bézier interpolation along the y-axis at the upwind x-coordinates. With the 2D Bézier interpolation given by Eq. (C.19), we find for each required quantity $q_{u,d}$:

$$
\begin{aligned}
q_u^{(ijk)} &= w_A^{(ijk)} q_{i-2\alpha, j-\beta, k-2\gamma} + w_B^{(ijk)} q_{i-\alpha, j-\beta, k-2\gamma} + w_C^{(ijk)} q_{i, j-\beta, k-2\gamma} \\
&+ w_D^{(ijk)} q_{i-2\alpha, j-\beta, k-\gamma} + w_E^{(ijk)} q_{i-\alpha, j-\beta, k-\gamma} + w_F^{(ijk)} q_{i, j-\beta, k-\gamma} \\
&+ w_G^{(ijk)} q_{i-2\alpha, j-\beta, k} + w_H^{(ijk)} q_{i-\alpha, j-\beta, k} + w_I^{(ijk)} q_{i, j-\beta, k} \\
&+ w_J^{(ijk)} q_{i-2\alpha, j-2\beta, k-\gamma} + w_K^{(ijk)} q_{i-\alpha, j-2\beta, k-\gamma} + w_L^{(ijk)} q_{i, j-2\beta, k-\gamma} \\
&+ w_M^{(ijk)} q_{i-2\alpha, j, k-\gamma} + w_N^{(ijk)} q_{i-\alpha, j, k-\gamma} + w_O^{(ijk)} q_{i, j, k-\gamma} \\
&+ w_P^{(ijk)} q_{i-\alpha, j-2\beta, k-2\gamma} + w_Q^{(ijk)} q_{i-\alpha, j, k-2\gamma} \\
&+ w_R^{(ijk)} q_{i-\alpha, j-2\beta, k} + w_S^{(ijk)} q_{i-\alpha, j, k} + w_{ijk} q_{ijk} \qquad (3.19) \\
q_d^{(ijk)} &= \tilde{w}_A^{(ijk)} q_{i-\alpha, j+\beta, k-\gamma} + \tilde{w}_B^{(ijk)} q_{i, j+\beta, k-\gamma} + \tilde{w}_C^{(ijk)} q_{i+\alpha, j+\beta, k-\gamma} \\
&+ \tilde{w}_D^{(ijk)} q_{i-\alpha, j+\beta, k} + \tilde{w}_E^{(ijk)} q_{i, j+\beta, k} + \tilde{w}_F^{(ijk)} q_{i+\alpha, j+\beta, k} \\
&+ \tilde{w}_G^{(ijk)} q_{i-\alpha, j+\beta, k+\gamma} + \tilde{w}_H^{(ijk)} q_{i, j+\beta, k+\gamma} + \tilde{w}_I^{(ijk)} q_{i+\alpha, j+\beta, k+\gamma} \\
&+ \tilde{w}_J^{(ijk)} q_{i-\alpha, j-\beta, k+\gamma} + \tilde{w}_K^{(ijk)} q_{i, j-\beta, k+\gamma} + \tilde{w}_L^{(ijk)} q_{i+\alpha, j-\beta, k+\gamma} \\
&+ \tilde{w}_M^{(ijk)} q_{i-\alpha, j, k+\gamma} + \tilde{w}_N^{(ijk)} q_{i, j, k+\gamma} + \tilde{w}_O^{(ijk)} q_{i+\alpha, j, k+\gamma} \\
&+ \tilde{w}_P^{(ijk)} q_{i+\alpha, j-\beta, k-\gamma} + \tilde{w}_Q^{(ijk)} q_{i+\alpha, j, k-\gamma} \\
&+ \tilde{w}_R^{(ijk)} q_{i+\alpha, j-\beta, k} + \tilde{w}_S^{(ijk)} q_{i+\alpha, j, k}, \qquad (3.20)
\end{aligned}
$$

where the coefficients $w^{(ijk)}$ and $\tilde{w}^{(ijk)}$ refer to the upwind and downwind interpolations corresponding to a considered point (ijk). Depending on the intersection surface, ten out of these 19 coefficients are set to zero. For the upwind interpolation, we have already included the local coefficient (ijk), which is only required when boundary conditions need to be specified (Sect. 3.2.4). We note that all (non-zero) interpolation coefficients may depend on the specific values of a considered quantity at the given grid points, via the interpolation parameter ω to ensure monotonicity. As in Sect. 3.2.1, also these monotonicity constraints result in non-linear Λ-operators.

3.2.4 Boundary conditions within the SC method

Since also our 3D SC method is formulated in Cartesian coordinates, the inner boundary is not necessarily aligned with the spatial grid (cf. Sect. 3.1.2), and the upwind (and downwind) interpolations need to be adapted near the stellar surface. For the upwind point, two situations may occur (see Fig. 3.4 for an example in the xz-plane): (i) The considered ray originates from the stellar surface (direction $\boldsymbol{n_1}$ in Fig. 3.4). In this case, we again use a core-halo approximation and set $I_u = I_c^+ = B_\nu(T_{rad})$. All other quantities are obtained from trilinear interpolation using the points $(E_u, F_u, H_u, I_u, N_u, O_u, S_u, p^{(ijk)})$ in Fig. 3.3, where representative estimates need to be defined at the core points (those points that are located inside the star). In hydrodynamic simulations, the analogue of these points are so-called 'ghost points'. (ii) The considered ray originates from a plane spanned by grid points that are partially lo-
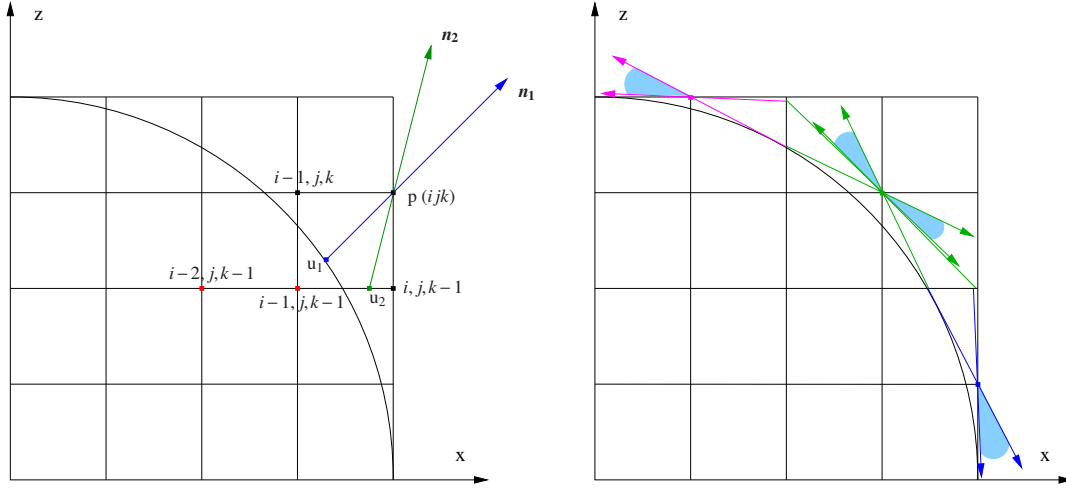
Figure 3.4: Left panel (from Hennicker et al. 2019): Boundary conditions for rays propagating in the xz-plane at y-level (j) with three different directions n_1, n_2, n_3, and upwind points u_1, u_2, u_3. For point u_1, the intensity is set to $I_u = I_c^+$ and all remaining quantities are obtained by bilinear interpolation from points $(i-1, j, k-1)$, $(i, j, k-1)$, $(i-1, j, k)$, and (ijk). The required quantities at point u_2 are found from Bézier interpolation using the values at $(i-2, j, k-1)$, $(i-1, j, k-1)$, $(i, j, k-1)$. The (unknown) quantities inside the core are indicated by red dots, and need to be reasonably approximated (see text). Right panel: Tangential rays for different grid points indicated with magenta, green, and blue arrows. Inward directed intensities, I_c^-, need to be specified only for directions within the blue shaded areas, because all other directions either originate directly from the stellar surface, or from outside of the atmosphere.

cated inside the star (direction n_2 in Fig. 3.4). Then, the interpolation is performed as in Sect. 3.2.3, using again representative estimates at the core-points.

Inside the core, we define $I_c^+ = S_L = S_C = B_\nu(T_{rad})$ and set I_c^- and all velocity components to zero, where I_c^- is the inward directed intensity which needs to be specified only in rare situations (Fig. 3.4, right panel). The opacities inside the star are found by extrapolation from the known values outside the star. While this procedure certainly introduces errors (e.g., by over-/underestimating the upwind source function in optically thin/thick cases, respectively), it is still favourable to extrapolating all values directly onto the stellar surface, mainly due to performance reasons[8]. In addition to the error introduced by the predefined values inside the core, the calculation of Δs_r is a certain issue, where Δs_r is the distance of the current grid point to the stellar surface. Since the radiative transfer near the stellar surface is (in most cases) very sensitive to the path length of a considered ray, Δs_r needs to be known exactly. Depending on the shape of the surface, Δs_r can be calculated analytically, or needs to be determined numerically. A numerical solution, however, might be time consuming and should be

---

[8] For a given grid point, the number of neighbouring grid points that can be used for extrapolation is not a priori clear, and depends on the shape of the stellar surface, and the considered direction of the ray. Indeed, there are 64 special cases that would have to be implemented explicitly. This is computationally not feasible.
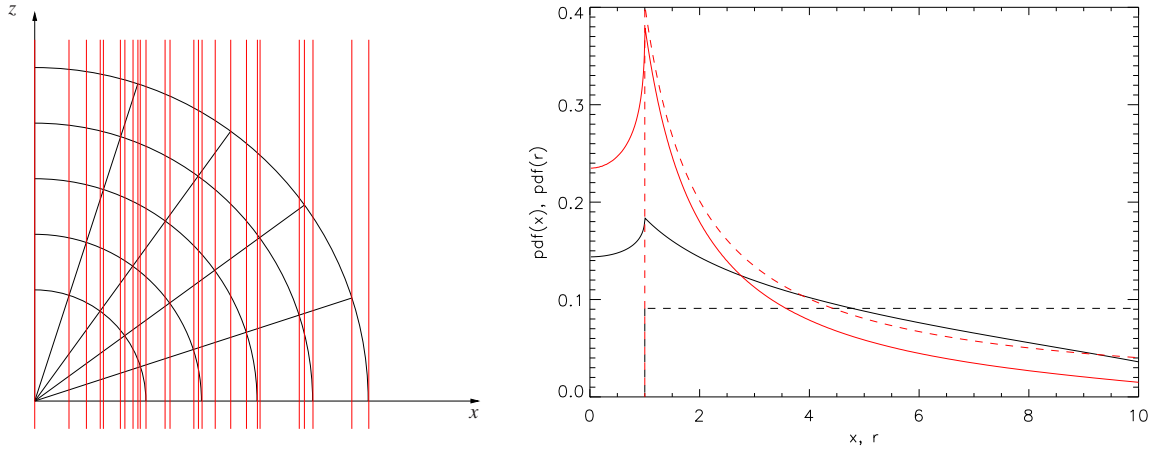
Figure 3.5: Left panel: Example for the distribution of x-coordinates (indicated with red lines) for a spherical input grid with equidistant (r, Θ) coordinates. Right panel (from Hennicker et al. 2019): Probability density functions of radial (dashed) and x (solid) coordinates for different spherical and Cartesian grids. In this example, two spherical grids are given in 2D as input to our 3D code, with uniformly (black) or logarithmically (red) distributed r-coordinates, and a uniformly distributed polar angle. The corresponding distributions of x-coordinates are calculated within our grid construction procedure (see text). Large values of the probability density functions correspond to a high resolution of x and r-coordinates.

avoided when possible.

Downwind quantities are always calculated from Eq. (3.20), using the estimates at the core points as defined above when necessary.

3.3 Grid construction[9]

Since the computation time of the 3D code scales with the number of grid points (per axis) to the third power, an elaborate grid construction is required to minimize the number of floating point operations, while enabling a reasonably high spatial resolution. Particularly when using the FVM, a reasonable grid should provide nearly equidistant step sizes of the optical depth in order to minimize errors introduced by the (first order) solution scheme. Since no grid refinement has been implemented for the FVM (yet), also the velocity field needs to be resolved to account for all resonance zones within the atmosphere. This latter property is also advantageous when the SC method is applied, since a large number of calls to the (computational expensive) grid refinement procedures can be avoided. Additionally, the (first or second order) interpolations of source functions and opacities perform best when the density structure is resolved.

Generally, we assume the wind structure (i.e., density, velocity field and temperature) to be given by an input model obtained from hydrodynamic simulations or external (semi)-analytic calculations.

---

[9] based on Hennicker et al. (2019, Appendix A).

Since the input grid is not necessarily compatible with our 3D FVM or SC solver, and to minimize interpolation errors when calculating upwind and downwind quantities, we construct an own grid that uses the distribution of the input-grid coordinates in an optimum way. When the input grid uses spherical coordinates (r, Θ, Φ), we define a joint probability distribution

$$f_{xz}(x,z) = f_r(r) f_\Theta(\Theta) |J|, \tag{3.21}$$

where $f_r(r)$ and $f_\Theta(\Theta)$ are the probability density functions derived from the distribution of the input coordinates, and $|J| = \sqrt{x^2 + z^2}$ is the Jacobian determinant. Since we consider only axisymmetric atmospheres in this thesis, we use the x-coordinate distribution also for the y-coordinates. We note that an explicit Φ-dependence can be included analogously, that is, by accounting for a different Jacobian determinant and multiplying Eq. (3.21) with $f_\Phi(\Phi)$. To calculate the probability density functions for x and z, we simply marginalize $f_{xz}(x, z)$ over z and x, respectively. Fig. 3.5 shows the probability density functions of the x-coordinates for two different input distributions of the radial grid. Here, the polar angle Θ has been assumed to be uniformly distributed for both examples.

The discretized coordinates are finally determined by demanding that the probabilities of selecting a (continuous) coordinate in each (discrete) interval shall be the same. For the x-coordinates, we obtain:

$$P(x \in [x_{i-1}, x_i]) = \int_{x_{i-1}}^{x_i} f_x(x) \mathrm{d}x \overset{!}{=} \int_{x_i}^{x_{i+1}} f_x(x) \mathrm{d}x = P(x \in [x_i, x_{i+1}]) \overset{!}{=}$$

$$\overset{!}{=} \text{const.} = \begin{cases} 1/N_{\text{core}} & \text{if } x \in [0, R_*] \\ 1/N_{\text{non-core}} & \text{else} \end{cases} . \tag{3.22}$$

Since the final number of core and non-core points depends on the slope of the probability density of the radial grid, yielding in worst cases a much larger number of core points than non-core points, and because the total number of used points is memory-limited, we define two input parameters N_{core} and $N_{\text{non-core}}$ to keep control on the final grid. For all test calculations (including those presented in Sect. 4.2), the best solution has always been found for a number of $N_{\text{core}}/N_{\text{non-core}} \in [0.25, 0.5]$. An explicit choice of N_{core} and $N_{\text{non-core}}$ corresponds to a re-normalization of the probability density function in the regimes $x, z \in [0, R_*]$ and $x, z \in [R_*, R_{\text{max}}]$, where R_{max} defines the border of the computational domain. We note that the same procedure can be used for an input grid given in Cartesian coordinates, with the probability density function of the input-grid coordinates derived directly from the corresponding (discrete) distribution.

3.4   Angular and frequency integration[10]

3.4.1   Angular integration

The mean intensity at each grid point is obtained from the solutions of the radiative transfer equation for many directions, where the distribution of these directions over the unit sphere depends on the

---

[10]based on Hennicker et al. (2018, Sect. 3.1), and Hennicker et al. (2019, Sect. 3.5).
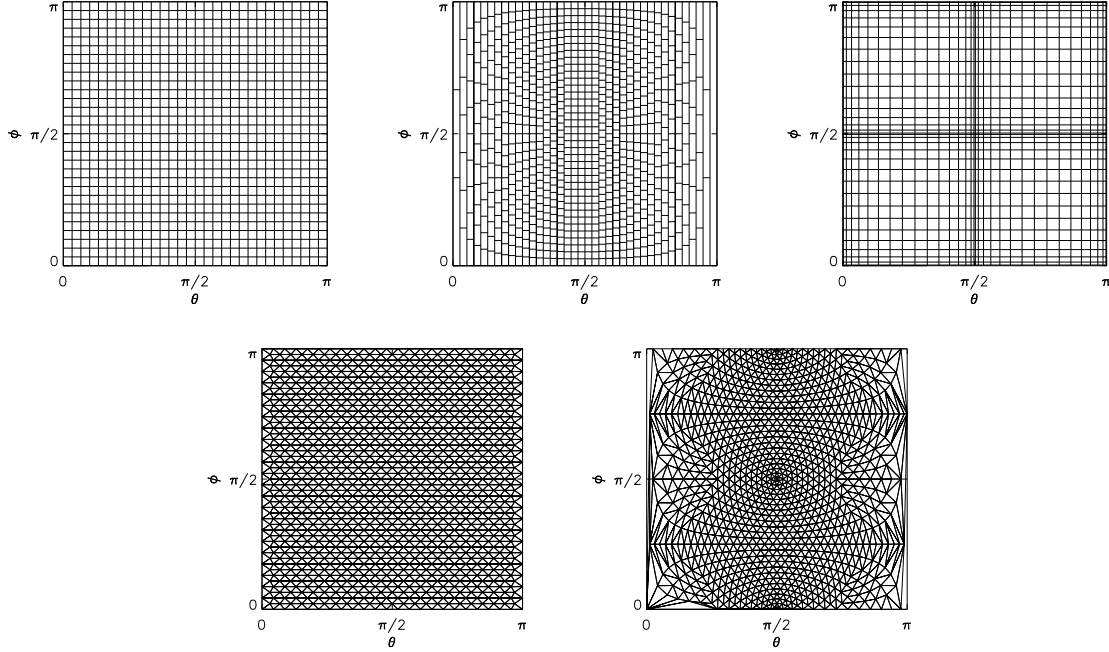
Figure 3.6: Different quadrature schemes for integrating the intensity over solid angle. The Trapezoidal, Simpson's, and Boole's rule use an equidistant quadrilateral grid (upper left panel), while the approach of Lobel & Blomme (2008) and the Gauss-Legendre quadrature apply a specific sampling of the solid angle, indicated in the middle and right panel of the upper row, respectively. The lower left and lower right panels show the triangular grid used for the barycentric interpolation approach, and the Lebedev nodes. Due to symmetry, we only display the polar angle within $\phi \in [0, \pi]$.

used quadrature formula. The resulting intensities are numerically integrated via

$$J_{ijk} = \frac{1}{4\pi} \int I_{ijk} \mathrm{d}\Omega = \sum_l w_l I_{ijk}(\Omega_l), \qquad (3.23)$$

with w_l the integration weight including the projection factor $\sin(\theta)$, and corresponding to a considered direction $\Omega_l = (\theta_l, \phi_l)$. The angular integration is particularly challenging for optically thin atmospheres, since in such situations each (spatial) grid point is illuminated by the stellar surface, and the distribution of intensities $I_{ijk}(\theta, \phi)$ becomes a 2D step-function in the θ-ϕ-plane (if no upwind interpolation errors were present). Depending on the considered position, the shape of $I_{ijk}(\theta, \phi)$ strongly varies. Thus, elaborate integration methods are required to resolve the star **and** its edges at any point of the atmosphere. Several different techniques and directional distributions have been implemented (see also Fig. 3.6):

Newton-Cotes quadratures: Within these methods, both the θ- and the ϕ-domain are discretized with equidistant steps, and the angular integration is performed using either the Trapezoidal, Simpson's or Boole's rule along the ϕ direction on each θ-level, followed by the integration

along θ. Thus, the solid-angle is approximated with quadrilaterals in the θ-ϕ plane. For equidistant grids, the actual distribution of directions becomes clustered towards the poles.

Trapezoidal rule as used by Lobel & Blomme (2008): This method uses the trapezoidal rule as described above, but with a decreasing number of azimuth grid points towards the poles to reasonably distribute the direction vectors on the unit sphere. For an equidistant θ-grid, Lobel & Blomme (2008) use an ansatz $d\Omega = $ const., and obtain different ϕ-grids on each θ-level. With $\Delta\phi_{eq}$ the ϕ-steps specified as input parameter at the equator, one easily obtains:

$$\Delta\Omega \approx \sin(\theta)\,\Delta\theta\Delta\phi = \text{const.} = \Delta\theta\Delta\phi_{eq} \quad \Longleftrightarrow \quad \Delta\phi(\theta) = \frac{\Delta\phi_{eq}}{\sin(\theta)}\,. \tag{3.24}$$

Gaussian quadrature: To increase the accuracy, we have implemented both a Gauss-Legendre and a Gauss-Chebyshev integration scheme (along θ and ϕ). An important property in this respect is that Gaussian-quadrature rules exactly integrate all (weighted)[11] polynomials up to degree $2n-1$, where n is the number of applied integration nodes. While this is (mathematically) the highest possible accuracy (e.g., Schwarz 1997), the major drawback of the Gaussian-quadrature schemes is that the integrations nodes are fixed and cannot be chosen arbitrarily. Furthermore, the directions are clustered towards the integration bounds, resulting in a poor sampling of the (complete) unit sphere. We note that the calculation of integration nodes for the Gauss-Legendre quadrature requires the inversion of a large matrix, which directly shows the advantage of a Cartesian grid, for which the angular nodes and weights are the same at all grid points, and can be calculated prior to the complete solution scheme. Using a spherical grid, Gaussian quadrature would become computationally very time-consuming, because the involved angles w.r.t. the coordinate system depend on position in the atmosphere.

Integration over triangles: All integration schemes mentioned thus far sample the θ-ϕ distribution of the specific intensity with quadrilaterals. For a (potentially) better sampling (particularly of the edges), we have implemented a triangular quadrature scheme, with the integration performed using barycentric coordinates to describe the variation of the specific intensity linearly within each triangle, or by applying Gaussian quadrature rules over the triangle. We note that the latter introduces negative integration weights and is therefore discarded to avoid negative mean intensities. Furthermore, since no additional information is used when compared to the quadrilateral approach, the triangular quadrature is not expected to give superior results.

Lebedev quadrature (see, e.g., Ahrens & Beylkin 2009, Beentjes 2015 and references therein): Finally, we have implemented the so-called Lebedev quadrature, which is optimized to exactly integrate the spherical harmonics up to a certain degree, with a (nearly) optimum distribution of direction vectors on the unit sphere.

Within the quadrilateral approaches, we split the integration into a sum over all octants to obtain a 'fair' angular resolution of the unit sphere (i.e., without preferring certain directions). We note already

---

[11] Within the Legendre and Chebyshev quadratures, the weight functions are defined as $w(x) = 1$ and $w(x) = 1/\sqrt{(1-x^2)}$, respectively.

here that the best results have been obtained using the Lebedev integration (Sect. 4.1.1 and Table 4.1). However, even for this (relatively elaborate) method, $N_\Omega \gtrsim 2000$ directions are required to obtain an acceptable numerical error. The corresponding angular resolution is – independent of the coordinate system – typical when calculating 3D radiative transfer problems in extended stellar atmospheres. For instance, Lobel & Blomme (2008) used $N_\Omega = 6400$ within their 3D finite-volume method.

Since the computation time for obtaining the mean intensity scales with the number of considered directions, it may be worth testing alternative quadrature schemes (and directional distributions) to minimize the number of required directions. For future work, we already plan to implement and test a (truly) uniform distribution of directions, determined from calculating the equilibrium positions of N equally charged particles (e.g., electrons) on the unit sphere. Then, each position can be associated with a direction vector, and might be assigned with an integration weight $1/N$.

3.4.2 Frequency integration

To calculate the scattering integral at a given point in the atmosphere, we apply the trapezoidal rule to integrate the specific intensity for a given direction over frequency. The scattering integral then reads:

$$\bar{J}_{ijk} = \frac{1}{4\pi} \int \int_{-\infty}^{\infty} I_{ijk} \Phi_x^{(ijk)} \mathrm{d}x \mathrm{d}\Omega = \frac{1}{4\pi} \int \int_{x_{\mathrm{obs}}^{(\mathrm{min})}}^{x_{\mathrm{obs}}^{(\mathrm{max})}} I_{ijk} \Phi_x^{(ijk)} \mathrm{d}x \mathrm{d}\Omega = \sum_l w_l \sum_x w_x I_{ijk} \Phi_x^{(ijk)}, \quad (3.25)$$

with w_x the frequency integration weight, and $x_{\mathrm{obs}}^{(\mathrm{min})}$ and $x_{\mathrm{obs}}^{(\mathrm{max})}$ the required frequency shift in the observer's frame, derived from the maximum absolute velocity occurring in the atmosphere:

$$x_{\mathrm{obs}}^{(\mathrm{min})} = \frac{-|v|_{\mathrm{max}} - 3v_{\mathrm{th}}(R_{\mathrm{max}})}{v_{\mathrm{th}}^*} \qquad x_{\mathrm{obs}}^{(\mathrm{max})} = \frac{|v|_{\mathrm{max}} + 3v_{\mathrm{th}}(R_{\mathrm{max}})}{v_{\mathrm{th}}^*}. \qquad (3.26)$$

To resolve the profile function at each point in the atmosphere, we demand that

$$\frac{\Delta x_{\mathrm{cmf}}}{\delta} \lesssim \frac{1}{3} \quad \Longleftrightarrow \quad \left[\frac{\Delta x_{\mathrm{obs}}}{\delta}\right]_{\boldsymbol{n}=\mathrm{const.}} \lesssim \frac{1}{3} \qquad (3.27)$$

at each position. Since the profile function depends on the ratio of fiducial to actual thermal width, the fiducial velocity should be set to the minimum thermal velocity present in the atmosphere. Then, the required resolution is found by determining the number of frequency points, N_ν, from the condition that $\Delta x_{\mathrm{obs}} = (x_{\mathrm{obs}}^{(\mathrm{max})} - x_{\mathrm{obs}}^{(\mathrm{min})})/(N_\nu - 1) \lesssim 1/3$. Since the comoving-frame frequency depends on the projected velocity, the corresponding integration nodes may not be centred around the profile maximum anymore. This issue is of only minor importance, and has been checked by a comparison to model calculations that use $\Delta x_{\mathrm{obs}} \lesssim 1/6$.[12] As outlined in Sect. 2.2.2, a number of $N_\nu \approx 1600$ frequency points would be required for typical wind terminal speeds and thermal velocities (if no micro-turbulent velocities were present). If, on the other hand, the micro-turbulent velocity is high, $v_{\mathrm{turb}} = 100 \,\mathrm{km\,s^{-1}}$, N_ν can be reduced considerably, by a factor of ten. Such high values are not un-typical in the winds

---

[12] While a highly resolved frequency grid ensures that the frequency nodes are found very near to the line centre, there is still no guarantee that the line centre is exactly matched. Such a requirement can only be provided by solving the radiative transfer in the comoving frame.

of hot stars (see below). Again, when compared to Lobel & Blomme (2008), who used $N_\nu = 100$
frequency points for an effective thermal velocity of $v_{th} = 30$ km s^{-1}, our frequency grid is much better
resolved, with ≈ 15 frequency points distributed over the complete line profile, whereas they resolved
the profile function with three frequency points only.

Microturbulence. To correctly treat the radiative transport in the line, we need to resolve the res-
onance zones, and demand that $\Delta(\boldsymbol{n} \cdot \boldsymbol{v}/v_{th}) \approx 1/3$ along a given direction. Again, for low micro-
turbulent velocities, we would require a resolution of at least 1600 grid points per spatial dimension
(for a spherical wind accounting for both hemispheres). On the other hand, including a large micro-
turbulent velocity ($v_{turb} = 100$ km s^{-1}), as applied here, results in a much lower required resolution,
both in space and frequency. Due to the linear (cubic) scaling of computation time with the number
of frequency (spatial) grid points, this results in a reduction of computation time by a factor of 10^4,
when compared to models without large micro-turbulent velocities. Putting it the other way round,
and already mentioning here that typical model-calculations within the 3D FVM take about 50 min-
utes of wallclock time per iteration (and using 16 processors, see Sect. 3.6), a large micro-turbulent
velocity is needed thus far to keep the computation time on a reasonable scale.

Hamann (1981) showed that such micro-turbulent velocities can indeed be used to correctly model
the black absorption troughs observed in the P Cygni profiles of hot star winds. From a theoretical
point of view, a large velocity dispersion mimics the effects of multiply non-monotonic velocity
fields, as originating from the line-driven instability (see, e.g., Lucy 1983, Puls et al. 1993).

Angular integration - revisited. When calculating line transitions, the location of resonance zones
at a given observer's frame frequency depends also on the considered direction. Thus, the profile
function additionally needs to be resolved by the angular grid. Defining ϑ as the angle between the
considered direction and the velocity vector at a given point, the resolution of the profile function is
given as:

$$\left[\frac{dx_{cmf}}{d\vartheta}\right]_{x_{obs}=const.} = -\frac{d(\cos(\vartheta)V)}{d\vartheta} = \sin(\vartheta)V \quad \Longleftrightarrow \quad [\Delta x_{cmf}]_{x_{obs}=const.} = V\sin(\vartheta)\Delta\vartheta, \qquad (3.28)$$

with V the absolute velocity at a given point in units of v_{th}^*. Thus, the lowest resolution of the
comoving-frame frequency is found for directions perpendicular to the flow, and depends on the ab-
solute value of the velocity. In extreme cases (e.g., $V \approx 2000$ km s$^{-1}/100$ km s$^{-1} = 20$), we obtain a
resolution of $\Delta x_{cmf}/\delta \approx 1.5$, when assuming that $\delta \approx 1$, $\Delta\vartheta \approx \sqrt{4\pi/N_\Omega}$, and $N_\Omega \approx 2000$. Obviously,
the profile function is not necessarily resolved by the angular grid. This problem, however, occurs
only in the outermost parts of the wind, where the absolute velocities are large. More importantly,
no resonance zone is completely neglected since $\Delta x_{cmf}/\delta < 6$. By performing test calculations using
a much finer angular resolution for spherically symmetric models, we found that the resulting error
is indeed very small. However, for very large absolute velocities ($v \gg 2000$ km s^{-1}), or if the thermal
velocity is small ($v_{th} \ll 100$ km s^{-1}), the angular resolution needs to be revised.

3.5 Λ-iteration[13]

By now, we are able to construct a formal solution for a given source function. In this section, we discuss the iteration procedure. The following discussion considers the line case alone, with a frequency-independent background continuum (i.e., constant continuum opacity and source function), assumed to be known (either in form of an optically thin continuum, or from previous calculations in the absence of the line). For convenience, we summarize the basic ideas and corresponding acceleration techniques via the accelerated Λ-iteration from first principles.

3.5.1 Matrix equation

To show that the Λ-formalism can also be applied to our 3D FVM and SC formulations, we derive a matrix equation for the intensity, mean intensity and scattering integral, and show that these equations are consistent with an affine representation of the Λ-operators. Since, however, the final approximate Λ-operator (ALO) will be calculated differently, a detailed description of the involved matrices is skipped in the following.

All 3D quantities are expressed as vectors of length $N_x \times N_y \times N_z$, by introducing a unique ordering of the (ijk)-triple:

$$m := i + N_x(j-1) + N_x N_y(k-1), \tag{3.29}$$

with $i,j,k \in [1, N_{x,y,z}]$, $m \in [1, N_x N_y N_z]$, and N_x, N_y, N_z the number of spatial grid points of the x, y, and z coordinates. Eq. (3.29) simply transforms a data cube to a 1D array. For the 3D FVM, we obtain, after replacing the (i,j,k)-indices in Eq. (3.6) with this unique index, m:

$$\frac{1}{b_m} I_m - \frac{c_m}{b_m} I_{m-\alpha} - \frac{d_m}{b_m} I_{m-\beta N_x} - \frac{e_m}{b_m} I_{m-\gamma N_x N_y} = \frac{a_m}{b_m} S_m^{(C)} + S_m^{(L)}, \tag{3.30}$$

where we have collected all intensity terms on the left-hand side. For the 3D SC method, we can proceed similarly by using the corresponding discretized radiative transfer equation, Eqs. (3.12)/(3.17), with upwind and downwind quantities substituted from Eqs. (3.19) and (3.20). However, since the interpolation coefficients often depend on the intensity (and source functions) to ensure monotonicity, a matrix equation similar to Eq. (3.30) can only be formulated after all interpolation parameters ω have been determined (for a given stratification of source functions and intensities). For further details, we refer to Sect. 3.5.2 and Appendix D. Eq. (3.30) can be written in matrix form,

$$T \cdot I = Q \cdot S^{(C)} + S^{(L)} + I_{inc}, \tag{3.31}$$

where I_{inc} describes the boundary conditions. Since we use a TLA with given opacity (i.e., the opacity does not change during the iteration), and consider time-independent boundary conditions, we combine the constant vectors from Eq. (3.31), $\widetilde{I}_{inc} := Q \cdot S^{(C)} + I_{inc}$. Inverting the matrix T yields:

$$I = T^{-1} \cdot S^{(L)} + T^{-1} \cdot \tilde{I}_{inc} =: \Lambda_{\Omega,\nu} \cdot S^{(L)} + \Xi_B^{(\Omega,\nu)}. \tag{3.32}$$

---

[13] based on Hennicker et al. (2018, Sect. 3.2), and Hennicker et al. (2019, Sect. 3.6).

The vector $\mathbf{\Xi}_{\mathrm{B}}^{(\Omega,\nu)}$ describes the contribution of the boundary conditions and the background continuum for a particular direction and frequency. To calculate the mean intensity and scattering integral, we integrate over all angles (and frequencies):

$$J = \frac{1}{4\pi}\int \boldsymbol{I}\mathrm{d}\Omega = \frac{1}{4\pi}\int \boldsymbol{\Lambda}_{\Omega,\nu}\cdot\boldsymbol{S}^{(\mathrm{L})} + \mathbf{\Xi}_{\mathrm{B}}^{(\Omega,\nu)}\mathrm{d}\Omega = \underbrace{\frac{1}{4\pi}\int \boldsymbol{\Lambda}_{\Omega,\nu}\mathrm{d}\Omega}_{=:\,\boldsymbol{\Lambda}_{\nu}}\cdot\boldsymbol{S}^{(\mathrm{L})} + \underbrace{\frac{1}{4\pi}\int \mathbf{\Xi}_{\mathrm{B}}^{(\Omega,\nu)}\mathrm{d}\Omega}_{=:\,\mathbf{\Xi}_{\mathrm{B}}^{(\nu)}} \quad (3.33)$$

$$\bar{J} = \frac{1}{4\pi}\int \boldsymbol{\Phi}_{x}\cdot\boldsymbol{I}\mathrm{d}x\mathrm{d}\Omega = \frac{1}{4\pi}\int \boldsymbol{\Phi}_{x}\cdot\boldsymbol{\Lambda}_{\Omega,\nu}\cdot\boldsymbol{S}^{(\mathrm{L})} + \boldsymbol{\Phi}_{x}\cdot\mathbf{\Xi}_{\mathrm{B}}^{(\Omega,\nu)}\mathrm{d}x\mathrm{d}\Omega =$$

$$= \underbrace{\frac{1}{4\pi}\int \boldsymbol{\Phi}_{x}\cdot\boldsymbol{\Lambda}_{\Omega,\nu}\mathrm{d}x\mathrm{d}\Omega}_{=:\,\boldsymbol{\Lambda}}\cdot\boldsymbol{S}^{(\mathrm{L})} + \underbrace{\frac{1}{4\pi}\int \boldsymbol{\Phi}_{x}\cdot\mathbf{\Xi}_{\mathrm{B}}^{(\Omega,\nu)}\mathrm{d}x\mathrm{d}\Omega}_{=:\,\mathbf{\Xi}_{\mathrm{B}}}, \quad (3.34)$$

with the diagonal matrix $\boldsymbol{\Phi}_{x}$ describing the local profile function, and $\mathbf{\Xi}_{\mathrm{B}}^{(\nu)}$, $\mathbf{\Xi}_{\mathrm{B}}$ representing the contribution of the boundary conditions and the background continuum to the mean intensity and scattering integral, respectively. As later shown in Sect. 3.5.3, an explicit calculation of these quantities is not required to obtain the finally used ALO. We note that also for the continuum case, which is calculated close (w.r.t. frequency) to the line, Eq. (3.33) is applicable, with a different $\boldsymbol{\Lambda}$-matrix and boundary contribution though. A comparison of Eqs. (3.32)-(3.34) with the standard $\boldsymbol{\Lambda}$-formalism for the formal solution of the intensity, mean intensity and scattering integral, directly shows that the $\boldsymbol{\Lambda}$-operator is an affine operator, i.e., a linear operator given by the $\boldsymbol{\Lambda}$-matrix plus a constant displacement vector $\mathbf{\Xi}_{\mathrm{B}}$ (see Puls 1991), also for our 3D method:

$$\boldsymbol{I} = \boldsymbol{\Lambda}_{\Omega,\nu}[S_{\mathrm{C,L}}] = \boldsymbol{\Lambda}_{\Omega,\nu}\cdot\boldsymbol{S}_{\mathrm{C,L}} + \mathbf{\Xi}_{\mathrm{B}}^{(\Omega,\nu)}, \quad (3.35)$$

$$\boldsymbol{J} = \boldsymbol{\Lambda}_{\nu}[S_{\mathrm{C}}] = \boldsymbol{\Lambda}_{\nu}\cdot\boldsymbol{S}^{(\mathrm{C})} + \mathbf{\Xi}_{\mathrm{B}}^{(\nu)}, \quad (3.36)$$

$$\bar{J} = \boldsymbol{\Lambda}[S_{\mathrm{L}}] = \boldsymbol{\Lambda}\cdot\boldsymbol{S}^{(\mathrm{L})} + \mathbf{\Xi}_{\mathrm{B}}, \quad (3.37)$$

with subscripts Ω and ν defining the dependence of the $\boldsymbol{\Lambda}$-operator on direction and frequency, respectively.

From equations (2.38) and (3.34), we could formulate an explicit solution of the radiation field already now. This, however, would require the calculation, storage and inversion of the complete $\boldsymbol{\Lambda}$-matrix, which is computationally prohibitive:

(i) The $\boldsymbol{\Lambda}$-matrix is a full matrix with $N_{\mathrm{x}}N_{\mathrm{y}}N_{\mathrm{z}}\times N_{\mathrm{x}}N_{\mathrm{y}}N_{\mathrm{z}}$ elements, which would require, for typical grid sizes of $N := N_{\mathrm{x}} = N_{\mathrm{y}} = N_{\mathrm{z}} = 93$, $N^{6} \approx 6.5\cdot 10^{11}$ numbers, equivalent to 5.2 TB data to be stored in memory, when double-precision numbers are used.

(ii) The $\boldsymbol{\Lambda}$-matrix elements can be obtained, at least in principle, by inversion (see also Puls 1991),

$$\Lambda_{m,n} = \bar{J}_{m}(\boldsymbol{S}^{(\mathrm{L})} = \boldsymbol{e}_{n}, \mathbf{\Xi}_{\mathrm{B}} = 0), \quad (3.38)$$

with the n-th unit vector $\boldsymbol{e}_{n}$, and matrix indices m,n related to the 3D indices (ijk) via Eq. (3.29). The m,n-th matrix-element thus describes the effect of a non-vanishing source function at grid point n onto grid point m. We emphasize that within the 3D SC method, Eq. (3.38) holds only

for pre-calculated interpolation parameters ω, obtained from an already known stratification of source functions. To calculate the complete $\boldsymbol{\Lambda}$-matrix, $N_x \times N_y \times N_z$ formal solutions would be required, which again is computationally prohibitive on reasonably well-resolved grids.

An iterative solution is therefore the only possibility to solve problems of this kind.

3.5.2   Accelerated Λ-iteration

In the following, we concentrate on the line case, noting that the continuum case can be treated in close analogy. The classical Λ-iteration scheme is defined by calculating a formal solution for a given source function using Eq. (3.37), followed by the calculation of a new source function by means of Eq. (2.38). For optically thick, scattering dominated atmospheres, however, this iteration scheme suffers from severe convergence problems (see Fig. 4.6 for the convergence behaviour of spherically symmetric test models). To overcome these problems, we apply an accelerated Λ-iteration scheme based on operator-splitting methods (Cannon 1973). For completeness, we mention here a similar approach, the 'non-linear multi-grid method' (see Fabiani Bendicho et al. 1997 and references therein), which has even better convergence properties, and, in contrast to the ALI method, does not depend on the spatial resolution of the grid[14]. Since, however, the multi-grid method is both complicated to implement and expensive in terms of computation time, we focus on the (at least for 1D problems well established) ALI method within this thesis. The original Λ-operator is then split into the combination:

$$\Lambda = \Lambda^{(A)} + (\Lambda - \Lambda^{(A)}), \tag{3.39}$$

where the first term is an appropriately chosen ALO acting on the new source function, $S_L^{(k)}$, and the second term acts on the previous one, $S_L^{(k-1)}$. For the converged solution, this scheme becomes an exact relation. Appropriately chosen means that $\Lambda^{(A)}$ should be easily calculated (preferentially, in parallel with the formal solution), and easily inverted. Moreover, the ALO should reflect the basic physical properties of the original Λ-operator, in order to significantly boost the convergence. Using also, and in analogy to the exact Λ-operator, an affine representation for the approximate one, $\Lambda^{(A)}[S] = \boldsymbol{\Lambda}^* \cdot \boldsymbol{S} + \boldsymbol{\Xi}_B$ (see above), and evaluating $\Lambda^{(A)}$ at the previous iteration step, $k-1$, we obtain:

$$
\begin{aligned}
S_L^{(k)} \;\;\overset{\text{Eq. (2.38)}}{=}\;\; & \boldsymbol{\zeta} \cdot \bar{\boldsymbol{J}}^{(k)} + \boldsymbol{\Psi} \;\;\overset{\text{Eq. (3.39)}}{\approx}\;\; \boldsymbol{\zeta} \cdot \Lambda_{k-1}^{(A)} \big[S_L^{(k)} \big] + \boldsymbol{\zeta} \cdot \big(\Lambda_{k-1} - \Lambda_{k-1}^{(A)} \big) \big[S_L^{(k-1)} \big] + \boldsymbol{\Psi} \\
= \;\; & \boldsymbol{\zeta} \cdot \big(\boldsymbol{\Lambda}_{k-1}^* \cdot S_L^{(k)} + \boldsymbol{\Xi}_B^{(k-1)} + \bar{\boldsymbol{J}}^{(k-1)} - \boldsymbol{\Lambda}_{k-1}^* \cdot S_L^{(k-1)} - \boldsymbol{\Xi}_B^{(k-1)} \big) + \boldsymbol{\Psi}.
\end{aligned}
$$

Here, the iteration indices $k-1$ and k are indicated as sub- or superscripts, $\boldsymbol{\zeta} := \mathbf{1} - \boldsymbol{\epsilon}_L$ is a diagonal matrix, and $\boldsymbol{\Psi} := \boldsymbol{\epsilon}_L \cdot \boldsymbol{B}_\nu(\boldsymbol{T})$ is the thermal contribution vector. For multi-level atoms, we emphasize that Λ and $\Lambda^{(A)}$ may change within the ALI-cycle due to the variation of opacities (induced by the subsequently updated occupation numbers). Furthermore, both operators might also change, even within the simplified TLA approach considered in this thesis, since the corresponding matrix elements

---

[14] Within the ALI method, the convergence behaviour is primarily determined by the optical-depth steps, $\Delta\tau_{x,y,z}$ and $\Delta\tau_{\text{ray}}$ within the FVM and SC methods, respectively, that severely affect the $\boldsymbol{\Lambda}$-matrix coefficients. The finer the grid, the poorer the convergence behaviour (Kunasz & Olson 1988).

depend on the source functions via the interpolation parameters ω_{k-1}, ω_k within the SC method using Bézier interpolations.

Rearranging terms, we find:

$$(\mathbf{1} - \zeta \cdot \mathbf{\Lambda}^*_{k-1}) \cdot \mathbf{S}^{(k)}_{\mathrm{L}} = \zeta \cdot \left(\bar{\mathbf{J}}^{(k-1)} - \mathbf{\Lambda}^*_{k-1} \cdot \mathbf{S}^{(k-1)}_{\mathrm{L}} \right) + \mathbf{\Psi}. \qquad (3.40)$$

Eq. (3.40) needs to be solved to obtain a new source function $\mathbf{S}^{(k)}_{\mathrm{L}}$. Since for the 3D SC method, however, $\mathbf{\Lambda}^*_{k-1}$ has been optimized only to ensure monotonicity in a specific step $k-1$ (based on source function $\mathbf{S}^{(k-1)}_{\mathrm{L}}$), the iteration scheme can oscillate due to oscillations in $\mathbf{\Lambda}^*_k$ and $\mathbf{\Lambda}^*_{k-1}$. Even worse, the new source function might become negative. To overcome these problems, non-linear situations need to be avoided (by providing almost constant $\mathbf{\Lambda}^*$-matrices over subsequent iteration steps). The following approach has proved to lead to a stable and convergent scheme: In the first four iteration steps, we apply purely linear interpolations ($\omega_{k-1} = \omega_k = 1$ and thus $\mathbf{\Lambda}^*_k = \mathbf{\Lambda}^*_{k-1}$), to obtain an already smooth stratification of source functions. Additionally, we globally define a minimum allowed interpolation parameter and demand that $\omega > \omega_{\min}$. Then, ω becomes constant (namely $\omega = \omega_{\min}$) in (most) critical situations, and again, $\mathbf{\Lambda}^*_k$ approaches $\mathbf{\Lambda}^*_{k-1}$. Whenever negative source functions or oscillations occur within the iteration scheme, $\omega_{\min}$ is gradually increased to unity. With this approach, we obtain an always convergent iteration scheme, with a formal solution obtained by using linear interpolations only in most challenging cases. Since the $\mathbf{\Lambda}^*$-matrices within the 3D FVM are constant over the complete iteration cycle, the above described problem is completely avoided.

The rate of convergence achieved by the accelerated $\mathbf{\Lambda}$-iteration scheme increases with the number of $\mathbf{\Lambda}$-matrix elements included in the ALO. To minimize the computation time of the complete procedure, the choice of the ALO is always a compromise between the number of matrix-elements to be calculated, and the resulting convergence speed. We could, for instance, choose $\mathbf{\Lambda}^{(A)} = \mathbf{\Lambda}$, which would result in the direct solution via inversion, and is computationally not feasible, as discussed above. On the other hand, choosing $\mathbf{\Lambda}^{(A)} = 0$ would result in the classical $\mathbf{\Lambda}$-iteration, with the known convergence problems. Olson et al. (1986) showed that an ALO containing only the diagonal of the exact $\mathbf{\Lambda}$-matrix is very efficient, because the matrix $(\mathbf{1} - \zeta \cdot \mathbf{\Lambda}^*)$ becomes diagonal, and Eq. (3.40) could be solved by a simple scalar division. Furthermore, the diagonal, i.e., the local part, already contributes most to the radiative transfer (at least in the critical optically thick case), and thus, is quite a good approximation for the original $\mathbf{\Lambda}$-operator. Such an ALO corresponds to the well known Jacobi-iteration (see also Trujillo Bueno & Fabiani Bendicho 1995 for a thoughtful discussion, also about a Gauss-Seidel method with successive overrelaxation in the context of the ALI).

In 3D calculations, however, a diagonal ALO will not converge fast enough (see Sect. 4.2.2). To achieve faster convergence rates, a multi-band ALO is favourable, as already shown by Olson & Kunasz (1987) for 1D cases, and extended to a 3D, long-characteristics solver by Hauschildt & Baron (2006), and thus implemented within our 3D FVM and SC framework. For such ALOs, the matrix $(\mathbf{1} - \zeta \cdot \mathbf{\Lambda}^*)$ is sparse, whereas its inverse is a full matrix, and cannot be stored due to the N^6 scaling of required memory. Therefore, we have already formulated Eq. (3.40) as a fix-point iteration, $\mathbf{A} \cdot \mathbf{S}^{(k)} = \mathbf{b}$, which can be solved for the new iterate by applying Jacobi or Gauss-Seidel methods. We found that a Jacobi-iteration, coupled with the storage of the iteration-matrix in coordinate-format (COO), is particularly fast and easy, because its computationally most expensive term is a matrix-

vector multiplication, which reduces to N_{NZ} operations only, where N_{NZ} is the number of non-zero elements (see, e.g., Tessem 2013 and Appendix E for further details).

3.5.3 Constructing the ALO

To construct a multi-band ALO as aimed at above, we need to calculate the corresponding elements of the exact Λ-matrix. This could be done, in principle, by using Eq. (3.32), which would require the inversion of $\boldsymbol{T}$. Since the local intensity – whether calculated within the FVM or SC method – depends solely on the intensities at the *upwind* side of a given direction (and on the local and neighbouring source functions), we can alternatively simply use Eq. (3.38), in combination with the discretized equation of radiative transfer of each method.

The Λ-matrix elements within the FVM.   The Λ-matrix elements for the FVM are calculated from Eq. (3.6). Since the (m,n)-th element of the Λ-matrix describes the impact of a non-vanishing source term at point $n \leftrightarrow (i'j'k')$ onto a point $m \leftrightarrow (ijk)$, the local contribution is given by $n = m$, whereas the coupling with directly neighbouring points is found from:

$$
\begin{aligned}
n(i-1,j,k) &= m-1 && \text{for } n_x > 0, & n(i+1,j,k) &= m+1 && \text{for } n_x < 0, \\
n(i,j-1,k) &= m-N_x && \text{for } n_y > 0, & n(i,j+1,k) &= m+N_x && \text{for } n_y < 0, \\
n(i,j,k-1) &= m-N_xN_y && \text{for } n_z > 0, & n(i,j,k+1) &= m+N_xN_y && \text{for } n_z < 0.
\end{aligned}
$$

One big advantage of the 3D FVM is that the exact elements of local and neighbouring terms can be easily calculated from Eq. (3.6),

$$
\Lambda_{m,m} = \frac{1}{4\pi} \int \int b_{ijk} \Phi_x^{(ijk)} \mathrm{d}\Omega \mathrm{d}x \tag{3.41}
$$

$$
\Lambda_{m,m-1} = \frac{1}{4\pi} \int \int_{n_x>0} b_{i-1jk} c_{ijk} \Phi_x^{(ijk)} \mathrm{d}\Omega \mathrm{d}x \tag{3.42}
$$

$$
\Lambda_{m,m-N_x} = \frac{1}{4\pi} \int \int_{n_y>0} b_{ij-1k} d_{ijk} \Phi_x^{(ijk)} \mathrm{d}\Omega \mathrm{d}x \tag{3.43}
$$

$$
\Lambda_{m,m-N_xN_y} = \frac{1}{4\pi} \int \int_{n_z>0} b_{ijk-1} e_{ijk} \Phi_x^{(ijk)} \mathrm{d}\Omega \mathrm{d}x \tag{3.44}
$$

$$
\Lambda_{m,m+1} = \frac{1}{4\pi} \int \int_{n_x<0} b_{i+1jk} c_{ijk} \Phi_x^{(ijk)} \mathrm{d}\Omega \mathrm{d}x \tag{3.45}
$$

$$
\Lambda_{m,m+N_x} = \frac{1}{4\pi} \int \int_{n_y<0} b_{ij+1k} d_{ijk} \Phi_x^{(ijk)} \mathrm{d}\Omega \mathrm{d}x \tag{3.46}
$$

$$
\Lambda_{m,m+N_xN_y} = \frac{1}{4\pi} \int \int_{n_z<0} b_{ijk+1} e_{ijk} \Phi_x^{(ijk)} \mathrm{d}\Omega \mathrm{d}x. \tag{3.47}
$$

We call this ALO 'direct neighbour' (DN)-ALO, to discriminate from the 'nearest neighbour' (NN)-ALO from Hauschildt & Baron (2006), who use all 26 surrounding grid points and the local term, whereas we are using the local term and the contribution from the six direct neighbours only[15]. Although it would be possible to include the other neighbouring terms in our calculations, we note that

---

[15]For tests of the convergence properties in Sect. 4.2.2, we also calculated a purely diagonal ALO by means of Eq. (3.41) alone.

the calculation of the ALO elements in parallel to the formal solution requires, in our case, already 50% of the calculation time, which would increase rapidly when including even more terms for the ALO. On the other hand, the inversion of the ALO, i.e., the calculation of the new iterate via Jacobi-iterations, requires only about 0.5% of the calculation time needed for the complete formal solution. We emphasize that the ALO needs to be calculated only once, because the opacity of the (simplified) TLA remains constant over subsequent iteration cycles. When considering multi-level atoms (as planned in the future), the situation changes, and the opacity depends on the occupation numbers, and thus, also on the radiation field. We therefore implemented the calculation of the ALO in parallel to the formal solution at each iteration step already at the current stage of our code.

The Λ-matrix elements within the SC method.   To calculate the Λ-matrix elements within the SC method (including all upwind and downwind interpolations), we extend the procedure developed by Olson & Kunasz (1987) and Kunasz & Olson (1988). A detailed derivation is given in Appendix D. Eqs. (D.1)-(D.27) correspond to the exact Λ-matrix elements for a local point and its 26 neighbours, and thus should give an excellent rate of convergence when included in the ALO (see, e.g., the 26-neighbour ALO of Phoenix/3D, Hauschildt & Baron 2006). As for the 3D FVM, all elements can be calculated in parallel to the formal solution also within our SC method. Again, this property becomes important when the ALO varies during the iteration scheme, that is, when applying monotonic Bézier interpolations (as discussed above), or when accounting for multi-level atoms. For the simplified continuum and the TLA considered in this thesis, the linear interpolation scheme is particularly advantageous in terms of computation time, since the corresponding ALO remains (similarly to the ALO within the FVM method) constant over all iteration steps, and therefore needs (in principle) to be calculated only once.

In Chapter 4 of this thesis, we analyse the convergence speed of the ALI for (i) a diagonal ALO given by Eq. (D.14), (ii) a 'direct-neighbour' (DN)-ALO given by Eqs. (D.5), (D.11), (D.13), (D.14), (D.15), (D.17), (D.23) and (iii) a 'nearest-neighbour' (NN)-ALO obtained from all Eqs. (D.1)-(D.27). We note that within our SC method, only a moderate reduction of computation time results when using the diagonal or DN-ALO, since the diagonal and direct-neighbour elements depend on several other neighbours through the inclusion of downwind interpolations. Since, however, the downwind-integration weight is generally negative, neglecting these terms will overestimate the considered matrix elements, potentially resulting in a divergent iteration scheme. On the other hand, when using purely linear interpolations (for the source contribution and upwind interpolations), the calculation of the ALO is greatly simplified since all coefficients c_{ijk} and w_A, w_B, w_C, w_D, w_G, w_J, w_K, w_L, w_M, w_P, w_Q, w_R vanish. For third-order upwind/downwind interpolations as used in IRIS (Ibgui et al. 2013a), the calculation of the ALO coefficients becomes computationally prohibitive at some point. Considering both interpolation techniques used in this thesis, the calculation of the diagonal, DN- and NN-ALO in parallel to the formal solution requires roughly 20%, 30% and 40% of the total computation time (of each applied interpolation method).

Ng-extrapolation.   To accelerate the iteration scheme further, we implemented the extrapolation technique from Ng (1974) (see also Olson et al. 1986). In order to use independent extrapolations, the

Ng-acceleration is applied in each fifth iteration step.

3.6   Timing[16]

When calculating line transitions, $N_\Omega \times N_\nu$ formal solutions of the equation of radiative transfer are required to calculate the scattering integrals. In order to obtain accurate angular and frequency integrals, the minimum number of integration nodes is basically fixed, and the computation time can only be further reduced by parallelization. Thus, we have parallelized the code over the frequency grid using OpenMP. We note that OpenMP creates a local copy of the 3D arrays representing the intensity and the (nearest-neighbour) Λ-matrix. With 27 Λ-matrix elements (per spatial grid point) included for the ALO calculations, the (spatial) resolution becomes therefore memory limited. A typical resolution of $N_x = N_y = N_z = 93$, however, is still feasible, and gives reasonable results.

As a first inspection of the performance of our methods, we applied a test calculation using the same grid as Lobel & Blomme (2008), with an equidistant grid-spacing and $N = 71^3$ grid points. For the 3D FVM and SC methods, we find computation times of $t_{\text{FVM}} \approx 0.037$s, $t_{\text{SC}}^{\text{(linear)}} \approx 0.138$s, and $t_{\text{SC}}^{\text{(Bézier)}} \approx 0.448$s per iteration, per CPU, and per angular and frequency grid point on an Intel Xeon X5650 (2.67 GHz) machine with 16 CPUs. As a reference, Wind3D requires about $t_{\text{FVM}}^{\text{Wind3D}} \approx 0.045$s on a somewhat slower architecture (Itanium-2 (1.5 GHz) CPUs, see Lobel & Blomme 2008). Since, however, our FVM algorithms require at least a factor of two more operations due to the calculation of the (non-local) approximate Λ-operator in parallel to the formal solution, we are convinced of the efficiency of our implementation of the FVM. For the 3D SC methods using linear/Bézier interpolations, the computation times are increased by a factor of roughly four/twelve, when compared to our 3D FVM. These differences originate from the computationally more challenging upwind/downwind interpolations, the integration of the discretized radiative transfer equation on (potentially) refined grids along a given ray, and from the calculation of an ALO including 26 neighbouring elements (instead of the six direct neighbours as used for the 3D FVM).

When using a non-uniform grid-spacing, the differences between the FVM and SC methods decrease, primarily because the number of calls to the SC grid-refinement procedure becomes diminished. For the models calculated in Sect. 4.2.3, typical computation times are $t_{\text{FVM}} \approx 0.8$ h, $t_{\text{SC}}^{\text{(linear)}} \approx 2$ h and $t_{\text{SC}}^{\text{(Bézier)}} \approx 6$ h per iteration.

3.7   A long-characteristics postprocessing routine

To calculate synthetic line profiles, we implemented a postprocessing LC solver based on Lamers et al. (1987), Busche & Hillier (2005), and Sundqvist et al. (2012). For an observer located at a distance $d \gg R_{\text{max}}$, where R_{max} is the radius of an emitting sphere (e.g., $R_{\text{max}} = R_*$ for a single star without wind), we can assume all rays incident on the detector to be parallel. The observed radiation flux per unit area can then be described by the z-component of Eq. (2.13):

$$F_\nu = \int_0^{2\pi} \int_0^{\pi/2} I_\nu(\vartheta, \varphi, d) \cos(\vartheta) \sin(\vartheta) \mathrm{d}\vartheta \mathrm{d}\varphi, \tag{3.48}$$

---

[16]based on Hennicker et al. (2018, Sect. 3.1), and Hennicker et al. (2019, Sect. 3.7).
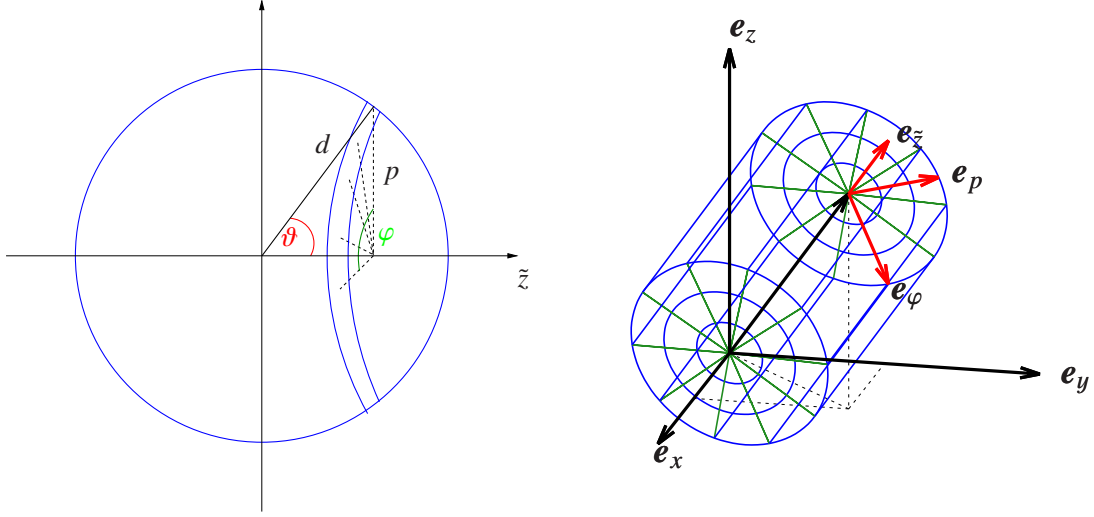
Figure 3.7: Geometry used for the LC postprocessing routine. Left panel (adapted from Mihalas 1978): Definition of ϑ and φ angles for calculating the flux in a direction $\tilde{z}$ through a sphere with radius d. For the considered annulus, p describes the impact parameter. Right panel: Coordinate system for calculating the emergent flux profile. While the Cartesian coordinate system $\boldsymbol{e}_x$, $\boldsymbol{e}_y$, $\boldsymbol{e}_z$ corresponds to the 3D SC/FVM solver, we use cylindrical coordinates with the $\tilde{z}$-axis aligned with the observer's direction under consideration to integrate over impact-parameter p and angle φ.

with ϑ, φ defined in Fig. 3.7. Since no radiation enters the sphere at a distance d, the ϑ-integral is limited to $\vartheta \in [0, \pi/2]$. With the impact parameter $p = d\sin(\vartheta)$, Eq. (3.48) can be rewritten:

$$\mathrm{d}p = d\cos(\vartheta)\mathrm{d}\vartheta\,, \qquad p(\vartheta = 0) = 0\,, \qquad p(\vartheta = \pi/2) = d$$

$$\Longrightarrow F_\nu = \frac{1}{d^2} \int_0^{2\pi} \int_0^d I_\nu(p,\varphi,d)p\,\mathrm{d}p\,\mathrm{d}\varphi = \frac{1}{d^2} \int_0^{2\pi} \int_0^{R_{\max}} I_\nu(p,\varphi,R_{\max})p\,\mathrm{d}p\,\mathrm{d}\varphi\,, \qquad (3.49)$$

where the second equality holds since the emitting region is limited to the radius of the emitting sphere, and because there is no additional absorption between $\tilde{z} \in [d, R_{\max}]$, such that $I_\nu(p,\varphi,d) = I_\nu(p,\varphi,R_{\max})$. To calculate the corresponding integrals numerically, the converged source function is used to derive the formal solution along characteristics in a cylindrical coordinate system, with the $\tilde{z}$-axis aligned with the line of sight (see Fig. 3.7). To this end, the p and φ-domains are discretized using $N_{\mathrm{p}} = 200$ and $N_\varphi = 80$ grid points. All quantities required on the rays are found by trilinear interpolation from the Cartesian 3D grid, and the equation of radiative transfer is integrated using linear interpolations. Finally, the flux is obtained by numerically integrating the emergent intensity over the projected disc with radius $R_{\max}$.
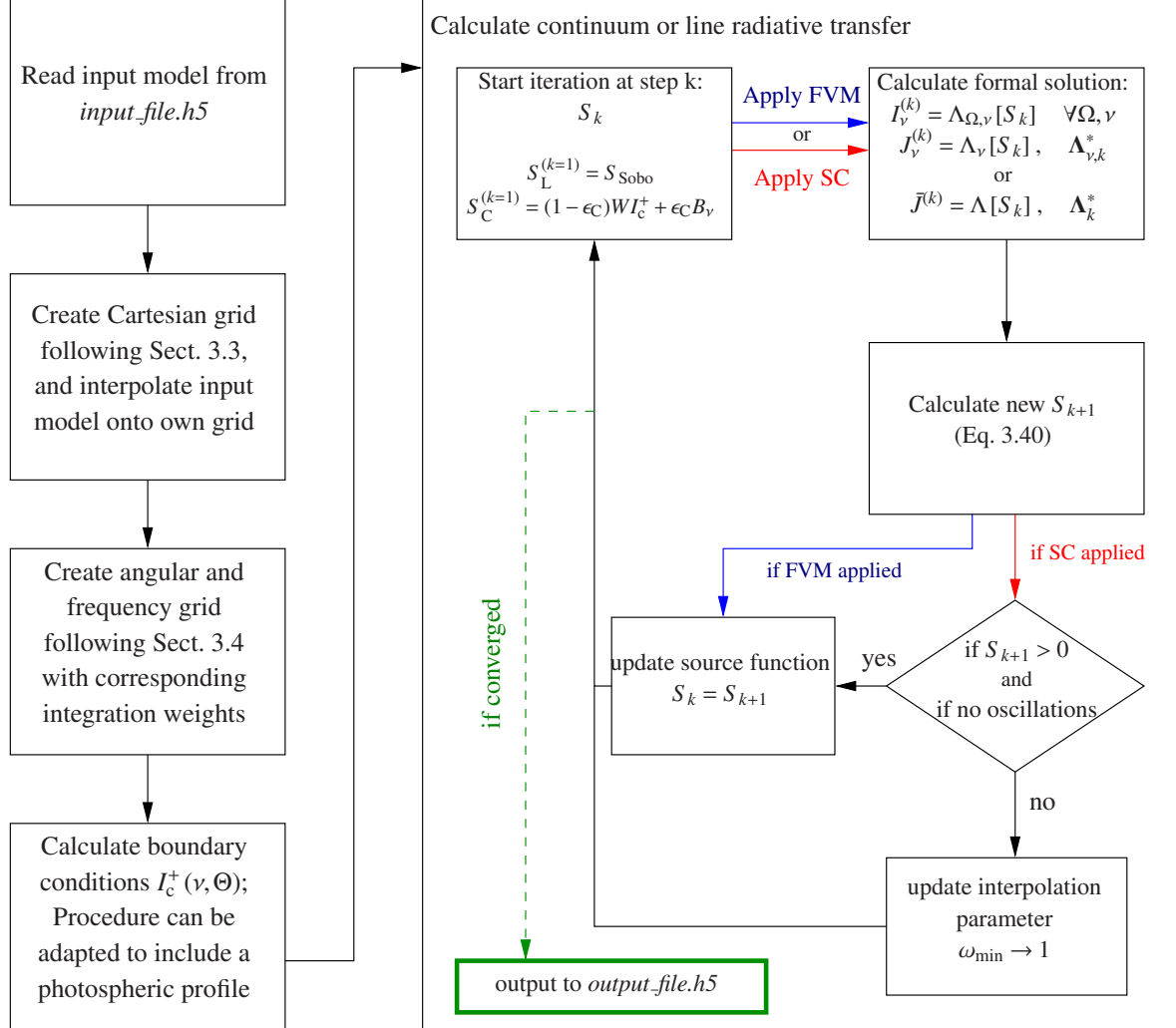
Figure 3.8: Flowchart for describing the program structure of the main part (*sc3d.eo*) of our 3D radiative transfer solvers, with W the dilution factor (see Eq. 4.1), and S_{Sobo} the line source function obtained from Sobolev theory (see Eq. A.17)

3.8 Summary and algorithmic implementation[17]

In this chapter, we have presented a differential (FVM) and an integral (SC) method tailored for the solution of 3D continuum- and line-scattering problems in the winds of hot stars. While the FVM considers all quantities at a given grid point as an average over the corresponding control volume, we

---

[17]based on Hennicker et al. (2019, Sect. 6).

have implemented both a purely linear interpolation scheme (for calculating upwind quantities and for the solution of the radiative transfer equation along a ray) within the SC method, as well as a second order, monotonic, Bézier technique. We use Cartesian coordinates with a non-uniform grid spacing to ensure a reasonable spatial resolution in important regions (i.e., where velocity and/or density gradients are large). As a first step towards full NLTE radiative transfer models, we consider a single resonance-line transition (approximated by a two-level-atom) assuming an optically thin background continuum, whereas for pure continuum problems we use the thermalization parameter, ϵ_C, and split the source function into a scattering and a thermal part. A generalization (including multi-level atoms) is planned for future applications. [†]An observer's-frame formulation allows us to consider arbitrary velocity fields (and density structures).[†]

To calculate strong scattering lines and optically thick, scattering dominated continua, we have implemented an accelerated Λ-iteration scheme using different non-local approximate Λ-operators, together with applying the Ng-extrapolation method for subsequent iterations.

To provide a flexible handling of our code, we have split the complete program into four (independent) subprograms:

(i) *model.eo*: Within this program, the hydrodynamic structure of the wind is set up either from semi-analytic models, or from hydrodynamic simulations. For the latter, the (input) file-structure is re-organized to a file structure that can be read in by our FVM and SC solvers.

(ii) *sc3d.eo*: Here, the wind-structure as obtained in step (i) is read in, and is interpolated onto a suitable own grid. Then, the radiative transfer is solved with the above described methods. Fig. 3.8 shows a flowchart summarizing the involved routines and solution methods. When convergence is obtained, an output-file is created storing the wind model and the (converged) source functions.

(iii) *modelspec.eo*: Similar to step (i), this program transforms an input-file (e.g., the output-file from step (ii)) to a file-structure that can be read in by the long-characteristics formal solver. For specific tests, we can easily calculate semi-analytic source functions, or even manipulate the source-function and wind-model obtained in step (ii) within this program.

(iv) *spec.eo*: This program reads the input-file created in step (iii), and calculates the emergent line profiles following Sect. 3.7.

With the numerical tools developed in this chapter, we are able to tackle 3D continuum and line scattering problems for arbitrary velocity fields. [†]Before applying our methods to first non-spherical problems though, we discuss the performance of the code by investigating the reliability of the applied methods in the following.[†] To this end, we consider several different test problems, for which either a theoretical solution is known (e.g., for zero-opacity models), or where an accurate solution can be found (e.g., for spherically symmetric test models).

Chapter 4

Tests and comparison of the FVM and SC method

This chapter has been copied – in parts – from Hennicker et al. (2018) and Hennicker et al. (2019).

4.1 Zero-opacity models[1]

4.1.1 Testing the angular integration

In this section, we briefly discuss the performance of different angular integration schemes when applied within a Cartesian coordinate system, by calculating the mean intensity at each point on the 3D grid for zero-opacity models. For a spherical star with radius R_*, the theoretical solution is simply given by:

$$J_{\text{theo}} = \frac{1}{4\pi} \int_{\Omega_c} I_c^+ \mathrm{d}\Omega = \frac{I_c^+}{2} \left(1 - \sqrt{1 - \left(\frac{R_*}{r}\right)^2} \right) =: W I_c^+ , \tag{4.1}$$

with Ω_c the solid angle subtended by the stellar disc, dilution factor W, and assuming an angle-independent intensity, I_c^+, emerging from the stellar surface. To test the angular integration scheme, we use the corresponding expression for the specific intensity at each position (ijk) (i.e., $I_{ijk} = I_c^+$ or $I_{ijk} = 0$ for rays hitting the core or not, respectively), and numerically integrate over solid angle using Eq. (3.23):

$$J_{\text{ex}} = \sum_l w_l I_{ijk}(\Omega_l) = \sum_l w_l \begin{cases} I_c^+ & \text{if ray hits the core} \\ 0 & \text{else} \end{cases} . \tag{4.2}$$

The mean realtive errors (w.r.t. all grid points, more precisely defined in Sect. 4.2) of the mean intensity as obtained from Eq. (4.2) with different integration methods, are summarized in Table 4.1 for a typical grid with $N_x = N_y = N_z = 133$ grid points. For the corresponding zero-opacity model

---

[1] Sect. 4.1.2 based on Hennicker et al. (2018, Sect. 4.2), and Hennicker et al. (2019, Sect. 4.1).

(with boundary condition I_c^+ and consistently applying $\chi = 0$), Table 4.1 additionally shows the mean relative errors as obtained when the intensities have been calculated with the 3D FVM and SC solvers using linear or Bézier interpolations (hereafter denoted by SClin and SCbez, respectively). Finally, in Fig. 4.1, we display the solution for the mean intensity, when calculated from Eq. (4.2) with different integration methods. We emphasize that the indicated error is the minimum error that can be achieved (for each considered angular resolution and integration method), even if the radiative transfer equation could be solved exactly, i.e., without numerical inaccuracies introduced by the discretization scheme. This issue cannot be solved by a simple renormalization of the integration weights, because the angular integration error becomes reduced for optically thick atmospheric models (see Sect. 4.2.3).
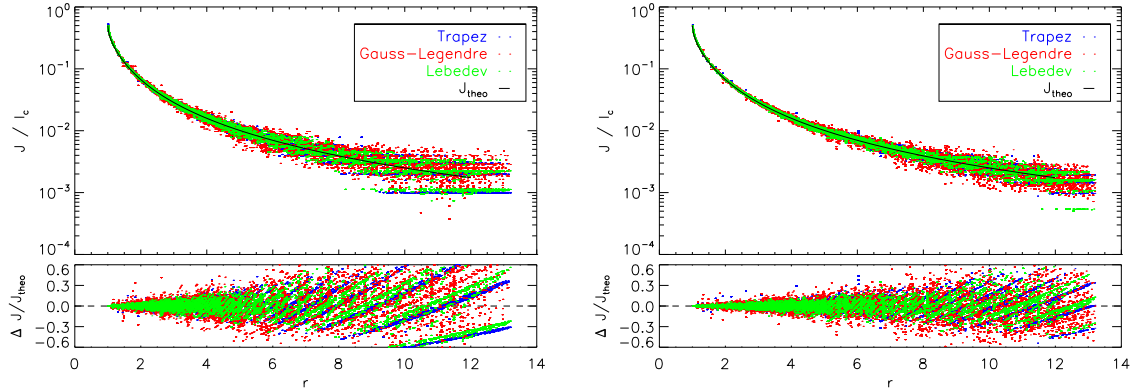
Figure 4.1: Mean intensity and corresponding relative error when calculated with the 'exact' solution for zero-opacity atmospheres (Eq. 4.2). The red, blue, and green dots indicate the mean intensities at all grid points with corresponding radii, $r = \sqrt{x_i^2 + y_j^2 + z_k^2}$, as obtained when applying the Trapezoidal rule (with nodes from Lobel & Blomme 2008), the Gauss-Legendre quadrature, and the Lebedev method, respectively. The left and right panels display the solution for $N_\Omega \approx 1000$ and for $N_\Omega \approx 2000$ directions.

Since both the Simpson's rule and the (linear) integration over triangles have been formulated only on equidistant angular grids thus far[2], the angular resolution within these methods is increased above the poles and decreased in equatorial regions (for a constant number of direction vectors). Thus, both methods yield a relatively low accuracy (particularly when compared with more elaborate integration schemes). For future tests, however, the angular resolution might be adapted by modifying the distribution of direction vectors to (potentially) increase the accuracy slightly.

The best results have been obtained using the Lebedev quadrature, followed by the Trapezoidal rule (with nodes from Lobel & Blomme 2008) and the Gauss-Legendre integration scheme. However, even when applying the Lebedev quadrature with $N_\Omega \approx 2000$ integration nodes, we only achieve an accuracy of $\approx 7 - 8\,\%$, because the angular distribution of the specific intensity at a given point, $I_{ijk}(\theta, \phi)$,

---

[2] We have also tested the integration over co-latitude by applying an equidistant μ-grid, with $\mu = \cos(\theta)$. Since, for a given ϕ-angle, such a formulation gives a coarser θ-resolution near the poles, thus yielding relatively inaccurate integrals over co-latitude in polar regions, we preferred to perform the integration in θ-space.

Table 4.1: Mean relative error (defined in Sect. 4.2) of the mean intensity for a zero-opacity model, obtained using different angular integration methods: (i) Simpson's rule with equidistant angular grid spacing, (ii) Linear interpolations on a triangular grid, (iii) Trapezoidal rule with nodes from Lobel & Blomme (2008), (iv) Gauss-Legendre integration, and (v) Lebedev integration. For $\overline{\Delta J}_{\mathrm{ex}}$, $\overline{\Delta J}_{\mathrm{SClin}}$, $\overline{\Delta J}_{\mathrm{SCbez}}$, and $\overline{\Delta J}_{\mathrm{FVM}}$, the incident intensities have been calculated exactly, and by the FVM and SC methods using linear or Bézier upwind interpolations.

	Simpson		Triangle		Trapez		Gauss-Legendre		Lebedev	
N_Ω	1035	2145	1073	2186	1037	2105	968	2048	974	2030
$\overline{\Delta J}_{\mathrm{ex}}\,[\%]$	17.6	10.4	14.4	9.6	12.1	8.0	14.3	9.4	11.2	7.7
$\overline{\Delta J}_{\mathrm{SClin}}\,[\%]$	14.3	11.6	11.8	11.1	11.3	10.8	10.9	10.8	10.8	10.8
$\overline{\Delta J}_{\mathrm{SCbez}}\,[\%]$	10.0	9.9	13.9	9.4	10.7	9.0	9.3	8.9	9.1	8.8
$\overline{\Delta J}_{\mathrm{FVM}}\,[\%]$	12.5	9.3	9.6	8.8	9.0	8.5	8.6	8.6	8.5	8.5

is theoretically described by a 2D step function in the zero-opacity case. Since the discontinuity is usually located at angles in between the applied angular nodes[3], the numerical integration of such 2D step functions becomes challenging. In regions far from the star, the solid angle subtended by the stellar disc is small, and only few directions contribute to the mean intensity. Thus, the angular integration becomes difficult particularly in such regions, whereas near to the stellar surface (where many direction vectors contribute), the associated error is less pronounced (see Fig. 4.1). With decreasing number of integration nodes, almost all integration schemes suffer from the same (severe) problems. ‡Particularly the Gauss-Legendre integration should only be applied when the distribution of intensities can be described by high order polynomials, that is, when $I_{\mathrm{ijk}}(\theta, \phi)$ is smoothed out (e.g., by numerical diffusion within the FVM/SC solution schemes, see Sect. 4.1.2).‡ When calculating the specific intensity with the FVM and SC methods (instead of adopting the theoretical value), the solution for the mean intensity is only slightly improved (if at all) with increasing angular grid resolution, for all applied integration methods. We note that the mean relative error does not converge to zero, due to numerical diffusion errors. Since the Lebedev-integration method performs best, also when the specific intensity has been calculated from the FVM or SC methods, we apply this quadrature scheme within all our calculations. We use $N_\Omega = 2030$ angular grid points throughout this thesis to avoid numerical artefacts (e.g., oscillations occurring when too few directions are used), and to ensure that no resonance-zone has been overlooked (see Sect. 3.4.2).

4.1.2 Searchlight-beam test

A first test of our 3D FVM and SC methods using linear and Bézier interpolations is the searchlight-beam test (e.g., Kunasz & Auer 1988). Within this test, we apply a zero-opacity model, and consider the illumination of the atmosphere by a central star for a single direction, here set to $\theta = 45°$ and $\phi = 0°$. Since, the discretized equation of radiative transfer for the SC method (Eqs. 3.12/3.17) and

---

[3] While the resolution of the angular grid for $N_\Omega \approx 2000$ is roughly $\Delta\theta \approx \Delta\phi \approx 6°$, corresponding to $\Delta\Omega \approx 36\,\mathrm{deg}^2$, the solid angle subtended by the stellar disc at radii $r = 2R_*$ and $r = 4R_*$ is approximately $2763\,\mathrm{deg}^2$ and $655\,\mathrm{deg}^2$, respectively.

for the FVM (Eq. 3.6) reduce (for zero-opacity models) to:

$$I_{ijk}^{(SC)} = I_{ijk}^{(u),(SC)}, \tag{4.3}$$

$$I_{ijk}^{(FVM)} = \frac{1}{1 + \frac{n_y \Delta x_i}{n_x \Delta y_j} + \frac{n_z \Delta x_i}{n_x \Delta z_k}} I_{i-\alpha,j,k}^{(FVM)} + \frac{1}{1 + \frac{n_x \Delta y_j}{n_y \Delta x_i} + \frac{n_z \Delta y_j}{n_y \Delta z_k}} I_{i,j-\beta,k}^{(FVM)} + \frac{1}{1 + \frac{n_x \Delta z_k}{n_z \Delta x_i} + \frac{n_y \Delta z_k}{n_z \Delta y_j}} I_{i,j-\beta,k}^{(FVM)}, \tag{4.4}$$

the searchlight-beam test extracts the effects of the applied interpolation scheme for the upwind intensity, and of the competition between the (finite) $\Delta x_i/\Delta y_j$, $\Delta x_i/\Delta z_k$, and $\Delta y_j/\Delta z_k$ terms. Generally, rays propagating parallel to the grid axes are nearly undisturbed by numerical artefacts, whereas those propagating at different angles are effectively widened, due to the propagation of intensity into neighbouring cells by 'numerical diffusion'. The upper panels of Fig. 4.2 show the propagation of the specific intensity scaled by I_c^+, in the xz-plane. To obtain a quantitative measure of this effect, the lower left and lower right panels of Fig. 4.2 display the specific intensity through a circular area perpendicular to the ray direction as a function of impact parameter p, and the specific intensity along the given direction at the centre of the beam, respectively. The corresponding exact solutions are given by a constant and rectangular function, respectively. Evidently, numerical diffusion plays a crucial role.

Along the beam centre, the SC methods perfectly reproduce the exact solution, whereas the FVM solution decreases significantly due to the finite grid-cell size. Considering the intensity through the perpendicular area, both SC methods perform better than the FVM, with slight advantages of the SCbez method when compared with the SClin method. Since, however, the searchlight beam remains almost collimated (with a relatively narrow profile across the beam centre, see lower left panel of Fig. 4.2) also for other directions not shown here, the angular distribution of the specific intensity is expected to reproduce the (theoretical) 2D step function relatively well, and the angular integration scheme thus becomes challenging (see Sect. 4.1.1). While this problem can be solved by applying elaborate integration methods (or by increasing the angular grid resolution), we stress that within the 3D SC methods, energy conservation is violated for our zero-opacity models, because the (nominal) specific intensity jumps from I_c^+ to zero for rays intersecting the stellar surface or not, due to the core-halo situation. As a consequence, almost all interpolations (and interpolation schemes) overestimate the specific intensity. In contrast, the number of photons entering and leaving a given grid cell is (nearly) conserved within the FVM by definition[4]. For optically thick models (where a 'sharp-edged' I_c^+ at the core plays a negligible or minor role), this effect should decrease though. The associated error can be quantified by calculating the corresponding flux, i.e., by integrating the specific intensity for a given direction over a corresponding perpendicular area (defined as a circle with virtually infinite radius). Such a flux as defined here constitutes the most demanding test case, and should not be confused with the flux density (i.e., the first moment of the specific intensity). Fig. 4.3 shows the resulting fluxes (normalized by the nominal value) for searchlight beams with different directions defined by $\theta = 45°$ and $\phi \in [0°, 90°]$. For different directions ϕ, the searchlight beams propagate through different domains of the spatial grid (with accordingly different grid-cell sizes). Due to the distinct behaviour of numerical diffusion errors within these domains, the total flux varies as a function of ϕ. Overall, the total fluxes for the SClin and SCbez methods are larger than theoretically constrained

---

[4] This statement, however, is not completely true for the FVM as formulated by Adam (1990), Lobel & Blomme (2008), and within this work, since all these implementations apply an (averaged) upwind approximation.
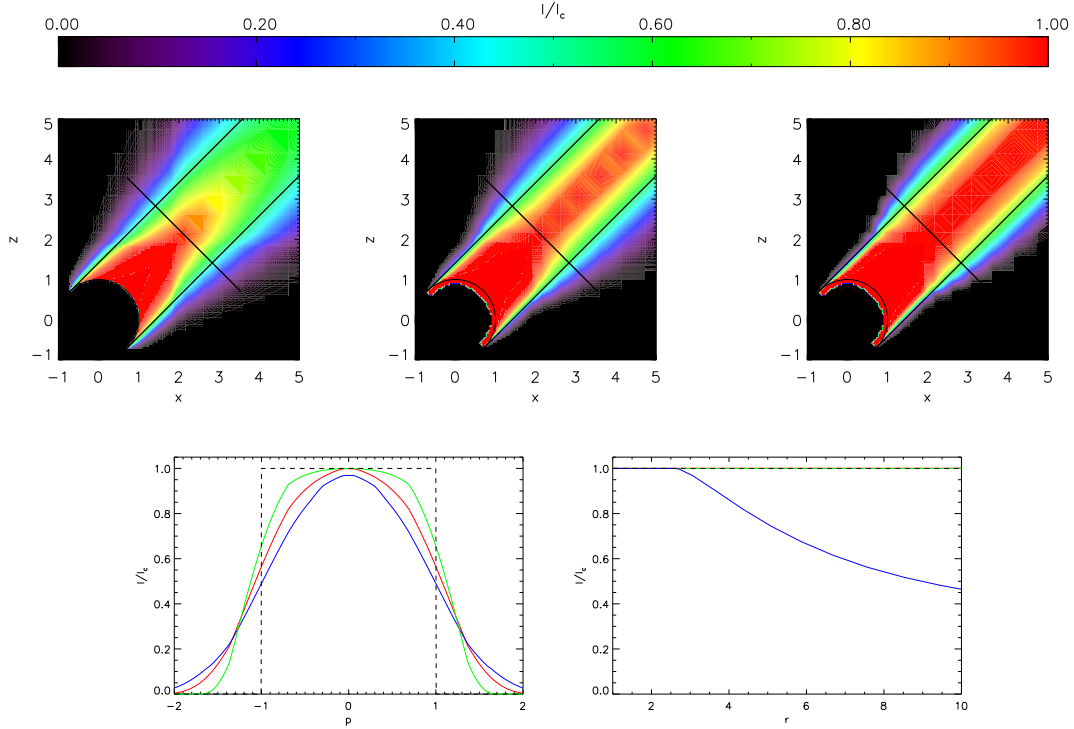
Figure 4.2: Searchlight-beam test for direction $\boldsymbol{n} = (1, 0, 1)$ (corresponding to $\theta = 45°$, $\phi = 0°$) and a typical grid resolution with $N_x = N_y = N_z = 133$ grid points. Upper panels: Contour plots of the specific intensity in the xz-plane, when calculated with the FVM and SC methods using linear or Bézier interpolations, from left to right. Within the stellar core (indicated by the solid circle), the specific intensity is set by the boundary condition (for the SC methods, see Sect. 3.2.4.). Lower left panel: Specific intensity through the perpendicular area indicated by the straight line in the upper panels. The blue, red, and green profiles correspond to the FVM, SClin, and SCbez methods, respectively. The dashed line indicates the theoretical profile. Lower right panel: As lower left panel, but along the centre of the searchlight beam. We note that the SC methods reproduce the exact solution at the centre of the beam, whereas the FVM solution decreases significantly for $r \gtrsim 2.5 R_*$. Upper left panel from Hennicker et al. (2018), and the remaining ones from Hennicker et al. (2019).

by $F_{\text{theo}} = 2\pi R_*^2 I_c^+$, whereas the FVM gives (despite a small error) reasonable results. This effect is largest in regions far from the star, and for diagonal directions. Thus, particularly in these regions, also the mean intensities (for optically thin atmospheres) are expected to become overestimated.

To address the impact of numerical diffusion on the solution for the mean intensity, Fig. 4.4 shows the mean intensity (scaled by its theoretical value obtained from the dilution factor) for zero-opacity models, on spherical surfaces at two distinct radii, $r = 1.1 R_*$ and $r = 3 R_*$. We find a clear pattern of the shape of the mean intensities. For the FVM, and in regions close to the star, the mean intensities are reasonably accurate on the axes, in contrast to the off-axes regions, where they become overestimated. Far from the star, the situation reverses, with reasonable results away from the axes, and an overestimate on the axes. This behaviour is explained in the following:
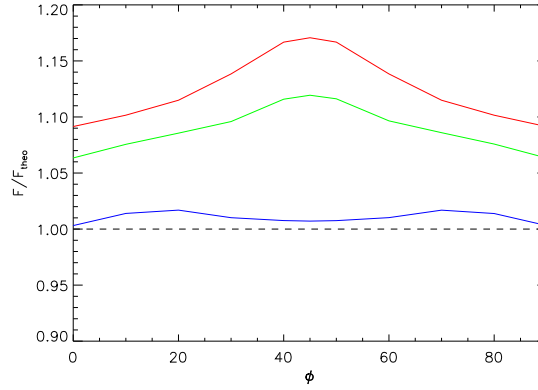
Figure 4.3: Photon flux as a function of direction angle ϕ (with fixed $\theta = 45°$) through corresponding perpendicular areas, and with the opacity set to zero. The central distance of all areas to the stellar surface has been set to $2R_*$. The same color coding as in Fig. 4.2 has been used. From Hennicker et al. (2019).

(i) For a given grid point on or close to a coordinate axis, and far from the stellar surface, core-rays, i.e., those originating from the stellar surface, remain nearly undisturbed by numerical diffusion. Without diffusion, only such core-rays would contribute to the mean intensity. Due to numerical diffusion, however, also non-core rays contribute, i.e., those which form a certain angle w.r.t. the considered grid axis, since they have been fed with intensity by corresponding core-rays propagating in the same direction (widening of the effective aperture, see above). Consequently, the mean intensity becomes overestimated.

(ii) For grid points far from the star, and away from the major axes, core-rays and non-core rays are both affected by numerical diffusion, resulting in an under- and over-estimation of the intensity, respectively. Consequently, there is a significant cancellation of both effects, and the mean intensity remains close to its expected value.

(iii) At points located on the grid axes close to the star, numerical diffusion plays only a minor role, mostly because the contributing non-core rays are propagating almost perpendicular to the considered axis, i.e., parallel to one of the other axes, with negligible diffusion errors.

(iv) Away from the axes, and close to the star, contributing non-core rays are significantly inclined w.r.t. the coordinate axes, and thus strongly fed by diffusion effects. Thus, the mean intensities become overestimated.

A similar behaviour of numerical diffusion is also found for the SC methods. The magnitude of the error, however, is significantly reduced, due to the higher accuracy of upwind interpolations (particularly for diagonal directions and close to the stellar surface). In regions far from the star, the mean intensities become overestimated for both SC methods (see above), with (slight) advantages of the Bézier technique when compared with the intensities obtained from linear interpolations.
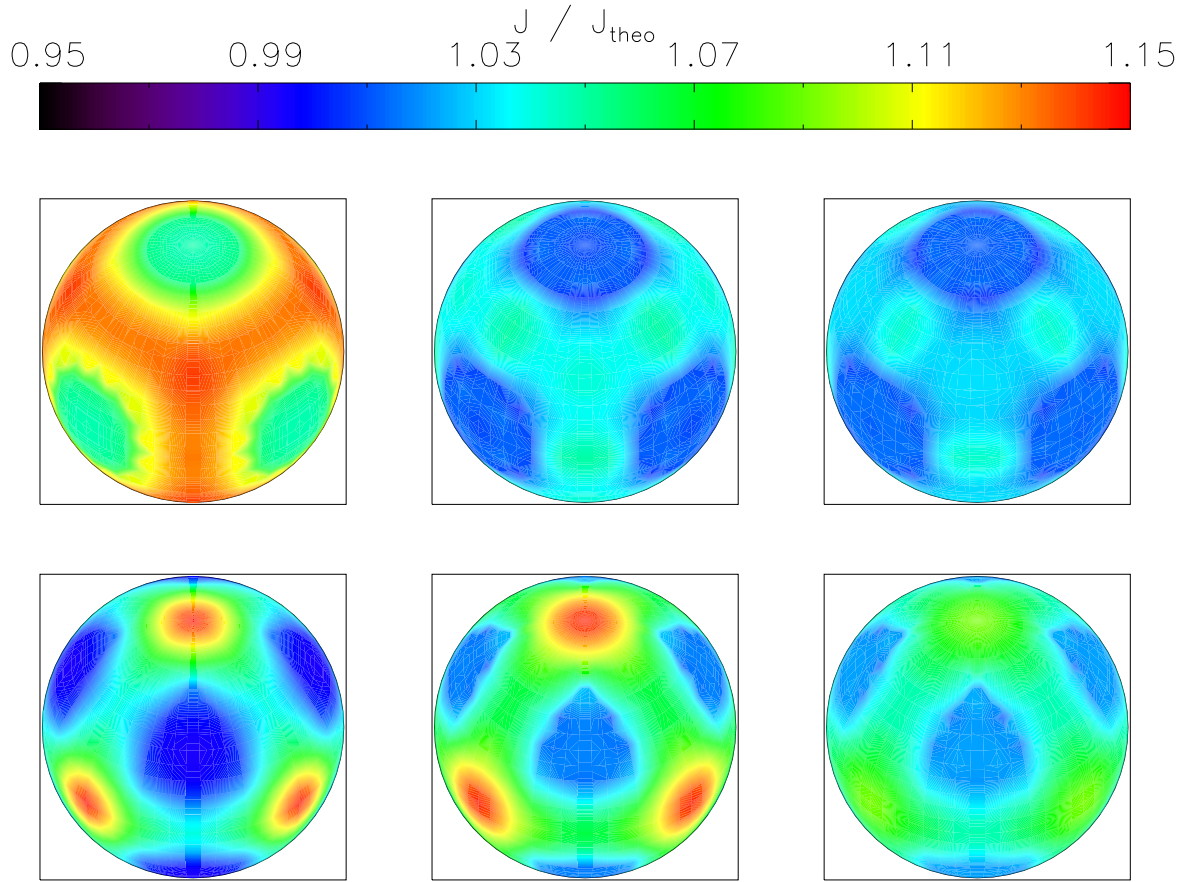
Figure 4.4: Contours of the mean intensity for a zero-opacity model, normalized by its theoretical value, on spherical surfaces, $r = 1.1 R_*$ (top row) and $r = 3 R_*$ (bottom row). The mean intensity as obtained from the FVM, SClin and SCbez methods are shown from left to right. The line of sight is along the vector $\boldsymbol{n} = (1, 1, 1)$. $N_x = N_y = N_z = 133$ grid points have been used. Upper left and lower left panels from Hennicker et al. (2018).

Due to the different effects for different ray directions and for different regions in the atmosphere, any underlying (e.g., spherical) symmetry of a specific problem will be broken. We emphasize that numerical diffusion errors can only be avoided by increasing the grid resolution, by using higher order upwind-interpolation schemes, or by applying the long-characteristics method for solving the equation of radiative transfer.

As the important part of the radiative transfer, however, is mainly located near to the star (where the densities are largest), and the numerical diffusion errors are not too large in this regime (up to a radius of $r \lesssim 3 - 4 R_*$), the 3D FVM and SC solution schemes should deliver (at least qualitatively) correct results. We note that numerical diffusion errors are expected to be most severe when photons propagate over large distances, for instance, when considering optically thin continua, or, in the line case, before they hit the resonance zones. Since the resonance zones are mostly quite narrow, while

Table 4.2: Input parameters used for our spherically symmetric test models. These parameters roughly correspond to the wind from the O4 supergiant ζ Pup, when assuming an unclumped wind.

T_{eff} [kK]	R_* [$R_\odot$]	v_{min} [km s^{-1}]	v_∞ [km s^{-1}]	β	$\dot{M}$ [$M_\odot$ yr^{-1}]	R_{max} [R_*]	v_{turb} [km s^{-1}]
40	19	10	2000	1	$5 \cdot 10^{-6}$	12	100

the path-length of freely propagating line photons is usually quite large (at least if the continuum is comparatively weak, as in most realistic conditions), numerical diffusion errors are of major concern for the line transfer.

4.2 Spherically symmetric winds[5]

In the following, we discuss the performance of the code when applied to spherically symmetric, stationary atmospheres. To this end, we compare the solutions obtained from the 3D FVM and SC methods, with those obtained from accurate 1D solvers[6].

4.2.1 Atmospheric model

The spherically symmetric models to be compared with are calculated from a prescribed β-velocity law and from the equation of continuity (Eq. 1.2). For stellar and wind parameters summarized in Table 4.2, the density stratification and the velocity field are completely determined. Effects of the temperature stratification are negligible for the considered scattering problems ($\epsilon_C = \epsilon_L = 10^{-6}$). The continuum and (frequency integrated) line opacities have been calculated from Eqs. (2.61), (2.62), with the electron density derived for a completely ionized H/He plasma with helium abundance $N_{\text{He}}/N_{\text{H}} = 0.1$. We have calculated three different continuum models by scaling the electron-scattering opacity with $k_C = [1, 10, 100]$, respectively. These models correspond to an optically thin, marginally optically thick, and optically thick atmosphere, with radial optical depths $\tau_r = [0.17, 1.7, 17]$. The line transport has been calculated for a weak, intermediate, and strong generic UV resonance line, with line-strengths $k_L = [1, 10^3, 10^5]$. To calculate the thermal width, we used $m_A = 12 m_p$, m_p being the proton mass. The total width of the line profile, however, is mainly controlled by the micro-turbulent velocity, where we use $v_{\text{turb}} = 100$ km s^{-1} throughout this thesis to minimize the computation time (see Sect. 3.4.2).

To obtain a reasonable resolution of the (spherically symmetric) wind on a Cartesian grid, we calculate the wind-model on a spherical grid within our first subprogram *model.eo*. The radial coordinates are computed such that the (radial) continuum optical-depth -and velocity-steps, $\Delta \tau_r$ and Δv_r, are (nearly) equidistant. The Cartesian x, y, and z-coordinates are then calculated following the grid-construction procedure described in Sect. 3.3. If not indicated explicitly, we use $N_x = N_y = N_z = 133$

---

[5] Sects. 4.2.1 to 4.2.3 based on Hennicker et al. (2018, Sect. 4), and Hennicker et al. (2019, Sect. 4.2).

[6] The 1D solution for the continuum transport has been found from the Rybicki-algorithm (combined with the solution of the moment equations using variable Eddington factors, see, e.g., Mihalas 1978). To calculate the line, a comoving-frame ray-by-ray solution scheme in *pz*-geometry has been applied, ensuring convergence by means of an accelerated Λ-iteration scheme using a diagonal ALO.
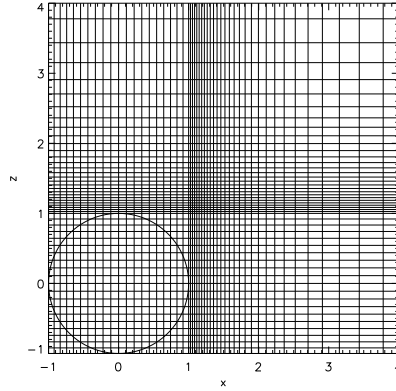
Figure 4.5: Spatial grid in the xz-plane with $N_x = N_y = N_z = 93$ grid points, as obtained from our grid-construction procedure for the spherically symmetric test models.

grid points for the continuum, and $N_x = N_y = N_z = 93$ grid points for the line formation, distributed over the complete range, $[-R_{max}, R_{max}]$, where R_{max} defines the spatial domain. We allow for a higher grid resolution within the continuum calculations, since only one frequency point needs to be considered, and we thus have lower computation times anyhow. For comparison, Lobel & Blomme (2008) used only $N_x = N_y = N_z = 71$ grid points for their (optically thin) models. A typical grid in the xz-plane is shown in Fig. 4.5. Particularly for the FVM (where no grid-refinement has been implemented thus far), the applied grid resolution is required to properly resolve the resonance zones (where the line opacity in the comoving frame and the corresponding profile function is non-negligible), and to obtain reasonable discretized optical-depth steps.

4.2.2 Convergence behaviour

To test the convergence behaviour of our ALI implementation with corresponding ALO, we consider the continuum and line formation in the stellar wind as described above. Fig. 4.6 shows the maximum relative corrections of the mean intensity (left panel) and scattering integral (right panel) after each iteration step. Different methods (FVM, SClin and SCbez), and different acceleration techniques (classical Λ-iteration, and diagonal-, direct-neighbour-, nearest-neighbour-ALO with the Ng-extrapolation switched on or off) have been applied. We display the continuum and line calculations for $k_C = [10, 100]$ and $k_L = [10, 10^5]$, respectively, using $N_x = N_y = N_z = 93$ spatial and $N_\Omega = 974$ angular grid points (to save computation time when calculating the slowly converging classical Λ-iteration). We usually stop the iteration scheme when the maximum relative corrections become less than 10^{-3} between subsequent iteration steps, emphasizing that a truly converged solution is only found when the curve describing subsequent relative corrections is sufficiently steep[7]. For instance,

---

[7] For linearly convergent iteration schemes, the steepness of the convergence curve is described by the relative corrections in subsequent iterations steps, $\Delta_k/\Delta_{k-1} = \text{const.} =: q$. To obtain a solution within a reasonable amount of computation time, we may demand that $q \lesssim 0.8$, corresponding to a reduction of relative errors by a factor of 10^{-3} every 30th iteration step.
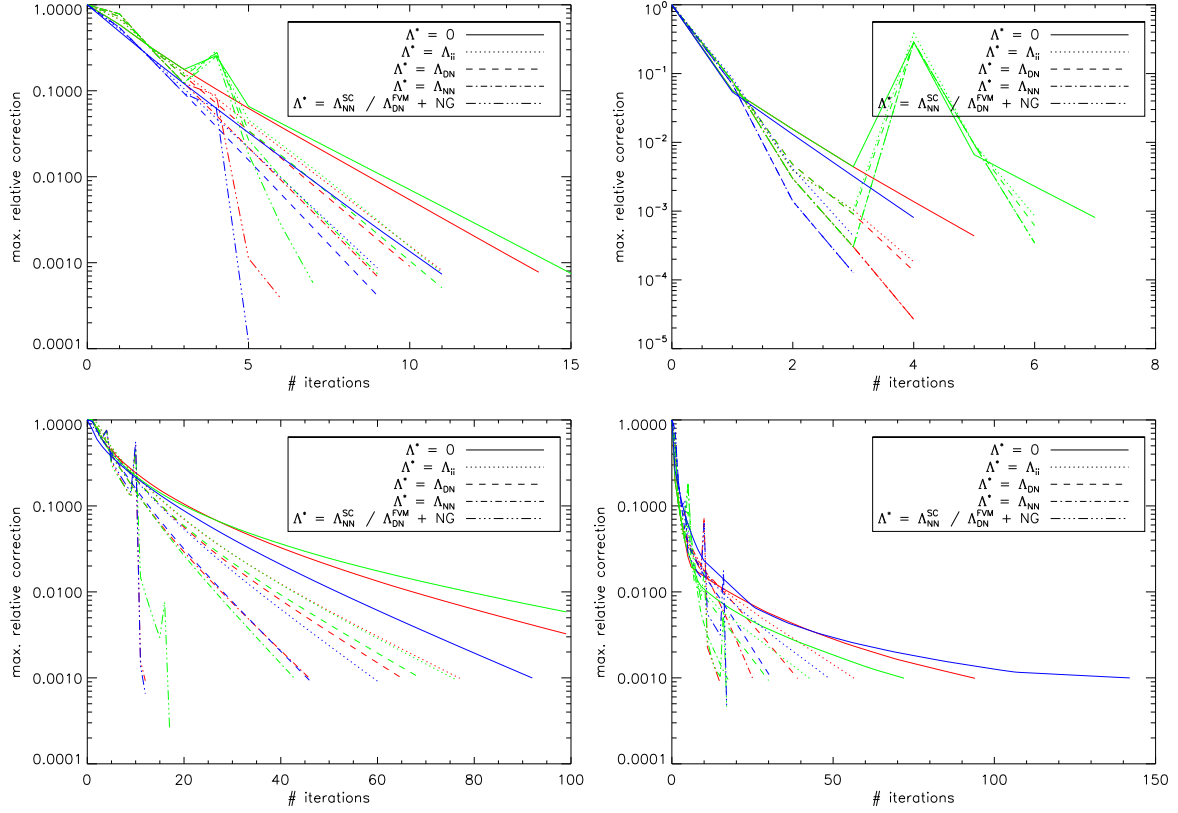
Figure 4.6: Convergence behaviour of the standard spherically symmetric model calculated with the 3D FVM (blue) and the 3D SC method using linear (red) or Bézier (green) interpolations. The left and right panels show the convergence behaviour of the continuum and line transfer for $\epsilon_C = \epsilon_L = 10^{-6}$, respectively, with maximum relative corrections between subsequent iteration steps calculated with respect to the mean intensity and scattering integral. While the upper row displays the optically thin models with $k_C = 10$ and $k_L = 10$, the lower row has been calculated using $k_C = 100$ and $k_L = 10^5$. Different acceleration techniques have been applied, where the NN-ALO has been implemented only for the SC method. From Hennicker et al. (2019).

the classical Λ-iteration (with $\Lambda^* = 0$) fails to converge for strong scattering lines (Fig. 4.6, lower right panel), since the relative corrections become almost constant in each iteration step ('false convergence', cf. Hubeny & Mihalas 2014).

Overall, and as expected, the number of iterations needed to obtain the converged solution is decreasing with increasing number of matrix elements used to define the ALO (see also Hauschildt et al. 1994 and Hauschildt & Baron 2006 for multi-band ALOs coupled to a 1D-SC and 3D-LC formal solution scheme, respectively). In most cases, the convergence of the SClin is faster than that of the SCbez method, because the interpolation scheme is intrinsically more localized (with stronger weights assigned to local Λ-matrix elements). The FVM always performs best, since only the direct neighbours directly influence the formal solution within this method. For parameters $k_C, k_L \leq 10$ (Fig. 4.6, upper panels), all ALOs yield a converged solution within $N_{iter} \approx 10$ iteration steps. When

applying the SCbez method, the first peak results from switching the linear interpolations to Bézier interpolations at the fifth iteration step. This peak is less pronounced for parameters $k_C, k_L = 100, 10^5$, since the maximum relative corrections are still relatively large in the first few iteration steps.

For the optically thick continuum model (Fig. 4.6, lower left panel), the classical Λ-iteration converges only very slowly (if at all), requiring $N_{\text{conv}}^{(\text{classical})} \gtrsim 90$ iterations until our convergence criterion of maximum relative corrections being less than 10^{-3} is fulfilled. On the other hand, when using the diagonal, DN- and NN-ALO within the SClin and SCbez method, the number of iterations until convergence is reduced from $N_{\text{iter}}^{\text{diag}} \approx 75$ to $N_{\text{iter}}^{\text{DN}} \approx 65$ and $N_{\text{iter}}^{\text{NN}} \approx 45$, respectively. For the FVM method, already the DN-ALO performs reasonably well with $N_{\text{iter}}^{\text{DN}} \approx 45$. The Ng-extrapolation significantly reduces N_{iter} further, and is required to obtain the converged solution in $\lesssim 20$ iteration steps for all applied methods.

Since the line transport is restricted to the finite widths of the resonance zones, and is therefore intrinsically much more local than the continuum, the convergence behaviour is accelerated considerably already by the diagonal and multi-band ALOs. For the strong line (Fig. 4.6, lower right panel), convergence is obtained within $N_{\text{iter}}^{\text{diag}} \approx 50 \pm 5$ and $N_{\text{iter}}^{\text{DN}} \approx 35 \pm 5$ iteration steps for the diagonal and DN-ALO, respectively. For the SC methods, the NN-ALO with the Ng-extrapolation scheme switched on again performs on the same level as the DN-ALO (+ Ng-extrapolation) within the FVM, and reduces the number of iteration steps until convergence to $\lesssim 20$.

In total, we conclude that a multi-band ALO is required for our implementation of 3D radiative transfer solvers to obtain a fast convergence behaviour. While a DN-ALO together with the Ng-extrapolation is typically sufficient for the FVM method, a NN-ALO is required when the SC methods using linear or Bézier interpolations are applied. These ALOs, however, also perform excellently for extreme test-cases, that is, for optically thick continua and strong lines in scattering dominated atmospheres.

4.2.3 Accuracy of continuum and line solutions

Convinced by the sound convergence properties (at least for the non-local ALOs), we investigate the accuracy of the FVM and SC methods in the following. To this end, we apply the DN- and NN-ALO for the 3D FVM and SC solution scheme, respectively, together with the Ng-extrapolation, and compare the obtained solutions with (almost) exact results (see begin of Sect. 4.2). For the converged solution then, all differences between the 1D and 3D FVM/SC methods originate only from the specific discretization of the radiative transfer equation. Fig. 4.7 shows the continuum and line solutions together with corresponding relative errors, obtained for the spherically symmetric model when calculated with the FVM, SClin, and SCbez methods and compared to the 'exact' 1D solution. The mean and maximum relative errors are shown for different regions in Table 4.3, where the mean and maximum relative errors of any quantity are defined throughout this work by

$$\overline{\Delta q} := \frac{1}{N} \sum_{i=1}^{N} \frac{|q_i - q_i^{(\text{exact})}|}{q_i^{(\text{exact})}}, \qquad \Delta q_{\text{max}} := \max_{\forall i \in [1,N]} \frac{|q_i - q_i^{(\text{exact})}|}{q_i^{(\text{exact})}},$$

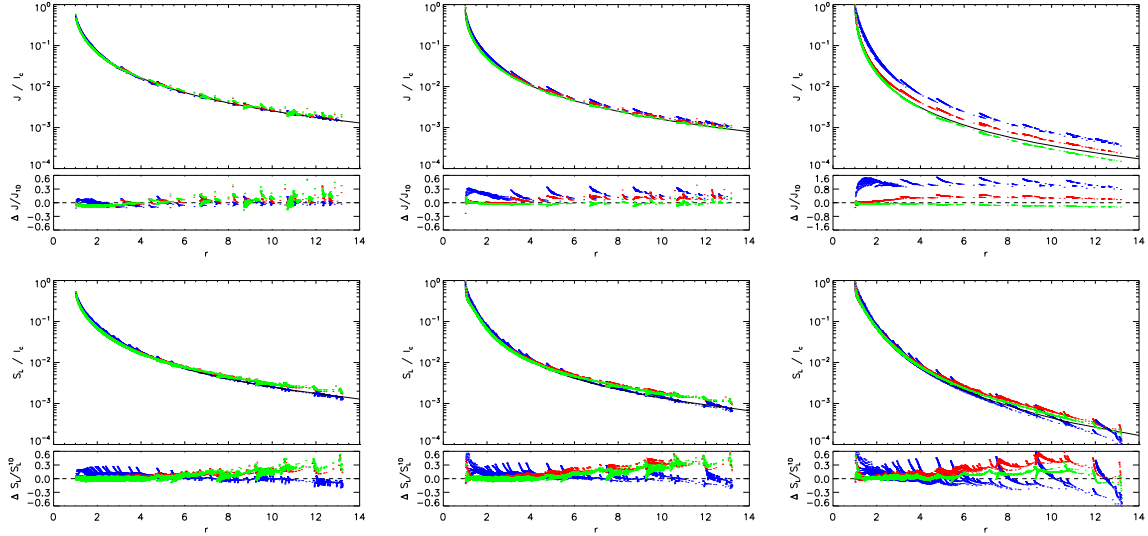with N the number of grid points within the considered region.

Figure 4.7: Solutions for the standard spherically symmetric model as calculated with the 3D FVM (blue) and 3D SC methods using linear (red) or Bézier (green) interpolations, compared to an accurate 1D solution (black solid line). The dots represent the solutions at specific grid points (with different latitudes and longitudes), where only a subset of all grid points is displayed to compress the image. Corresponding errors are indicated at the bottom of each chart. The top panel shows the mean intensity for the continuum transfer as a function of radius, with $\epsilon_C = 10^{-6}$ and $k_C = [1, 10, 100]$ from left to right. The bottom panel shows the line source function with $\epsilon_L = 10^{-6}$, and $k_L = [10^0, 10^3, 10^5]$ from left to right. From Hennicker et al. (2019).

Continuum. For the continuum models, the solutions obtained from the 3D SC methods are superior to the solution obtained from the FVM in most cases. Particularly near the stellar surface (at $r \lesssim 3R_*$), both SC methods are in good agreement with the 1D solution (see Fig. 4.7, top panel, and bottom of each chart for the radial dependence of the relative errors). When considering the most challenging problem of optically thick, scattering dominated atmospheres, the mean relative errors of the SClin and SCbez method for the complete calculation region are on the 20- and 10%-level, respectively. For such models, the FVM breaks down due to the order of accuracy[8], and a (high order) SC method is indeed required to solve the radiative transfer with reasonable accuracy. For marginally optically thick continua, the mean relative errors of the SClin and SCbez methods are on the 5%-level and below. While the FVM (with a mean relative error $\approx 20\%$) allows for a qualitative interpretation of the radiation field for such models, the SC methods should be used for quantitative discussions. The optically thin model calculations give mean relative errors on the order of 5% for all methods, with the maximum relative error being lowest for the FVM. Since, additionally, the computation times of the SClin and SCbez methods are typically highest (see Sect. 3.6), the FVM is to be preferred when calculating optically thin continua. For the SC methods, we note that all errors originate from the interplay between upwind/downwind interpolations of opacities, source functions and intensities, and

---

[8] The first-order FVM is sufficiently accurate if $\exp(-\Delta\tau) \approx 1 - \Delta\tau$, i.e., if the optical-depth steps, $\Delta\tau$, are small.

Table 4.3: Mean and maximum relative errors of the FVM and SClin, SCbez methods, when applied to the spherically symmetric test models. The mean relative errors are listed for different regions with $r \in [R_*, 3R_*]$, $r \in [3R_*, R_{max}]$ and $r \in [R_*, R_{max}]$, from top to bottom.

$\overline{\Delta J}$ [%] for $r \in [R_*, 3R_*]$					$\overline{\Delta S_L}$ [%] for $r \in [R_*, 3R_*]$			
k_C	τ_r	FVM	SClin	SCbez	k_L	FVM	SClin	SCbez
10^0	0.17	3.4	6.2	6.6	10^0	8.7	2.0	2.4
10^1	1.17	18	1.2	2.2	10^3	9.4	2.0	2.6
10^2	17.0	120	9.7	5.7	10^5	10	3.3	2.2

$\overline{\Delta J}$ [%] for $r \in [3R_*, R_{max}]$					$\overline{\Delta S_L}$ [%] for $r \in [3R_*, R_{max}]$			
k_C	τ_r	FVM	SClin	SCbez	k_L	FVM	SClin	SCbez
10^0	0.17	5.2	4.4	4.3	10^0	4.8	5.9	4.7
10^1	1.17	22	10	3.7	10^3	5.9	10	5.1
10^2	17.0	120	36	16	10^5	12	19	6.2

$\overline{\Delta J}$ [%] for $r \in [R_*, R_{max}]$					$\overline{\Delta S_L}$ [%] for $r \in [R_*, R_{max}]$			
k_C	τ_r	FVM	SClin	SCbez	k_L	FVM	SClin	SCbez
10^0	0.17	4.4	5.2	5.4	10^0	6.3	4.5	3.9
10^1	1.17	20	6.0	3.0	10^3	7.2	7.0	4.2
10^2	17.0	120	2 3	11	10^5	11	13	4.7

ΔJ_{max} [%] for $r \in [R_*, R_{max}]$					$\Delta S_{L,max}$ [%] for $r \in [R_*, R_{max}]$			
k_C	τ_r	FVM	SClin	SCbez	k_L	FVM	SClin	SCbez
10^0	0.17	17	51	49	10^0	27	46	45
10^1	1.17	36	39	14	10^3	73	50	45
10^2	17.0	150	46	24	10^5	70	65	55

the integration of the discretized radiative transfer equation. Numerical diffusion and the associated violation of energy conservation influences the converged solution particularly in the optically thin regime.

Line transition. The mean relative errors for the line transition are on the order of $5 - 10\%$, with increasing accuracy from strong to weak lines, and slight advantages of the SCbez method when compared to the FVM and SClin method (that yield a similar error). Particularly for the FVM, the errors in the line case are lower than those for the continuum, because the radiative transfer is much more local[9], and thus, the error is not being propagated through the complete grid. On the other hand,

---

[9] We emphasize that for the line transfer, the ratio of the photon destruction probability, ϵ_L, to the photon escape probability, is less than unity for all our models, indicating that the line-transfer is, in principle, non-local. However, for the considered spherically symmetric problems, no multiple resonances arise, and the line is formed within a single, well-localized
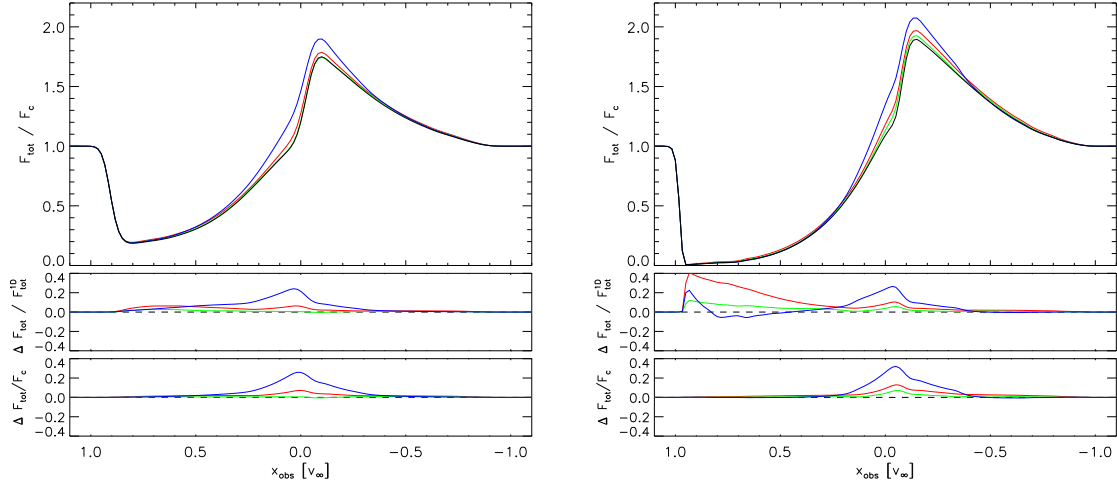
Figure 4.8: Emergent flux profiles of an intermediate ($k_L = 10^3$, left panel) and strong ($k_L = 10^5$, right panel) line. The blue, red, and green curves correspond to the solution of the FVM, SClin, and SCbez methods, respectively. The reference profile (black solid line) has been derived from the 'exact' 1D source function interpolated onto the 3D Cartesian grid. Corresponding relative and absolute errors are shown at the bottom of each chart. For all profiles, the continuum level has been determined from a zero-opacity model. From Hennicker et al. (2019).

numerical diffusion plays a larger role (see Sect. 4.1.2), resulting in minimum errors of $\approx 5\%$ even for very weak lines. The radial stratification of relative errors for each considered line is shown in the lower panel of Fig. 4.7, bottom of each chart. While the FVM gives largest errors near the stellar surface (at $r \lesssim 3R_*$), both SC techniques are in excellent agreement with the 1D solution in such regions. At larger radii, however, the SC solutions are generally overestimated when compared to the 1D solution, due to numerical diffusion errors.

The distinct behaviour of the applied solution schemes in different atmospheric regions finally determines the quality of emergent flux profiles.

Emergent flux profile. The converged source functions are used to calculate the emergent flux profiles using the postprocessing LC solver as described in Sect. 3.7. To extract the error resulting from the FVM and SC methods alone, we interpolated the 'exact' 1D source function onto our 3D grid, and calculated the reference profile using the same technique. The continuum has been calculated within the LC postprocessing routine from a zero-opacity model given by the unattenuated illumination from the projected stellar disc. Then, the differences of line profiles are exclusively related to the differences of line source functions. Fig. 4.8 shows the line profiles with corresponding absolute and relative errors for the intermediate ($k_L = 10^3$) and strong ($k_L = 10^5$) line, obtained from the converged source functions from above.

The line profiles are in good agreement with the 1D solution for both applied SC methods, with

---

resonance region.

slight advantages of the SCbez method when compared to the SClin. Major (relative) deviations arise particularly at large frequency shifts on the blue side, due to the enlarged source functions in corresponding resonance regions (i.e., at large radii in front of the star). At such frequency shifts, however, the line profile is mainly controlled by absorption, and the absolute error remains small. At low frequency shifts, the emission peak becomes slightly overestimated, particularly when considering the strong line. The corresponding resonance regions are mainly located near to the star (at low absolute velocities), and in the whole plane perpendicular to the line of sight (with low projected velocities). For the intermediate line, the emission from this plane at large radii only plays a minor role, due to relatively small optical-depth increments along the line of sight. Thus, both SC methods are in excellent agreement with the 1D reference profile. With increasing line strength, however, the emission from the outer wind region contributes significantly to the line formation, and the discrepancies between the 1D and the SClin/SCbez methods become more pronounced. For the FVM, the emission part becomes overestimated for all line profiles, due to the typically enhanced source functions close to the stellar surface (i.e., at low absolute velocities). For all test calculations, the Bézier method performs best, closely followed by the SClin method and (far behind) the FVM.

With Fig. 4.8 and the argumentation from above, we conclude that (at least) a short-characteristics solution scheme is required to enable a quantitative interpretation of UV resonance line profiles, where both the linear and Bézier interpolation techniques perform similarly well. The less accurate (however computationally cheaper) FVM can still be applied for qualitative discussions.

4.2.4 Flux conservation

As a last test of our 3D solution schemes, we consider purely scattering continua ($\epsilon_C = 0$) within the spherically symmetric wind model described above. Since photons are neither thermally created nor absorbed for such problems, the radiative flux density is conserved (at least in theory). With the definition of the Eddington flux (Eq. 2.13) and of the mean intensity (Eq. 2.10), flux conservation can easily be derived by considering the first (angular) moment of the radiative transfer equation (Eq. 2.53):

$$\frac{1}{4\pi} \int \boldsymbol{n} \cdot \boldsymbol{\nabla} I_\nu \mathrm{d}\Omega = \frac{1}{4\pi} \int \chi_\nu S_\nu \mathrm{d}\Omega - \frac{1}{4\pi} \int \chi_\nu I_\nu \mathrm{d}\Omega$$

$$\implies \boldsymbol{\nabla} H_\nu = \chi_\nu J_\nu \frac{1}{4\pi} \int \mathrm{d}\Omega - \chi_\nu \frac{1}{4\pi} \int I_\nu \mathrm{d}\Omega = 0, \tag{4.5}$$

where we have used that $S_\nu = J_\nu$ for the considered scattering problem, and that the continuum opacity and mean intensity are independent of solid angle. Additionally, one can easily show, that the ϑ and φ components of the Eddington flux, H_ϑ and H_φ, vanish due to symmetry, where ϑ and φ are the co-latitude and azimuth in a local spherical coordinate system of a considered point (i, j, k) with radial coordinate pointing along the position vector of that point. The Eddington flux is then solely given by its radial component, H_r:

$$\boldsymbol{\nabla} H_\nu = \frac{1}{r^2} \frac{\partial \left(r^2 H_r \right)}{\partial r} = 0 \iff H_r r^2 = \mathrm{const.}. \tag{4.6}$$

Fig. 4.9 shows the components of the Eddington flux as obtained from the FVM and SC methods, with the tangential components scaled by the radial ones. For all applied models, the tangential com-
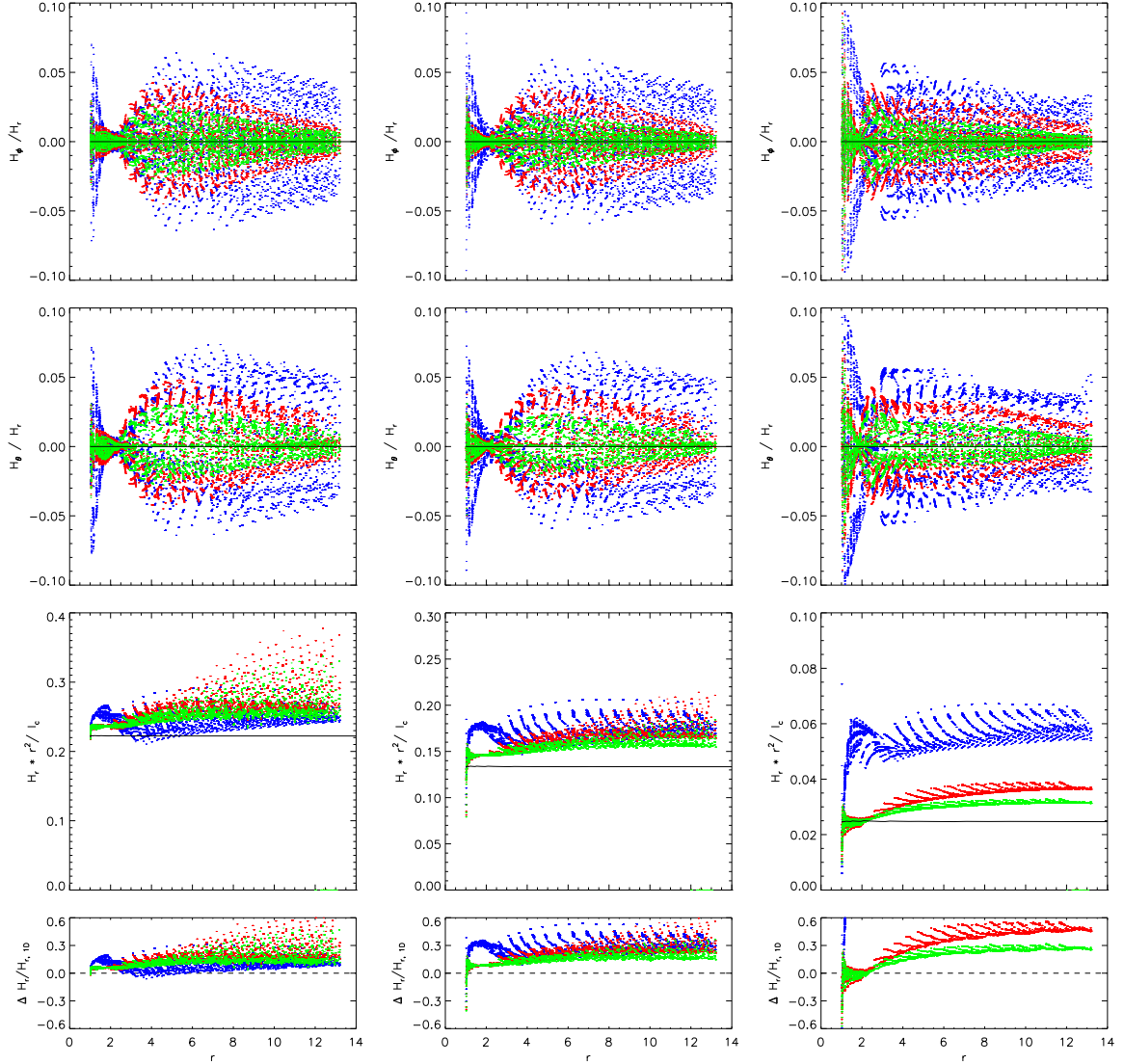
Figure 4.9: φ, ϑ, and r components (from top to bottom) of the Eddington flux as obtained from the FVM and SC methods, when applied to spherically symmetric atmospheres with $\epsilon_C = 0$ and $k_C = [1, 10, 100]$ from left to right. The same color-coding as in Fig. 4.7 has been used, with the black solid line indicating the 1D solutions (with $H_\vartheta^{(1D)} = H_\varphi^{(1D)} = 0$). The tangential components as obtained from the 3D solution methods have been scaled by the corresponding radial ones. The bottom panel shows the relative errors of the radial components of the Eddington flux when compared with the 1D solution.

ponents of the Eddington flux are small, yielding $H_\vartheta, H_\varphi \lesssim H_r/20$ in most cases, and with somewhat larger deviations found for the marginally optically thick and optically thick models, when calculated with the FVM. Also when concentrating on the radial component, the FVM performs reasonably well

only for the optically thin model with $k_C = 1$. Particularly in regions far from the stellar surface, the SC methods show a relatively large scatter for this model, due to numerical diffusion errors. With increasing k_C, the FVM overestimates the radiative flux, resulting from the order of accuracy. Although the SC methods show superior results, the relative error, when compared to the 1D solution, are still on the $10-40\%$ level. Most importantly, however, the Eddington flux (scaled with r^2) remains approximately constant for all applied methods, as theoretically constrained. For the FVM, the scatter of the radial flux component is largest, and becomes significantly reduced for the SC methods. Particularly for the SC solution scheme using Bézier interpolations, $H_r r^2$ is limited to a relatively narrow range.

We conclude that at least the theoretically constrained qualitative behaviour of the flux components can be approximately reproduced by our FVM and SC methods. However, as pointed out in Sect. 1.2.3, already small (tangential) flux components can have a severe impact on the wind structure (e.g., preventing the formation of a disc in the context of Sect. 1.2.3), and this problem needs to be solved when our multi-D radiative transfer methods shall be coupled with radiation-hydrodynamic solution schemes. Thus, a more detailed investigation of the flux components is planned for the future. In this respect, increasing the spatial grid resolution, or even reformulating the discretized 3D radiative transfer equation by applying spherical coordinates, might become inevitable.

4.3 Summary[10]

In this chapter, we have investigated the reliability of the numerical tools developed in Chapter 3, mostly by applying our 3D code to spherically symmetric conditions. Several different tests have been performed to understand certain shortcomings of the one or other method, and to probe the ALI-cycle and the angular integration schemes:

Angular integration: For zero-opacity models, we showed that the Lebedev quadrature performs best for obtaining the mean intensity on a typical 3D spatial grid, and that a number of $N_\Omega \gtrsim 2000$ directions is sufficient to accurately perform the solid angle integration within the 3D FVM and SC methods.

Numerical Diffusion: Due to significant numerical diffusion, intrinsic to both the FVM and SC methods, we found a minimum error for the mean intensity and line source function of roughly 5% when considering optically thin continua and weak lines. Additionally, the (e.g., spherical) symmetry of a considered problem is broken, due to the distinct behaviour of numerical diffusion for different ray directions, and in different regions of the atmosphere. Numerical diffusion errors, however, can be minimized by increasing the grid resolution.

Convergence behaviour: With increasing complexity of the approximate Λ-operator (i.e., from a purely diagonal ALO to a direct-neighbour and nearest-neighbour ALO, the latter including 26 neighbouring terms), the rate of convergence is generally improved. When applying the non-local ALOs within our 3D FVM and SC methods, we obtained a satisfying convergence behaviour, with relative corrections between subsequent iterates of less than 10^{-3} within 20

---

[10]based on Hennicker et al. (2018, Sect. 7), and Hennicker et al. (2019, Sect. 6).

iteration steps, even for the most challenging test cases. Due to this convergence behaviour, we were able to analyse the performance of our methods for such optically thick, scattering dominated atmospheres.

Pure continuum: We have estimated the error of the applied methods in different regimes, by investigating spherically symmetric test models within our 3D SC framework, and with a 3D finite-volume method, where both solution schemes have been formulated on a 3D Cartesian grid. To our knowledge, this is the first study, where different 3D solution schemes for spherical problems have been compared, and their precision explored. When rated against the solution obtained from (accurate) 1D solvers, we found a mean relative error for the converged continuum source function of roughly $5 - 10\%$ and $5 - 20\%$ when using Bézier and linear interpolations, respectively. Particularly for optically thick continua, the (first order) FVM method breaks down, and a (high order) SC or LC method is required to accurately solve the radiative transfer. This problem, however, arises only at large optical depths (e.g., when considering the winds of Wolf-Rayet stars), and is of only minor importance for the winds of OB stars with (at most) marginally optically thick atmospheres.

Line transitions: When considering the solution for the line source function for different line-strength parameters, the mean relative errors of both SC methods are on the 10%-level and below, with slight advantages of the Bézier technique, compared to purely linear interpolations. The resulting synthetic line profiles are calculated with a long-characteristics postprocessing routine, using the corresponding converged source functions. The SC method using Bézier interpolations almost perfectly matches the 1D reference profiles for all our models (i.e., for weak and strong lines). When linear interpolations are used, we obtain slight deviations, originating mainly in the outer wind regions. In contrast, the 3D FVM always overestimates the emission, due to an overestimation of the line source function in regions near to the stellar surface.

Flux conservation: For purely scattering atmospheres, we investigated in how far our 3D FVM and SC methods reproduce the theoretically requested conservation of the radiative flux. Within our 3D solution schemes, we found that the tangential components are – almost consistent with theory – small ($H_\vartheta, H_\varphi \lesssim 5\% \, H_r$), when compared with the radial one. The radial component, $r^2 H_r$, on the other hand is generally overestimated when compared with an accurate 1D solution, and remains only approximately constant over the radial coordinate. Particularly for the FVM, this point requires further investigations.

Overall, the 3D SC methods typically yield a higher accuracy than the FVM, with slight advantages when using Bézier interpolations instead of linear ones. Nevertheless, all methods have their own advantages and disadvantages, particularly when also accounting for the computation time (with fastest turn-around times for the FVM method). Thus, the 3D FVM method should be used for qualitative interpretations and for finding (rough) estimates of the parameters of interest, while the SC methods are to be preferred when aiming at a quantitative analysis of line profiles, and for optically thick continua. All methods can readily be applied to non-spherical problems.

Chapter 5

Applications

This chapter has been copied – to a major part – from Hennicker et al. (2018) and Hennicker et al. (2019).

5.1 Wind ablation[1]

Using 3D radiation-hydrodynamic simulations, Kee (2015) and Kee et al. (2016) modelled the ablation of circumstellar discs around massive stars, due to radiative line driving. They showed that a significant line force arises due to the coupling of non-radially streaming photons to the non-radial velocity field of circumstellar discs (see also Kee et al. 2016, their Figure 1). The line force has been calculated within a Sobolev approach, by means of line-strength distribution functions. Contrasted to the original formulation by CAK, they followed the parameterization by Gayley (1995). The full 3D line acceleration can then be written as[2]

$$\boldsymbol{g}_{\text{lines}} \approx \frac{\kappa_{\text{e}}\bar{Q}}{(1-\alpha)c(Q_0\kappa_{\text{e}}c\rho)^\alpha} \int \left(\boldsymbol{n}\cdot\boldsymbol{\nabla}\cdot(\boldsymbol{n}\cdot\boldsymbol{v})\right)^\alpha I(\boldsymbol{n})\boldsymbol{n}\mathrm{d}\Omega, \tag{5.1}$$

where $\boldsymbol{n}$ and $\boldsymbol{v}$ describe the direction of the considered ray and the velocity-vector, respectively. ρ is the density, $\bar{Q}$, Q_0, and α describe the line-strength distribution, and were taken from the calibration of Puls et al. (2000, their Table 2), for the considered T_{eff}.

Table 5.1: Stellar and wind parameters for the wind-ablation model. The line-strength parameters have been set to $\alpha = 0.66$, $\bar{Q} = 2500$, and $Q_0 = 2200$.

T_{eff} [kK]	R_* [$R_\odot$]	$\log g$	v_{min} [km s^{-1}]	v_∞ [km s^{-1}]	β	$\dot{M}_{\text{wind}}$ [$M_\odot$yr^{-1}]
36	9.4	3.9	22	2200	1	$1.5 \cdot 10^{-7}$

---

[1] copied from Hennicker et al. (2018, Sect. 5).
[2] Strictly speaking, Eq. (5.1) holds only when the strongest line is optically thick. See Kee (2015, Chapter 2), for a complete derivation and discussion.
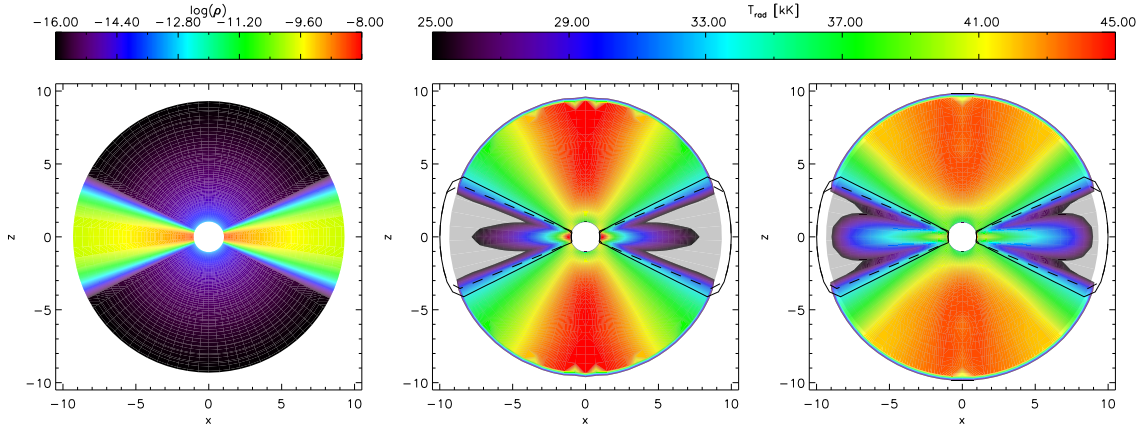
Figure 5.1: Left panel: Density structure for the wind-ablation model with $\tau_{\mathrm{disc}} = 1400$, in the *xz*-plane. The middle and right panels display the radiation temperatures as obtained by the 3D FVM and 3D SC method (using linear interpolations), respectively. Additionally, the density contours corresponding to a decrease in line force by $f = 10$ (solid) and $f = 100$ (dashed) are displayed. Both contours indicate the transition region from wind to disc (see text). The grey colour corresponds to radiation temperatures less than the colour-coded minimum value. Left and middle panel from Hennicker et al. (2018).

For optically thin continua (e.g., in classical Be stars), the incident intensity $I(\boldsymbol{n})$ can be directly replaced by the intensity originating from the stellar core[3], I_{c}^{+}, and Eq. (5.1) can be solved by quadrature, for a given density and velocity structure. For accreting high-mass stars (see Sect. 1.2.6), that is, for massive objects in their late formation phases, however, the circumstellar discs are optically thick, and at least two major problems arise:

Firstly, due to absorption and scattering processes, the incident intensity at a considered point needs to be calculated by a global solution of the radiation field, which is very time consuming in hydrodynamic simulations. Kee (2015) developed an efficient method to delimit the contribution by either calculating the absorption part alone (giving a lower limit of the incident intensity), or assuming the disc to be optically thin (giving an upper limit). A comparison between the irradiation obtained from their method to the irradiation obtained from our 3D code (including scattering of photons) will be presented in future studies, and shall not be discussed here.

In this thesis, we consider the second problem of optically thick environments: Since the disc partly blocks the irradiation from the star, the radiation field might become considerably reduced. However, since the density in the wind-ablation regions is not too different from the density in the wind, it is this (ionizing) radiation field, which mainly determines the ionization stages of the considered plasma, and consequently might influence the line-strength distribution function. To address this issue, we proceed as follows: First, the radiation field for a specific hydrodynamic structure (see

---

[3] Due to gravity darkening, the intensity emerging from the stellar core of rapidly rotating stars (e.g., Be stars) becomes latitude dependent. For the O7 model discussed below, we assumed negligible rotation rates to remain consistent with Kee et al. (2016).

below) is computed by our 3D code, and the resulting mean intensity is translated to a corresponding radiation temperature (using $J_\nu =: W \cdot B_\nu(T_{rad})$ with dilution factor W; the derived radiation temperature would correspond to T_{eff} if the star had an optically thin, spherically symmetric atmosphere). Corresponding line-strength parameters could again be obtained from Puls et al. (2000). In regions where the local radiation temperature is similar to the effective one, one can safely assume that the parameters of the line-strength distribution remain at their original input values, and indeed can be used to calculate the line force throughout all following hydro-timesteps. If, on the other hand, T_{rad} differed significantly from T_{eff}, the line-strength distribution would need to be consistently adapted within the hydrodynamical evolution.

For our analysis, we used a wind+Keplerian-disc model similar to the initial conditions for the accreting O7-star system as considered by Kee et al. (2016). This model describes such objects as already defined in Sect. 1.2.6 as accreting high-mass stars (see also Hosokawa et al. 2010, Kuiper et al. 2016). The wind and stellar parameters are given in Table 5.1, following Kee et al. (2016). A radial optical depth of the disc, $\tau_{disc} = 1400$, has been adopted. We approximated the continuum by pure Thomson-scattering, $\epsilon_C = 0$, to ensure frequency independence. This is a fair assumption for the 500-2000 Å range, where the majority of line-driving happens (e.g., Puls et al. 2000). Of course, we would expect thermalization in the disc's deeper layers. Due to the dominating $\rho^{-\alpha}$-dependence of the line force (Eq. 5.1) and the large densities inside the disc, however, most of the wind-ablation occurs at the surface layers, and we do not need to care about the details in the inner parts. This fact is even more important, since it allows us to apply our 3D FVM method, although being aware of the large errors of the continuum transfer for optically thick media.

To ensure that the transition region from the wind to the disc is not subject to (larger) numerical uncertainties, we have performed a test calculation with doubled grid resolution ($N_x^{test} = N_y^{test} = N_z^{test} = 265$). Although we found, as expected, differences in the inner part of the disc, our results for the outer part and the wind region are (almost) identical. Furthermore, we have compared the solution as obtained from the FVM with corresponding ones when calculated with the SC method using linear interpolations. At least in the considered wind-ablation regions, both solutions are fairly consistent (see Fig. 5.1, middle and right panel). In these regions, we can therefore safely assume, that the obtained solutions are only mildly affected by numerical artefacts.

The density structure and radiation temperature (the latter computed by our code) are shown in Fig. 5.1. The radiation temperature in the wind (here: along the z-axis) exceeds the effective temperature by a factor of roughly 1.25. In order to ensure that this is not a numerical effect, we have checked this issue by calculating the same wind model, however applying an optically thin disc with $\tau_{disc} = 1.4 \cdot 10^{-3}$. For such a model, T_{rad} and T_{eff} turned out to be fairly identical. We thus conclude that the enhancement of radiation temperature in our original model is due to additional irradiation of the wind from the disc, by scattering off photons from the disc. Most likely, this effect will induce latitudinal line-force components (also to be addressed in forthcoming investigations).

Wind-ablation dominates in the transition region between wind and disc. We define this region by calculating the decrease in line force by a certain factor, f, due to density effects alone, that means assuming the same ionization stages and the same velocity structure. Such a reduction of line force or

line acceleration is easily cast into an enhancement of density via Eq. (5.1),

$$\frac{g_{\text{lines}}^{(\text{disc})}(r, \Theta)}{g_{\text{lines}}^{(\text{wind})}(r)} < \frac{1}{f} \quad \leftrightarrow \quad \left(\frac{\rho_{\text{disc}}(r, \Theta)}{\rho_{\text{wind}}(r)}\right)^{\alpha} > f, \tag{5.2}$$

where the radius-dependent quantities from the wind can be measured along the z-axis. In this picture, f should be chosen such that the corresponding decrease in line force represents the border from the wind region to the region where the line force is negligible (i.e., inside the disc). As a first guess, we adopted $f = 10$, and display the corresponding density contour in Fig. 5.1. Since a factor $f = 10$ seems to be somewhat artificial, we additionally display the density contour corresponding to $f = 100$.

From our simulations, we then find that both contours are located within a range of T_{rad} between roughly 31 and 33 kK, which is of the same order as the effective temperature, $T_{\text{eff}} = 36$ kK. We thus conclude that the ionization stages at the disc surface are not changing too much, when compared to the ionization stages in the wind, and that the line-strength parameterization of the wind can also be used to calculate the line force at the surface of such optically thick circumstellar discs. Due to significant scattering of photons off the disc, a multi-D description of the radiative transfer might need to be incorporated into the hydrodynamic simulations, to account for all force components.

5.2 Dynamical magnetospheres: HD191612[4]

As a first application of the FVM to line transitions, we modelled UV resonance lines in dynamical magnetospheres, that is, in atmospheres which form in slowly rotating magnetic OB stars (in contrast to the so-called centrifugal magnetospheres, which form in fast rotating magnetic OB stars). As a prototypical case, we considered the Of?p star HD191612, which has a negligible equatorial rotation speed of $v_{\text{rot}} \approx 1.4 \, \text{km}\,\text{s}^{-1}$ (Howarth et al. 2007, Sundqvist et al. 2012). Marcolino et al. (2013) already calculated corresponding resonance lines for this star, by extending the 3D formal solver developed by Sundqvist et al. (2012) to a '3D Sobolev with exact integration' method (SEI, Lamers et al. 1987), and applying this method to a set of 100 2D MHD-simulation snapshots, equidistantly distributed over the azimuth-angle to enable a 3D description of the atmosphere. At least for the H_α line (where the source function is taken from prototypical 1D NLTE-calculations), such a patching-technique produces quite similar results as full 3D MHD simulations (see ud-Doula et al. 2013). In Sect. 5.2.1, we use the same simulations as a benchmark for our 3D code, and compare the obtained line profiles to those from Marcolino et al. (2013). In Sect. 5.2.2, we calculate analogous line profiles for the ADM model developed by Owocki et al. (2016), to investigate in how far their simplified description of the magnetosphere can be used as a reasonable substitute for elaborate MHD simulations. We already note here, that such a simplified approach would be favourable to MHD simulations, because it provides (within the applied approximations) an average, steady state solution for the magnetospheric structure, and avoids time-consuming hydrodynamic simulations.

---

[4] copied from Hennicker et al. (2018, Sect. 6).

5.2.1 MHD models

To understand the behaviour of the line profiles presented below, we first explain the basic charac-
teristics of (non-rotating) magnetic winds. For a more detailed discussion, we refer the reader to the
seminal work by ud-Doula & Owocki (2002) and ud-Doula et al. (2008). These authors introduced
a magnetic dipole field as an initial condition, and evolved the (initially spherical) stellar wind ac-
cording to the MHD equations. Within ideal MHD[5], the material follows the (closed) magnetic-field
lines in regions where the magnetic energy exceeds the kinetic energy of the wind (close to the star),
whereas, in the opposite case, the field lines follow the (almost radial) mass flow (far from the star).
The border of both regions can be roughly described by the Alfvén-Radius, $R_A \approx 0.3 + (\eta_* + 0.25)^{1/4}$,
with wind-confinement parameter $\eta_* := (B_p^2 R_*^2)/(4\dot{M}_{B=0} v_\infty)$, and B_p the polar magnetic-field strength
evaluated at the stellar radius (see ud-Doula et al. 2008, and Sect. 1.2.5).

Within closed-field regions, material originating from opposite footpoints shocks (and accumu-
lates) in the equatorial plane. Due to the $1/\rho^\alpha$-dependence of the line-force (see Eq. 5.1), the net-force
becomes dominated by gravity, and produces an inflow along the magnetic field lines in a 'snake-like'
pattern.

In the open-field regions, the presence of the magnetic field, together with a frozen-in mass flow,
results in a density decrease when compared with spherically symmetric models, due to the faster-
than-radial expansion of the flow-tube area (see Figure 7 in ud-Doula & Owocki 2002). Consequently,
the line-force becomes increased, resulting in higher terminal velocities than in 1D non-magnetic
models. A single snapshot and an azimuthal average of the applied MHD simulations are shown in
Fig. 5.2.

Based on such MHD simulations, Sundqvist et al. (2012) calculated corresponding H_α-line pro-
files, while Marcolino et al. (2013) investigated the UV resonance-line formation. To remain consis-
tent with the calculations by Marcolino et al. (2013), we apply $\epsilon_L = 0$, and use their description of the
line-strength parameter, κ_0, originally introduced by Hamann (1980). κ_0 is related to the line-strength
parameter from Eq. (2.61) by

$$\kappa_0 = \frac{1}{4\pi m_p} \frac{\dot{M}}{R_* v_\infty^2} \frac{1 + I_{He} Y_{He}}{1 + 4Y_{He}} \sigma_e v_{th}^* k_L, \tag{5.3}$$

with $I_{He} = 2$ and $Y_{He} = N_{He}/N_H = 0.1$, the number of free electrons per helium atom, and helium
abundance by number, respectively.

Although we use a micro-turbulent velocity of $v_{turb} = 100 \ \mathrm{km\,s^{-1}}$ for the determination of the
source function, we calculate the final line profile (somewhat inconsistently) for $v_{turb} = 50 \ \mathrm{km\,s^{-1}}$, as
done by Marcolino et al. (2013). The line profiles obtained from our 3D code and the SEI line profiles
from Marcolino et al. (2013) are displayed in Fig. 5.3, for two different line-strength parameters, κ_0
= 0.1 and 1.0, respectively.

The agreement between the two methods is excellent. The minor differences in the emission part
are related to two effects: Firstly, the methods for determining the source functions (SEI implying
very narrow resonance lines vs. FVM accounting for much broader ones, due to $v_{turb} = 100 \ \mathrm{km\,s^{-1}}$)
are quite different, and a certain deviation must be present. Secondly, the (general) overestimation of

---

[5] Ideal MHD is a fair approximation in hot star winds, due to the high conductivity.
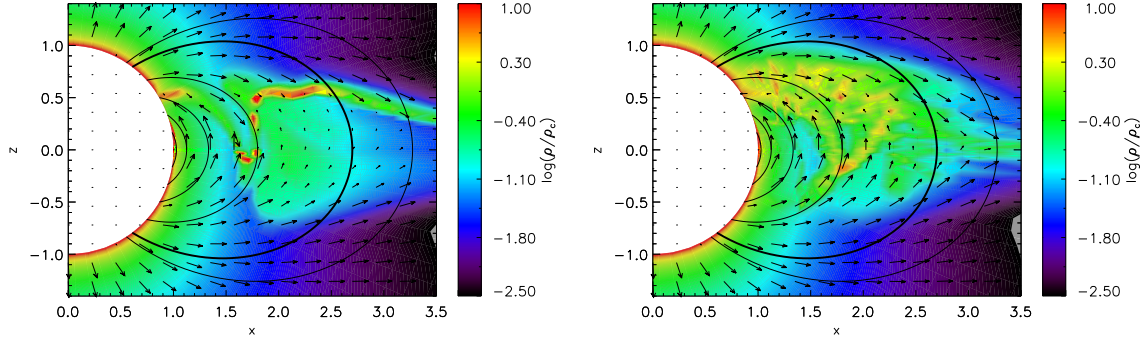
Figure 5.2: Left panel: density structure for an example snapshot from the MHD simulations for HD191612, as performed by Sundqvist et al. (2012). Right panel: azimuthal average of the MHD simulations. In both figures, the density has been normalized by a typical downflow density, $\rho_c :=$ $\dot{M}_{B=0}/(4\pi R_*^2 v_{esc})$, with $\dot{M}_{B=0}$ from Table 5.2, and $v_{esc} \approx 800\,\text{km}\,\text{s}^{-1}$ the photospheric escape velocity. The velocity field is displayed by arrows, with the length of the velocity vectors limited to 0.5 v_{esc}. We additionally show the dipole magnetic field of the ADM models used in Sect. 5.2.2 (solid lines, and thick solid line for $R_A = 2.7 R_*$). The corresponding magnetic axis is aligned with the z-axis. The grey colour corresponds to densities outside the range indicated on the right. From Hennicker et al. (2018).
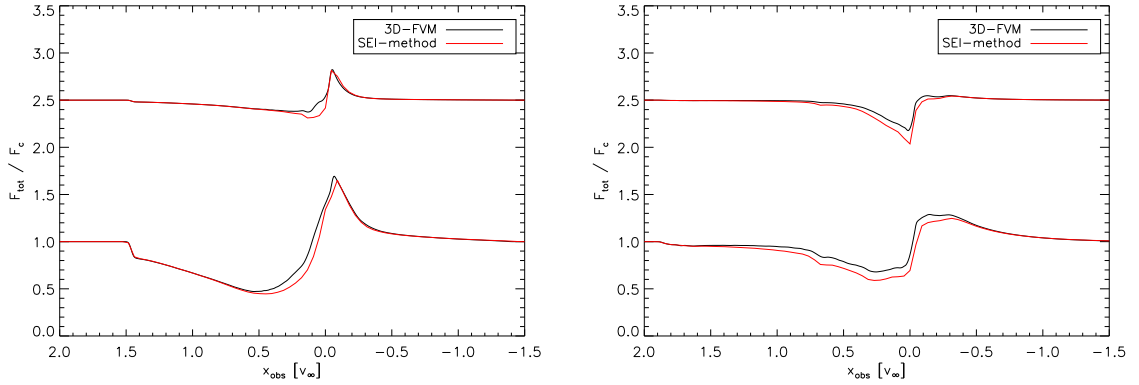
Figure 5.3: UV resonance-line profiles for the MHD models, as obtained from our 3D FVM code (black) and from the SEI method by Marcolino et al. (2013) (red). Two different line-strength parameters, $\kappa_0 = 0.1$ and 1.0, have been used. For convenience, the line profiles for $\kappa_0 = 0.1$ have been shifted vertically by 1.5. The left and right panels show the synthetic line profiles for pole-on and equator-on observers, respectively. The abscissa has been scaled to $v_\infty = 2700$ km s^{-1}, the 'observed' 1D value applied by Marcolino et al. (2013). From Hennicker et al. (2018).

the scattering integrals and thus source functions due to the FVM might play a role as well. Also the absorption parts of the line profiles observed equator-on (lower panel of Fig. 5.3) are not perfectly matched. This (small) effect is most likely simply due to different formulations of the numerical solvers.

Table 5.2: Stellar and wind parameters of HD191612 (upper row). T_{eff}, $\log g$, R_*, $\dot{M}$, v_∞ have been derived by Howarth et al. (2007), and B_{p} is adopted from Wade et al. (2011). For the ADM model, we adapted the mass-loss rate and terminal velocity at the pole (bottom row), to be consistent with the MHD simulations from Fig. 5.2.

T_{eff} [kK]	R_* [$R_\odot$]	$\log g$	v_∞ [km s^{-1}]	$\dot{M}$ [$M_\odot$yr^{-1}]	B_{p} [G]
35	14.5	3.5	2700	$1.6 \cdot 10^{-6}$	2450
			$v_\infty^{\text{(pole)}}$ [km s^{-1}]	$\dot{M}_{\text{B}=0}$ [$M_\odot$yr^{-1}]	R_{A} [R_*]
			3963	$1.1 \cdot 10^{-6}$	2.7

A comparison of these line profiles with those from corresponding spherically symmetric models has already been performed by Marcolino et al. (2013), and we summarize only the most important characteristics: (1) The absorption trough for pole-on and equator-on observers extends beyond the 1D terminal velocity, as expected from the MHD atmospheric structure. We note that such a large extension has not been observed for HD191612. (2) The emission for equator-on observers is reduced (compared to the 1D case), due to the lower densities in the emission plane (e.g., the polar plane for line-centre frequencies with $x_{\text{obs}} = 0$). (3) The particular form of the line profiles is determined by the different mapping of projected velocities for different observer directions.

Given the overall agreement of the two different methods, we conclude that the SEI and our 3D FVM solutions are consistent. Since both methods are completely independent, this result shows two points: Firstly, our 3D FVM performs well also for non-spherical 3D wind structures, and secondly, also the 3D SEI method as applied by Marcolino et al. (2013) is validated. We emphasize, however, that the 'simple' Sobolev approach can only be applied for single lines (and steep velocity fields), whereas situations with line overlap (e.g., resonance doublets) can be computed in a comparatively simple way only by our 3D method. Being highly confident that the line formation in (arbitrary) wind structures is described correctly, we are able to study the UV line formation within the ADM model.

5.2.2 ADM models

Owocki et al. (2016) developed an analytic description of dynamical magnetospheres, in order to set a framework similar to the β-velocity-field prescription for spherically symmetric winds. This ADM formalism provides a time-independent, steady-state solution for dynamical magnetospheres, which is comparable to the average of several MHD-simulation snapshots, and has been corroborated by a comparison of synthetic H$_\alpha$ lines with observations. The formation of resonance lines within the ADM framework, however, has not been analysed yet, and is the focus of this section. For that purpose, we aim at modelling the MHD atmospheric structure from above with the ADM method, and compare the resulting line profiles.

Within the ADM method, Owocki et al. (2016) divide the atmosphere into two major zones. The border between both regions is given by the condition $r_{\text{m}} = R_{\text{A}}$, where the apex-radius, r_{m}, is defined as the distance between the origin and the intersection of magnetic equator and closed dipole magnetic-field line attached to a considered point (see left panel of Fig. 5.5 for clarification). In the following,
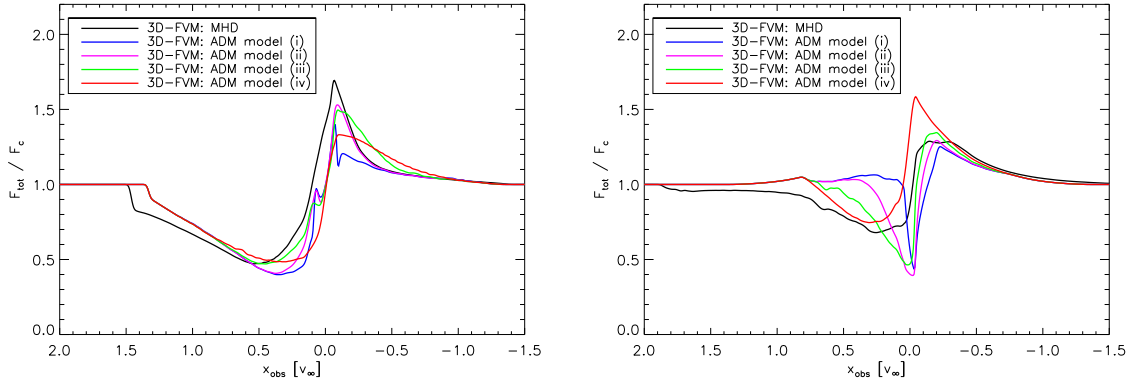
Figure 5.4: UV resonance-line profiles obtained from our 3D FVM code, for the MHD simulation (black, as Fig. 5.3), and the different ADM models, (i) to (iv) (see text). The line-strength parameter has been set to $\kappa_0 = 1$. The left and right panels show the synthetic profiles for pole-on and equator-on view, respectively. As in Fig. 5.3, the abscissa has been scaled to $v_\infty = 2700$ km s^{-1}, the 'observed' 1D value applied by Marcolino et al. (2013). From Hennicker et al. (2018).

we call these two regions the 'closed-field region' ($r_m < R_A$) and the 'outer wind' ($r_m > R_A$). The closed-field region consists of three different components:

- wind-upflow component: The magnetic loops are fed with material ejected from the stellar surface. The matter flow follows the dipole magnetic-field lines, with absolute velocities calculated from a β-velocity law, using $\beta = 1$.

- post-shock component: The collision of outflows following the B-field lines from opposite footpoints leads to a shock at the magnetic equator, resulting in a hot and dense post-shock region. The extent of this region is controlled by a (dimensionless) cooling parameter, χ_∞, where $1/\chi_\infty$ describes the efficiency of radiative cooling by X-ray emission (see ud-Doula et al. 2014 for details). In test calculations, however, this component turned out to have only very small influence on the UV line formation. Thus, and to keep the model as simple as possible, we neglect the post-shock component in this work.

- cooled-downflow component: As the post-shock gas cools, its density increases, and the line-force decreases. Thus, the cooled and compressed gas is pulled back onto the stellar surface by gravity, resulting in a downflow starting at the magnetic equator. The gas is accelerated from zero velocity along the B-field lines to the escape speed at the stellar surface.

For their H_α analysis, Owocki et al. (2016) only considered the cooled downflow, because of the mostly larger densities of this component. Since the infall occurs in episodic infall events, the closed-field region is actually highly structured, and these authors found rather large 'clumping factors' (see Sect. 1.2.2), of the order of several tens. Under the assumption of clumps that are optically thin, this clumping factor can be used to translate the actual (structured) density-distribution to the mean opacities and emissivities of recombination lines (ρ^2-processes, see e.g., Puls et al. 2008). For the UV

resonance-line formation (linear in ρ), micro-clumping (i.e., optically thin clumping) has no direct impact on the mean opacities. Therefore, and because of the different densities and velocities within the upflow and downflow components, an explicit description of the structured medium is required when considering UV resonance lines. As it is not a priori clear how to treat the combination of the above mentioned components, we consider four different approaches, and model the closed-field region by:

(i) Applying only the cooled-downflow component.

(ii) Introducing a statistical treatment, where the probabilities of using either the wind-upflow or the cooled downflow-component when calculating the radiative transfer are here defined as

$$P_{\mathrm{w}} := \frac{\rho_{\mathrm{w}}}{\rho_{\mathrm{w}} + \rho_{\mathrm{c}}}, \qquad P_{\mathrm{c}} := \frac{\rho_{\mathrm{c}}}{\rho_{\mathrm{w}} + \rho_{\mathrm{c}}} = 1 - P_{\mathrm{w}}.$$

This approach preferentially chooses the component with higher density and lower velocity[6], in other words, that component with the larger timescale for the matter flow.

(iii) Introducing flux-tubes that alternating consist of the downflow and upflow component.

(iv) Applying only the wind-upflow component.

The models are ordered such that the contribution of the wind-upflow component is increasing from model (i) to (iv).

As a zeroth-order approximation, Owocki et al. (2016) model the outer wind (at $r_{\mathrm{m}} > R_{\mathrm{A}}$) by the wind-upflow component, that means by a flow following closed magnetic-field lines even in that region. This is a fair assumption for modelling the polar regions, since it accounts for the faster than radial decline of the density (see also Owocki & ud-Doula 2004). Moreover, the magnetic field lines are nearly radial in these regions, thus resulting in a nearly radial outflow similar to the MHD simulations. On the other hand, the velocity vectors near the equatorial regions are modelled with a large latitudinal component, whereas they are radially directed within the (more realistic) MHD simulations. Thus, a match of the ADM and MHD magnetospheric structure in the equatorial region cannot be achieved within the standard formulation. With respect to UV line formation, this is the major drawback of the ADM formalism, and will influence the line formation (see below).

To set the base density, Owocki et al. (2016) introduced the mass-loss rate of the star if it had no magnetic field, $\dot{M}_{\mathrm{B}=0}$, which determines the loop-feeding rate. With the input parameters from Table 5.2, the dynamical magnetosphere can be modelled according to the recipe from Owocki et al. (2016)[7]. We used the values of $\dot{M}_{\mathrm{B}=0}$ and $v_{\infty}^{\mathrm{(pole)}}$ in Table 5.2, right panel, to adapt the ADM model to the MHD simulations. For our model parameters, the Alfvén-Radius, $R_{\mathrm{A}} = 2.7\,R_*$, has been calculated from the mass-loss rate, terminal velocity, and magnetic-field strength.[8] We stress that the adopted mass-loss

---

[6] Both quantities are connected by the continuity equation.

[7] We have increased the wind-upflow and cooled-downflow densities by a factor of two, which is missing in their original equations.

[8] For the input parameters given in Table 5.2, we actually would obtain $R_{\mathrm{A}} \approx 3\,R_*$. However, taking $R_{\mathrm{A}} \approx 2.7\,R_*$ is somewhat more consistent with the magnetospheric structure obtained within the MHD simulations (cf. Fig. 5.2).

rate is not necessarily the 'true' one, nor the mass-loss rate the star would have if no magnetic field was present. For the applied ADM models, the resulting density stratification, magnetic-field lines and velocity vectors in the *xz*-plane are shown in the left panel of Fig. 5.5. Here and in the following, the equatorial plane coincides with the plane of the magnetic equator, since we assume the magnetic axis to be aligned with the *z*-axis.

Compared to the MHD structure (see Fig. 5.2), the ADM densities in the closed-field region are best represented by model (ii) and (iii), that is, by a combination of downflow and upflow component. In the outer wind near the equator, the densities are underestimated due to the aforementioned different description of the velocity field (see Fig. 5.5, left panel).

Once again we apply $\epsilon_L = 0$, and compare the corresponding line profiles with line-strength parameter, $\kappa_0 = 1$, for equator-on and pole-on observers, with the line profiles obtained from the MHD simulations (see Fig. 5.4). For clarification, Fig. 5.5 additionally displays all line profiles with their emission and absorption parts. The differences between the profile-sets can be explained as follows.

For pole-on observers: With increasing contribution from the upflow component, the emission peak becomes broader, because the emitting volume at intermediate to high velocities increases. Simultaneously, the cooled downflow component with only low absolute velocities decreases, resulting in a lower emission peak near the line centre. An exception is model (i), for which the emission peak at low frequency shifts is lowest, because the emission of the upflow component near the star (with high densities and low velocities) is missing. When compared to the line profiles from the MHD simulations, the best result is obtained for model (ii), that is, for the statistical description of upflow and downflow component in the closed-field region. Even for this model, however, we only get a relatively poor match with the MHD profiles. Since our ADM models cover a large range of combinations of upflow and downflow component (including the most extreme cases of a pure upflow and a pure downflow), this finding suggests that the outer wind region is inadequately modelled. Indeed, the major differences of the line profiles can be explained (at least qualitatively) by the different description of the outer wind: (1) In the ADM models, the emission peaks close to line centre (i.e., at $x_{\text{obs}} \approx 0$, with corresponding resonance zones at projected velocities $\boldsymbol{n} \cdot \boldsymbol{v} \approx 0$) are underestimated compared to the MHD model, since within all ADM models also the mass flow in the outer wind is adopted to follow closed magnetic field lines. This assumption becomes problematic in equatorial regions, since here the ADM wind flows almost perpendicular to the plane, whereas it is almost radial in the MHD case. Consequently, when viewed pole on, only large projected velocities are present in the corresponding area of the equatorial plane, where the latter creates a large part of low-velocity emission in the MHD model. This part is now missing in the ADM models, and the emitting area is almost limited to the downflow component (with generally low projected velocities). Thus, the profile becomes shallower than in the MHD case. (2) Within the blue absorption trough, the absorption column in front of the star is slightly decreased, because the velocity vectors are once again following the magnetic field lines, and do not perfectly match the MHD simulations. The differences of the line profiles can thus be explained by the different description of the outer wind region alone.

For equator-on observers, the emission peak of the ADM models becomes stronger and shifted to the blue side with increasing contribution of the upflow component. Additionally, the absorption part on the blue side increases, while it decreases on the red side. This behaviour is readily explained: As the upflow contribution in front of the star (with projected velocities directed towards the observer,
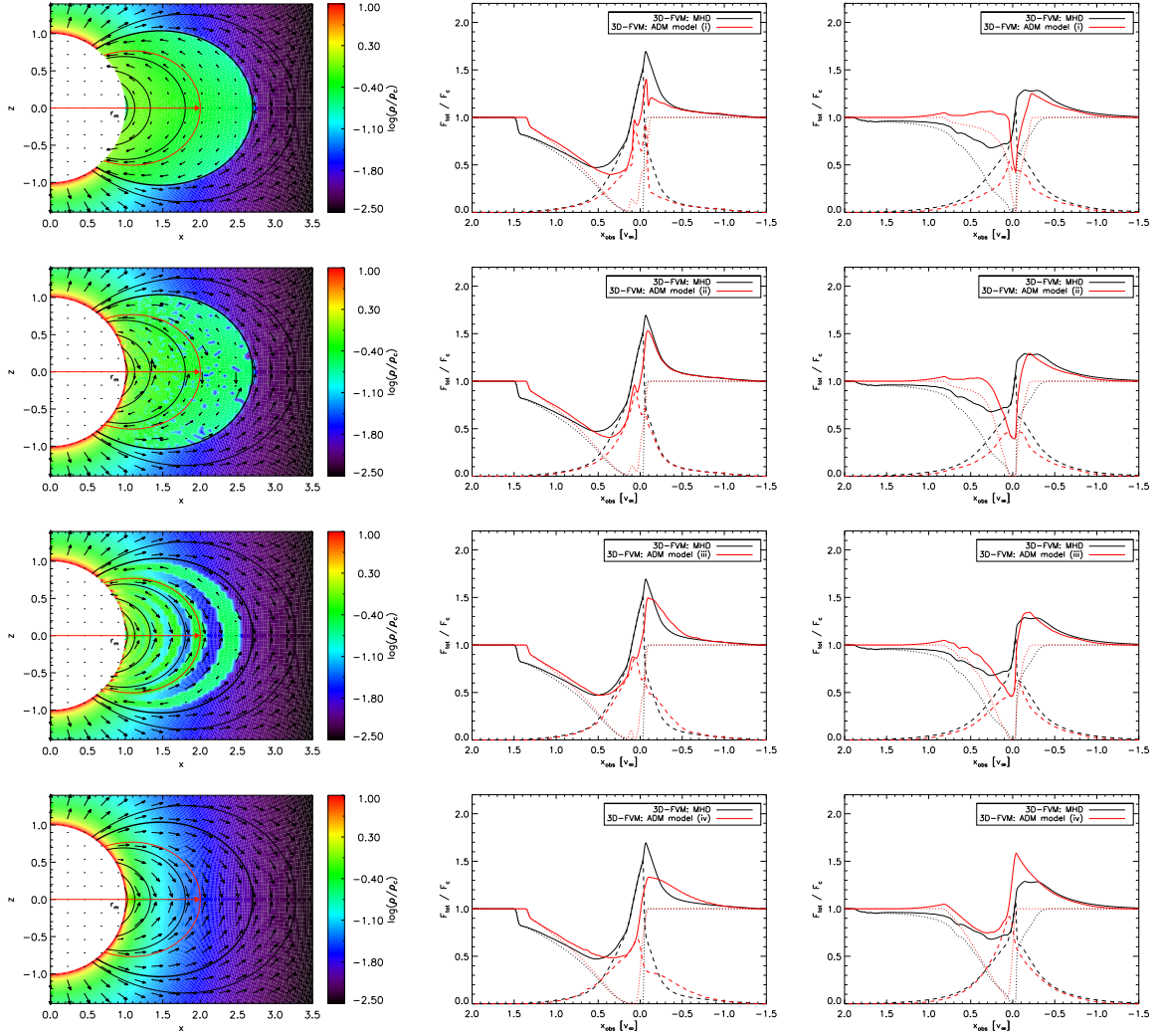
Figure 5.5: Left panel: As Fig. 5.2, but for the corresponding ADM model structures. To clarify the definition of the apex radius, r_m, we have displayed a specific value, $r_m=2\,R_*$, as a red arrow, where this value corresponds to all points located on the red magnetic-field line. In the closed-field region (inside $r_m=R_A$, displayed by a thick line), the models contain, from top to bottom: (i) The cooled-downflow component alone. (ii) A statistical approach for the downflow and upflow component. (iii) Alternating flux tubes with cooled-downflow and wind-upflow component. (iv) The wind-upflow component alone. Middle panel: As Fig. 5.4, for pole-on observers, and for the different ADM models (i) to (iv). The dashed and dotted lines display the emission part and the absorption part of the line profiles, respectively. Right panel: As middle panel, but for equator-on observers. From Hennicker et al. (2018).

thus affecting the blue side of the profile) grows, the downwind contribution (with projected velocities directed away from the observer, and affecting the red side of the profile) is diminished. Consequently, the absorption in front of the star increases on the blue side, and decreases on the red one. Again, when

compared to the MHD model, none of the obtained profiles provides a good agreement. While model (iv) reproduces the absorption part on the blue side relatively well, the red-sided absorption part is highly underestimated. On the other hand, a better model for the red-sided absorption (e.g., model iii) underestimates the absorption part on the blue side. In fact, it is not possible to simultaneously model the blue and red absorption by only tuning the composition of the closed-field region, suggesting that (at least) the outer wind needs to be treated differently. For instance, assuming a radial outflow in the equatorial plane of the outer wind region would increase the blue-sided absorption (and emission), while preserving the rather good behaviour of model (iii) on the red side.

Taking all this evidence together, we conclude that the (present) ADM model needs to be improved for the modelling of UV resonance lines, at least in the outer wind. Such a re-formulation then needs to include a consistent description of the actual velocity and density stratification, accounting for the delicate interplay between B-field and wind.

5.3   Rotating winds[9]

As a first application of the 3D SC method to non-spherical atmospheres, we consider the UV resonance-line formation in the winds of (fast) rotating O stars. Fast rotation has two immediate consequences on the stellar geometry and wind structure: (i) The surface of any rotating star becomes distorted, with R_{eq}/R_{pole} approaching 3/2 for rotational speeds near the critical velocity (Collins 1963 assuming a Roche model, and the critical velocity defined by Eq. 5.5 for $\Omega = 1$). (ii) The emergent flux depends on the (local) effective gravity (corrected for the centrifugal acceleration), and thus, decreases towards the equator ('gravity darkening', see von Zeipel 1924, and Maeder 1999, Maeder & Meynet 2000 for uniform and shellular rotation, respectively). As outlined in Sect. 1.2.3, gravity darkening together with the effects of non-radial line forces predicts a prolate wind structure, whereas latitudinal variations of ionization stages (particularly near the bi-stability jump) still allow for an oblate rotating wind.

As a consequence of the distinct wind structure resulting from a particular model, the wind lines of rotating stars are expected to differ as a function of rotational speed and inclination. To predict UV resonance-line profiles of fast rotating stars, we calculate the source function of a prototypical resonance-line transition including the effects of gravity darkening (described here by the von-Zeipel description) and surface distortion (obtained from a Roche model) for models with different rotational velocities. As a first step, we use a wind description that is consistent with the prolate wind model. For all calculations, we apply the SClin method.

5.3.1   Wind model

To obtain a model for the structure of rotating winds, we apply a two-dimensional version of the VH-1 code[10] developed by J. M. Blondin and co-workers. Our model includes the effects of surface distortion and gravity darkening. Using a 1D input model derived from radiation driven wind theory including finite cone angle corrections (CAK and Pauldrach et al. 1986) for the first time step, the

---

[9] copied from Hennicker et al. (2019, Sect. 5).
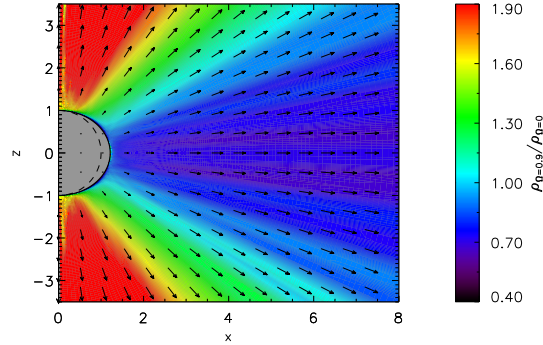
[10] http://wonka.physics.ncsu.edu/pub/VH-1/

Figure 5.6: Contours of the density in the xz-plane (z being the rotation axis) for a prototypical rotating O star with $L_* = 10^6 L_\odot$, $M_* = 52.5 M_\odot$, $R_p = 19 R_\odot$, and $v_{rot} = 432 \, \text{km s}^{-1}$ (corresponding to $\Omega = 0.9$). The density has been scaled by values from the non-rotating model with $\Omega = 0$. While the thick solid line corresponds to the surface of the (distorted) star, the dashed line would correspond to a spherical surface. Additionally, the velocity vectors are displayed. From Hennicker et al. (2019).

Table 5.3: Specific parameters used and obtained for the rotating wind models. For a given stellar luminosity $L_* = 10^6 L_\odot$, stellar mass $M_* = 52.5 M_\odot$, and polar radius $R_p = 19 R_\odot$, rows two to eight display the rotation parameter Ω, the equatorial radius R_{eq}, the polar and equatorial effective temperature $T_{eff,p}$, $T_{eff,eq}$, the total mass loss rate $\dot{M}$, and the polar and equatorial terminal velocity $v_{\infty,p}$, $v_{\infty,eq}$, for different equatorial rotation speeds v_{rot}.

v_{rot} [km s^{-1}]	0	210	294	432
Ω	0	0.5	0.7	0.9
R_{eq} [R_p]	1	1.04	1.09	1.22
$T_{eff,p}$ [kK]	41.84	42.44	43.07	44.66
$T_{eff,eq}$ [kK]	41.84	40.61	39.28	35.20
$\dot{M}$ [$10^{-6} M_\odot \text{yr}^{-1}$]	2.70	2.73	2.79	2.93
$v_{\infty,p}$ [km s^{-1}]	2781	2989	3255	3159
$v_{\infty,eq}$ [km s^{-1}]	2781	2651	2556	2273

radiation hydrodynamic equations (accounting for non-radial line forces) are solved until a (quasi) stationary solution is obtained (see Cranmer & Owocki 1995 and Owocki et al. 1996 for the description of the line force). Assuming azimuthal symmetry, the resulting 2D density and velocity structure is then used as input for our 3D SC code. Table 5.3 summarizes specific parameters used and obtained for our model calculations. While the surface integrated mass flux, $\dot{M}$, becomes only slightly increased with increasing rotational speed, the polar (equatorial) terminal velocities are significantly enhanced (reduced). For the fastest rotating model ($v_{rot} = 432 \, \text{km s}^{-1}$), Fig. 5.6 shows corresponding density contours in the xz-plane. The z-axis is aligned with the rotation axis. To explicitly show the prolate wind structure, we have scaled the density by the density resulting from the non-rotating (spherically
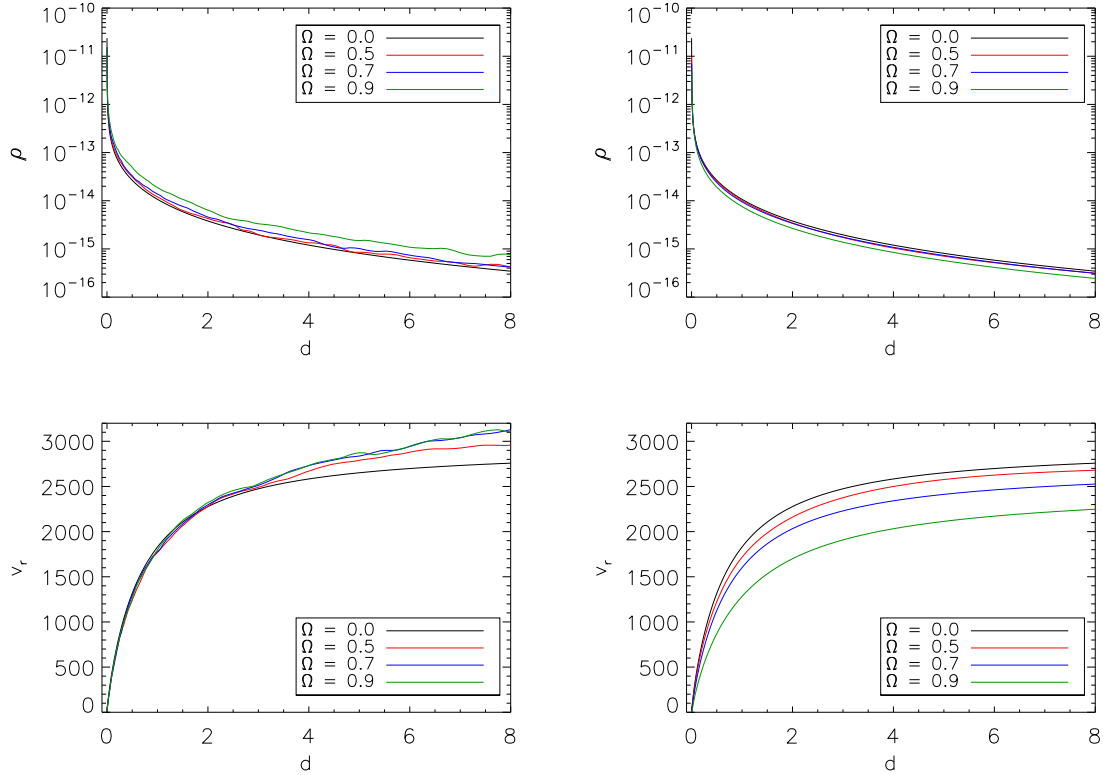
Figure 5.7: Density and radial velocity as a function of distance from the stellar surface in polar (left panels) and equatorial (right panels) regions, for different rotation parameters Ω. From Hennicker et al. (2019).

symmetric) model, as a function of distance from the stellar surface. For different rotational speeds, Fig. 5.7 displays the density and radial velocity along the polar axis and along an (arbitrarily defined) axis in the equatorial plane. When compared with the spherically symmetric wind, the densities of the rotating models are enhanced in polar regions, and become reduced in equatorial ones. Further, the radial velocity along the polar axis remains nearly the same, except in regions far from the star, where the terminal velocity of all rotating models becomes enhanced with increasing v_{rot}. On the other hand, the radial velocity in equatorial regions is significantly reduced at all distances, when compared to the non-rotating wind, and the deviations from spherical symmetry become more pronounced with increasing rotational velocity. Although we have averaged the hydrodynamic simulations over the last 20 time steps, the atmospheric structure still suffers from small numerical artefacts.

To calculate the stellar surface distortion, we consider the gravitational potential of the star accounting for the effects of centrifugal forces. Under reasonable assumptions, we can approximate this potential by a Roche model (e.g., Cranmer & Owocki 1995, see also Sect. 1.2.3 and Eq. 1.3). The surface of the star is then defined on equipotential lines and can be calculated by setting

$\Phi(R_p, \Theta = 0) = \Phi(R_*(\Theta), \Theta)$, with R_p the polar radius. Solving the resulting cubic equation, one finds:

$$\frac{R_*(\Omega, \Theta)}{R_p} = \frac{3}{\Omega \sin(\Theta)} \cos\left(\frac{\pi + \cos^{-1}(\Omega \sin(\Theta))}{3}\right), \tag{5.4}$$

with $\Omega = \omega/\omega_{\mathrm{crit}}$ the ratio of the actual to the critical ('breakup') angular velocity. Defining the rotational speed at the equator, v_{rot}, as input parameter, one easily obtains (cf. Cranmer & Owocki 1995, their Eq. 27):

$$\Omega = \frac{v_{\mathrm{rot}}}{R_{\mathrm{eq}}} \frac{1}{\omega_{\mathrm{crit}}} \tag{5.5}$$

$$R_{\mathrm{eq}} = \frac{R_p}{1 - v_{\mathrm{rot}}^2 R_p / 2GM_*}, \tag{5.6}$$

with equatorial radius R_{eq}. Following Maeder & Meynet (2000), we use the actual stellar mass to calculate the equatorial radius and critical velocity, without correcting for Thomson-accelerations. Additionally, we note that our stellar models are well below the Eddington limit ($\Gamma_e \approx 0.5$). Thus, the critical angular velocity is simply given by $\omega_{\mathrm{crit}} = (8GM_*/27R_p^3)^{1/2}$. Instead of using Eq. (5.4) in our final implementation, we approximate the stellar surface by a spheroid with semi-major axes $a = b = R_{\mathrm{eq}}$ and semi-minor axis $c = R_p$:

$$\frac{R_*(\Theta)}{R_p} = \frac{R_{\mathrm{eq}}}{\sqrt{R_p^2 \sin^2(\Theta) + R_{\mathrm{eq}}^2 \cos^2(\Theta)}}. \tag{5.7}$$

Such a formulation greatly simplifies the calculation of the intersection of a given ray with the stellar surface (required for the boundary conditions, see Sect. 3.2.4). For the most extreme test case considered here ($\Omega = 0.9$), the maximum error on $R_*(\Theta)$ due to this approximation is well below the 2%-level, and rapidly decreases for lower rotational velocities.

To calculate the intensity emerging from the stellar core, we set $I_c^+(\Theta) = B_\nu(T_{\mathrm{eff}}(\Theta))$, with the effective temperature as a function of co-latitude. For a given luminosity of the star, L_*, we obtain (see also Petrenz & Puls 1996):

$$T_{\mathrm{eff}}(\Theta) = \left[\frac{L_*}{2\pi\sigma_B \Sigma} |g|^{4\beta_Z}\right]^{1/4} \tag{5.8}$$

$$\Sigma = \int_0^\pi |g|^{4\beta_Z} \frac{R_*^2(\Theta) \sin(\Theta)}{-g_r/|g|} d\Theta,$$

with σ_B the Stefan Boltzmann constant, and the surface integrated effective gravity Σ derived from $g(\Theta) = -\nabla\Phi(R_*(\Theta), \Theta)$. The parameter β_Z describes the gravity darkening law in terms of $T_{\mathrm{eff}}(\Theta) \propto |g(\Theta)|^{\beta_Z}$. As originally formulated by von Zeipel (1924), $\beta_Z = 1/4$. Though β_Z might be lower (e.g., Domiciano de Souza et al. 2014, Gagnier et al. 2019), for simplicity we nevertheless used $\beta_Z = 1/4$. As long as we assume constant ionization fractions and a predefined hydro-model (which strongly depends on β_Z), the effect of β_Z on the line profiles will be minor anyway, at least if the von-Zeipel parameter is not too far from its original value (as to be expected in radiative envelopes).
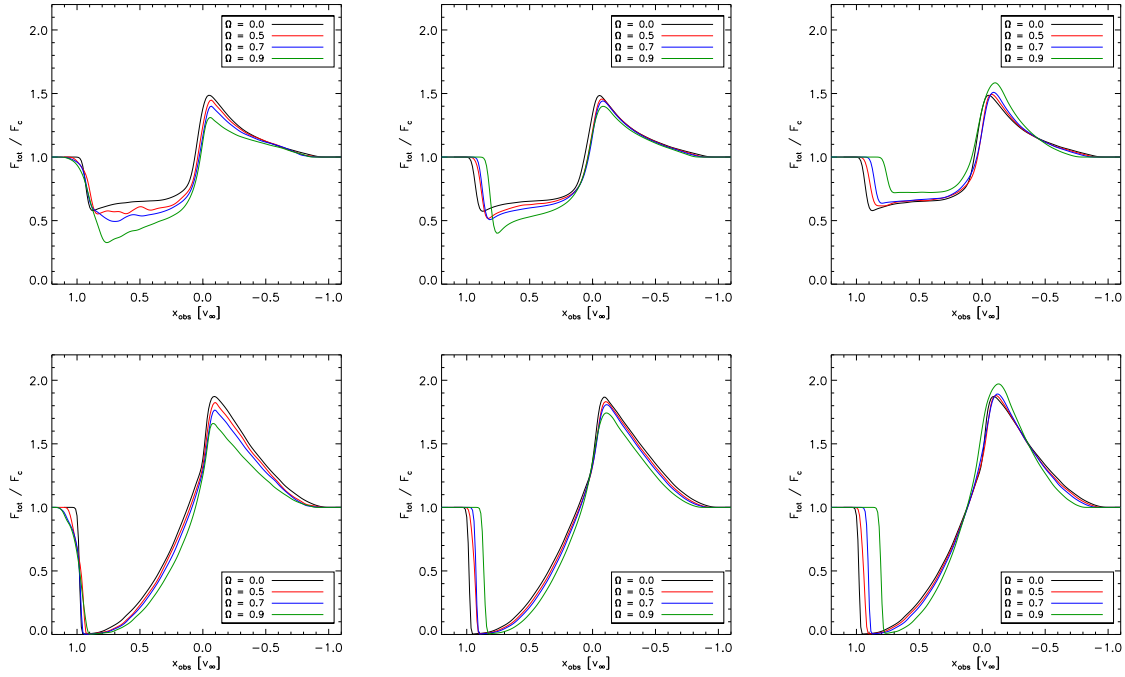
Figure 5.8: Predicted emergent flux profiles for the rotating star models with $\Omega = [0, 0.5, 0.7, 0.9]$ (see Table 5.3). The upper and lower panels show the intermediate and strong line with $k_{\mathrm{L}} = 10^3$ and $k_{\mathrm{L}} = 10^5$, respectively. The inclination angle has been set to $\sin(i) = [0, 0.707, 1]$ from left to right. From Hennicker et al. (2019).

5.3.2 Line formation

For our test models, we use $v_{\mathrm{micro}} = 100\,\mathrm{km\,s^{-1}}$, and calculate the frequency integrated opacity from Eq. 2.61 for an intermediate and a strong line with line-strength parameter $k_{\mathrm{L}} = 10^3$ and $k_{\mathrm{L}} = 10^5$. To obtain the source function, we apply the 3D SClin method and set $\epsilon_{\mathrm{L}} = 10^{-6}$. The resulting (normalized) line profiles are shown in Fig. 5.8 for different rotational velocities and inclination angles. Additionally, we display the continuum flux used for normalization in Fig. 5.9. Due to gravity darkening and surface distortion, the continuum depends on the rotation rate and inclination, with largest fluxes found for high rotation rates and low inclinations (resulting from the higher temperatures in polar regions and a larger projected stellar disc). In Figs. 5.8 and 5.9, the x-axes have been normalized to an (arbitrarily chosen) terminal velocity $v_\infty = 3000\,\mathrm{km\,s^{-1}}$.

The behaviour of the line profiles can be qualitatively explained with the hydrodynamic structure:

(i) For pole on observers ($\sin(i) = 0$, left panel of Fig. 5.8), the absorption column in front of the star is enhanced with increasing rotational velocity due to the larger densities (and opacities) in polar regions. Thus, the absorption trough (of unsaturated lines) becomes more pronounced. The absorption edge of the intermediate lines is found at slightly lower velocities than expected from the hydrodynamic simulations, because the optical depths of the corresponding resonance regions are too low to efficiently contribute to the absorption. When considering the strong

lines, the optical depth is larger, and the absorption edge is more consistent with the actual terminal velocity. For both applied line strength parameters, the emission peak becomes weaker with increasing rotation rate, particularly at low projected velocities on the red side of the line centre (for negative x_{obs}). This effect can be partly explained by the reduced emission from the equatorial plane, due to the lower densities in these regions. More importantly, however, is the increased continuum flux that mainly determines the (normalized) height of the emission peak.

(ii) When increasing the inclination towards equator-on observers ($\sin(i) = 1$, right panel of Fig. 5.8), the behaviour is reversed. For such directions, the continuum plays an only minor role, since the lower (equatorial) effective temperatures of the rotating models are nearly compensated by the enlarged projected stellar disc. With increasing rotation parameter, the absorption trough of the intermediate line becomes reduced and shifted towards lower terminal velocities, consistent with the hydrodynamical model. When considering the strong line, the absorption becomes saturated, and only the impact of the different terminal velocities can be observed. Additionally, and for both line strengths, the absorption slightly extends towards the red side, because of (negative) projected line of sight velocities near the stellar surface induced by rotation. For the fastest rotating model with $\Omega = 0.9$, this effect becomes suppressed due to an increased emission from the (dense) prolate wind structure. This latter effect is only moderate for lower rotational speeds.

Based on the current hydrodynamic wind structure, we would therefore expect to observe either rather low terminal velocities or relatively deep absorption troughs for fast rotating stars, and we are able – at least in principle – to check the theory by comparing our synthetic spectra with (past or future) UV observations, planned for the future.

Finally, if the projected rotational velocity is known (e.g., measured from the broadening of photospheric lines in the optical), one might even estimate the actual rotational velocity from UV resonance lines. This latter point becomes clear from Fig. 5.10, where we predict the line profiles of models with different rotational speed for a given $v\sin(i)$ (set here to $200\,\mathrm{km\,s^{-1}}$). Since, at least for the intermediate line, the profile shapes differ, $\sin(i)$ could be derived if $v\sin(i)$ was known. Of course, such constraints will become feasible only if the underlying models correctly describe the wind structure (including possibly varying ionization stages) of rotating stars.

5.4   Summary[11]

In this Chapter, we applied our 3D radiative transfer code to first non-spherical problems, in order to answer specific questions related to current research, and to show the capabilities of our numerical tools.

As a first application to continuum-scattering problems, we estimated the radiation temperatures of wind-ablation models, focussing on the transition region between a line-driven wind and the optically thick circumstellar disc (as present during the late phases of massive star formation in accreting high mass stars). We found a reduction of radiation temperatures by only few percent, which indicates

---

[11] based on Hennicker et al. (2018, Sect. 7), and Hennicker et al. (2019, Sect. 6).
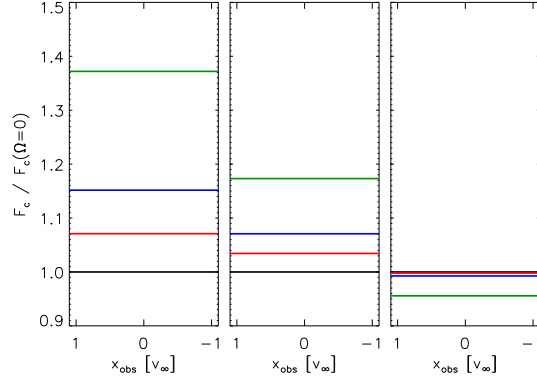
Figure 5.9: Continuum fluxes for different inclinations $\sin(i) = [0, 0.707, 1]$ from left to right, and different rotation parameters (using the same color coding as in Fig. 5.8). The continuum fluxes have been scaled by the corresponding flux obtained from the non-rotating model. From Hennicker et al. (2019).
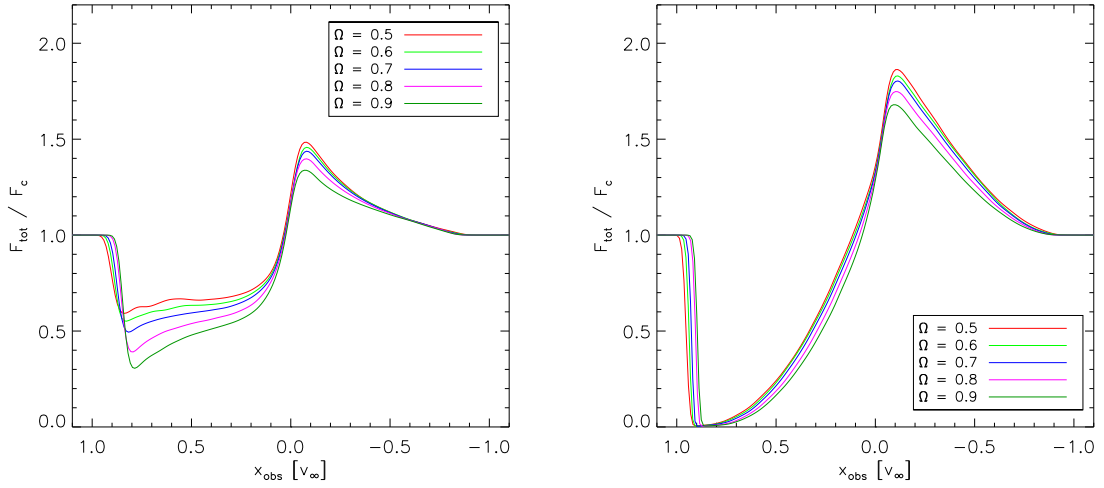
Figure 5.10: Predicted emergent flux profiles for the rotating star models with $\Omega = [0.5, 0.6, 0.7, 0.8, 0.9]$, and different inclination angles such that $v\sin(i) = 200\,\mathrm{km\,s^{-1}}$ for all models. The left and right panels display the intermediate ($k_L = 10^3$) and strong ($k_L = 10^5$) line, respectively. From Hennicker et al. (2019).

that the ionization stages in this region should be (almost) the same as in the wind. Thus, a line-distribution formalism with the same set of line-strength parameters as used in the wind can be applied to obtain the line acceleration that finally ablates the disc. To analyse the complete evolution of optically thick circumstellar discs, the impact of continuum scattering on latitudinal forces still needs to be investigated, and is left to future studies.

As a benchmark for our 3D FVM code regarding the line transfer in non-spherical models, we considered the same MHD simulations of dynamical magnetospheres as used by Marcolino et al.

(2013), and compared the resulting UV resonance-line profiles to those obtained from their 3D-SEI analysis. The profiles as viewed both polar-on and equator-on are in excellent agreement. These findings validate the 3D-SEI method for such atmospheric models, and further indicate that also our 3D FVM performs well. We emphasize that for more complex problems (e.g., when accounting for line overlaps of resonance doublets or multiplets), the SEI method becomes complex, and the 3D FVM presumably is advantageous for calculating corresponding line transitions.

We additionally applied the analytic dynamical magnetosphere framework (ADM, Owocki et al. 2016), and modelled the atmospheric structure by adopting four different descriptions of the closed-field regions (where the magnetic-field energy exceeds the wind kinetic energy). A comparison between the obtained line profiles and those for the MHD simulations from above showed significant differences. These were explained by the (somewhat insufficient) description of the outer wind region within the (present) ADM formulation, primarily in the equatorial plane. An improvement of the underlying assumptions is planned for future work.

As a first application of the 3D SC code to non-spherical problems, we considered the resonance-line formation in the winds of (fast) rotating O stars. Assuming azimuthal symmetry, the hydrodynamic structure for a prototypical O star with different rotation rates has been calculated by means of the 2D VH-1 code. We have included the effects of surface distortion and gravity darkening into our 3D radiative transfer framework. Given the hydrodynamic models, we are able to predict the shape of line profiles for different rotational speeds and inclination angles. When compared with a (non-rotating) spherically symmetric wind (obtained using the same stellar parameters), rotating stars should either show relatively low terminal velocities (for equator-on observers) or deeper absorption troughs (for pole-on observers). The latter effect, however, would only be observable when considering intermediate (i.e., unsaturated) lines. Additionally, we showed that the line profile shapes vary as a function of rotational speed at a given $v\sin(i)$. Thus, assuming that $v\sin(i)$ was known (e.g., from photospheric line modelling), one could estimate the rotational speed, though with a rather large uncertainty, since the differences of the line profiles are only moderate. We emphasize that other effects (such as clumping or a flatter gravity darkening law) may additionally shape the line profiles. When analysing UV observations of fast rotating stars, the 3D radiative transfer code developed in this work certainly will help to understand the manifestations of various (aforementioned) effects, and to distinguish between different theoretical predictions (e.g., prolate vs. oblate wind structures).

Chapter 6

Summary and outlook

As outlined in Chapter 1, a detailed understanding of hot, massive stars is required – among other topics – to explain the feedback of kinetic energy, radiation, and nuclear processed material to their host galaxies during all evolutionary stages. To push theory forward, a quantitative description of radiative transfer is required for both hydrodynamical modelling and calculating synthetic spectra. Nowadays, the physics within 1D spherically symmetric models is relatively well understood, whereas non-spherical effects need to be analysed with more elaborate, multi-D tools.

In this thesis, we have developed a 3D radiative transfer code, which, in its current state, is able to calculate both the UV resonance-line formation and a (simplified) continuum, in rapidly expanding stellar atmospheres (e.g., in the winds of hot, massive stars). We have implemented two independent methods, the finite-volume method and the short-characteristics method, which differ in required computation time, and in obtained accuracy. For both solution schemes, we have performed extensive tests. Additionally, we have applied our code to first non-spherical problems, related to wind ablation, rapidly rotating winds, and dynamical magnetospheres. For a more detailed discussion about the implementation, testing, and first applications of the code, we refer to the individual chapter summaries, Sect. 3.8, Sect. 4.3, and Sect. 5.4, respectively.

In the following, we give an outlook on future projects and plans related to this work, by discussing further applications and improvements of our 3D code.

6.1   Further applications

In Sect. 5.2, we have shown that a simplified description of (slowly rotating) magnetic winds by the analytic dynamical magnetosphere framework cannot reproduce the expected line profiles, when compared with magneto-hydrodynamic models. To avoid such elaborate MHD simulations, the ADM model needs to be modified. In this respect, the outer wind regions are of prime importance, as shown in Sect. 5.2.2. To extend the ADM, the magnetic-field lines in such regions need to be re-arranged (quasi)-radially, and in such a way that the complete outer wind is 'automatically' described by only few input parameters, e.g., the magnetic-field strength and terminal velocity at the magnetic pole, B_{pole}, $v_\infty^{(\mathrm{pole})}$, and the mass-loss rate of the star if there was no magnetic field present, $\dot{M}_{\mathrm{B=0}}$. Ideally then, also the latitudinal variation of mass flux and terminal velocity, $\dot{m}(\Theta)$ and $v_\infty(\Theta)$, would be-

come properly specified for a large parameter space. To validate the (still to be developed) modified ADM model, one could compare the atmospheric structure with (time-averaged) MHD simulations (which might themselves suffer from specific numerical inaccuracies), or rate the synthetic line profiles against observations. Our 3D code can easily provide such synthetic line profiles for various wind models. Since, however, UV resonance lines typically appear as multiplets[1], as a first, immediate, and presumably relatively simple objective for future studies, we aim at extending our resonance-line description (thus far only implemented for singlets) to include resonance doublets.

With the extension to doublet-lines, also rapidly rotating OB stars can be studied in more detail. For a better understanding of the wind from such objects, corresponding observations for a wide range of rotational properties and spectral types would be required. ‡Ideal testbeds for future investigations of fast rotating winds are the stars VFTS102 (O9 Vnnne, Dufton et al. 2011) and VFTS285 (O7.5 Vnnn, Walborn et al. 2012), both rotating at nearly their critical velocity.‡ As a first step, we could then model synthetic line profiles, focussing on the different description of prolate vs. oblate wind structures, and on various gravity-darkening prescriptions (e.g., von-Zeipel model with different β_Z exponents, or the ω-model). Unfortunately, however, high signal-to-noise observations of rapidly rotating OB stars in the UV spectral range are rare (if such observed spectra exist at all), and will neither be provided in the near future (at least for the required large parameter space), due to missing UV capabilities of next-generation telescopes. We therefore aim at extending our code to calculate synthetic line profiles also in the optical regime (e.g., to predict the H_α line, see Sect. 6.3 regarding future developments), where many more observations exist. To this end, we will need to implement multi-level atoms in the near future. We note, that current H_α-modelling in rapidly rotating stars is typically performed by adopting the level populations from 1D calculations, and using a multi-D formal solution to calculate the synthetic line profiles. A comparison of this simplified (and thus less time consuming) approach with consistent 3D level populations is also planned for future studies.

Another topic of interest is the impact of clumping on the line formation in the atmospheres of hot stars. State-of-the art (1D) modelling relies on a statistical 1D description of the clump distribution, discarding inhomogeneities of the velocity field, and the angular distribution of the clumped and inter-clump medium (porosity). Since, however, clumping severely affects the line diagnostics of both recombination lines (most importantly, H_α) and UV resonance lines, a correct treatment of the structured wind is urgently needed. With our 3D radiative transfer solver, we are able to test various clumping prescriptions via synthetic UV line profiles, accounting for porosity effects and for inhomogeneities of the velocity field. Due to the small length scale of clumps, however, such investigations require low micro-turbulent velocities, and thus become challenging for our solution methods in terms of computation time. Before turning towards the investigation of different clumping scenarios, we therefore aim at certain numerical improvements of our code (see Sect. 6.2). Furthermore, different clumping approaches should also be compared via H_α, again indicating the importance for implementing multi-level atoms within our 3D framework (see Sect. 6.3).

‡Finally, we note that our tools are, of course, not limited to magnetic or rotating stars. Indeed, almost any kind of stellar outflows that deviate from spherical symmetry (with non-relativistic velocity fields) can be investigated‡, e.g., to address open questions related to colliding winds in close binaries,

---

[1] In most cases, the lower state consists of two fine-structure levels.

the impact of (non-radial) pulsations on the resonance-line formation, or to large-scale variability induced by co-rotating interaction regions.

Besides the above mentioned applications with respect to spectrum synthesis, we plan to extend the tools developed in this thesis, such that the non-local coupling of the radiation field with all flow variables can be incorporated within multi-D hydrodynamic solution methods (see Sect. 6.3). Among many other problems, we can then investigate, e.g., the impact of latitudinal line-force components on the wind in accreting high-mass stars.

6.2   Numerical improvements

A major drawback of 3D radiative transfer methods (as developed in this thesis, and in general) is the required computation time. In the (near) future, we will therefore develop a parallelization strategy that is suitable also for 'super-computers'. Additionally, we plan to implement specific numerical improvements that reduce the number of required floating point operations, while still enabling a reasonable accuracy.

Achieving this objective, however, is difficult, because the minimum number of spatial grid points, and of the frequency and angular integration nodes, is basically fixed, in order to resolve all resonance zones with corresponding profile functions, and to obtain an accurate angular integration. The latter might be improved, noting that any (accurate) angular integration scheme – at least for optically thin continua – has to resolve the central star and its edges at each point in the atmosphere. This circumstance constitutes the major difficulty within the FVM and SC method, since the specific intensity for a given direction at a considered grid point depends on the intensity at the neighbouring points. Thus, in contrast to the LC method (where the intensities at all grid points can be calculated independently for each direction), the angular grid needs to be defined globally, yielding a resolution of 'only' $\Delta\theta \approx \Delta\phi \approx 6°$ even for $N_\Omega \approx 2000$ directions. For future studies, we therefore aim at implementing and testing a mixed scheme, where the major part of the radiative transfer consists of the FVM/SC method using only 'few' N_Ω directions (on the order of few hundreds), extended by a LC method with $N_\Omega^{(LC)}(x,y,z) \approx 20$ directions independently defined for each grid point, such that the central star and its edges become resolved. This way, we might be able to reduce the computation time, while potentially even improving the accuracy. We note, however, that such an approach can only be applied to the continuum transport, since the line profile at each spatial grid point and each frequency node needs to be resolved by the angular grid.

In this respect, also the reduction of micro-turbulent velocities (as required for analysing different clumping laws) poses a severe problem. Probably, solving this issue without a 'brute-force' approach by increasing the number of frequency and angular integration nodes, will turn out to be complex, if possible at all. Particularly when accounting for a multitude of lines, low micro-turbulent velocities are presumably not feasible in terms of computation time, except for super-computers.

Another problem that still needs to be solved is the violation of flux conservation introduced by numerical diffusion and the order of accuracy within the FVM and SC methods (Sect. 4.2.4). To tackle this issue, we might implement and formulate the SC method on a spherical grid[2], and investigate in

---

[2] We remind that the FVM is difficult to formulate in spherical coordinates (Sect. 2.2.7). Furthermore, since the flux-

how far numerical diffusion affects the finally obtained solution for such coordinate systems. At least if the stellar surface and wind-structure is 'almost' spherical (e.g., for non-magnetic, homogeneous winds with only moderate rotation rates), a curved grid certainly becomes advantageous to describe all flow variables. We emphasize, however, that the solution scheme becomes computationally expensive, by introducing additional angular interpolations for the upwind intensities (which still give rise to numerical diffusion and are intrinsic to any SC solution scheme). To avoid any numerical diffusion errors, which are tightly coupled with the flux-conservation problem, we therefore might have to implement the LC method, combined with a suitable parallelization strategy. In this case, also the angular integration could be significantly improved, by defining suitable directions that depend on the considered grid points.

6.3   Future developments

The long-term objective of our work is the development of a 3D atmosphere code, that incorporates – similarly to state-of-the art 1D spectral synthesis tools – the full NLTE rate equations, in order to obtain a consistent solution for the radiation field and the level populations in arbitrary stellar atmospheres. To test the basic methods for solving the radiative transfer including scattering, in this thesis we presented a first step towards such models by adopting a two-level-atom approach and a simplified continuum. The obvious next step is the combination of the continuum and the line transition, to correctly treat the radiative transfer when continuum- and line-opacities are of the same order (e.g., in the line wings). Additionally, this description will serve as a test case for the accelerated Λ-iteration scheme when including a multitude of lines with line overlaps. When all tests have been passed, we plan to successively implement several multi-level atoms (for which the formal solution of the radiative transfer equation should pose no major problem), focussing on the calculation of new level populations via the NLTE rate equations coupled with a non-local ALI scheme. Storing the level populations for a multitude of elements, each possessing a (potentially) large number of levels, might become problematic in terms of memory capacity though.

Furthermore, we additionally need to account for a consistent description of the photosphere and the transition to the wind, due to the typically strongly varying formation depths of different line transitions. Thus, including a (reasonable) photospheric model is also planned for the future. In this respect, the major problem arises from the small scale height of the photosphere, therefore requiring a rather high resolution in the deep atmospheric layers. As a first step, we plan to include the photosphere with a 'brute-force' approach by applying a high resolution, provided either by mesh-refinement methods, or with a highly resolved spherical grid. For a distorted photosphere (as found in, e.g., rapidly rotating stars), however, the formulation in spherical coordinates might loose its advantage in describing the flow variables. Furthermore, the formulation of the FVM and SC methods would become complex (see the discussion in Sect. 6.2). Alternatively, we will test to sample the photosphere by several planar patches distributed over the complete surface. Within the latter approach, curvature effects within the photosphere are discarded, and the outer boundary conditions need to be provided from the wind

---

conservation problem within the FVM is primarily introduced by the low-order solution scheme (which cannot be circumvented), we only discuss the SC method in the following.

regime.

Another project we are aiming at is the coupling of our 3D radiative transfer solver with hydro-dynamic solution schemes, in order to consistently solve the radiation-hydrodynamic equations in various kinds of hot-star atmospheres. In this respect, the major difficulty is introduced by the non-local character of the radiation field in scattering dominated environments. A detailed treatment of the non-local radiation field is usually prohibitive within hydrodynamic simulations, due to the immense computational effort. Thus, current radiation-hydrodynamic codes typically rely on purely local ex-pressions for all radiation variables (such as the radiative flux, and the radiative forces) by, e.g., apply-ing the Sobolev method for calculating line forces in (optically thin) rapidly expanding winds, or by describing the radiation field via 'flux-limited diffusion' (FLD)[3] when continuum processes contribute most to the radiation pressure. To validate (or falsify) the FLD approach for scattering dominated at-mospheres, we plan to extend our continuum radiative-transfer solver to a (still simplified) description over the complete frequency range, and to couple the developed tools with specific hydrodynamics codes (e.g., MPI-AMRVAC developed at KU Leuven, see Keppens et al. 2003, Porth et al. 2014, Xia et al. 2018). By a comparison of our 3D radiative transfer with the FLD approach, we will be able to understand potential shortcomings of the FLD in more detail, and might even calibrate the FLD such that it is still applicable also at intermediate optical depths and in scattering dominated environments. The finally developed radiation-hydrodynamics modules could then be used, e.g., to model, for the first time, the violent eruptions as observed in Luminous Blue Variables (presumably originating from inhomogeneous, porous, continuum-driven winds). With the tools presented here (and further devel-oped in the future), we will thus be able to understand many open questions related to mass loss from porous atmospheres and continuum-driven outbursts, which, in turn, will provide a better constraint on, e.g., kinetic energy and radiative feedback, and the end products of nearby and distant (Pop III) stars.

Of course, there is still a long way to go, until fully consistent 3D NLTE models can either be applied to the spectrum synthesis of hot, massive stars, or can be coupled with multi-D hydrodynamic solution schemes. The first step, however, has been taken in this thesis work, and the way 'only' needs to be followed until its end.

---

[3] Within FLD, the radiative transport is treated as a diffusive process reproducing the correct limiting cases for optically thick and optically thin environments. When scattering processes play a significant role, and in the transition regime from optically thin to optically thick layers, this approach might have to be revised.

Appendix A

3D Sobolev method

In this chapter, we derive the 3D Sobolev method[1] for calculating resonance-line transitions (in the absence of a background continuum) following Rybicki & Hummer (1978). For this method, we consider the equation of radiative transfer as given in Eq. (2.47), and assume the line opacity to be given by a frequency-independent part and the (normalized) profile function, $\chi_\nu = \bar{\chi}\Phi_\nu$ (e.g., Eq. 2.28). For any point $\boldsymbol{r}$ under consideration, the specific intensity for a given observer's frame frequency ν can then be calculated as:

$$
\begin{aligned}
I_\nu(\boldsymbol{r}) \quad = \quad & I_{\text{inc}} \exp\Big[-\underbrace{\int_0^{\Delta s} \bar{\chi}(s)\Phi_\nu(s)\mathrm{d}s}_{\text{(I)}}\Big] \\
+ \quad & \exp\Big[-\underbrace{\int_0^{\Delta s} \bar{\chi}(s)\Phi_\nu(s)\mathrm{d}s}_{\text{(I)}}\Big] \cdot \underbrace{\int_0^{\Delta s} S_{\text{L}}(s)\exp\Big[\underbrace{\int_0^s \bar{\chi}(s')\Phi_\nu(s')\mathrm{d}s'}_{\text{(II)}}\Big]\bar{\chi}(s)\Phi_\nu(s)\mathrm{d}s}_{\text{(III)}},
\end{aligned}
\qquad \text{(A.1)}
$$

where the geometry of the problem is shown in Fig. A.1. To proceed further, we define the Sobolev length as the length over which the comoving-frame frequency changes by one Doppler width, $\Delta\nu_{\text{D}}$, or, in other words, as the length over which the projected velocity changes by v_{th}:

$$
\Delta\nu_{\text{D}} = \nu_{ij}\frac{\Delta(\boldsymbol{nv})}{c} =: \frac{\nu_{ij}}{c}\frac{\mathrm{d}(\boldsymbol{nv})}{\mathrm{d}s}\Delta s_{\text{Sobo}} \quad\Longleftrightarrow\quad \Delta s_{\text{Sobo}} = \frac{1}{\dfrac{\mathrm{d}(\boldsymbol{nV})}{\mathrm{d}s}},
\qquad \text{(A.2)}
$$

where $\boldsymbol{V}$ is the velocity vector normalized to the thermal velocity. In the following, we consider the variation of the intensity along a ray, $I_\nu(\boldsymbol{r})$, in the vicinity of a resonance region $\boldsymbol{r}_0$ with interaction length defined by the Sobolev length. For steep velocity gradients, Sobolev (1960) noted that the (frequency integrated) opacity and the source function along the ray can be assumed to be constant over the interaction region, yielding $\bar{\chi}(s) \approx \bar{\chi}(\boldsymbol{r}_0) = \text{const.}$ and $S_{\text{L}}(s) \approx S_{\text{L}}(\boldsymbol{r}_0) = \text{const.}$. When additionally approximating the projected velocity along the ray by a linear function (at least within the contributing

---

[1] The 1D Sobolev method in spherically symmetric, rapidly expanding atmospheres can be deduced from the 3D description by simply replacing the required derivative of the projected velocity along a ray by the corresponding spherical term.
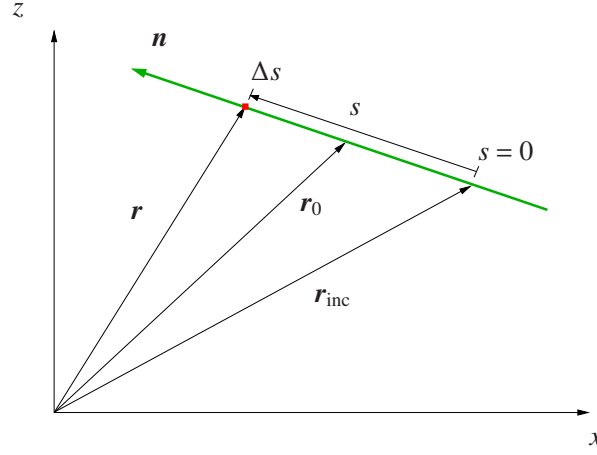
Figure A.1: Geometry for deriving the 3D Sobolev approximation at a given point $\boldsymbol{r}$ indicated by the red dot with a resonance point $\boldsymbol{r}_0$. The path length s is measured along a given ray with $s := 0$ at the beginning of the ray. Adapted from Rybicki & Hummer (1978).

resonance region), and using a Doppler profile for describing the profile function, Eq. (A.1) can be solved analytically. The optical depth integrals yield:

$$(\text{I}) \approx \int_0^{\Delta s} \bar{\chi}(s')\Phi_\nu(s')\mathrm{d}s' = \frac{\bar{\chi}(\boldsymbol{r}_0)}{\sqrt{\pi}\Delta\nu_\mathrm{D}} \int_0^{\Delta s} \exp\left[-\left(\frac{\nu-\nu_{ij}}{\Delta\nu_\mathrm{D}} - V_n(\boldsymbol{r}_0) + \left.\frac{\mathrm{d}V_n}{\mathrm{d}s}\right|_{\boldsymbol{r}_0}\Delta s_0 - \left.\frac{\mathrm{d}V_n}{\mathrm{d}s}\right|_{\boldsymbol{r}_0} s'\right)^2\right]\mathrm{d}s'$$
(A.3)

$$(\text{II}) \approx \int_0^{s} \bar{\chi}(s')\Phi_\nu(s')\mathrm{d}s' = \frac{\bar{\chi}(\boldsymbol{r}_0)}{\sqrt{\pi}\Delta\nu_\mathrm{D}} \int_0^{s} \exp\left[-\left(\frac{\nu-\nu_{ij}}{\Delta\nu_\mathrm{D}} - V_n(\boldsymbol{r}_0) + \left.\frac{\mathrm{d}V_n}{\mathrm{d}s}\right|_{\boldsymbol{r}_0}\Delta s_0 - \left.\frac{\mathrm{d}V_n}{\mathrm{d}s}\right|_{\boldsymbol{r}_0} s'\right)^2\right]\mathrm{d}s',$$
(A.4)

where V_n is the projected velocity along the ray, and $\Delta s_0 = |\boldsymbol{r}_\mathrm{inc} - \boldsymbol{r}_0|$. Defining x as the argument of the profile function:

$$x = \frac{\nu-\nu_{ij}}{\Delta\nu_\mathrm{D}} - V_n(\boldsymbol{r}_0) + \left.\frac{\mathrm{d}V_n}{\mathrm{d}s}\right|_{\boldsymbol{r}_0}\Delta s_0 - \left.\frac{\mathrm{d}V_n}{\mathrm{d}s}\right|_{\boldsymbol{r}_0} s' \iff \mathrm{d}x = -\left.\frac{\mathrm{d}V_n}{\mathrm{d}s}\right|_{\boldsymbol{r}_0}\mathrm{d}s'$$
(A.5)

$$x(0) = \frac{\nu-\nu_{ij}}{\Delta\nu_\mathrm{D}} - V_n(\boldsymbol{r}_0) + \frac{\Delta s_0}{\Delta s_\mathrm{Sobo}(\boldsymbol{r}_0)} \overset{\Delta s_\mathrm{Sobo}\to 0}{\longrightarrow} \infty$$
(A.6)

$$x(s) = t$$
(A.7)

$$x(\Delta s) = t_r = \frac{\nu-\nu_{ij}}{\Delta\nu_\mathrm{D}} - V_n(\boldsymbol{r}_0) + \left.\frac{\mathrm{d}V_n}{\mathrm{d}s}\right|_{\boldsymbol{r}_0}\Delta s_0 - \left.\frac{\mathrm{d}V_n}{\mathrm{d}s}\right|_{\boldsymbol{r}_0}\Delta s,$$
(A.8)

we finally obtain:

$$(\text{I}) = \tau_\mathrm{Sobo}\frac{1}{\sqrt{\pi}}\int_{t_r}^{\infty} \mathrm{e}^{-x^2}\mathrm{d}x = \tau_\mathrm{Sobo}\frac{1}{2}\mathrm{erfc}(t_r) := \tau_\mathrm{Sobo}w(t_r)$$
(A.9)

$$(\text{II}) = \tau_\mathrm{Sobo}\frac{1}{\sqrt{\pi}}\int_{t}^{\infty} \mathrm{e}^{-x^2}\mathrm{d}x = \tau_\mathrm{Sobo}\frac{1}{2}\mathrm{erfc}(t) := \tau_\mathrm{Sobo}w(t),$$
(A.10)

with the complementary error function erfc(t), and the Sobolev optical depth $\tau_{\text{Sobo}} :=$ $\bar{\chi}(\mathbf{r}_0)/(\Delta\nu_{\text{D}}\,\mathrm{d}V_n/\mathrm{d}s)$. The Sobolev optical depth describes the typical line optical depth at a given point $\mathbf{r}_0$ after the ray has passed the complete resonance zone, and can become - depending on the considered line transition - very large. We emphasize that τ_{Sobo} is independent of the profile width, since the thermal velocity used for normalization of the projected velocity cancels with the Doppler width. Using the same substitution as defined in Eqs. (A.5)-(A.8), the source integral (III) yields after some algebra:

$$\text{(III)} = S_{\text{L}}(\mathbf{r}_0)\tau_{\text{Sobo}}\frac{1}{\sqrt{\pi}}\int_{t_r}^{\infty}\mathrm{e}^{\tau_{\text{Sobo}}w(t)}\mathrm{e}^{-t^2}\mathrm{d}t = S_{\text{L}}(\mathbf{r}_0)\left(\mathrm{e}^{\tau_{\text{Sobo}}w(t_r)}-1\right). \tag{A.11}$$

Inserting Eqs. (A.9)-(A.11) into the original equation, we finally obtain for the specific intensity at a point $\mathbf{r}$ with given observer's frame frequency such that $\mathbf{r}_0$ is a resonance point:

$$I_\nu(\mathbf{r}) = I_{\text{inc}}\mathrm{e}^{-\tau_{\text{Sobo}}w(t_r)} + S_{\text{L}}(\mathbf{r}_0)\left(1 - \mathrm{e}^{-\tau_{\text{Sobo}}w(t_r)}\right), \tag{A.12}$$

$$w(t_r) = \frac{1}{2}\text{erfc}(t_r) = \frac{1}{2}\text{erfc}\left(\frac{\nu-\nu_{ij}}{\Delta\nu_{\text{D}}} - V_n(\mathbf{r}_0) + \left.\frac{\mathrm{d}V_n}{\mathrm{d}s}\right|_{\mathbf{r}_0}\Delta s_0 - \left.\frac{\mathrm{d}V_n}{\mathrm{d}s}\right|_{\mathbf{r}_0}\Delta s\right), \tag{A.13}$$

$$\tau_{\text{Sobo}} = \frac{c\bar{\chi}(\mathbf{r}_0)}{\nu_{ij}|\mathrm{d}v_n/\mathrm{d}s|_{\mathbf{r}_0}}. \tag{A.14}$$

Thus, if the comoving-frame frequency is much larger than the transition frequency, e.g., if considering a position $\mathbf{r}$ in front of the resonance zone with $V_n(\mathbf{r}) \ll V_n(\mathbf{r}_0)$, then $t_r \to \infty$, $w(t_r) \to 0$, and thus $I_\nu(\mathbf{r}) \to I_{\text{inc}}$, as required. Similarly, for positions behind the resonance region where the comoving-frame frequency is much smaller than the line-transition frequency, e.g., if $V_n(\mathbf{r}) \gg V_n(\mathbf{r}_0)$, then $t_r \to -\infty$, $w(t_r) \to 1$, and $I_\nu(\mathbf{r}) \to I_{\text{inc}}\mathrm{e}^{-\tau_{\text{Sobo}}(\mathbf{r}_0)} + S_{\text{L}}(\mathbf{r}_0)\left(1 - \mathrm{e}^{-\tau_{\text{Sobo}}(\mathbf{r}_0)}\right)$. Thus, the intensity at a given point behind the resonance zone depends solely on local quantities at the resonance zone, and on the incident intensity in front of the resonance zone. Of course, these solutions are only valid for monotonic velocity fields, i.e., if only one resonance point is found along the ray.

The variation of the specific intensity along a ray at a given observer's frame frequency can also be expressed as the variation of the specific intensity with frequency at the resonance point $\mathbf{r}_0$. Thus, the scattering integral at $\mathbf{r}_0$ can be obtained by integrating the profile weighted intensity at $\mathbf{r}_0$ over frequency:

$$\begin{aligned}
\bar{I}_\nu(\mathbf{r}_0) &= \int_0^{\infty} I_\nu(\mathbf{r}_0)\Phi_\nu(\mathbf{r}_0)\mathrm{d}\nu \\
&= \frac{1}{\sqrt{\pi}\Delta\nu_{\text{D}}}\int_0^{\infty}\left[I_{\text{inc}}\mathrm{e}^{-\tau_{\text{Sobo}}(\mathbf{r}_0)w(t_r)} + S_{\text{L}}(\mathbf{r}_0)\left(1 - \mathrm{e}^{-\tau_{\text{Sobo}}(\mathbf{r}_0)w(t_r)}\right)\right]\exp\left[-\left(\frac{\nu-\nu_{ij}}{\Delta\nu_{\text{D}}} - V_n(\mathbf{r}_0)\right)^2\right]\mathrm{d}\nu \\
&= \frac{1}{\sqrt{\pi}}\int_{-\infty}^{\infty}\left[I_{\text{inc}}\mathrm{e}^{-\tau_{\text{Sobo}}(\mathbf{r}_0)w(t_r)} + S_{\text{L}}(\mathbf{r}_0)\left(1 - \mathrm{e}^{-\tau_{\text{Sobo}}(\mathbf{r}_0)w(t_r)}\right)\right]\mathrm{e}^{-t_r^2}\mathrm{d}t_r \\
&= \int_0^1 I_{\text{inc}}\mathrm{e}^{-\tau_{\text{Sobo}}(\mathbf{r}_0)w} + S_{\text{L}}(\mathbf{r}_0)\left(1 - \mathrm{e}^{-\tau_{\text{Sobo}}(\mathbf{r}_0)w}\right)\mathrm{d}w \\
&= I_{\text{inc}}\frac{1 - \mathrm{e}^{-\tau_{\text{Sobo}}(\mathbf{r}_0)}}{\tau_{\text{Sobo}}(\mathbf{r}_0)} + S_{\text{L}}(\mathbf{r}_0)\left[1 - \frac{1 - \mathrm{e}^{-\tau_{\text{Sobo}}(\mathbf{r}_0)}}{\tau_{\text{Sobo}}(\mathbf{r}_0)}\right],
\end{aligned} \tag{A.15}$$

where I_{inc} should be evaluated at the line centre, $\nu = \nu_{ij} + V_n \Delta \nu_{\mathrm{D}}$. Eq. (A.15) is a general solution which also holds for non-monotonic velocity fields, since the coupling of different resonance points can be incorporated by identifying I_{inc} with the emergent intensity from a previous resonance region. This non-local coupling, however, severely complicates the calculation of the scattering integral. For simplicity, we only consider monotonic flows in the following, such as found in, e.g., smooth 1D spherically symmetric wind models. Assuming an optically thin background continuum, I_{inc} is simply given by the intensity emerging from the stellar core, I_{c}, if a considered ray originates from the core, and zero else. Since Eq. (A.15) is valid for each r_0, we can replace r_0 by r, and find:

$$\bar{J}(\boldsymbol{r}) = \frac{1}{4\pi} \int \bar{I}(\boldsymbol{r}) \mathrm{d}\Omega = [1 - \beta(\boldsymbol{r})] S_{\mathrm{L}}(\boldsymbol{r}) + \beta_{\mathrm{c}}(\boldsymbol{r}) I_{\mathrm{c}}, \tag{A.16}$$

with

$$\beta(\boldsymbol{r}) = \frac{1}{4\pi} \int_\Omega \frac{1 - \mathrm{e}^{-\tau_{\mathrm{Sobo}}(\boldsymbol{r},\Omega)}}{\tau_{\mathrm{Sobo}}(\boldsymbol{r},\Omega)} \mathrm{d}\Omega, \qquad\qquad \beta_{\mathrm{c}}(\boldsymbol{r}) = \frac{1}{4\pi} \int_{\Omega_{\mathrm{c}}} \frac{1 - \mathrm{e}^{-\tau_{\mathrm{Sobo}}(\boldsymbol{r},\Omega)}}{\tau_{\mathrm{Sobo}}(\boldsymbol{r},\Omega)} \mathrm{d}\Omega,$$

and Ω_{c} corresponding to directions intersecting the stellar core. The Ω-dependence of the Sobolev optical depth is introduced by the gradient of the projected velocity along a given direction. Eq. (A.16) can be used to calculate the source function, e.g., within the two-level-atom approach, $S_{\mathrm{L}} = (1 - \epsilon_{\mathrm{L}}) \bar{J} + \epsilon_{\mathrm{L}} B$, yielding (see also Rybicki & Hummer 1978):

$$S_{\mathrm{L}}(\boldsymbol{r}) = \frac{(1 - \epsilon_{\mathrm{L}}) \beta_{\mathrm{c}}(\boldsymbol{r}) I_{\mathrm{c}} + \epsilon_{\mathrm{L}} B_{\nu_{ij}}}{\epsilon_{\mathrm{L}} + (1 - \epsilon_{\mathrm{L}}) \beta(\boldsymbol{r})}. \tag{A.17}$$

Thus, for monotonic velocity fields, the source function and scattering integral can be calculated within the Sobolev approach from purely local quantities, contrasted to the specific intensity, which, at a considered position $\boldsymbol{r}$ with velocity $\boldsymbol{v}$, depends on the conditions at the resonance zone r_0. We emphasize that also the radiative force becomes a purely local quantity. Within hydrodynamic simulations of rapidly expanding atmospheres, the radiative force exerted by line-scattering and absorption is therefore typically calculated from Sobolev theory.

Appendix B

On the finite-volume methods and stability

In this chapter, we briefly motivate our decision for implementing the (low-order) vertex-centred FVM (Sect. 3.1), by showing that (nearly) all other descriptions of the FVM result in an unstable[1] solution scheme. To this end, we only consider the 1D case, which already illustrates the fundamental problems. A formulation in more dimensions can be applied straight-forward, but is beyond the scope of this discussion. An overview of the stable and unstable finite-volume methods presented in this Chapter is shown in Fig. B.1.

In 1D, the time-independent equation of radiative transfer for a ray propagating along the x-axis, integrated over a control volume, $\mathscr{V}_c$, with surface, $\mathscr{S}_c$, yields:

$$\int_{\mathscr{S}_c} I \, \mathrm{d}\mathscr{S} = \int_{\mathscr{V}_c} \chi(S - I) \, \mathrm{d}\mathscr{V}, \tag{B.1}$$

where the surface integral in 1D reduces to the difference of the specific intensity at the control-volume boundaries, and the volume integral within the cell-centred and vertex-centred FVM is performed over $[x_{i-1}, x_i]$ and $[x_{i-1/2}, x_{i+1/2}]$, respectively. From Eq. (B.1), one can derive various solution schemes, by adopting an (in principle) arbitrary functional behaviour of the opacity, source function, and intensity within the considered volume. In the following, we present different approximations applied within the cell-centred and vertex-centred FVM, respectively, and analyse the corresponding discretized radiative transfer equations with respect to 'stability'. All quantities are assumed to be represented on a discrete grid, $\{x_i\}$.

1D cell-centred FVM with linear interpolations. The simplest approach to solve Eq. (B.1) within the cell-centred FVM, is by applying the Trapezoidal rule. In one dimension, we then find:

$$I_i - I_{i-1} = \int_{x_{i-1}}^{x_i} \chi(S - I) \, \mathrm{d}x \approx (\chi_{i-1}S_{i-1} + \chi_i S_i)\frac{\Delta x}{2} - (\chi_{i-1}I_{i-1} + \chi_i I_i)\frac{\Delta x}{2}, \tag{B.2}$$

---

[1] Strictly speaking, the term 'numerical stability analysis' refers to the growth/decay of disturbances by the discretization scheme applied to differential equations. Here, we define an 'unstable' solution method as a numerical scheme that potentially results in negative – thus unphysical – specific intensities.
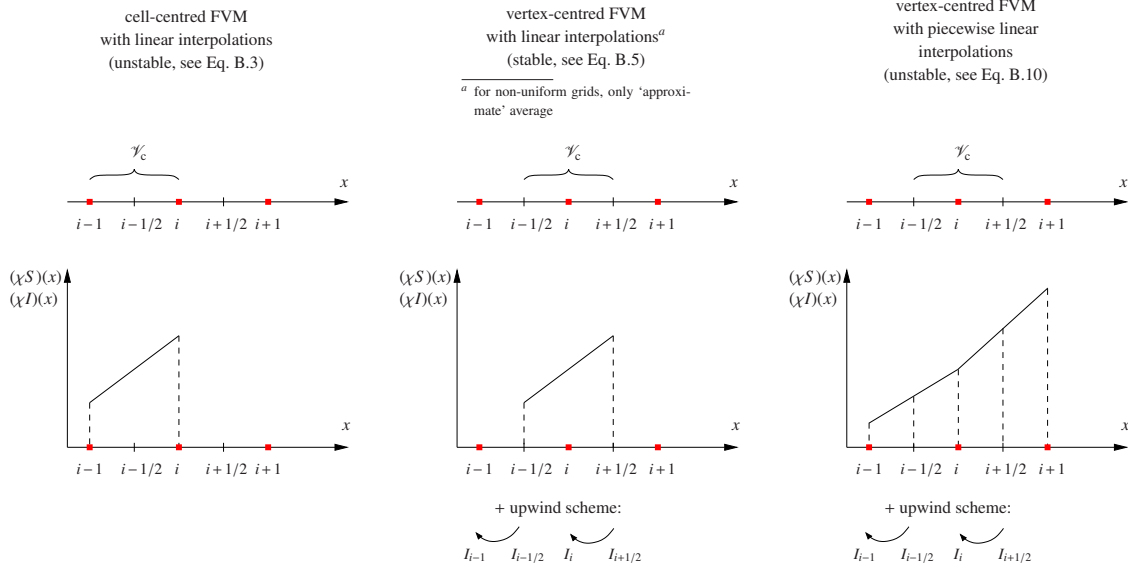
Figure B.1: Different 1D finite-volume methods, with the functions $(\chi S)(x)$ and $(\chi I)(x)$ within the indicated control-volume, $\mathscr{V}_c$, approximated by linear (left and middle panel) and piecewise linear interpolations (right panel). While the left panel displays the (low-order) cell-centred FVM, the middle and right panels represent the stable and an unstable vertex-centred FVM (see text). All quantities are only stored at the grid points (indicated by the red dots).

with $\Delta x = x_i - x_{i-1}$ defining the control volume. Solving for the intensity at a grid point x_i, we easily obtain:

$$I_i = \frac{(\chi_i S_i + \chi_{i-1} S_{i-1})\dfrac{\Delta x}{2}}{1 + \dfrac{\chi_i \Delta x}{2}} + \frac{1 - \dfrac{\chi_{i-1}\Delta x}{2}}{1 + \dfrac{\chi_i \Delta x}{2}} I_{i-1}. \tag{B.3}$$

Considering only absorption terms, the solution scheme obviously gives unphysical (i.e., negative) results, if the opacity is large ($\Delta\tau > 1$), and cannot be applied for our purposes. This argumentation can be extended also to interpolation schemes of higher order (e.g., applying a quadratic interpolation in the interval $[x_{i-1}, x_{i+1}]$). Thus, an alternative formulation of the FVM has to be used.

1D vertex-centred FVM with linear interpolations. Using linear interpolations to approximate the quantities (χI) and (χS) within the control volume of the vertex-centred FVM, Eq. (B.1) becomes:

$$\begin{aligned}
I_{i+1/2} - I_{i-1/2} &= \int_{x_{i-1/2}}^{x_{i+1/2}} \chi(S - I)\, \mathrm{d}x \\
&\approx (\chi_{i-1/2} S_{i-1/2} + \chi_{i+1/2} S_{i+1/2})\frac{\Delta x}{2} - (\chi_{i-1/2} I_{i-1/2} + \chi_{i+1/2} I_{i+1/2})\frac{\Delta x}{2} \\
&= (\chi_i S_i - \chi_i I_i)\Delta x, \tag{B.4}
\end{aligned}$$

where the last equality holds only for linearly approximated quantities on an equidistant grid with $\Delta x = x_{i+1/2} - x_{i-1/2} = x_i - x_{i-1}$. For non-uniform grids, the last line of Eq. (B.4) can be interpreted

as the integral over a suitable average of the quantities $(\chi I) - (\chi S)$. Using the upwind approximation (i.e., setting $I_{i-1/2} \to I_{i-1}$ and $I_{i+1/2} \to I_i$), and solving Eq. (B.4) for the intensity at a grid point x_i, we find:

$$I_i = \frac{\chi_i \Delta x_i}{1 + \chi_i \Delta x_i} S_i + \frac{1}{1 + \chi_i \Delta x_i} I_i, \tag{B.5}$$

which, in contrast to the corresponding 'unstable' vertex-centred method described above, gives always positive values for the intensity, independent from $\Delta \tau$. In this respect, also the upwind approximation is of prime importance to ensure a stable solution scheme.

1D vertex-centred FVM with piecewise linear interpolations. Since the 1D vertex-centred FVM from above suffers from severe numerical diffusion errors (see Sect. 4.1.2), one might aim at increasing the accuracy by applying higher order methods. However, as shown in the following, already extending the FVM with piecewise linear interpolations of the quantities (χI) and (χS) in the intervals $[x_{i-1}, x_i]$, and $[x_i, x_{i+1}]$, results again in an unstable solution scheme. With such piecewise linear approximations, the volume integral can be calculated as:

$$\int_{x_{i-1/2}}^{x_{i+1/2}} (\chi S - \chi I) \, dx = \int_{x_{i-1/2}}^{x_i} (\chi S - \chi I) \, dx + \int_{x_i}^{x_{i+1/2}} (\chi S - \chi I) \, dx. \tag{B.6}$$

With the integrals of an arbitrary piecewise linear function f:

$$\int_{x_{i-1/2}}^{x_i} \left[f_{i-1} + \frac{f_i - f_{i-1}}{\Delta x_i} (x - x_{i-1}) \right] dx = \cdots = \frac{\Delta x_i}{8} f_{i-1} + \frac{3 \Delta x_i}{8} f_i \tag{B.7}$$

$$\int_{x_i}^{x_{i+1/2}} \left[f_i + \frac{f_{i+1} - f_i}{\Delta x_{i+1}} (x - x_i) \right] dx = \cdots = \frac{3 \Delta x_{i+1}}{8} f_i + \frac{\Delta x_{i+1}}{8} f_{i+1}, \tag{B.8}$$

we finally obtain for the discretized equation of radiative transfer:

$$I_{i+1/2} - I_{i-1/2} = \langle \chi S \rangle - \frac{\chi_{i-1} \Delta x_i}{8} I_{i-1} - \frac{3 \chi_i (\Delta x_i + \Delta x_{i+1})}{8} I_i - \frac{\chi_{i+1} \Delta x_{i+1}}{8} I_{i+1}, \tag{B.9}$$

where $\langle \chi S \rangle$ describes the source-integral. Again, using the upwind approximation to calculate the intensities at the control-volume surfaces, we find for the intensity at a grid point x_{i+1}:

$$I_{i+1} = \frac{8 \langle \chi S \rangle}{\chi_{i+1} \Delta x_{i+1}} + \frac{8 - \chi_{i-1} \Delta x_i}{\chi_{i+1} \Delta x_{i+1}} I_{i-1} + \frac{8 - 3 \chi_i (\Delta x_i + \Delta x_{i+1})}{\chi_{i+1} \Delta x_{i+1}} I_i. \tag{B.10}$$

Thus, even for the most trivial (higher order) vertex-centred FVM, i.e., using piecewise linear interpolations and the upwind approximation to solve the volume and surface integrals, respectively, we obtain an 'unstable' solution scheme with potentially negative intensities (in the pure absorption case, here for roughly $\Delta \tau \gtrsim 16/7 \approx 2.3$).

Appendix C

Bézier interpolation

This chapter has been copied from Hennicker et al. (2019, Appendix B and C).

C.1   1D Bézier interpolation[1]

In this section, we discuss an interpolation technique using quadratic Bézier curves (e.g., Auer 2003, Schwarz 1997). Such curves are generally constructed from three given points b_0, b_1, b_2 (see Fig. C.1, left panel), and have the following useful properties:

 (i) The boundary points, b_0 and b_2 are reproduced exactly by the Bézier curve.

 (ii) The straight connections $(b_1 - b_0)$ and $(b_2 - b_1)$ define the tangent lines of the curve at b_0 and b_2, respectively.

 (iii) Any point on the Bézier curve is located in the convex hull of b_0, b_1, b_2.

In a 2D plane described by coordinates x and y, the quadratic Bézier curve is parameterized as:

$$b(t) = \begin{pmatrix} x(t) \\ y(t) \end{pmatrix} = (1-t)^2 \, b_0 + 2t(1-t) \, b_1 + t^2 b_2 \, , \tag{C.1}$$

with $t \in [0, 1]$, and $b_0 = (x_0, y_0)$, $b_1 = (x_1, y_1)$, $b_2 = (x_2, y_2)$. With Eq. (C.1), the properties (i)-(iii) can be exploited to construct a monotonic interpolation scheme by identifying b_0, b_2 with two given data points (x_0, f_0), (x_2, f_2), and defining b_1 as a free (and tunable) parameter. Thus, b_1 is commonly named 'control point', and is only required to set the slope of the Bézier curve. To reproduce the underlying function best, and to preserve monotonicity of the resulting curve, the control point should be chosen with care.

In the following, we present a Bézier-interpolation technique for an interval $x \in [x_{i-1}, x_i]$, given three data points, (x_{i-1}, f_{i-1}), (x_i, f_i), (x_{i+1}, f_{i+1}). The interpolation formulas corresponding to the interval $x \in [x_i, x_{i+1}]$ are given at the end of this section.

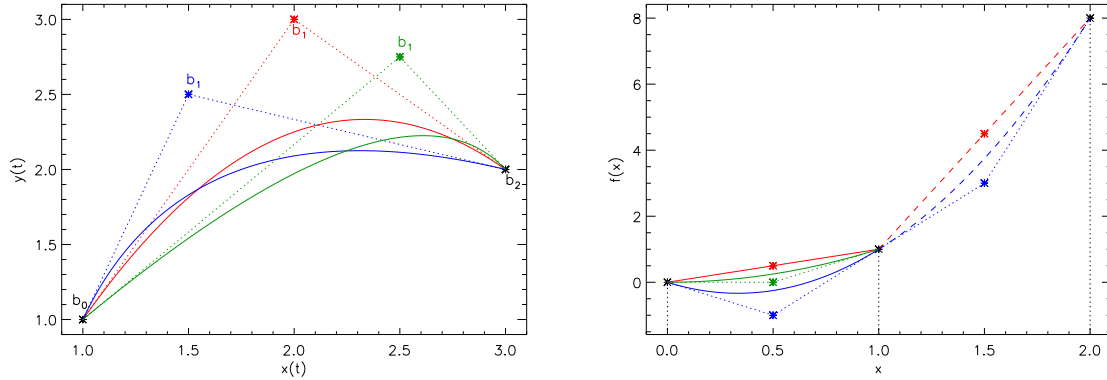[1] copied from Hennicker et al. (2019, Appendix B).

Figure C.1: Left panel: Bézier curves (solid lines) for three given points $\boldsymbol{b}_0$, $\boldsymbol{b}_1$, $\boldsymbol{b}_2$. The blue, red and green lines represent the resulting curves for different control points $\boldsymbol{b}_1$. The straight connections of the control points (colored asterisks) with the data points are indicated by the dotted lines. Right panel: Different interpolation techniques for a set of three data points at x-coordinates indicated by the dotted vertical lines. The solid and dashed lines correspond to the interpolation in the different intervals $[x_{i-1}, x_i]$ and $[x_i, x_{i+1}]$, respectively. Linear interpolations, quadratic interpolations (connecting all three data points), and a **monotonic** Bézier curve (with ω calculated from Eq. (C.5) in the interval $[x_{i-1}, x_i]$) are indicated in red, blue and green. Since the quadratic interpolation is already monotonic in the interval $[x_i, x_{i+1}]$, the monotonic Bézier curve coincides with the dashed, blue line. From Hennicker et al. (2019).

Interval $[x_{i-1}, x_i]$. A quadratic Bézier curve in the interval $[x_{i-1}, x_i]$ is given from Eq. (C.1):

$$\begin{pmatrix} x(t) \\ f(x(t)) \end{pmatrix} = (1-t)^2 \begin{pmatrix} x_{i-1} \\ f_{i-1} \end{pmatrix} + 2t(1-t) \begin{pmatrix} x_c \\ f_c \end{pmatrix} + t^2 \begin{pmatrix} x_i \\ f_i \end{pmatrix}, \tag{C.2}$$

with (x_c, f_c) the control point. The abscissa of the control point, x_c, can be chosen arbitrarily (at least in principle). To obtain a second-order interpolation scheme, however, x_c needs to be located at the centre of the data-point's abscissae [2], and is therefore set to $x_c = (x_{i-1} + x_i)/2$. Then, the quadratic Bézier interpolation scheme is given by:

$$\begin{aligned} f(x) &= (1-t)^2 f_{i-1} + 2t(1-t)f_c + t^2 f_i \\ t &= (x - x_{i-1})/(x_i - x_{i-1}), \end{aligned} \tag{C.3}$$

where t has been determined from the definition of x_c and Eq. (C.2). Since the straight connection of the control point (x_c, f_c) with the data point (x_i, f_i) defines the tangent line of the Bézier curve at this data point, f_c is calculated as

$$f_c = f_i - \left.\frac{\mathrm{d}f}{\mathrm{d}x}\right|_{x_i} \frac{\Delta x_i}{2},$$

---

[2] If x_c was located at, e.g., $x_c = x_{i-1} + 3/4(x_i - x_{i-1})$, one can easily show that the resulting Bézier curve never reproduces the unit parabola for any ordinate value f_c.

with $\Delta x_i = x_i - x_{i-1}$. The unknown derivative at x_i needs to be approximated. Using also the information from the next data point, (x_{i+1}, f_{i+1}), and assigning a weight ω to the forward and backward derivatives (obtained from finite differences), we find

$$f_c = f_i - \frac{\Delta x_i}{2}\left(\omega\frac{f_i - f_{i-1}}{\Delta x_i} + (1-\omega)\frac{f_{i+1} - f_i}{\Delta x_{i+1}}\right), \tag{C.4}$$

with $\Delta x_{i+1} = x_{i+1} - x_i$. With a proper choice of ω, we can adjust the Bézier curve to our needs by shifting the control point up or down. For instance, setting $\omega = \Delta x_{i+1}/(\Delta x_i + \Delta x_{i+1})$ results in the unique parabola connecting the three given data points, while $\omega = 1$ would yield the linear interpolation. To avoid overshoots and negative function values, we demand that the Bézier curve shall be monotonic in the interval $[x_{i-1}, x_i]$. Noting that monotonicity is obtained when the control point is located in the interval $f_c \in [f_{i-1}, f_i]$, corresponding ω-values should lie in between the following limits:

$$\omega_{i-1}^{[i-1,i]} \quad := \quad \omega(f_c^{[i-1,i]} = f_{i-1}) = 1 + \frac{1}{1 - \frac{f_{i+1}-f_i}{f_i-f_{i-1}}\frac{\Delta x_i}{\Delta x_{i+1}}} \tag{C.5}$$

$$\omega_i^{[i-1,i]} \quad := \quad \omega(f_c^{[i-1,i]} = f_i) = \frac{1}{1 - \frac{f_i-f_{i-1}}{f_{i+1}-f_i}\frac{\Delta x_{i+1}}{\Delta x_i}}, \tag{C.6}$$

where the superscript $[i-1, i]$ denotes that ω corresponds to the interpolation scheme in the left interval, $[x_{i-1}, x_i]$. In the final implementation, we avoid the division by zero if $f_i = f_{i-1}$ or $f_i = f_{i+1}$, of course. Our standard interpolation is then performed as follows: (i) We calculate ω such that we obtain the unique parabola connecting all three data points. (ii) If ω lies outside the allowed limits from Eq. (C.5) and (C.6), we adjust ω to yield monotonic interpolations. In Fig. C.1, we display the monotonic Bézier curve resulting from a ω-parameter calculated by means of Eq. (C.5), together with linear and quadratic interpolations (the latter connecting the three data points). Since monotonicity is always obtained for $\omega \in [\omega_{i-1}, \omega_i]$, we can define even stricter limits in order to avoid oscillations during the iteration scheme, by e.g., setting $\omega = 1$ to obtain purely linear interpolations (see Sect. 3.5.2).

To calculate the elements of the (approximate) $\boldsymbol{\Lambda}$-matrix, the interpolation coefficients are required. Combining Eqs. (C.3) and (C.4) then gives:

$$f(x \in [x_{i-1}, x_i]) = \tilde{a}^{[i-1,i]}f_{i-1} + \tilde{b}^{[i-1,i]}f_i + \tilde{c}^{[i-1,i]}f_{i+1}, \tag{C.7}$$

with

$$\tilde{a}^{[i-1,i]} \quad = \quad 1 + (\omega - 2)\frac{x - x_{i-1}}{x_i - x_{i-1}} + (1-\omega)\left(\frac{x - x_{i-1}}{x_i - x_{i-1}}\right)^2 \tag{C.8}$$

$$\tilde{b}^{[i-1,i]} \quad = \quad \frac{(1-\omega)\Delta x_i + (2-\omega)\Delta x_{i+1}}{\Delta x_{i+1}}\frac{x - x_{i-1}}{x_i - x_{i-1}}$$

$$+ \quad (\omega - 1)\frac{\Delta x_i + \Delta x_{i+1}}{\Delta x_{i+1}}\left(\frac{x - x_{i-1}}{x_i - x_{i-1}}\right)^2 \tag{C.9}$$

$$\tilde{c}^{[i-1,i]} \quad = \quad \frac{(\omega - 1)\Delta x_i}{\Delta x_{i+1}}\frac{x - x_{i-1}}{x_i - x_{i-1}}$$

$$- \quad \frac{(\omega - 1)\Delta x_i}{\Delta x_{i+1}}\left(\frac{x - x_{i-1}}{x_i - x_{i-1}}\right)^2. \tag{C.10}$$

The interpolation formula for the right interval $[x_i, x_{i+1}]$ uses the same data points as above. Since the value of the control point needs to be calculated at a different x-coordinate, $x_c = (x_{i+1} + x_i)/2$, we cannot simply substitute indices. Using

$$
\begin{aligned}
f(x) &= (1-t)^2 f_i + 2t(1-t) f_c + t^2 f_{i+1} & \text{(C.11)} \\
t &:= (x - x_i)/(x_{i+1} - x_i) & \\
f_c &= f_i + \frac{\Delta x_{i+1}}{2}\left(\omega \frac{f_{i+1} - f_i}{\Delta x_{i+1}} + (1-\omega)\frac{f_i - f_{i-1}}{\Delta x_i} \right), & \text{(C.12)}
\end{aligned}
$$

we obtain for this interval:

$$
f(x \in [x_i, x_{i+1}]) = \tilde{a}^{[i,i+1]} f_{i-1} + \tilde{b}^{[i,i+1]} f_i + \tilde{c}^{[i,i+1]} f_{i+1}, \tag{C.13}
$$

with

$$
\begin{aligned}
\tilde{a}^{[i,i+1]} &= \frac{(\omega-1)\Delta x_{i+1}}{\Delta x_i} \frac{x - x_i}{x_{i+1} - x_i} \\
&\quad - \frac{(\omega-1)\Delta x_{i+1}}{\Delta x_i}\left(\frac{x - x_i}{x_{i+1} - x_i} \right)^2 & \text{(C.14)} \\
\tilde{b}^{[i,i+1]} &= 1 - \frac{\omega\Delta x_i + (\omega-1)\Delta x_{i+1}}{\Delta x_i} \frac{x - x_i}{x_{i+1} - x_i} \\
&\quad + (\omega-1)\frac{\Delta x_i + \Delta x_{i+1}}{\Delta x_i}\left(\frac{x - x_i}{x_{i+1} - x_i} \right)^2 & \text{(C.15)} \\
\tilde{c}^{[i,i+1]} &= \omega\frac{x - x_i}{x_{i+1} - x_i} + (1-\omega)\left(\frac{x - x_i}{x_{i+1} - x_i}, \right)^2 & \text{(C.16)}
\end{aligned}
$$

and

$$
\begin{aligned}
\omega_i^{[i,i+1]} &:= \omega(f_c^{[i,i+1]} = f_i) = \frac{1}{1 - \frac{f_{i+1}-f_i}{f_i-f_{i-1}}\frac{\Delta x_i}{\Delta x_{i+1}}} & \text{(C.17)} \\
\omega_{i+1}^{[i,i+1]} &:= \omega(f_c^{[i,i+1]} = f_{i+1}) = 1 + \frac{1}{1 - \frac{f_i-f_{i-1}}{f_{i+1}-f_i}\frac{\Delta x_{i+1}}{\Delta x_i}}. & \text{(C.18)}
\end{aligned}
$$

The corresponding Bézier curves for different ω-parameters ($\omega = 1$ for linear and $\omega = \Delta x_i/(\Delta x_i + \Delta x_{i+1})$ for continuous quadratic interpolations) are also shown in Fig. C.1. We note that the Bézier interpolation gives a continuous function in the complete interval $[x_{i-1}, x_{i+1}]$ only for those ω-values that define the parabola connecting all three data points.

C.2   2D Bézier interpolation[3]

To interpolate upwind and downwind quantities, a 2D interpolation scheme is required. Fig. C.2 displays the geometry for a 2D rectangular area, with grid points indicated by the black dots. With this setup, we perform a 2D Bézier interpolation by applying three 1D Bézier interpolations along the

---

[3] copied from Hennicker et al. (2019, Appendix C).
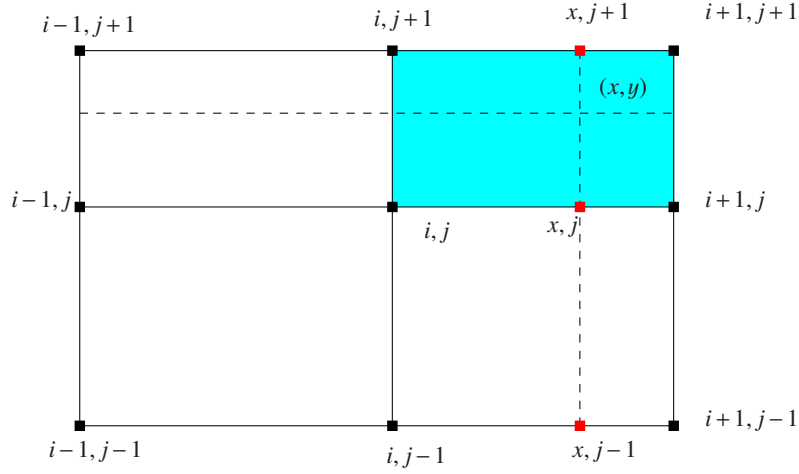
Figure C.2: 2D interpolation for upwind or downwind quantities required in the cyan shaded area. The 2D Bézier interpolation consists of three 1D interpolations to obtain the values at the desired x-coordinate (indicated by red dots), followed by a 1D interpolation along the y-coordinate using the obtained values at the red dots. From Hennicker et al. (2019).

x-axis on each y-level at $(j-1)$, (j), $(j+1)$, followed by another 1D Bézier interpolation along y at the desired x-coordinate. Within the cyan shaded interval, we obtain with the 1D Bézier interpolation given by Eqs. (C.13)-(C.16):

$$
\begin{aligned}
f(x,y) \quad = \quad & \tilde{a}_y \tilde{a}_x^{(j-1)} f_{i-1,j-1} + \tilde{a}_y \tilde{b}_x^{(j-1)} f_{i,j-1} + \tilde{a}_y \tilde{c}_x^{(j-1)} f_{i+1,j-1} \\
+ \quad & \tilde{b}_y \tilde{a}_x^{(j)} f_{i-1,j} + \tilde{b}_y \tilde{b}_x^{(j)} f_{i,j} + \tilde{b}_y \tilde{c}_x^{(j)} f_{i+1,j} \\
+ \quad & \tilde{c}_y \tilde{a}_x^{(j+1)} f_{i-1,j+1} + \tilde{c}_y \tilde{b}_x^{(j+1)} f_{i,j+1} + \tilde{c}_y \tilde{c}_x^{(j+1)} f_{i+1,j+1},
\end{aligned}
\tag{C.19}
$$

where the subscripts of the interpolation coefficients indicate the coordinate used for each 1D interpolation. We note that all upwind and downwind interpolations are performed in the upper right interval of a given surface, in order to obtain a simple representation of the Λ-matrix elements.

Appendix D

ALO coefficients within the 3D SC method

This chapter has been copied from Hennicker et al. (2019, Appendix D).

In the following, we derive the Λ-matrix coefficients used to construct the approximate Λ-operator. We note that the obtained matrix elements can also be used for any other (2nd or lower order) interpolation scheme using the same geometry, with different interpolation coefficients though.

For a source function set to unity at grid point (ijk) and zero everywhere else, we consider all 27 points ranging from $(i-\alpha, j-\beta, k-\gamma)$ to $(i+\alpha, j+\beta, k+\gamma)$. The corresponding matrix coefficients are derived from Eq. (3.38), using the discretized equation of radiative transfer, Eqs. (3.12)/(3.17), with upwind and downwind interpolations defined by Eqs. (3.19) and (3.20). We further consider only the $\Lambda_{\Omega\nu}$-operator, since the integration over frequency and/or solid angle is straightforward. Each Λ-matrix element then corresponds to the intensity (resulting from $S_{ijk} = 1$) at a considered grid point p (not necessarily identical to (ijk)), and consists of an emission term (defined by the interpolated source functions and optical-depth steps at the corresponding upwind, current and downwind points), and the irradiation from the upwind point (defined by the upwind intensity and upwind optical-depth step). The upper and lower panel of Fig. D.1 show an example in 2D considering the points $(i-\alpha, j-\beta)$ and $(i, j-\beta)$ for a source function $S_{ij} = 1$.

In the following, we sketch the derivation of the (3D) matrix element for the first neighbour, and only present the solution for the remaining ones. To save space, we skip the indices Ω, ν. The m,n-th Λ-element is written as Λ_m^n, with matrix indices n,m calculated from Eq. (3.29). While n corresponds to the 3D indices of the local grid point ($S_{ijk} = S_n = 1$), m represents the neighbouring
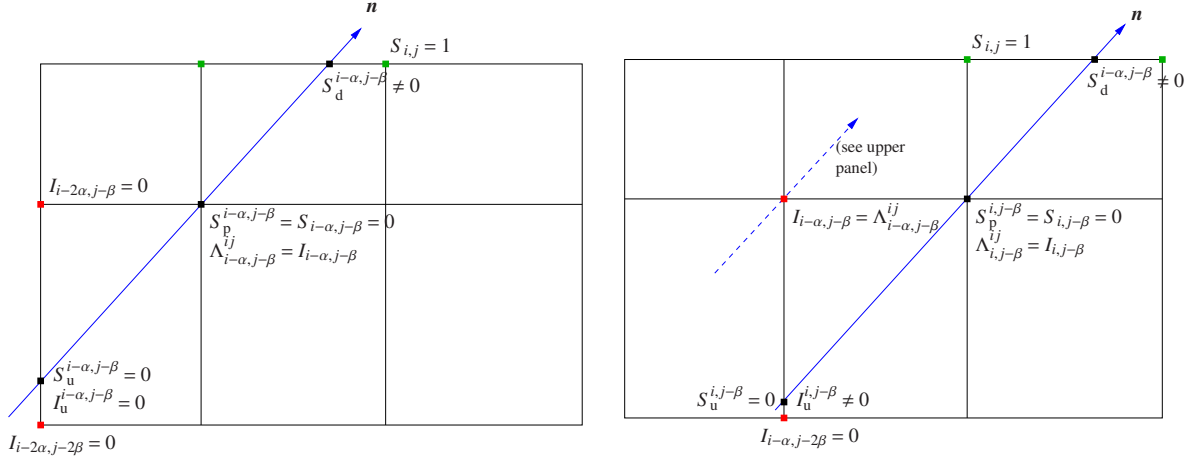
Figure D.1: 2D example for calculating the $\mathbf{\Lambda}_{\Omega,\nu}$-matrix elements at a grid point $i-\alpha, j-\beta$ (left panel) and $i, j-\beta$ (right panel). The matrix elements correspond to the intensity at the considered grid points calculated for a source function $S_{ij} = 1$ and zero everywhere else. For such a configuration, the downwind source function is interpolated from grid points indicated with the green dots, while the upwind source function and upwind intensity are obtained from the red dots (for simplicity we here assume linear interpolations for determining upwind and downwind quantities). We emphasize that the upwind intensity vanishes only when considering the grid point $i-\alpha, j-\beta$. From Hennicker et al. (2019).

point, $(i-\alpha, j-\beta, k-\gamma)$. Applying Eq. (3.38) to the specific intensity at point m, we obtain:

$$
\begin{aligned}
\Lambda_m^n &= I_m\left(\mathbf{S} = \mathbf{e}_n, \mathbf{\Phi}_B = 0\right) \\
= \Lambda_{i-\alpha,j-\beta,k-\gamma}^{ijk} &= I_{i-\alpha,j-\beta,k-\gamma}\left(S_{ijk} = \delta_{\tilde{i},i}\delta_{\tilde{j},j}\delta_{\tilde{k},k}\right) \\
&= a_{i-\alpha,j-\beta,k-\gamma}S_u^{(i-\alpha,j-\beta,k-\gamma)}\left(S_{ijk} = \delta_{\tilde{i},i}\delta_{\tilde{j},j}\delta_{\tilde{k},k}\right) \\
&+ b_{i-\alpha,j-\beta,k-\gamma}S_p^{(i-\alpha,j-\beta,k-\gamma)}\left(S_{ijk} = \delta_{\tilde{i},i}\delta_{\tilde{j},j}\delta_{\tilde{k},k}\right) \\
&+ c_{i-\alpha,j-\beta,k-\gamma}S_d^{(i-\alpha,j-\beta,k-\gamma)}\left(S_{ijk} = \delta_{\tilde{i},i}\delta_{\tilde{j},j}\delta_{\tilde{k},k}\right) \\
&+ d_{i-\alpha,j-\beta,k-\gamma}I_u^{(i-\alpha,j-\beta,k-\gamma)}\left(S_{ijk} = \delta_{\tilde{i},i}\delta_{\tilde{j},j}\delta_{\tilde{k},k}\right),
\end{aligned}
$$

with boundary contribution $\mathbf{\Phi}_B$, n-th unit vector $\mathbf{e}_n$ and $\delta_{\tilde{i},i}$, $\delta_{\tilde{j},j}$, $\delta_{\tilde{k},k}$ the Kronecker-δ for all possible $x_{\tilde{i}}$, $y_{\tilde{j}}$ and $z_{\tilde{k}}$ coordinates, respectively. S_u and S_d are the upwind and downwind source functions corresponding to a considered short characteristic at grid point $p \leftrightarrow (i-\alpha, j-\beta, k-\gamma)$, S_p is the source function at the grid point[1], I_u is the upwind intensity, and a, b, c, d are the integration coefficients for this particular short characteristic. All upwind and downwind quantities are to be interpolated from neighbouring grid points. We use the notation w, $\hat{w}$, $\tilde{w}$, to identify different interpolation coefficients corresponding to the upwind source function, upwind intensity, and downwind source function, re-

---

[1] $S_p \neq 0$ only when considering the grid point $p \leftrightarrow (ijk)$. Then, $S_d^{(ijk)} = 0$, and $S_u^{(ijk)} \neq 0$ only when the upwind point is located on the stellar surface (Eq. D.14).

spectively. Using Eqs. (3.19) and (3.20) to interpolate upwind and downwind quantities, we find:

$$
\begin{aligned}
\Lambda^{ijk}_{i-\alpha,j-\beta,k-\gamma} = a_{i-\alpha,j-\beta,k-\gamma} \cdot [\,&w_{\mathrm{A}} S_{i-3\alpha,j-2\beta,k-3\gamma} + w_{\mathrm{B}} S_{i-2\alpha,j-2\beta,k-3\gamma} + w_{\mathrm{C}} S_{i-\alpha,j-2\beta,k-3\gamma} \\
+\quad &w_{\mathrm{D}} S_{i-3\alpha,j-2\beta,k-2\gamma} + w_{\mathrm{E}} S_{i-2\alpha,j-2\beta,k-2\gamma} + w_{\mathrm{F}} S_{i-\alpha,j-2\beta,k-2\gamma} \\
+\quad &w_{\mathrm{G}} S_{i-3\alpha,j-2\beta,k-\gamma} + w_{\mathrm{H}} S_{i-2\alpha,j-2\beta,k-\gamma} + w_{\mathrm{I}} S_{i-\alpha,j-2\beta,k-\gamma} \\
+\quad &w_{\mathrm{J}} S_{i-3\alpha,j-3\beta,k-2\gamma} + w_{\mathrm{K}} S_{i-2\alpha,j-3\beta,k-2\gamma} + w_{\mathrm{L}} S_{i-\alpha,j-3\beta,k-2\gamma} \\
+\quad &w_{\mathrm{M}} S_{i-3\alpha,j-\beta,k-2\gamma} + w_{\mathrm{N}} S_{i-2\alpha,j-\beta,k-2\gamma} + w_{\mathrm{O}} S_{i-\alpha,j-\beta,k-2\gamma} \\
+\quad &w_{\mathrm{P}} S_{i-2\alpha,j-3\beta,k-3\gamma} + w_{\mathrm{Q}} S_{i-2\alpha,j-\beta,k-3\gamma} + w_{\mathrm{R}} S_{i-2\alpha,j-3\beta,k-\gamma} \\
+\quad &w_{\mathrm{S}} S_{i-2\alpha,j-\beta,k-\gamma} + w_{i-\alpha,j-\beta,k-\gamma} S_{i-\alpha,j-\beta,k-\gamma}\,] \\
+ b_{i-\alpha,j-\beta,k-\gamma}& S_{i-\alpha,j-\beta,k-\gamma} \\
+ c_{i-\alpha,j-\beta,k-\gamma} \cdot [\,&\tilde{w}_{\mathrm{A}} S_{i-2\alpha,j,k-2\gamma} + \tilde{w}_{\mathrm{B}} S_{i-\alpha,j,k-2\gamma} + \tilde{w}_{\mathrm{C}} S_{i,j,k-2\gamma} \\
+\quad &\tilde{w}_{\mathrm{D}} S_{i-2\alpha,j,k-\gamma} + \tilde{w}_{\mathrm{E}} S_{i-\alpha,j,k-\gamma} + \tilde{w}_{\mathrm{F}} S_{i,j,k-\gamma} \\
+\quad &\tilde{w}_{\mathrm{G}} S_{i-2\alpha,j,k} + \tilde{w}_{\mathrm{H}} S_{i-\alpha,j,k} + \tilde{w}_{\mathrm{I}} S_{ijk} \\
+\quad &\tilde{w}_{\mathrm{J}} S_{i-2\alpha,j-2\beta,k} + \tilde{w}_{\mathrm{K}} S_{i-\alpha,j-2\beta,k} + \tilde{w}_{\mathrm{L}} S_{i,j-2\beta,k} \\
+\quad &\tilde{w}_{\mathrm{M}} S_{i-2\alpha,j-\beta,k} + \tilde{w}_{\mathrm{N}} S_{i-\alpha,j-\beta,k} + \tilde{w}_{\mathrm{O}} S_{i,j-\beta,k} \\
+\quad &\tilde{w}_{\mathrm{P}} S_{i,j-2\beta,k-2\gamma} + \tilde{w}_{\mathrm{Q}} S_{i,j-\beta,k-2\gamma} + \tilde{w}_{\mathrm{R}} S_{i,j-2\beta,k-\gamma} + \tilde{w}_{\mathrm{S}} S_{i,j-\beta,k-\gamma}\,] \\
+ d_{i-\alpha,j-\beta,k-\gamma}[\,&\hat{w}_{\mathrm{A}} I_{i-3\alpha,j-2\beta,k-3\gamma}(S_{ijk}=1) + \cdots + \quad \hat{w}_{\mathrm{S}} I_{i-2\alpha,j-\beta,k-\gamma}(S_{ijk}=1)\,],
\end{aligned}
$$

with the upwind intensity interpolated from the same points as the upwind source function, and a compact notation for the interpolation coefficients (with skipped superscripts). Since only $S_{ijk}=1$ (and zero everywhere else), and because the upwind intensity vanishes (for this particular grid point, see Fig. D.1 for an example in 2D), we finally obtain:

$$
\Lambda^{ijk}_{i-\alpha,j-\beta,k-\gamma} = c_{i-\alpha,j-\beta,k-\gamma} \tilde{w}_{\mathrm{I}}^{(i-\alpha,j-\beta,k-\gamma)} \tag{D.1}
$$

The matrix element for a point $(i-\alpha, j-\beta, k-\gamma)$ with a non-vanishing source function at point (ijk) is thus solely given by the integration coefficient $c_{i-\alpha,j-\beta,k-\gamma}$ from the discretized EQRT multiplied with the interpolation coefficient for the downwind source function of point I (corresponding to grid point (ijk), see Fig. 3.3). The other neighbours are obtained analogously, without vanishing incident intensities, however. Accounting also for the interpolation of upwind source functions and intensities when necessary, we find:

$$
\Lambda^{ijk}_{i,j-\beta,k-\gamma} = c_{i,j-\beta,k-\gamma} \tilde{w}_{\mathrm{H}}^{i,j-\beta,k-\gamma} + d_{i,j-\beta,k-\gamma} \hat{w}_{\mathrm{S}}^{i,j-\beta,k-\gamma} \Lambda^{ijk}_{i-\alpha,j-\beta,k-\gamma} \tag{D.2}
$$

$$
\Lambda^{ijk}_{i+\alpha,j-\beta,k-\gamma} = c_{i+\alpha,j-\beta,k-\gamma} \tilde{w}_{\mathrm{G}}^{i+\alpha,j-\beta,k-\gamma} + d_{i+\alpha,j-\beta,k-\gamma} \hat{w}_{\mathrm{S}}^{i+\alpha,j-\beta,k-\gamma} \Lambda^{ijk}_{i,j-\beta,k-\gamma} \tag{D.3}
$$

$$
\Lambda^{ijk}_{i-\alpha,j,k-\gamma} = c_{i-\alpha,j,k-\gamma} \tilde{w}_{\mathrm{O}}^{i-\alpha,j,k-\gamma} + d_{i-\alpha,j,k-\gamma} \hat{w}_{\mathrm{I}}^{i-\alpha,j,k-\gamma} \Lambda^{ijk}_{i-\alpha,j-\beta,k-\gamma} \tag{D.4}
$$

$$
\Lambda^{ijk}_{i,j,k-\gamma} = c_{i,j,k-\gamma} \tilde{w}_{\mathrm{N}}^{i,j,k-\gamma} + d_{i,j,k-\gamma} \cdot \left[\hat{w}_{\mathrm{H}}^{i,j,k-\gamma} \Lambda^{ijk}_{i-\alpha,j-\beta,k-\gamma} + \hat{w}_{\mathrm{I}}^{i,j,k-\gamma} \Lambda^{ijk}_{i,j-\beta,k-\gamma} + \hat{w}_{\mathrm{S}}^{i,j,k-\gamma} \Lambda^{ijk}_{i-\alpha,j,k-\gamma} \right] \tag{D.5}
$$

$$\Lambda^{ijk}_{i+\alpha,j,k-\gamma} = c_{i+\alpha,j,k-\gamma}\tilde{w}^{i+\alpha,j,k-\gamma}_{\text{M}} + d_{i+\alpha,j,k-\gamma}\cdot\left[\hat{w}^{i+\alpha,j,k-\gamma}_{\text{D}}\Lambda^{ijk}_{i-\alpha,j-\beta,k-\gamma}\right.$$
$$\left. + \hat{w}^{i+\alpha,j,k-\gamma}_{\text{H}}\Lambda^{ijk}_{i,j-\beta,k-\gamma} + \hat{w}^{i+\alpha,j,k-\gamma}_{\text{I}}\Lambda^{ijk}_{i+\alpha,j-\beta,k-\gamma} + \hat{w}^{i+\alpha,j,k-\gamma}_{\text{S}}\Lambda^{ijk}_{i,j,k-\gamma}\right] \tag{D.6}$$

$$\Lambda^{ijk}_{i-\alpha,j+\beta,k-\gamma} = c_{i-\alpha,j+\beta,k-\gamma}\tilde{w}^{i-\alpha,j+\beta,k-\gamma}_{\text{L}} + d_{i-\alpha,j+\beta,k-\gamma}\hat{w}^{i-\alpha,j+\beta,k-\gamma}_{\text{I}}\Lambda^{ijk}_{i-\alpha,j,k-\gamma} \tag{D.7}$$

$$\Lambda^{ijk}_{i,j+\beta,k-\gamma} = c_{i,j+\beta,k-\gamma}\tilde{w}^{i,j+\beta,k-\gamma}_{\text{K}} + d_{i,j+\beta,k-\gamma}\cdot\left[\hat{w}^{i,j+\beta,k-\gamma}_{\text{R}}\Lambda^{ijk}_{i-\alpha,j-\beta,k-\gamma}\right.$$
$$\left. + \hat{w}^{i,j+\beta,k-\gamma}_{\text{H}}\Lambda^{ijk}_{i-\alpha,j,k-\gamma} + \hat{w}^{i,j+\beta,k-\gamma}_{\text{I}}\Lambda^{ijk}_{i,j,k-\gamma} + \hat{w}^{i,j+\beta,k-\gamma}_{\text{S}}\Lambda^{ijk}_{i-\alpha,j+\beta,k-\gamma}\right] \tag{D.8}$$

$$\Lambda^{ijk}_{i+\alpha,j+\beta,k-\gamma} = c_{i+\alpha,j+\beta,k-\gamma}\tilde{w}^{i+\alpha,j+\beta,k-\gamma}_{\text{J}} + d_{i+\alpha,j+\beta,k-\gamma}\cdot\left[\hat{w}^{i+\alpha,j+\beta,k-\gamma}_{\text{R}}\Lambda^{ijk}_{i,j-\beta,k-\gamma} + \hat{w}^{i+\alpha,j+\beta,k-\gamma}_{\text{G}}\Lambda^{ijk}_{i-\alpha,j,k-\gamma}\right.$$
$$\left. + \hat{w}^{i+\alpha,j+\beta,k-\gamma}_{\text{H}}\Lambda^{ijk}_{i,j,k-\gamma} + \hat{w}^{i+\alpha,j+\beta,k-\gamma}_{\text{I}}\Lambda^{ijk}_{i+\alpha,j,k-\gamma} + \hat{w}^{i+\alpha,j+\beta,k-\gamma}_{\text{S}}\Lambda^{ijk}_{i,j+\beta,k-\gamma}\right] \tag{D.9}$$

$$\Lambda^{ijk}_{i-\alpha,j-\beta,k} = c_{i-\alpha,j-\beta,k}\tilde{w}^{i-\alpha,j-\beta,k}_{\text{F}} + d_{i-\alpha,j-\beta,k}\hat{w}^{i-\alpha,j-\beta,k}_{\text{O}}\Lambda^{ijk}_{i-\alpha,j-\beta,k-\gamma} \tag{D.10}$$

$$\Lambda^{ijk}_{i,j-\beta,k} = c_{i,j-\beta,k}\tilde{w}^{i,j-\beta,k}_{\text{E}} + d_{i,j-\beta,k}\cdot\left[\hat{w}^{i,j-\beta,k}_{\text{N}}\Lambda^{ijk}_{i-\alpha,j-\beta,k-\gamma} + \hat{w}^{i,j-\beta,k}_{\text{O}}\Lambda^{ijk}_{i,j-\beta,k-\gamma} + \hat{w}^{i,j-\beta,k}_{\text{S}}\Lambda^{ijk}_{i-\alpha,j-\beta,k}\right] \tag{D.11}$$

$$\Lambda^{ijk}_{i+\alpha,j-\beta,k} = c_{i+\alpha,j-\beta,k}\tilde{w}^{i+\alpha,j-\beta,k}_{\text{D}} + d_{i+\alpha,j-\beta,k}\cdot\left[\hat{w}^{i+\alpha,j-\beta,k}_{\text{M}}\Lambda^{ijk}_{i-\alpha,j-\beta,k-\gamma}\right.$$
$$\left. + \hat{w}^{i+\alpha,j-\beta,k}_{\text{N}}\Lambda^{ijk}_{i,j-\beta,k-\gamma} + \hat{w}^{i+\alpha,j-\beta,k}_{\text{O}}\Lambda^{ijk}_{i+\alpha,j-\beta,k-\gamma} + \hat{w}^{i+\alpha,j-\beta,k}_{\text{S}}\Lambda^{ijk}_{i,j-\beta,k}\right] \tag{D.12}$$

$$\Lambda^{ijk}_{i-\alpha,j,k} = c_{i-\alpha,j,k}\tilde{w}^{i-\alpha,j,k}_{\text{S}} + d_{i-\alpha,j,k}\cdot\left[\hat{w}^{i-\alpha,j,k}_{\text{F}}\Lambda^{ijk}_{i-\alpha,j-\beta,k-\gamma} + \hat{w}^{i-\alpha,j,k}_{\text{O}}\Lambda^{ijk}_{i-\alpha,j,k-\gamma} + \hat{w}^{i-\alpha,j,k}_{\text{I}}\Lambda^{ijk}_{i-\alpha,j-\beta,k}\right] \tag{D.13}$$

$$\Lambda^{ijk}_{ijk} = a_{ijk}w_{ijk} + b_{ijk} + d_{ijk}\cdot\left[\hat{w}^{ijk}_{\text{E}}\Lambda^{ijk}_{i-\alpha,j-\beta,k-\gamma} + \hat{w}^{ijk}_{\text{F}}\Lambda^{ijk}_{i,j-\beta,k-\gamma} + \hat{w}^{ijk}_{\text{N}}\Lambda^{ijk}_{i-\alpha,j,k-\gamma}\right.$$
$$\left. + \hat{w}^{ijk}_{\text{O}}\Lambda^{ijk}_{i,j,k-\gamma} + \hat{w}^{ijk}_{\text{H}}\Lambda^{ijk}_{i-\alpha,j-\beta,k} + \hat{w}^{ijk}_{\text{I}}\Lambda^{ijk}_{i,j-\beta,k} + \hat{w}^{ijk}_{\text{S}}\Lambda^{ijk}_{i-\alpha,j,k}\right] \tag{D.14}$$

$$\Lambda^{ijk}_{i+\alpha,j,k} = a_{i+\alpha,j,k}w^{(i+\alpha,j,k)}_{\text{S}} + d_{i+\alpha,j,k}\cdot\left[\hat{w}^{i+\alpha,j,k}_{\text{D}}\Lambda^{ijk}_{i-\alpha,j-\beta,k-\gamma} + \hat{w}^{i+\alpha,j,k}_{\text{E}}\Lambda^{ijk}_{i,j-\beta,k-\gamma}\right.$$
$$+ \hat{w}^{i+\alpha,j,k}_{\text{F}}\Lambda^{ijk}_{i+\alpha,j-\beta,k-\gamma} + \hat{w}^{i+\alpha,j,k}_{\text{M}}\Lambda^{ijk}_{i-\alpha,j,k-\gamma} + \hat{w}^{i+\alpha,j,k}_{\text{N}}\Lambda^{ijk}_{i,j,k-\gamma} + \hat{w}^{i+\alpha,j,k}_{\text{O}}\Lambda^{ijk}_{i+\alpha,j,k-\gamma}$$
$$\left. + \hat{w}^{i+\alpha,j,k}_{\text{G}}\Lambda^{ijk}_{i-\alpha,j-\beta,k} + \hat{w}^{i+\alpha,j,k}_{\text{H}}\Lambda^{ijk}_{i,j-\beta,k} + \hat{w}^{i+\alpha,j,k}_{\text{I}}\Lambda^{ijk}_{i+\alpha,j-\beta,k} + \hat{w}^{i+\alpha,j,k}_{\text{S}}\Lambda^{ijk}_{ijk}\right] \tag{D.15}$$

$$\Lambda^{ijk}_{i-\alpha,j+\beta,k} = c_{i-\alpha,j+\beta,k}\tilde{w}^{(i-\alpha,j+\beta,k)}_{\text{R}} + d_{i-\alpha,j+\beta,k}\cdot\left[\hat{w}^{i-\alpha,j+\beta,k}_{\text{L}}\Lambda^{ijk}_{i-\alpha,j-\beta,k-\gamma}\right.$$
$$\left. + \hat{w}^{i-\alpha,j+\beta,k}_{\text{F}}\Lambda^{ijk}_{i-\alpha,j,k-\gamma} + \hat{w}^{i-\alpha,j+\beta,k}_{\text{O}}\Lambda^{ijk}_{i-\alpha,j+\beta,k-\gamma} + \hat{w}^{i-\alpha,j+\beta,k}_{\text{I}}\Lambda^{ijk}_{i-\alpha,j,k}\right] \tag{D.16}$$

$$\Lambda_{i,j+\beta,k}^{ijk} = a_{i,j+\beta,k} w_{\mathrm{I}}^{(i,j+\beta,k)} + d_{i,j+\beta,k} \cdot \Big[\hat{w}_{\mathrm{E}}^{i,j+\beta,k} \Lambda_{i-\alpha,j,k-\gamma}^{ijk} + \hat{w}_{\mathrm{F}}^{i,j+\beta,k} \Lambda_{i,j,k-\gamma}^{ijk}$$
$$+ \hat{w}_{\mathrm{H}}^{i,j+\beta,k} \Lambda_{i-\alpha,j,k}^{ijk} + \hat{w}_{\mathrm{I}}^{i,j+\beta,k} \Lambda_{ijk}^{ijk} + \hat{w}_{\mathrm{K}}^{i,j+\beta,k} \Lambda_{i-\alpha,j-\beta,k-\gamma}^{ijk} + \hat{w}_{\mathrm{L}}^{i,j+\beta,k} \Lambda_{i,j-\beta,k-\gamma}^{ijk}$$
$$+ \hat{w}_{\mathrm{N}}^{i,j+\beta,k} \Lambda_{i-\alpha,j+\beta,k-\gamma}^{ijk} + \hat{w}_{\mathrm{O}}^{i,j+\beta,k} \Lambda_{i,j+\beta,k-\gamma}^{ijk} + \hat{w}_{\mathrm{R}}^{i,j+\beta,k} \Lambda_{i-\alpha,j-\beta,k}^{ijk} + \hat{w}_{\mathrm{S}}^{i,j+\beta,k} \Lambda_{i-\alpha,j+\beta,k}^{ijk} \Big] \qquad \text{(D.17)}$$

$$\Lambda_{i+\alpha,j+\beta,k}^{ijk} = a_{i+\alpha,j+\beta,k} w_{\mathrm{H}}^{(i+\alpha,j+\beta,k)} + d_{i+\alpha,j+\beta,k} \cdot \Big[\hat{w}_{\mathrm{D}}^{i+\alpha,j+\beta,k} \Lambda_{i-\alpha,j,k-\gamma}^{ijk} +$$
$$+ \hat{w}_{\mathrm{E}}^{i+\alpha,j+\beta,k} \Lambda_{i,j,k-\gamma}^{ijk} + \hat{w}_{\mathrm{F}}^{i+\alpha,j+\beta,k} \Lambda_{i+\alpha,j,k-\gamma}^{ijk} + \hat{w}_{\mathrm{G}}^{i+\alpha,j+\beta,k} \Lambda_{i-\alpha,j,k}^{ijk}$$
$$+ \hat{w}_{\mathrm{H}}^{i+\alpha,j+\beta,k} \Lambda_{ijk}^{ijk} + \hat{w}_{\mathrm{I}}^{i+\alpha,j+\beta,k} \Lambda_{i+\alpha,j,k}^{ijk} \hat{w}_{\mathrm{J}}^{i+\alpha,j+\beta,k} \Lambda_{i-\alpha,j-\beta,k-\gamma}^{ijk}$$
$$+ \hat{w}_{\mathrm{K}}^{i+\alpha,j+\beta,k} \Lambda_{i,j-\beta,k-\gamma}^{ijk} + \hat{w}_{\mathrm{L}}^{i+\alpha,j+\beta,k} \Lambda_{i+\alpha,j-\beta,k-\gamma}^{ijk} + \hat{w}_{\mathrm{M}}^{i+\alpha,j+\beta,k} \Lambda_{i-\alpha,j+\beta,k-\gamma}^{ijk}$$
$$+ \hat{w}_{\mathrm{O}}^{i+\alpha,j+\beta,k} \Lambda_{i+\alpha,j+\beta,k-\gamma}^{ijk} + \hat{w}_{\mathrm{R}}^{i+\alpha,j+\beta,k} \Lambda_{i,j-\beta,k}^{ijk} + \hat{w}_{\mathrm{S}}^{i+\alpha,j+\beta,k} \Lambda_{i,j+\beta,k}^{ijk} \Big] \qquad \text{(D.18)}$$

$$\Lambda_{i-\alpha,j-\beta,k+\gamma}^{ijk} = c_{i-\alpha,j-\beta,k+\gamma} \tilde{w}_{\mathrm{C}}^{(i-\alpha,j-\beta,k+\gamma)} + d_{i-\alpha,j-\beta,k+\gamma} \hat{w}_{\mathrm{O}}^{i-\alpha,j-\beta,k+\gamma} \Lambda_{i-\alpha,j-\beta,k}^{ijk} \qquad \text{(D.19)}$$

$$\Lambda_{i,j-\beta,k+\gamma}^{ijk} = c_{i,j-\beta,k+\gamma} \tilde{w}_{\mathrm{B}}^{(i,j-\beta,k+\gamma)} + d_{i,j-\beta,k+\gamma} \cdot \Big[\hat{w}_{\mathrm{N}}^{i,j-\beta,k+\gamma} \Lambda_{i-\alpha,j-\beta,k}^{ijk}$$
$$+ \hat{w}_{\mathrm{O}}^{i,j-\beta,k+\gamma} \Lambda_{i,j-\beta,k}^{ijk} + \hat{w}_{\mathrm{Q}}^{i,j-\beta,k+\gamma} \Lambda_{i-\alpha,j-\beta,k-\gamma}^{ijk} + \hat{w}_{\mathrm{S}}^{i,j-\beta,k+\gamma} \Lambda_{i-\alpha,j-\beta,k+\gamma}^{ijk} \Big] \qquad \text{(D.20)}$$

$$\Lambda_{i+\alpha,j-\beta,k+\gamma}^{ijk} = c_{i+\alpha,j-\beta,k+\gamma} \tilde{w}_{\mathrm{A}}^{(i+\alpha,j-\beta,k+\gamma)} + d_{i+\alpha,j-\beta,k+\gamma} \cdot \Big[\hat{w}_{\mathrm{M}}^{i+\alpha,j-\beta,k+\gamma} \Lambda_{i-\alpha,j-\beta,k}^{ijk} + \hat{w}_{\mathrm{N}}^{i+\alpha,j-\beta,k+\gamma} \Lambda_{i,j-\beta,k}^{ijk}$$
$$+ \hat{w}_{\mathrm{O}}^{i+\alpha,j-\beta,k+\gamma} \Lambda_{i+\alpha,j-\beta,k}^{ijk} + \hat{w}_{\mathrm{Q}}^{i+\alpha,j-\beta,k+\gamma} \Lambda_{i,j-\beta,k-\gamma}^{ijk} + \hat{w}_{\mathrm{S}}^{i+\alpha,j-\beta,k+\gamma} \Lambda_{i,j-\beta,k+\gamma}^{ijk} \Big] \qquad \text{(D.21)}$$

$$\Lambda_{i-\alpha,j,k+\gamma}^{ijk} = c_{i-\alpha,j,k+\gamma} \tilde{w}_{\mathrm{Q}}^{(i-\alpha,j,k+\gamma)} + d_{i-\alpha,j,k+\gamma} \cdot \Big[\hat{w}_{\mathrm{C}}^{i-\alpha,j,k+\gamma} \Lambda_{i-\alpha,j-\beta,k-\gamma}^{ijk}$$
$$+ \hat{w}_{\mathrm{F}}^{i-\alpha,j,k+\gamma} \Lambda_{i-\alpha,j-\beta,k}^{ijk} + \hat{w}_{\mathrm{I}}^{i-\alpha,j,k+\gamma} \Lambda_{i-\alpha,j-\beta,k+\gamma}^{ijk} + \hat{w}_{\mathrm{O}}^{i-\alpha,j,k+\gamma} \Lambda_{i-\alpha,j,k}^{ijk} \Big] \qquad \text{(D.22)}$$

$$\Lambda_{i,j,k+\gamma}^{ijk} = a_{i,j,k+\gamma} w_{\mathrm{O}}^{(i,j,k+\gamma)} + d_{i,j,k+\gamma} \cdot \Big[\hat{w}_{\mathrm{B}}^{i,j,k+\gamma} \Lambda_{i-\alpha,j-\beta,k-\gamma}^{ijk} + \hat{w}_{\mathrm{C}}^{i,j,k+\gamma} \Lambda_{i,j-\beta,k-\gamma}^{ijk}$$
$$+ \hat{w}_{\mathrm{E}}^{i,j,k+\gamma} \Lambda_{i-\alpha,j-\beta,k}^{ijk} + \hat{w}_{\mathrm{F}}^{i,j,k+\gamma} \Lambda_{i,j-\beta,k}^{ijk} + \hat{w}_{\mathrm{H}}^{i,j,k+\gamma} \Lambda_{i-\alpha,j-\beta,k+\gamma}^{ijk} + \hat{w}_{\mathrm{I}}^{i,j,k+\gamma} \Lambda_{i,j-\beta,k+\gamma}^{ijk}$$
$$+ \hat{w}_{\mathrm{N}}^{i,j,k+\gamma} \Lambda_{i-\alpha,j,k}^{ijk} + \hat{w}_{\mathrm{O}}^{i,j,k+\gamma} \Lambda_{ijk}^{ijk} + \hat{w}_{\mathrm{Q}}^{i,j,k+\gamma} \Lambda_{i-\alpha,j,k-\gamma}^{ijk} + \hat{w}_{\mathrm{S}}^{i,j,k+\gamma} \Lambda_{i-\alpha,j,k+\gamma}^{ijk} \Big] \qquad \text{(D.23)}$$

$$\Lambda_{i+\alpha,j,k+\gamma}^{ijk} = a_{i+\alpha,j,k+\gamma} w_{\mathrm{N}}^{(i+\alpha,j,k+\gamma)} + d_{i+\alpha,j,k+\gamma} \cdot \Big[\hat{w}_{\mathrm{A}}^{i+\alpha,j,k+\gamma} \Lambda_{i-\alpha,j-\beta,k-\gamma}^{ijk} + \hat{w}_{\mathrm{B}}^{i+\alpha,j,k+\gamma} \Lambda_{i,j-\beta,k-\gamma}^{ijk}$$
$$+ \hat{w}_{\mathrm{C}}^{i+\alpha,j,k+\gamma} \Lambda_{i+\alpha,j-\beta,k-\gamma}^{ijk} + \hat{w}_{\mathrm{D}}^{i+\alpha,j,k+\gamma} \Lambda_{i-\alpha,j-\beta,k}^{ijk} + \hat{w}_{\mathrm{E}}^{i+\alpha,j,k+\gamma} \Lambda_{i,j-\beta,k}^{ijk} + \hat{w}_{\mathrm{F}}^{i+\alpha,j,k+\gamma} \Lambda_{i+\alpha,j,k}^{ijk}$$
$$+ \hat{w}_{\mathrm{G}}^{i+\alpha,j,k+\gamma} \Lambda_{i-\alpha,j-\beta,k+\gamma}^{ijk} + \hat{w}_{\mathrm{H}}^{i+\alpha,j,k+\gamma} \Lambda_{i,j-\beta,k+\gamma}^{ijk} + \hat{w}_{\mathrm{I}}^{i+\alpha,j,k+\gamma} \Lambda_{i+\alpha,j-\beta,k+\gamma}^{ijk} + \hat{w}_{\mathrm{M}}^{i+\alpha,j,k+\gamma} \Lambda_{i-\alpha,j,k}^{ijk}$$
$$+ \hat{w}_{\mathrm{N}}^{i+\alpha,j,k+\gamma} \Lambda_{ijk}^{ijk} + \hat{w}_{\mathrm{O}}^{i+\alpha,j,k+\gamma} \Lambda_{i+\alpha,j,k}^{ijk} + \hat{w}_{\mathrm{Q}}^{i+\alpha,j,k+\gamma} \Lambda_{i,j,k-\gamma}^{ijk} + \hat{w}_{\mathrm{S}}^{i+\alpha,j,k+\gamma} \Lambda_{i,j,k+\gamma}^{ijk} \Big] \qquad \text{(D.24)}$$

$$\Lambda_{i-\alpha,j+\beta,k+\gamma}^{ijk} = c_{i-\alpha,j+\beta,k+\gamma} \tilde{w}_{\mathrm{P}}^{(i-\alpha,j+\beta,k+\gamma)} + d_{i-\alpha,j+\beta,k+\gamma} \cdot \Big[\hat{w}_{\mathrm{C}}^{i-\alpha,j+\beta,k+\gamma} \Lambda_{i-\alpha,j,k-\gamma}^{ijk} + \hat{w}_{\mathrm{F}}^{i-\alpha,j+\beta,k+\gamma} \Lambda_{i-\alpha,j,k}^{ijk}$$
$$+ \hat{w}_{\mathrm{I}}^{i-\alpha,j+\beta,k+\gamma} \Lambda_{i-\alpha,j,k+\gamma}^{ijk} + \hat{w}_{\mathrm{L}}^{i-\alpha,j+\beta,k+\gamma} \Lambda_{i-\alpha,j-\beta,k}^{ijk} + \hat{w}_{\mathrm{O}}^{i-\alpha,j+\beta,k+\gamma} \Lambda_{i-\alpha,j+\beta,k}^{ijk} \Big] \qquad \text{(D.25)}$$

$$
\begin{aligned}
\Lambda^{ijk}_{i,j+\beta,k+\gamma} = {} & a_{i,j+\beta,k+\gamma} w_{\mathrm{F}}^{(i,j+\beta,k+\gamma)} + d_{i,j+\beta,k+\gamma} \cdot \Big[\hat{w}_{\mathrm{B}}^{i,j+\beta,k+\gamma} \Lambda^{ijk}_{i-\alpha,j,k-\gamma} + \hat{w}_{\mathrm{C}}^{i,j+\beta,k+\gamma} \Lambda^{ijk}_{i,j,k-\gamma} \\
& + \hat{w}_{\mathrm{E}}^{i,j+\beta,k+\gamma} \Lambda^{ijk}_{i-\alpha,j,k} + \hat{w}_{\mathrm{F}}^{i,j+\beta,k+\gamma} \Lambda^{ijk}_{ijk} + \hat{w}_{\mathrm{H}}^{i,j+\beta,k+\gamma} \Lambda^{ijk}_{i-\alpha,j,k+\gamma} \\
& + \hat{w}_{\mathrm{I}}^{i,j+\beta,k+\gamma} \Lambda^{ijk}_{i,j,k+\gamma} + \hat{w}_{\mathrm{K}}^{i,j+\beta,k+\gamma} \Lambda^{ijk}_{i-\alpha,j-\beta,k} + \hat{w}_{\mathrm{L}}^{i,j+\beta,k+\gamma} \Lambda^{ijk}_{i,j-\beta,k} \\
& + \hat{w}_{\mathrm{N}}^{i,j+\beta,k+\gamma} \Lambda^{ijk}_{i-\alpha,j+\beta,k} + \hat{w}_{\mathrm{O}}^{i,j+\beta,k+\gamma} \Lambda^{ijk}_{i,j+\beta,k} + \hat{w}_{\mathrm{P}}^{i,j+\beta,k+\gamma} \Lambda^{ijk}_{i-\alpha,j-\beta,k-\gamma} \\
& + \hat{w}_{\mathrm{Q}}^{i,j+\beta,k+\gamma} \Lambda^{ijk}_{i-\alpha,j+\beta,k-\gamma} + \hat{w}_{\mathrm{R}}^{i,j+\beta,k+\gamma} \Lambda^{ijk}_{i-\alpha,j-\beta,k+\gamma} + \hat{w}_{\mathrm{S}}^{i,j+\beta,k+\gamma} \Lambda^{ijk}_{i-\alpha,j+\beta,k-\gamma} \Big]
\end{aligned}
\tag{D.26}
$$

$$
\begin{aligned}
\Lambda^{ijk}_{i+\alpha,j+\beta,k+\gamma} = {} & a_{i+\alpha,j+\beta,k+\gamma} w_{\mathrm{E}}^{(i+\alpha,j+\beta,k+\gamma)} + d_{i+\alpha,j+\beta,k+\gamma} \cdot \Big[\hat{w}_{\mathrm{A}}^{i+\alpha,j+\beta,k+\gamma} \Lambda^{ijk}_{i-\alpha,j,k-\gamma} + \\
& + \hat{w}_{\mathrm{B}}^{i+\alpha,j+\beta,k+\gamma} \Lambda^{ijk}_{i,j,k-\gamma} \hat{w}_{\mathrm{C}}^{i+\alpha,j+\beta,k+\gamma} \Lambda^{ijk}_{i+\alpha,j,k-\gamma} + \hat{w}_{\mathrm{D}}^{i+\alpha,j+\beta,k+\gamma} \Lambda^{ijk}_{i-\alpha,j,k} \\
& + \hat{w}_{\mathrm{E}}^{i+\alpha,j+\beta,k+\gamma} \Lambda^{ijk}_{ijk} + \hat{w}_{\mathrm{F}}^{i+\alpha,j+\beta,k+\gamma} \Lambda^{ijk}_{i+\alpha,j,k} + \hat{w}_{\mathrm{G}}^{i+\alpha,j+\beta,k+\gamma} \Lambda^{ijk}_{i-\alpha,j,k+\gamma} + \\
& + \hat{w}_{\mathrm{H}}^{i+\alpha,j+\beta,k+\gamma} \Lambda^{ijk}_{i,j,k+\gamma} + \hat{w}_{\mathrm{I}}^{i+\alpha,j+\beta,k+\gamma} \Lambda^{ijk}_{i+\alpha,j,k+\gamma} + \hat{w}_{\mathrm{J}}^{i+\alpha,j+\beta,k+\gamma} \Lambda^{ijk}_{i-\alpha,j-\beta,k} \\
& + \hat{w}_{\mathrm{K}}^{i+\alpha,j+\beta,k+\gamma} \Lambda^{ijk}_{i,j-\beta,k} + \hat{w}_{\mathrm{L}}^{i+\alpha,j+\beta,k+\gamma} \Lambda^{ijk}_{i+\alpha,j-\beta,k} + \hat{w}_{\mathrm{M}}^{i+\alpha,j+\beta,k+\gamma} \Lambda^{ijk}_{i-\alpha,j+\beta,k} \\
& + \hat{w}_{\mathrm{N}}^{i+\alpha,j+\beta,k+\gamma} \Lambda^{ijk}_{i,j+\beta,k} + \hat{w}_{\mathrm{O}}^{i+\alpha,j+\beta,k+\gamma} \Lambda^{ijk}_{i+\alpha,j+\beta,k} + \hat{w}_{\mathrm{P}}^{i+\alpha,j+\beta,k+\gamma} \Lambda^{ijk}_{i,j-\beta,k-\gamma} \\
& + \hat{w}_{\mathrm{Q}}^{i+\alpha,j+\beta,k+\gamma} \Lambda^{ijk}_{i,j+\beta,k-\gamma} + \hat{w}_{\mathrm{R}}^{i+\alpha,j+\beta,k+\gamma} \Lambda^{ijk}_{i,j-\beta,k+\gamma} + \hat{w}_{\mathrm{S}}^{i+\alpha,j+\beta,k+\gamma} \Lambda^{ijk}_{i,j+\beta,k+\gamma} \Big]
\end{aligned}
\tag{D.27}
$$

Since the integration and interpolation coefficients need to be calculated only once at each considered grid point (here denoted by (u,v,w), to avoid confusion), we obtain the $\mathbf{\Lambda}$-matrix coefficients by substituting indices. For Eq. (D.1), we find:

$$
\Lambda^{ijk}_{i-\alpha,j-\beta,k-\gamma} = \Lambda^{u+\alpha,v+\beta,w+\gamma}_{uvw} = c_{uvw} \tilde{w}_{\mathrm{I}}^{uvw},
\tag{D.28}
$$

and proceed analogously for all other elements in Eqs. (D.2)-(D.27). Thus, the ALO can be calculated in parallel to the formal solution scheme.

Appendix E

Jacobi iteration with sparse matrices

In this Chapter, we briefly describe the inversion of the non-local approximate Λ-operator (Sect. 3.5.2) to calculate a new iterate of the source function. To this end, we describe the system of linear equations (Eq. 3.40) with a matrix equation $A \cdot x = b$, where A is a diagonally dominant $N \times N$ matrix, and x, b are vectors of dimension N, with N the total number of grid points within the computational domain. Such systems can be solved by applying the Jacobi-iteration (e.g., Schwarz 1997):

$$\sum_{j=1}^{N} a_{ij} x_j - b_j = 0 \qquad\qquad \forall i \in [1,N]$$

$$\overset{\text{solving for } x_i}{\Longrightarrow} \qquad \underbrace{x_i}_{\substack{=: \text{ new iterate} \\ (k+1)}} = \frac{1}{a_{ii}} \left[b_j - \sum_{\substack{j=1 \\ j \neq i}}^{N} a_{ij} \underbrace{x_j}_{\substack{=: \text{ old iterate} \\ (k)}} \right] \qquad\qquad \forall i \in [1,N]$$

$$\Longrightarrow \quad x_i^{(k+1)} = x_i^{(k)} + \frac{1}{a_{ii}} \left[b_j - \sum_{j=1}^{N} a_{ij} x_j^{(k)} \right] \qquad\qquad \forall i \in [1,N]. \qquad (E.1)$$

Thus, the calculation of $x^{(k+1)}$ mainly consists of a simple matrix-vector multiplication $A \cdot x^{(k)}$. For non-local approximate Λ-operators, the corresponding matrix A is a sparse matrix, and Eq. (E.1) can be simplified further by considering *sparse matrix-vector multiplication* algorithms (e.g., Tessem 2013). In this respect, the storage of A in sparse formats becomes particularly important due to memory limitations (see the discussion in Sect. 3.5.1). In the following, we apply the coordinate-format (COO), and store all N_{NZ} non-zero entries of A in a single array, together with the corresponding column and row indices. Thus, the storage of the (sparse) $N \times N$ matrix A is reduced to $3 \times N_{\text{NZ}}$ elements. E.g., for an (arbitrary) 3×3 matrix, the COO is defined as:

$$\begin{pmatrix} a_{11} & a_{12} & 0 \\ 0 & a_{22} & 0 \\ a_{31} & 0 & a_{33} \end{pmatrix} \longrightarrow \begin{matrix} d = & (a_{11}, & a_{12}, & a_{22}, & a_{31}, & a_{33}) \\ r = & (1, & 1, & 2, & 3, & 3) \\ c = & (1, & 2, & 2, & 1, & 3) \end{matrix} , \qquad (E.2)$$

with d, r, c describing the matrix entries with corresponding row and column indices, respectively. To calculate the matrix-vector multiplication, we can simply loop through the N_{NZ} points, since all other

terms are zero:

$$y_i = \sum_{j=1}^{N_{NZ}} d_j x_{c_j} \qquad \text{if} \qquad r_j = i \qquad \forall i \in [1, N], \tag{E.3}$$

such that $y = A \cdot x$. Within the final implementation, the if-statement is not required, and we can solve the matrix-vector-multiplication in a single loop (see also Algorithm 2 of Tessem 2013, and the example below):

Algorithm 1 Calculate $y = A \cdot x$ in COO sparse format

---

    initialize y=array(length=N, type=float, entries=0)
    initialize x=array(length=N, type=float, entries=x-vector elements)
    initialize r=array(length=N_{NZ}, type=integer, entries=row-indices of non-zero matrix elements)
    initialize c=array(length=N_{NZ}, type=integer, entries=col-indices of non-zero matrix elements)
    initialize d=array(length=N_{NZ}, type=float, entries=non-zero matrix elements)

    for $i = 1, N_{NZ}$ **do**
      $y[r[i]] \leftarrow y[r[i]] + d[i] \cdot x[c[i]]$
    end for

For instance, the 3×3 example given in Eq. (E.2) yields:

$$i = 1: \quad \underbrace{y[\overset{1}{r[1]}]}_{y_1} \leftarrow \underbrace{y[\overset{1}{r[1]}]}_{y_1} + \underbrace{d[1]}_{a_{11}} \cdot \underbrace{x[\overset{1}{c[1]}]}_{x_1} = 0 + a_{11}x_1$$

$$i = 2: \quad \underbrace{y[\overset{1}{r[2]}]}_{y_1} \leftarrow \underbrace{y[\overset{1}{r[2]}]}_{y_1} + \underbrace{d[2]}_{a_{12}} \cdot \underbrace{x[\overset{2}{c[2]}]}_{x_2} = a_{11}x_1 + a_{12}x_2$$

$$i = 3: \quad \underbrace{y[\overset{2}{r[3]}]}_{y_2} \leftarrow \underbrace{y[\overset{2}{r[3]}]}_{y_2} + \underbrace{d[3]}_{a_{22}} \cdot \underbrace{x[\overset{2}{c[3]}]}_{x_2} = 0 + a_{22}x_2$$

$$i = 4: \quad \underbrace{y[\overset{3}{r[4]}]}_{y_3} \leftarrow \underbrace{y[\overset{3}{r[4]}]}_{y_3} + \underbrace{d[4]}_{a_{31}} \cdot \underbrace{x[\overset{1}{c[4]}]}_{x_1} = 0 + a_{31}x_1$$

$$i = 5: \quad \underbrace{y[\overset{3}{r[5]}]}_{y_3} \leftarrow \underbrace{y[\overset{3}{r[5]}]}_{y_3} + \underbrace{d[5]}_{a_{33}} \cdot \underbrace{x[\overset{3}{c[5]}]}_{x_3} = a_{31}x_1 + a_{33}x_3,$$

which is just the result of the standard multiplication:

$$\begin{pmatrix} a_{11} & a_{12} & 0 \\ 0 & a_{22} & 0 \\ a_{31} & 0 & a_{33} \end{pmatrix} \begin{pmatrix} x_1 \\ x_2 \\ x_3 \end{pmatrix} = \begin{pmatrix} a_{11}x_1 + a_{12}x_2 \\ a_{22}x_2 \\ a_{31}x_1 + a_{33}x_3 \end{pmatrix}.$$

Since in each step i, only the r_i-th component of $\boldsymbol{y}$ is accessed, Algorithm 1 remains valid also if the non-zero matrix elements are not ordered according to an increasing row-index. With Eq. E.1, the Jacobi-iteration for sparse matrices in COO-format finally reads:

$$\boldsymbol{x}^{(k+1)} = \boldsymbol{x}^{(k)} + \frac{\boldsymbol{b}}{\text{diag}(\boldsymbol{A})} - \frac{\boldsymbol{y}^{(k)}}{\text{diag}(\boldsymbol{A})}, \tag{E.4}$$

where $\boldsymbol{y}^{(k)}$ is obtained from Algorithm 1 for a given iterate $\boldsymbol{x}^{(k)}$, and $\boldsymbol{b}/\text{diag}(\boldsymbol{A})$, $\boldsymbol{y}^{(k)}/\text{diag}(\boldsymbol{A})$ describe a component-wise division.

Bibliography

Abbott, B. P., Abbott, R., Abbott, T. D., Abernathy, M. R., Acernese, F., Ackley, K., Adams, C., Adams, T., Addesso, P., Adhikari, R. X., & et al. 2016: *Observation of Gravitational Waves from a Binary Black Hole Merger*, Physical Review Letters, 116, 061102

Adam, J. 1990: *Line formation in accretion disks*, A&A, 240, 541

Ahrens, C. & Beylkin, G. 2009: *Rotationally invariant quadratures for the sphere*, in Proceedings of the Royal Society A: Mathematical, Physical and Engineering Sciences, Vol. 465

Alecian, E., Wade, G. A., Catala, C., Grunhut, J. H., Landstreet, J. D., Bagnulo, S., Böhm, T., Folsom, C. P., Marsden, S., & Waite, I. 2013: *A high-resolution spectropolarimetric survey of Herbig Ae/Be stars - I. Observations and measurements*, MNRAS, 429, 1001

Amarsi, A. M., Asplund, M., Collet, R., & Leenaarts, J. 2016: *Non-LTE oxygen line formation in 3D hydrodynamic model stellar atmospheres*, MNRAS, 455, 3735

Auer, L. 2003: *Formal Solution: EXPLICIT Answers*, in Astronomical Society of the Pacific Conference Series, Vol. 288, Stellar Atmosphere Modeling, ed. I. Hubeny, D. Mihalas, & K. Werner, 3

Babel, J. & Montmerle, T. 1997: *X-ray emission from Ap-Bp stars: a magnetically confined wind-shock model for IQ Aur.*, A&A, 323, 121

Beentjes, C. H. L. 2015: *Quadrature on a Spherical Surface*, Tech. rep., University of Oxford

Bjorkman, J. E. & Cassinelli, J. P. 1993: *Equatorial disk formation around rotating stars due to Ram pressure confinement by the stellar wind*, ApJ, 409, 429

Bodenheimer, P. H. 2011, Principles of Star Formation (Springer-Verlag Berlin Heidelberg)

Braithwaite, J. 2006: *A differential rotation driven dynamo in a stably stratified star*, A&A, 449, 451

Bresolin, F., Crowther, P. A., & Puls, J., eds. 2008, IAU Symposium, Vol. 250, IAU 250 Massive Stars as Cosmic Engines

Busche, J. R. & Hillier, D. J. 2000: *An Efficient Short Characteristic Solution for the Transfer Equation in Axisymmetric Geometries Using a Spherical Coordinate System*, ApJ, 531, 1071

Busche, J. R. & Hillier, D. J. 2005: *Spectroscopic Effects of Rotation in Extended Stellar Atmospheres*, AJ, 129, 454

Cannon, C. J. 1973: *Frequency-Quadrature Perturbations in Radiative-Transfer Theory*, ApJ, 185, 621

Castor, J. I. 1972: *Radiative Transfer in Spherically Symmetric Flows*, ApJ, 178, 779

Castor, J. I., Abbott, D. C., & Klein, R. I. 1975: *Radiation-driven winds in Of stars*, ApJ, 195, 157

Charbonneau, P. & MacGregor, K. B. 2001: *Magnetic Fields in Massive Stars. I. Dynamo Models*, ApJ, 559, 1094

Cherepashchuk, A. M. 1976: *Detectability of Wolf-Rayet binaries from X rays*, Soviet Astronomy Letters, 2, 138

Collins, II, G. W. 1963: *Continuum Emission from a Rapidly Rotating Stellar Atmosphere.*, ApJ, 138, 1134

Cranmer, S. R. & Owocki, S. P. 1995: *The effect of oblateness and gravity darkening on the radiation driving in winds from rapidly rotating B stars*, ApJ, 440, 308

Cranmer, S. R. & Owocki, S. P. 1996: *Hydrodynamical Simulations of Corotating Interaction Regions and Discrete Absorption Components in Rotating O-Star Winds*, ApJ, 462, 469

Crowther, P. A., Hirschi, R., Walborn, N. R., & Yusof, N. 2012: *Very Massive Stars and the Eddington Limit*, in Astronomical Society of the Pacific Conference Series, Vol. 465, Proceedings of a Scientific Meeting in Honor of Anthony F. J. Moffat, ed. L. Drissen, C. Robert, N. St-Louis, & A. F. J. Moffat, 196

de Mink, S. E., Langer, N., Izzard, R. G., Sana, H., & de Koter, A. 2013: *The Rotation Rates of Massive Stars: The Role of Binary Interaction through Tides, Mass Transfer, and Mergers*, ApJ, 764, 166

Domiciano de Souza, A., Kervella, P., Moser Faes, D., Dalla Vedova, G., Mérand, A., Le Bouquin, J.-B., Espinosa Lara, F., Rieutord, M., Bendjoya, P., Carciofi, A. C., Hadjara, M., et al. 2014: *The environment of the fast rotating star Achernar. III. Photospheric parameters revealed by the VLTI*, A&A, 569, A10

Dufton, P. L., Dunstall, P. R., Evans, C. J., Brott, I., Cantiello, M., de Koter, A., de Mink, S. E., Fraser, M., Hénault-Brunet, V., Howarth, I. D., Langer, N., et al. 2011: *The VLT-FLAMES Tarantula Survey: The Fastest Rotating O-type Star and Shortest Period LMC Pulsar—Remnants of a Supernova Disrupted Binary?*, ApJ, 743, L22

Dufton, P. L., Langer, N., Dunstall, P. R., Evans, C. J., Brott, I., de Mink, S. E., Howarth, I. D., Kennedy, M., McEvoy, C., Potter, A. T., Ramírez-Agudelo, O. H., et al. 2013: *The VLT-FLAMES Tarantula Survey. X. Evidence for a bimodal distribution of rotational velocities for the single early B-type stars*, A&A, 550, A109

Dullemond, C. P. & Turolla, R. 2000: *An efficient algorithm for two-dimensional radiative transfer in axisymmetric circumstellar envelopes and disks*, A&A, 360, 1187

Eddington, A. S. 1925: *Circulating currents in rotating stars*, The Observatory, 48, 73

Ercolano, B., Barlow, M. J., & Storey, P. J. 2005: *The dusty MOCASSIN: fully self-consistent 3D photoionization and dust radiative transfer models*, MNRAS, 362, 1038

Ercolano, B., Barlow, M. J., Storey, P. J., & Liu, X. W. 2003: *MOCASSIN: a fully three-dimensional Monte Carlo photoionization code*, MNRAS, 340, 1136

Ercolano, B., Drake, J. J., Raymond, J. C., & Clarke, C. C. 2008: *X-Ray-Irradiated Protoplanetary Disk Atmospheres. I. Predicted Emission-Line Spectrum and Photoevaporation*, ApJ, 688, 398

Ercolano, B. & Gritschneder, M. 2011: *Ionization feedback in star formation simulations: the role of diffuse fields*, MNRAS, 413, 401

Espinosa Lara, F. & Rieutord, M. 2011: *Gravity darkening in rotating stars*, A&A, 533, A43

Fabiani Bendicho, P., Trujillo Bueno, J., & Auer, L. 1997: *Multidimensional radiative transfer with multilevel atoms. II. The non-linear multigrid method.*, A&A, 324, 161

Feldmeier, A., Puls, J., Reile, C., Pauldrach, A. W. A., Kudritzki, R. P., & Owocki, S. P. 1995: *Shocks and Shells in Hot Star Winds*, Ap&SS, 233, 293

Ferrario, L., Pringle, J. E., Tout, C. A., & Wickramasinghe, D. T. 2009: *The origin of magnetism on the upper main sequence*, MNRAS, 400, L71

Friend, D. B. & Abbott, D. C. 1986: *The theory of radiatively driven stellar winds. III - Wind models with finite disk correction and rotation*, ApJ, 311, 701

Gagnier, D., Rieutord, M., Charbonnel, C., Putigny, B., & Espinosa Lara, F. 2019: *Critical angular velocity and anisotropic mass loss of rotating stars with radiation-driven winds*, A&A, 625, A88

Gal-Yam, A., Mazzali, P., Ofek, E. O., Nugent, P. E., Kulkarni, S. R., Kasliwal, M. M., Quimby, R. M., Filippenko, A. V., Cenko, S. B., Chornock, R., Waldman, R., et al. 2009: *Supernova 2007bi as a pair-instability explosion*, Nature, 462, 624

Gayley, K. G. 1995: *An Improved Line-Strength Parameterization in Hot-Star Winds*, ApJ, 454, 410

Georgiev, L. N., Hillier, D. J., & Zsargó, J. 2006: *2D non-LTE modeling for axisymmetric winds. Method and test cases*, A&A, 458, 597

Gräfener, G., Koesterke, L., & Hamann, W.-R. 2002: *Line-blanketed model atmospheres for WR stars*, A&A, 387, 244

Gritschneder, M., Naab, T., Walch, S., Burkert, A., & Heitsch, F. 2009: *Driving Turbulence and Triggering Star Formation by Ionizing Radiation*, ApJ, 694, L26

Grunhut, J. H., Wade, G. A., Neiner, C., Oksala, M. E., Petit, V., Alecian, E., Bohlender, D. A., Bouret, J. C., Henrichs, H. F., Hussain, G. A. J., Kochukhov, O., et al. 2017: *The MiMeS survey of Magnetism in Massive Stars: magnetic analysis of the O-type stars*, MNRAS, 465, 2432

Hamann, W.-R. 1980: *The expanding envelope of Zeta Puppis - A detailed UV-line fit*, A&A, 84, 342

Hamann, W.-R. 1981: *Line formation in expanding atmospheres - On the validity of the Sobolev approximation*, A&A, 93, 353

Hauschildt, P. H. 1992: *A fast operator perturbation method for the solution of the special relativistic equation of radiative transfer in spherical symmetry*, J. Quant. Spec. Radiat. Transf., 47, 433

Hauschildt, P. H. & Baron, E. 2006: *A 3D radiative transfer framework. I. Non-local operator splitting and continuum scattering problems*, A&A, 451, 273

Hauschildt, P. H., Störzer, H., & Baron, E. 1994: *Convergence properties of the accelerated Λ-iteration method for the solution of radaitive transfer problems.*, J. Quant. Spec. Radiat. Transf., 51, 875

Hayek, W., Asplund, M., Carlsson, M., Trampedach, R., Collet, R., Gudiksen, B. V., Hansteen, V. H., & Leenaarts, J. 2010: *Radiative transfer with scattering for domain-decomposed 3D MHD simulations of cool stellar atmospheres. Numerical methods and application to the quiet, non-magnetic, surface of a solar-type star*, A&A, 517, A49

Heger, A., Fryer, C. L., Woosley, S. E., Langer, N., & Hartmann, D. H. 2003: *How Massive Single Stars End Their Life*, ApJ, 591, 288

Hennicker, L., Puls, J., Kee, N. D., & Sundqvist, J. O. 2018: *3D radiative transfer: Continuum and line scattering in non-spherical winds from OB stars*, A&A, 616, A140

Hennicker, L., Puls, J., Kee, N. D., & Sundqvist, J. O. 2019: *A 3D short-characteristics method for continuum and line scattering problems in the winds of hot stars*, A&A, accepted

Hillier, D. J. & Miller, D. L. 1998: *The Treatment of Non-LTE Line Blanketing in Spherically Expanding Outflows*, ApJ, 496, 407

Holzreuter, R. & Solanki, S. K. 2012: *Three-dimensional non-LTE radiative transfer effects in Fe I lines. I. Flux sheet and flux tube geometries*, A&A, 547, A46

Hosokawa, T., Yorke, H. W., & Omukai, K. 2010: *Evolution of Massive Protostars Via Disk Accretion*, ApJ, 721, 478

Howarth, I. D., Walborn, N. R., Lennon, D. J., Puls, J., Nazé, Y., Annuk, K., Antokhin, I., Bohlender, D., Bond, H., Donati, J.-F., Georgiev, L., et al. 2007: *Towards an understanding of the Of?p star HD 191612: optical spectroscopy*, MNRAS, 381, 433

Hubber, D. A., Ercolano, B., & Dale, J. 2016: *Observing gas and dust in simulations of star formation with Monte Carlo radiation transport on Voronoi meshes*, Monthly Notices of the Royal Astronomical Society, 456, 756

Hubeny, I. & Mihalas, D. 2014, Theory of Stellar Atmospheres (Princeton University Press)

Hummer, D. G. & Rybicki, G. B. 1985: *The Sobolev approximation for line formation with continuous opacity*, ApJ, 293, 258

Ibgui, L., Hubeny, I., Lanz, T., & Stehlé, C. 2013a: *IRIS: a generic three-dimensional radiative transfer code*, A&A, 549, A126

Ibgui, L., Hubeny, I., Lanz, T., Stehlé, C., González, M., & Chièze, J. P. 2013b: *3D Spectral Radiative Transfer with IRIS: Application to the Simulation of Laboratory Models of Accretion Shocks in Young Stellar Objects*, in Astronomical Society of the Pacific Conference Series, Vol. 474, Numerical Modeling of Space Plasma Flows (ASTRONUM2012), ed. N. V. Pogorelov, E. Audit, & G. P. Zank, 66

Jones, H. P. 1973: *The Formation of Resonance Lines in Multidimensional Media. III. Interpolation Functions, Accuracy, and Stability*, ApJ, 185, 183

Jones, H. P. & Skumanich, A. 1973: *The Formation of Resonance Lines in Multidimensional Media. II. Radiation Operators and Their Numerical Representation*, ApJ, 185, 167

Kee, N. D. 2015: *Radiative ablation of disks around massive stars*, PhD thesis, University of Delaware

Kee, N. D., Owocki, S., & Sundqvist, J. O. 2016: *Line-driven ablation of circumstellar discs - I. Optically thin decretion discs of classical Oe/Be stars*, MNRAS, 458, 2323

Keppens, R., Nool, M., Tóth, G., & Goedbloed, J. P. 2003: *Adaptive Mesh Refinement for conservative systems: multi-dimensional efficiency evaluation*, Computer Physics Communications, 153, 317

Keszthelyi, Z., Wade, G. A., & Petit, V. 2017: *The evolution of magnetic hot massive stars: Implementation of the quantitative influence of surface magnetic fields in modern models of stellar evolution*, in IAU Symposium, Vol. 329, The Lives and Death-Throes of Massive Stars, ed. J. J. Eldridge, J. C. Bray, L. A. S. McClelland, & L. Xiao, 250–254

Kozyreva, A. 2014: *Pair instability supernovae: Evolution, explosion, nucleosynthesis*, PhD thesis, Friedrich-Wilhelms-Universität Bonn

Kudritzki, R.-P. & Puls, J. 2000: *Winds from Hot Stars*, ARA&A, 38, 613

Kuiper, R. & Hosokawa, T. 2018: *First hydrodynamics simulations of radiation forces and photoionization feedback in massive star formation*, A&A, 616, A101

Kuiper, R., Turner, N. J., & Yorke, H. W. 2016: *Protostellar Outflows and Radiative Feedback from Massive Stars. II. Feedback, Star-formation Efficiency, and Outflow Broadening*, ApJ, 832, 40

Kuiper, R., Yorke, H. W., & Turner, N. J. 2015: *Protostellar Outflows and Radiative Feedback from Massive Stars*, ApJ, 800, 86

Kunasz, P. & Auer, L. H. 1988: *Short characteristic integration of radiative transfer problems - Formal solution in two-dimensional slabs*, J. Quant. Spec. Radiat. Transf., 39, 67

Kunasz, P. B. & Olson, G. L. 1988: *Short characteristic solution of the non-LTE line transfer problem by operator perturbation. II - The two-dimensional planar slab*, J. Quant. Spec. Radiat. Transf., 39, 1

Lamers, H. J. G. L. M., Cerruti-Sola, M., & Perinotto, M. 1987: *The 'SEI' method for accurate and efficient calculations of line profiles in spherically symmetric stellar winds*, ApJ, 314, 726

Lamers, H. J. G. L. M. & Morton, D. C. 1976: *Mass ejection from the O4f star Zeta Puppis.*, ApJS, 32, 715

Leenaarts, J. & Carlsson, M. 2009: *MULTI3D: A Domain-Decomposed 3D Radiative Transfer Code*, in Astronomical Society of the Pacific Conference Series, Vol. 415, The Second Hinode Science Meeting: Beyond Discovery-Toward Understanding, ed. B. Lites, M. Cheung, T. Magara, J. Mariska, & K. Reeves, 87

Lobel, A. & Blomme, R. 2008: *Modeling Ultraviolet Wind Line Variability in Massive Hot Stars*, ApJ, 678, 408

Lucy, L. B. 1967: *Gravity-Darkening for Stars with Convective Envelopes*, ZAp, 65, 89

Lucy, L. B. 1971: *The Formation of Resonance Lines in Extended and Expanding Atmospheres*, ApJ, 163, 95

Lucy, L. B. 1983: *The formation of resonance lines in locally nonmonotonic winds. II - an amplitude diagnostic*, ApJ, 274, 372

Lucy, L. B. 1999a: *Computing radiative equilibria with Monte Carlo techniques*, A&A, 344, 282

Lucy, L. B. 1999b: *Improved Monte Carlo techniques for the spectral synthesis of supernovae*, A&A, 345, 211

Lucy, L. B. 2002: *Monte Carlo transition probabilities*, A&A, 384, 725

Lucy, L. B. & Solomon, P. M. 1970: *Mass Loss by Hot Stars*, ApJ, 159, 879

Maeder, A. 1999: *Stellar evolution with rotation IV: von Zeipel's theorem and anisotropic losses of mass and angular momentum*, A&A, 347, 185

Maeder, A. & Meynet, G. 2000: *Stellar evolution with rotation. VI. The Eddington and Omega -limits, the rotational mass loss for OB and LBV stars*, A&A, 361, 159

Maeder, A. & Meynet, G. 2004: *Stellar evolution with rotation and magnetic fields. II. General equations for the transport by Tayler-Spruit dynamo*, A&A, 422, 225

Marcolino, W. L. F., Bouret, J.-C., Sundqvist, J. O., Walborn, N. R., Fullerton, A. W., Howarth, I. D., Wade, G. A., & ud-Doula, A. 2013: *Phase-resolved ultraviolet spectroscopy of the magnetic Of?p star HD 191612*, MNRAS, 431, 2253

Mason, B. D., Hartkopf, W. I., Gies, D. R., Henry, T. J., & Helsel, J. W. 2009: *The High Angular Resolution Multiplicity of Massive Stars*, AJ, 137, 3358

Mihalas, D. 1978, Stellar atmospheres (2nd edition) (San Francisco: W. H. Freeman and Co., 1978)

Mullan, D. J. 1984: *Corotating interaction regions in stellar winds*, ApJ, 283, 303

Neiner, C., Morin, J., & Alecian, E. 2015: *The "Binarity and Magnetic Interactions in various classes of stars" (BinaMIcS) project*, in SF2A-2015: Proceedings of the Annual meeting of the French Society of Astronomy and Astrophysics, 213–216

Ng, K.-C. 1974: *Hypernetted chain solutions for the classical one-component plasma up to Gamma equals 7000*, J. Chem. Phys., 61, 2680

Olson, G. L., Auer, L. H., & Buchler, J. R. 1986: *A rapidly convergent iterative solution of the non-LTE line radiation transfer problem*, J. Quant. Spec. Radiat. Transf., 35, 431

Olson, G. L. & Kunasz, P. B. 1987: *Short characteristic solution of the non-LTE transfer problem by operator perturbation. I. The one-dimensional planar slab.*, J. Quant. Spec. Radiat. Transf., 38, 325

Owocki, S. 2010: *Hot-Star Mass-Loss Mechanisms: Winds and Outbursts*, in Astronomical Society of the Pacific Conference Series, Vol. 425, Hot and Cool: Bridging Gaps in Massive Star Evolution, ed. C. Leitherer, P. D. Bennett, P. W. Morris, & J. T. Van Loon, 199

Owocki, S. P., Castor, J. I., & Rybicki, G. B. 1988: *Time-dependent models of radiatively driven stellar winds. I - Nonlinear evolution of instabilities for a pure absorption model*, ApJ, 335, 914

Owocki, S. P., Cranmer, S. R., & Gayley, K. G. 1996: *Inhibition FO Wind Compressed Disk Formation by Nonradial Line-Forces in Rotating Hot-Star Winds*, ApJ, 472, L115

Owocki, S. P., Gayley, K. G., & Cranmer, S. R. 1998: *Effects of Gravity Darkening on Radiatively Driven Mass Loss from Rapidly Rotating Stars*, in Astronomical Society of the Pacific Conference Series, Vol. 131, Properties of Hot Luminous Stars, ed. I. Howarth, 237

Owocki, S. P., Gayley, K. G., & Shaviv, N. J. 2004: *A Porosity-Length Formalism for Photon-Tiring-limited Mass Loss from Stars above the Eddington Limit*, ApJ, 616, 525

Owocki, S. P. & Rybicki, G. B. 1984: *Instabilities in line-driven stellar winds. I. Dependence on perturbation wavelength.*, ApJ, 284, 337

Owocki, S. P. & ud-Doula, A. 2004: *The Effect of Magnetic Field Tilt and Divergence on the Mass Flux and Flow Speed in a Line-driven Stellar Wind*, ApJ, 600, 1004

Owocki, S. P., ud-Doula, A., Sundqvist, J. O., Petit, V., Cohen, D. H., & Townsend, R. H. D. 2016: *An 'analytic dynamical magnetosphere' formalism for X-ray and optical emission from slowly rotating magnetic massive stars*, MNRAS, 462, 3830

Patankar, S. V. 1980, Numerical heat transfer and fluid flow, Series on Computational Methods in Mechanics and Thermal Science (Hemisphere Publishing Corporation, 1980)

Pauldrach, A., Puls, J., & Kudritzki, R. P. 1986: *Radiation-driven winds of hot luminous stars - Improvements of the theory and first results*, A&A, 164, 86

Pauldrach, A. W. A., Hoffmann, T. L., & Lennon, M. 2001: *Radiation-driven winds of hot luminous stars. XIII. A description of NLTE line blocking and blanketing towards realistic models for expanding atmospheres*, A&A, 375, 161

Penny, L. R. & Gies, D. R. 2009: *A FUSE Survey of the Rotation Rates of Very Massive Stars in the Small and Large Magellanic Clouds*, ApJ, 700, 844

Petit, V., Keszthelyi, Z., MacInnis, R., Cohen, D. H., Townsend, R. H. D., Wade, G. A., Thomas, S. L., Owocki, S. P., Puls, J., & ud-Doula, A. 2017: *Magnetic massive stars as progenitors of 'heavy' stellar-mass black holes*, MNRAS, 466, 1052

Petit, V., Owocki, S. P., Wade, G. A., Cohen, D. H., Sundqvist, J. O., Gagné, M., Maíz Apellániz, J., Oksala, M. E., Bohlender, D. A., Rivinius, T., Henrichs, H. F., et al. 2013: *A magnetic confinement versus rotation classification of massive-star magnetospheres*, MNRAS, 429, 398

Petrenz, P. & Puls, J. 1996: *Hα line formation in hot star winds: the influence of rotation.*, A&A, 312, 195

Petrenz, P. & Puls, J. 2000: *2-D non-LTE models of radiation driven winds from rotating early-type stars. I. Winds with an optically thin continuum*, A&A, 358, 956

Petrov, B., Vink, J. S., & Gräfener, G. 2016: *Two bi-stability jumps in theoretical wind models for massive stars and the implications for luminous blue variable supernovae*, MNRAS, 458, 1999

Pittard, J. M. 2009: *3D models of radiatively driven colliding winds in massive O+O star binaries - I. Hydrodynamics*, MNRAS, 396, 1743

Porth, O., Xia, C., Hendrix, T., Moschou, S. P., & Keppens, R. 2014: *MPI-AMRVAC for Solar and Astrophysics*, ApJS, 214, 4

Prilutskii, O. F. & Usov, V. V. 1976: *X rays from Wolf-Rayet binaries*, Soviet Ast., 20, 2

Puls, J. 1991: *Approximate lambda-operators working at optimum convergence rate. II - Line transfer in expanding atmospheres*, A&A, 248, 581

Puls, J., Owocki, S. P., & Fullerton, A. W. 1993: *On the synthesis of resonance lines in dynamical models of structured hot-star winds*, A&A, 279, 457

Puls, J., Springmann, U., & Lennon, M. 2000: *Radiation driven winds of hot luminous stars. XIV. Line statistics and radiative driving*, A&AS, 141, 23

Puls, J., Urbaneja, M. A., Venero, R., Repolust, T., Springmann, U., Jokuthy, A., & Mokiem, M. R. 2005: *Atmospheric NLTE-models for the spectroscopic analysis of blue stars with winds. II. Line-blanketed models*, A&A, 435, 669

Puls, J., Vink, J. S., & Najarro, F. 2008: *Mass loss from hot massive stars*, A&A Rev., 16, 209

Ramírez-Agudelo, O. H., Simón-Díaz, S., Sana, H., de Koter, A., Sabín-Sanjulían, C., de Mink, S. E., Dufton, P. L., Gräfener, G., Evans, C. J., Herrero, A., Langer, N., et al. 2013: *The VLT-FLAMES Tarantula Survey. XII. Rotational velocities of the single O-type stars*, A&A, 560, A29

Rieutord, M., Espinosa Lara, F., & Putigny, B. 2016: *An algorithm for computing the 2D structure of fast rotating stars*, Journal of Computational Physics, 318, 277

Rivero González, J. G., Puls, J., Najarro, F., & Brott, I. 2012: *Nitrogen line spectroscopy of O-stars. II. Surface nitrogen abundances for O-stars in the Large Magellanic Cloud*, A&A, 537, A79

Rivinius, T., Carciofi, A. C., & Martayan, C. 2013: *Classical Be stars. Rapidly rotating B stars with viscous Keplerian decretion disks*, A&A Rev., 21, 69

Rozanov, A. 2001: *Modeling of radiative transfer through a spherical planetary atmosphere: Application to atmospheric trace gases retrieval from occultation- and limb-measurements in UV–Vis–NIR*, PhD thesis, Universität Bremen

Rubio-Díez, M. M., Najarro, F., García, M., & Sundqvist, J. O. 2017: *Re-examing the Upper Mass Limit of Very Massive Stars: VFTS 682, an isolated ∼ 130$M_\odot$ twin for R136's WN5h core stars*, in IAU Symposium, Vol. 329, The Lives and Death-Throes of Massive Stars, ed. J. J. Eldridge, J. C. Bray, L. A. S. McClelland, & L. Xiao, 131–135

Rybicki, G. B. & Hummer, D. G. 1978: *A generalization of the Sobolev method for flows with nonlocal radiative coupling.*, ApJ, 219, 654

Rybicki, G. B. & Lightman, A. P. 1986, Radiative Processes in Astrophysics, 400

Sana, H., de Koter, A., de Mink, S. E., Dunstall, P. R., Evans, C. J., Hénault-Brunet, V., Maíz Apellániz, J., Ramírez-Agudelo, O. H., Taylor, W. D., Walborn, N. R., Clark, J. S., et al. 2013: *The VLT-FLAMES Tarantula Survey. VIII. Multiplicity properties of the O-type star population*, A&A, 550, A107

Schneider, F. R. N., Podsiadlowski, P., Langer, N., Castro, N., & Fossati, L. 2016: *Rejuvenation of stellar mergers and the origin of magnetic fields in massive stars*, MNRAS, 457, 2355

Schwarz, H. R. 1997, Numerische Mathematik (B. G. Teubner, Stuttgart 1997)

Seelmann, A. M., Hauschildt, P. H., & Baron, E. 2010: *A 3D radiative transfer framework . VII. Arbitrary velocity fields in the Eulerian frame*, A&A, 522, A102

Shaviv, N. J. 1998: *The Eddington Luminosity Limit for Multiphased Media*, ApJ, 494, L193

Simón-Díaz, S. & Herrero, A. 2014: *The IACOB project. I. Rotational velocities in northern Galactic O- and early B-type stars revisited. The impact of other sources of line-broadening*, A&A, 562, A135

Smith, N. & Owocki, S. P. 2006: *On the Role of Continuum-driven Eruptions in the Evolution of Very Massive Stars and Population III Stars*, ApJ, 645, L45

Sobolev, V. V. 1960, Moving envelopes of stars (Cambridge: Harvard University Press, 1960)

Spruit, H. C. 1999: *Differential rotation and magnetic fields in stellar interiors*, A&A, 349, 189

Spruit, H. C. 2002: *Dynamo action by differential rotation in a stably stratified stellar interior*, A&A, 381, 923

Stenholm, L. G., Stoerzer, H., & Wehrse, R. 1991: *An efficient method for the solution of 3-D radiative transfer problems*, J. Quant. Spec. Radiat. Transf., 45, 47

Stevens, I. R., Blondin, J. M., & Pollock, A. M. T. 1992: *Colliding winds from early-type stars in binary systems*, ApJ, 386, 265

Sundqvist, J. O., Owocki, S. P., & Puls, J. 2018: *2D wind clumping in hot, massive stars from hydrodynamical line-driven instability simulations using a pseudo-planar approach*, A&A, 611, A17

Sundqvist, J. O., Puls, J., & Feldmeier, A. 2010: *Mass loss from inhomogeneous hot star winds. I. Resonance line formation in 2D models*, A&A, 510, A11+

Sundqvist, J. O., ud-Doula, A., Owocki, S. P., Townsend, R. H. D., Howarth, I. D., & Wade, G. A. 2012: *A dynamical magnetosphere model for periodic Hα emission from the slowly rotating magnetic O star HD 191612*, MNRAS, 423, L21

Sweet, P. A. 1950: *The importance of rotation in stellar evolution*, MNRAS, 110, 548

Tessem, T. 2013, Master's thesis, University of Bergen

Townsend, R. H. D. & Owocki, S. P. 2005: *A rigidly rotating magnetosphere model for circumstellar emission from magnetic OB stars*, MNRAS, 357, 251

Townsend, R. H. D., Owocki, S. P., & Howarth, I. D. 2004: *Be-star rotation: how close to critical?*, MNRAS, 350, 189

Trujillo Bueno, J. & Fabiani Bendicho, P. 1995: *A Novel Iterative Scheme for the Very Fast and Accurate Solution of Non-LTE Radiative Transfer Problems*, ApJ, 455, 646

ud-Doula, A., Owocki, S., Townsend, R., Petit, V., & Cohen, D. 2014: *X-rays from magnetically confined wind shocks: effect of cooling-regulated shock retreat*, MNRAS, 441, 3600

ud-Doula, A. & Owocki, S. P. 2002: *Dynamical Simulations of Magnetically Channeled Line-driven Stellar Winds. I. Isothermal, Nonrotating, Radially Driven Flow*, ApJ, 576, 413

ud-Doula, A., Owocki, S. P., & Townsend, R. H. D. 2008: *Dynamical simulations of magnetically channelled line-driven stellar winds - II. The effects of field-aligned rotation*, MNRAS, 385, 97

ud-Doula, A., Sundqvist, J. O., Owocki, S. P., Petit, V., & Townsend, R. H. D. 2013: *First 3DMHD simulation of a massive-star magnetosphere with application to Hα emission from θ^1 Ori C*, MN-RAS, 428, 2723

van Loon, J. T. 2010: *The Effects of Red Supergiant Mass Loss on Supernova Ejecta and the Circumburst Medium*, in Astronomical Society of the Pacific Conference Series, Vol. 425, Hot and Cool: Bridging Gaps in Massive Star Evolution, ed. C. Leitherer, P. D. Bennett, P. W. Morris, & J. T. Van Loon, 279

van Noort, M., Hubeny, I., & Lanz, T. 2002: *Multidimensional Non-LTE Radiative Transfer. I. A Universal Two-dimensional Short-Characteristics Scheme for Cartesian, Spherical, and Cylindrical Coordinate Systems*, ApJ, 568, 1066

Vanbeveren, D. 1991: *The evolution of massive close binaries revised.*, A&A, 252, 159

Vath, H. M. 1994: *Three-dimensional radiative transfer on a massively parallel computer*, A&A, 284, 319

Vink, J. S., de Koter, A., & Lamers, H. J. G. L. M. 1999: *On the nature of the bi-stability jump in the winds of early-type supergiants*, A&A, 350, 181

von Zeipel, H. 1924: *The radiative equilibrium of a rotating system of gaseous masses*, MNRAS, 84, 665

Wade, G. A., Grunhut, J. H., & MiMeS Collaboration. 2012: *The MiMeS Survey of Magnetism in Massive Stars*, in Astronomical Society of the Pacific Conference Series, Vol. 464, Circumstellar Dynamics at High Resolution, ed. A. C. Carciofi & T. Rivinius, 405

Wade, G. A., Howarth, I. D., Townsend, R. H. D., Grunhut, J. H., Shultz, M., Bouret, J.-C., Fullerton, A., Marcolino, W., Martins, F., Nazé, Y., Ud Doula, A., et al. 2011: *Confirmation of the magnetic oblique rotator model for the Of?p star HD 191612*, MNRAS, 416, 3160

Walborn, N. R., Sana, H., Taylor, W. D., Simón-Díaz, S., & Evans, C. J. 2012: *Two Remarkable Spectroscopic Categories of Young O Stars from the VLT-FLAMES Tarantula Survey*, in Astronomical Society of the Pacific Conference Series, Vol. 465, Proceedings of a Scientific Meeting in Honor of Anthony F. J. Moffat, ed. L. Drissen, C. Robert, N. St-Louis, & A. F. J. Moffat, 490

Walder, R., Folini, D., & Meynet, G. 2012: *Magnetic Fields in Massive Stars, Their Winds, and Their Nebulae*, Space Sci. Rev., 166, 145

Weber, J. A., Pauldrach, A. W. A., Knogl, J. S., & Hoffmann, T. L. 2013: *Three-dimensional modeling of ionized gas. I. Did very massive stars of different metallicities drive the second cosmic reionization?*, A&A, 555, A35

White, R. L., Becker, R. H., Fan, X., & Strauss, M. A. 2003: *Probing the Ionization State of the Universe at z>6*, AJ, 126, 1

Willott, C. J., Delfosse, X., Forveille, T., Delorme, P., & Gwyn, S. D. J. 2005: *First Results from the Canada-France High-z Quasar Survey: Constraints on the z = 6 Quasar Luminosity Function and the Quasar Contribution to Reionization*, ApJ, 633, 630

Woosley, S. & Janka, T. 2005: *The physics of core-collapse supernovae*, Nature Physics, 1, 147

Woosley, S. E. 1993: *Gamma-ray bursts from stellar mass accretion disks around black holes*, ApJ, 405, 273

Woosley, S. E. & Heger, A. 2006: *The Supernova Gamma-Ray Burst Connection*, in American Institute of Physics Conference Series, Vol. 836, Gamma-Ray Bursts in the Swift Era, ed. S. S. Holt, N. Gehrels, & J. A. Nousek, 398–407

Xia, C., Teunissen, J., El Mellah, I., Chané, E., & Keppens, R. 2018: *MPI-AMRVAC 2.0 for Solar and Astrophysical Applications*, ApJS, 234, 30

Yorke, H. W. & Sonnhalter, C. 2002: *On the Formation of Massive Stars*, ApJ, 569, 846

Zahn, J.-P. 1992: *Circulation and turbulence in rotating stars*, A&A, 265, 115

Zahn, J. P., Brun, A. S., & Mathis, S. 2007: *On magnetic instabilities and dynamo action in stellar radiation zones*, A&A, 474, 145

Zsargó, J., Hillier, D. J., & Georgiev, L. N. 2006: *2D non-LTE modeling for axi-symmetric winds. II. A short characteristic solution for radiative transfer in rotating winds*, A&A, 447, 1093

Zsargó, J., Hillier, D. J., & Georgiev, L. N. 2008: *Axi-symmetric models of B[e] supergiants. I. The effective temperature and mass-loss dependence of the hydrogen and helium ionization structure*, A&A, 478, 543

Acknowledgements

First and foremost, I would like to express my deep gratitude to my supervisor Jo Puls, for all the time and effort he invested into my scientific education. I am very thankful, not only for supporting me during this thesis work with new suggestions and ideas, but indeed for virtually everything I learned from him during the last few years. Without his support, this thesis would not have been realized. In particular, I am deeply grateful for the many discussions we had, his mere endless patience and his honesty, and for encouraging me to face various problems that appeared during this thesis work. Not only I am thankful within the scientific context, but also for many funny moments we experienced together, if at lunch, or during the one or other biking trip. I really appreciate this exceptional supervision.

Many thanks are also to my colleagues Jon Sundqvist and Dylan Kee for many fruitful discussions about several interesting topics related to astronomy. In this respect, I am particularly grateful for the expertise of these two persons, which they always were eager to share. I am looking forward to continue the collaboration in the near future, and hopefully also for the next years and maybe even decades.

Very special thanks are also dedicated to my family, friends, and their unsurpassed fellowship. All of these people were always so incredibly interested in my work, and in my personal happiness and well-being. They provided so much fun and love, and always could make me laugh when needed. In the end, their friendship gave me the strength to handle even the (admittedly only few) bad phases during the last few years (and for all the years before). Although everyone would deserve to be named personally here, I will only mention the two most important groups in the following, namely my good friends from the football team and the complete 'Pasing-connection', as well as my friends from the schooldays within the 'Neuhausen-connection'. By name, I want to particularly thank my parents Eva-Maria and Rolf, my twin brother, best friend and certainly best part of my life, Luca, together with his girlfriend Hanna, and my long-term flatmates Bianca and Katrin, with whom I spent most of my free time in the last few years.